MULTIPHASE PHENOMENA

IN A VIBRATING COLUMN REACTOR

By

ADAM LELAND STILL

Bachelor of Science

Oklahoma State University

Stillwater, Oklahoma

2010

Submitted to the Faculty of the
Graduate College of the
Oklahoma State University
in partial fulfillment of
the requirements for
the Degree of
MASTER OF SCIENCE
July, 2012

MULTIPHASE PHENOMENA

IN A VIBRATING COLUMN REACTOR

Thesis Approved:

Dr. Afshin J. Ghajar

Thesis Adviser

Dr. Frank W. Chambers

Dr. Khaled A. Sallam

Dr. Sheryl A. Tucker

Dean of the Graduate College

ACKNOWLEDGMENTS

"Entrust your works to the Lord and your plans will succeed." – Proverbs 16:3

I would first like to give thanks to God, who established the guiding principles by which bubbles form and travel and all the complexities of multiphase fluid dynamics, who made me, and who ultimately led me to the opportunity to explore these mysteries.

Thanks to the faculty, staff and students at Oklahoma State University who helped this project come to life. To my advisor Dr. A.J. Ghajar who listened enough to let me find my own answer, pushed me enough to question it, and believed enough to let me test it. Also, many thanks to my committee members Dr. K.A. Sallam and Dr. F.W. Chambers whose instruction have contributed both to my knowledge of fluids and to this work. I would like to thank Dr. R.D. Delahoussaye for his particularly valuable insight concerning vibrating machines, linkages and mechanisms, without which this project would have been much easier and far less successful. Considerable thanks go to Swanand Baghwat for navigating the mire of purchasing and tracking parts as well as Erik Gonzales and Dr. Rosenberger for their donation of expertise in optics and use of the lab respectively. My thanks go to John Gage, Chris and Collin at the manufacturing lab for their considerable expertise and assistance in transforming my designs into realities. I would also like to thank my assistant Luke Walker for spending his free time to help on this project. There is no currency more valuable than knowledge.

I would like to acknowledge Dr. Timothy O'Hern and Sandia National Laboratories who provided the funding for this project and my graduate studies, and my manager John Lorio who provided both flexibility and understanding so that I could complete this task.

Finally I would be remiss if I didn't thank my family for their support through the course of this work. I would like to thank my parents. Thanks also go to my wife Natalie who was wise enough to tell me when to relax, and stern enough to get me to work. Finally, to my children Ella and Connor who provided the best distractions.

TABLE OF CONTENTS

Chapter Page

LIST OF TABLES

LIST OF FIGURES

Figure Page

Figure Page

Figure Page

Figure Page

Figure Page

Figure Page

Figure Page

NOMENCLATURE

A	Amplitude of vibration (m)
A_{cs}	Cross Sectional flow area (m^2)
A_{proj}	Projected two dimensional area (m^2)
a	Interfacial surface area (surface area per unit mixture volume; m^{-1})
$\tilde{a}$	Complex variable in Mathieu equation
Bj	Bjerknes number ($\rho HA^2\omega^4/2gp_e$)
C	Dissolved oxygen concentration (mg/L)
C^*	Dissolved oxygen concentration at saturation or equilibrium (mg/L)
C_D	Drag coefficient
C_d	Baffle discharge coefficient
C_f	Coefficient of friction
d_b	Bubble diameter (m)
d_e	Volume equivalent diameter (m)
d_{eq}	Area equivalent diameter (m)
d_{32}	Sauter mean diameter (m)
F	Force (N)
f	Frequency (s^{-1})
g	Gravitational acceleration (m/s^2)
h	Liquid height above point of interest (m)
H	Total liquid column height (m)

h_T	Henry's constant
I	Light intensity
K	Correlation constant used by Buchanan et al. (1962)
k	Correlation constant used by Oliveira and Ni (2001)
k_L	Liquid mass transfer coefficient (m/s)
k_La	Volumetric mass transfer coefficient (s^{-1})
m	Mass of a particle (kg)
N_b	Number of baffles per unit length (m^{-1})
n	Index of refraction
P	Power (W)
P_m	Specific power input (W/kg)
p_e	External or ambient pressure (Pa)
p_s	Hydrostatic pressure (Pa)
p_T	Total pressure (Pa)
p_v	Vibration pressure (Pa)
ΔP	Differential pressure (Pa)
Q_G	Gas phase flow rate (m^3/s)
q	Complex variable in Mathieu equation
R	Column radius (m)
Re	Reynolds number (Ud/ν)
Re_v	Vibration Reynolds number ($\omega A r_0/\nu$)
r	Bubble radius (m)
r_0	Mean bubble radius (m)
s	Signal Voltage (V)
t	Time (s)

U_b	Bubble velocity (m/s)
U_G	Gas phase velocity (m/s)
U_{SG}	Superficial gas velocity (m/s)
u	Fluid velocity (m/s)
u_p	Particle velocity (m/s)
V	Volume (m^3)
V_G	Gas phase volume (m^3)
V_L	Liquid phase volume (m^3)
V_p	Particle volume (m^3)
V_0	Initial bubble volume (m^3)
ΔV	Change in bubble volume (m^3)
x_i	Liquid phase mole fraction
y_i	Gas phase mole fraction
z	Vertical position of a fluid body (m)

Greek characters

γ	Liquid specific weight (-)
ε	Void fraction (gas holdup) (-)
θ	Incidence angle (deg)
λ	Complex variable related to particle terminal velocity in Mathieu equation
μ	Dynamic liquid viscosity (Pa-s)
ν	Kinematic liquid viscosity (m/s)
π	Number pi (3.1416)
ρ	Liquid phase density (kg/m^3)
ρ_G	Gas phase density (kg/m^3)
ρ_p	Particle density (kg/m^3)

σ	Liquid-gas surface tension (N/m)
τ	Complex variable in Mathieu equation
ϕ_U	Conductivity signal
χ	Coefficient of virtual mass in Langevin equation
ω	Angular frequency (rad/s)
ω_c	Cut-out frequency (rad/s)
ω_s	Stabilization frequency (rad/s)

Subscripts

b	Bubble
c	Characteristic
G	Gas phase
i	Gas species placeholder or Gas Injector when referring to diameter
L	Liquid phase
m	Manometer fluid or mass specific as in the case of specific input power
U	Flow condition
v	Vibrational
0	Initial or static condition; incident
1	Final or secondary condition; optical medium 1
2	Optical medium 2
avg	Average
max	Maximum

Abbreviations

AC	Alternating current
BCR	Bubble column reactor
CCD	Charge coupled device
CMC	Carboxy-methyl-cellulose
CMOS	Complementary metal-oxide semiconductor
CT	Computer tomography
DO	Dissolved oxygen
HM	Harmonic mode
ID	Inner diameter
OD	Outer diameter
2D	Two dimensional
3D	Three dimensional

CHAPTER I

INTRODUCTION

Multiphase flow is a complicated and unique combination of two or more phases interacting in a distinct flow pattern. There are many situations in which two or three phases will be present with a real system. It is important in the application of engineered systems to understand how each of the phases interacts with the boundary conditions and with each other to produce the overall flow condition. Multiphase flows are often present in piping networks and reactors used in the petroleum and chemical processing industry. In some cases, two phases are introduced together specifically to interact with each other, such as in the case of a bubble column reactor (BCR). BCRs operate by introducing gas into a liquid or liquid-solid mixture in order to dissolve the gas into the mixture. BCRs have many applications which are important to industry and they provide a unique advantage of being simple, cheap and relatively easy to operate.

There are many applications for BCRs including being used for aeration of organic organisms in bio-reactors, hydrogenation of coal-slurries to produce synthetic fuels used in the Fischer-Tropsch process, and gasification of solvent for chemical reactions. Over the past 5 years several military and civilian aircraft have been qualified for and started to fly with synthetic fuel blends produced from the Fischer-Tropsch process. In fact, United State Air Force fighters and bombers including the A-10, C-17, KC-135, and F-22 have been approved to fly with synthetic fuel as well as A380 and other civilian passenger aircraft flying overseas and international flights (U.S. Department of Defense, 2010; U.S. Air Force 2007; Vogelaar, 2011; Vogelaar, 2010). Domestic flights within the US have even begun using synthetic fuel blends as United Airlines

ran a first flight demonstration in an Airbus A319 (Environmental Leader, 2010). As synthetic fuels become more and more prevalent in our society it becomes increasing critical to improve efficiency in production tools and methodologies, namely BCRs.

It was discovered in the early 60's that vibration could help improve efficiency in BCR processes by increasing mass transfer rate. Some additional research expanded the theory, but it was not until the early 2000's that the science was reinvigorated. Recent research has gone so far as to develop theoretical, physics based models to try and predict mass transfer and void fraction in BCR systems undergoing vibration. These models were tested in a limited manner, but have yet to be fully understood or validated against a large body of experimental data. Additionally, there is still a need for fundamental research to understand the multiphase flow properties in vibrating systems including those for vibrating BCR or other related systems.

Therefore, a fundamental understanding of the multiphase flow properties such as void fraction and bubble size distribution as well as the related mass transfer properties are crucial to understanding and thereby improving the operation of BCRs. Improving efficiency of BCRs is a necessary step to improving the lives of people who use these products daily. It is with this concept in mind that the current research is carried out. The purpose of this research is to design, build, and validate an experimental set up, and to conduct experiments with the set up that increase the understanding of multiphase flow in a vibrating bubble column reactor.

CHAPTER II

LITERATURE REVIEW

A review of the relevant literature pertaining to multiphase flow in bubble columns was performed. The literature can be divided into three sections. The first section provides a brief history of the most pertinent work including the fundamentals of the suspected physical forces driving the phenomena. Since this work is largely experimental the second section will give a summary of previous researcher's experiments including: testing procedures, equipment, and results. Finally a short foray into related and relevant literature is presented to provide a platform for some of the technologies and methods used in this research.

Before proceeding it may be beneficial to review some of the common physical properties and definitions typically used. The product of mass transfer coefficient (k_L**)** and interfacial surface area per unit mixture volume (a) gives rise to the volumetric mass transfer coefficient, (k_La) which is often used to indicate the rate at which chemical reactions are occurring. For simplicity, the volumetric mass transfer coefficient (k_La) will generally be referred to as the mass transfer rate. Specific to a bubble column reactor (BCR) and other aerated systems, k_La provides the rate at which a gas is dissolved into a liquid based upon the concentration gradient by,

$$\frac{dC}{dt} = k_L a\left(C^* - C\right) \tag{2.1}$$

where C is the concentration of dissolved gas in the liquid, C^* is the saturation concentration and t represents time. The interfacial area of a bubble (a) can be determined by the mean bubble diameter (d_b) and the void fraction (gas holdup) (ε) if the bubble is considered to be uniformly spherical by,

$$a = 6\frac{\varepsilon}{d_b} \tag{2.2}$$

However, it should be noted that this is an approximation used by some to simplify large reactor systems, or for the purpose of modeling (Xue, 2004; Knopf et al., 2005a; Waghmere et al., 2008). Experimentally, the bubbles are observed to be smaller ($d_b < 5\,\text{mm}$) in vibrating column reactors due to hydrodynamic breakup (Harbaum and Houghton, 1962), but the spherical bubble assumption is generally considered good for smaller diameters due to capillary effects ($d_b < 2$ mm) (Raju, 2011). Also, in most instances the bubble surface geometry can be seen to constantly change as it is formed and rises (Minnaert, 1933; Manasseh et al. 2001; Kulkarni and Joshi, 2005). This oscillation affects both the bubble volume and the shape, but it is generally noted that the shape oscillations primarily influence mass transfer at the interface (Ghiaasiaan, 2008) which is important to this study.

Void fraction is often required to derive specific interfacial area and hence the volumetric mass transfer coefficient as discussed. The void fraction is defined as the ratio of volume occupied by the gas phase (V_G) to the total volume ($V_G + V_L$)in a multiphase system given by,

$$\varepsilon = \frac{V_G}{V_L + V_G} \tag{2.3}$$

There have been various attempts to classify the size of the bubble by a characteristic length. A few researchers have measured bubble chord length, and they presented the bubble size as a as a probability distribution with a representative mean diameter (Wu et al., 2008; Xue et al.,

2008a; Xue et al., 2008b). The advantage of this method is that it does not have to rely on the assumption of a spherical bubble. Many researchers, however, prefer to use a mean bubble diameter based upon the Sauter mean diameter (d_{32}) calculated as the ratio of the representative bubble volume to the bubble area (Oliviera and Ni, 2001; Krishna et al., 2000; Waghmare et al., 2008),

$$d_{32} = \frac{\sum_{i=1}^{n} n_i d_{b,i}^3}{\sum_{i=1}^{n} n_i d_{b,i}^2} \tag{2.4}$$

The Sauter mean diameter is usually preferred when photographic methods are used to measure projected bubble areas from two dimensional (2D) pictures. Assuming a spherical bubble gives the equivalent diameter of each bubble by (Oliviera and Ni, 2001),

$$d_{eq} = \sqrt{\frac{4}{\pi} A_{proj}} \tag{2.5}$$

The equivalent diameter is used in Eq. (2.4) to calculate the bubble mean diameter for each experiment.

Another critical element in BCR research is the velocity of the gas phase within the liquid medium, and is typically quoted in terms of superficial gas velocity (U_{SG}) or bubble velocity (U_b). Superficial gas velocity is not the true phase velocity like the bubble velocity but rather is a representation of the area or volume averaged phase velocity. U_{SG} can be written in terms of void fraction and average velocity of the gas phase (U_G) by,

$$\langle U_{SG} \rangle = \frac{Q_G}{A_{cs}} = \langle \varepsilon \rangle \langle U_G \rangle \tag{2.6}$$

Bubble velocity (U_b) or gas velocity (U_G) is seen in the literature as a measure of the actual phase velocity, but it should be noted that U_b is used as a specific description of a particular condition in which individual bubbles or clouds are noted or measured. In stationary bubble columns with no flow U_b is simply the rise velocity. However, when there is flow in/out of the column, or when the fluid column is moving U_b can be related to the slip velocity and the void fraction typically through a correlation (Ellenberger and Krishna, 2003). Specifically in the case of an oscillating BCR, U_b is an important indication of the forces acting on the bubble as will be discussed in the following sections.

2.1. History of Vibrating BCR Research

2.1.1. Harbaum and Houghton

The first evidence of vibrating a BCR is documented by Harbaum and Houghton (1960). After noting the work of Minnaert (1933), Smith (1935), and others they reasoned that vibrating a bubbly flow could have an impact on mass and heat transfer, and attempted to measure the effect of frequency and amplitude of sonic vibrations on the rate of CO_2 absorption in a column of water. In their work the absorption rate of CO_2 was seen to peak at particular frequencies. In their follow on work, Harbaum and Houghton (1962) showed that mass transfer rate (k_La) was not necessarily linked to the amplitude or the input power, but could be "attributed to 'resonance effects' associated with frequency alone." Furthermore their work began to differentiate the frequency effects on k_L and a individually. The results (Figure 2.1) showed an increase in mass transfer was primarily due to an increase in interfacial area (a) caused by an increase in void fraction (ε) at specific frequencies rather than an increase in mass transfer coefficient (k_L) which showed a marked dip at the same frequency.

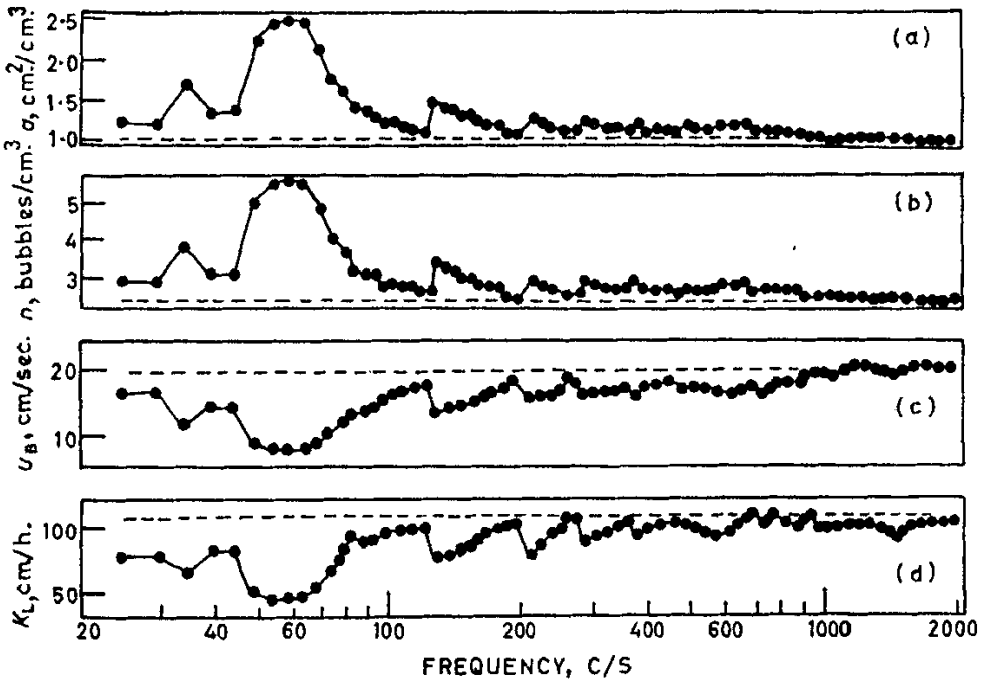

Figure 2.1: Effect of vibration frequency on interfacial area, bubble number density, bubble velocity and mass transfer for a water column with CO_2 (Harbaum and Houghton, 1962)

Observations made by Harbaum and Houghton (1962) indicated that vibration causes the bubbles to become smaller and more spherical, but tends to elongate the bubbles in the direction of motion. No qualitative discussion of bubble size was offered in that particular work. Houghton continued his work on particles suspended in a sinusoidal velocity field by approaching the problem using a force balance on the particle (Houghton 1963). The velocity of the fluid (u) is described by (Appendix A),

$$u = A\omega\cos(\omega t) \tag{2.7}$$

The following force balance can be made on a particle in the fluid medium.

$$\begin{gathered}(\rho_p + \chi\rho)V_\rho \frac{du_p}{dt} = (\rho - \chi\rho_p)V_\rho g - C_D|u_p - u|^n \operatorname{sgn}(u_p - u) + (1+\chi)\rho V_\rho \frac{du}{dt} + B(t) \\ \operatorname{sgn}(u_p - u) = \begin{cases} 1, u_p - u > 0 \\ -1, u_p - u < 0 \end{cases}\end{gathered} \tag{2.8}$$

Equation (2.8) is called a non-linear Langevin equation where χ is termed the "coefficient of virtual mass" and represents the additional portion of inertia attributed to the mass of fluid displaced with the particle during oscillation. χ has been experimentally found to be near 0.5 and is assumed to be such for calculations. The assumed constants are: fluid density (ρ), particle density (ρ_p), particle volume (V_p), and gravitational acceleration (g). C_D represents the overall drag coefficient which is assumed to be a lumped term constituting both the profile and pressure drag. The second term thus describes the friction forces acting opposite to the motion of the particle, and is modeled as an *n*th power drag law for spherical bodies in a motionless fluid where n = 1 would represent Stoke's flow and n = 2 would represent a typical viscid flow with a separated boundary layer. The sgn function is applied to show that the direction of the drag force is dependent on the condition that the particle is moving faster or slower than the fluid medium. The third term describes the "virtual mass" force as the mass of fluid volume displaced by the particle (bubble) accelerating with the fluid. Finally the fourth term on the right is simply a transient drag component caused by a deviation from streamline flow given by (Houghton, 1963):

$$B(t) = C_D r\left(\frac{\rho}{\pi\mu}\right)^{1/2} \int_0^t \left(\frac{du_p}{dt'} - \frac{du}{dt'}\right) \frac{dt'}{\sqrt{t-t'}} \tag{2.9}$$

It can be shown that Eq. (2.8) will decompose to a linearized steady state solution similar to a Mathieu equation, assuming n = 2 and the transient ($B(t)$) goes to zero, given by (Houghton, 1963),

$$\frac{d^2\psi}{d\tau^2} + \left(\tilde{a} - 2q\cos(2\tau)\right)\psi = 0 \tag{2.10}$$

where,

$$\tilde{a} = -\left(\frac{4\beta^2}{\omega^2}\right)\left(\lambda + \frac{B(t)}{C_D}\right)\mathrm{sgn}\left(u_p - u\right)$$

$$q = 2\beta A\left(\frac{\beta}{\alpha} - 1\right)\mathrm{sgn}\left(u_p - u\right)$$

$$\tau = \frac{1}{2}\omega t$$

The Mathieu equation is "modified" in that $\tilde{a}$ is not a constant, being a function of the transient (*B(t)*). However, transient effects should go to zero as the system goes to a steady state or $\lim_{t\to\infty} B(t) = 0$, and has been seen to be true experimentally in examining time dependence of C_D in air flows over spheres (Torobin and Gauvin, 1961). Therefore the transient term can be ignored.

The particle displacement (*z*) is related to ψ by the following:

$$\psi = \exp\left(\beta z + \beta A\,\mathrm{sgn}\left(u_p - u\right)\cos\left(\omega t\right)\right) \tag{2.11}$$

where,

$$\beta = C_D / V_p\left(\rho_p + \chi\rho\right) \tag{2.12}$$

$$\lambda = gV_p\left(\rho - \rho_p\right)/C_D \tag{2.13}$$

$$\alpha = C_D / \rho V_p\left(1 + \chi\right) \tag{2.14}$$

While the equations above are complex to solve analytically they can be interpreted easily using the Mathieu stability diagram (Figure 2.2), where the shaded regions are stable solutions to Eq. (2.11).

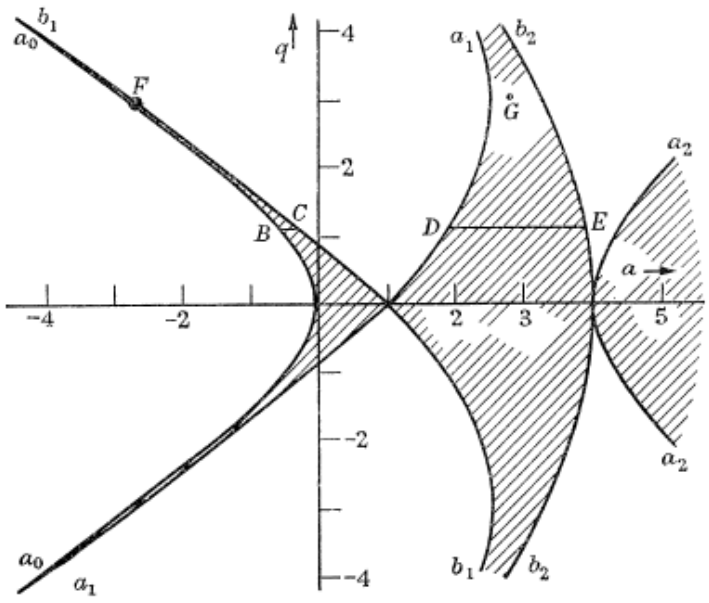

Figure 2.2: Mathieu stability diagram (Houghton, 1963)

The important implication is that careful selection of the frequency and amplitude will result in a stable trajectory of the particle (bubble). In other words, choosing ω and A such that the product of $\tilde{a}$ and q are positive will result in a motionless bubble (with respect to a fixed reference). However, there are cases as seen in Figure 2 in which it is possible to achieve partial stability when the product of $\tilde{a}$ and q are not positive. These small partial stability regions are then dominated by the "terminal velocity" term (λ), which is a function of the fluid and bubble densities, drag coefficient, and bubble volume. Thus, "it should therefore be possible to predict the behavior of particles in an oscillating fluid by the use of drag coefficients obtained from measurements of the terminal velocity" (Houghton, 1963).

2.1.2. Buchanan, Jameson, and Oedjoe

Following Harbaum and Houghton (1960, 1962), Buchanan et al. (1962) explored the effect of vibration on bubble migration in a liquid column. They were the first to report unified bubble migration which acts against buoyancy at certain frequencies, and a critical frequency at

which bubbles can be seen to become stable. A critical frequency was derived with the help of electromagnetic–hydrodynamic analogies (Bjerknes, 1906) as shown below (Buchanan et al., 1962).

Imagine a bubble placed at a location, (h) below the surface of a fluid body undergoing an oscillatory motion defined by,

$$z = A\sin(\omega t) \tag{2.15}$$

where z is the position relative to a fixed position, A is the amplitude and ω is the angular frequency at any time, t as shown in Figure 2.3.

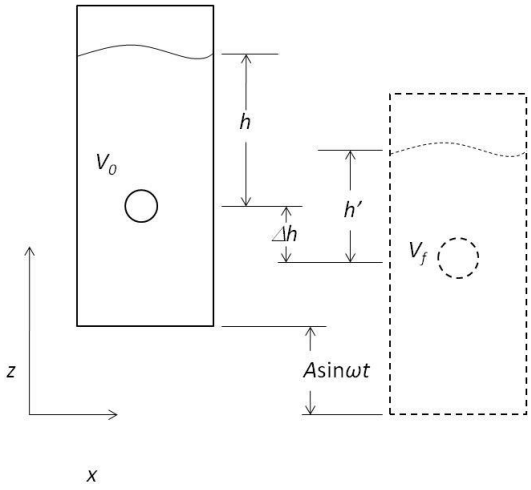

Figure 2.3: Diagram of bubble motion in an oscillating fluid column

The following assumptions can be made:

1. The bubble's resonant pulsation frequency is greater than the vibration frequency
2. The bubble is large enough to neglect surface tension effects
3. The bubble expands and contracts isothermally
4. Bubble internal pressure follows Boyle's law
5. Spherical momentum effects caused by the bubble surface oscillation are negligible

The instantaneous total pressure can be described by,

$$p_T = p_e + p_s + p_v \tag{2.16}$$

where p_e is the ambient pressure, p_s is the hydrostatic pressure and p_v is the pressure due to vibration. The vibration pressure is given by Buchanan et al. (1962),

$$p_v = -\rho h \omega^2 A \sin \omega t \tag{2.17}$$

where ρ is the fluid density. Therefore utilizing the hydrostatic equation the total pressure can be expressed as,

$$p_T = p_e + \rho g h - \rho h \omega^2 A \sin(\omega t) \tag{2.18}$$

Next, the instantaneous bubble volume is taken to be,

$$V = V_0 + \Delta V \sin(\omega t) \tag{2.19}$$

where V_0 is the initial bubble volume at $p_v = 0$ and ΔV is the minimum or maximum volume displacement about V_0. By combining Eqs. (2.18) and (2.19) and drawing upon Boyle's law ($p_0 V_0 = p_1 V_1$) it can be shown that,

$$\frac{\Delta V \sin(\omega t)}{V_0} = \frac{\rho h \omega^2 A \sin(\omega t)}{p_0 - \rho h \omega^2 A \sin(\omega t)} \tag{2.20}$$

Examining the relationship closely reveals that the ratio is at a maximum at $\sin(\omega t) = 1$, or in practical terms when the fluid column is at the top of its stroke. Therefore Eq. (2.20) is reduced to,

$$\frac{\Delta V_{\max}}{V_0} = \frac{\rho h \omega^2 A}{p_0 - \rho h \omega^2 A} \tag{2.21}$$

where p_0 is simply the total pressure at the initial condition,

$$p_0 = p_e + \rho g h \tag{2.22}$$

Bjerknes (1906) makes the following claim:

"Any body which participates in the translator motion of a fluid mass is subject to a kinetic buoyancy equal to the product of the acceleration of the translator motion multiplied by the mass of [fluid] displaced by the body"

Applying this principle to a force balance on the bubble gives,

$$F(t) = \rho(V_0 + \Delta V \sin(\omega t))g - \rho(V_0 + \Delta V \sin(\omega t))A\omega^2 \sin(\omega t) \tag{2.23}$$

(Note: Buchanan et al. (1962) erroneously neglects the liquid density term in their derivation. Addition of the term is required to properly account for the mass of the fluid and is added in the revised derivation offered by Waghmare (2008)). Simplifying gives,

$$F(t) = \rho(V_0 + \Delta V \sin(\omega t))(g - \omega^2 A \sin(\omega t)) \tag{2.24}$$

The instantaneous force can be integrated over a complete period to give the average force,

$$F_{avg} = \frac{1}{T}\int_0^T F(t)dt = \rho\left(V_0 g - \frac{1}{2}\omega^2 A \Delta V_{\max}\right) \tag{2.25}$$

The motion of the bubble (relative to the fluid) will be zero when the average force is zero giving,

$$\frac{\Delta V_{\max}}{V_0} = \frac{2g}{\omega^2 A} \tag{2.26}$$

Therefore, a critical frequency (ω_s) at which this stationary bubble motion exists can be found by manipulating equations (2.26) and (2.21) to give,

$$\omega_s^{\,2} A = \mp\left(g + \sqrt{3g^2 + \frac{2gp_e}{\rho h}} \right) \tag{2.27}$$

It is important to note that the selection of minus/plus for the right hand side of the equation corresponds to the relative maximum or minimum of the bubble volume achieved at the top and bottom of the stroke as would be expected for oscillatory motion. Buchanan et al. (1962) is mainly concerned with finding this frequency and another "cut-out" frequency (ω_c) which is related to the stabilization frequency by,

$$\omega_s^{\,2} = K\omega_c^{\,2} \tag{2.28}$$

where K is a correlation coefficient. The value of K was found to be nearly 1 showing that there was a good agreement between the stabilization frequency and the cut-out frequency (Figure 2.4).

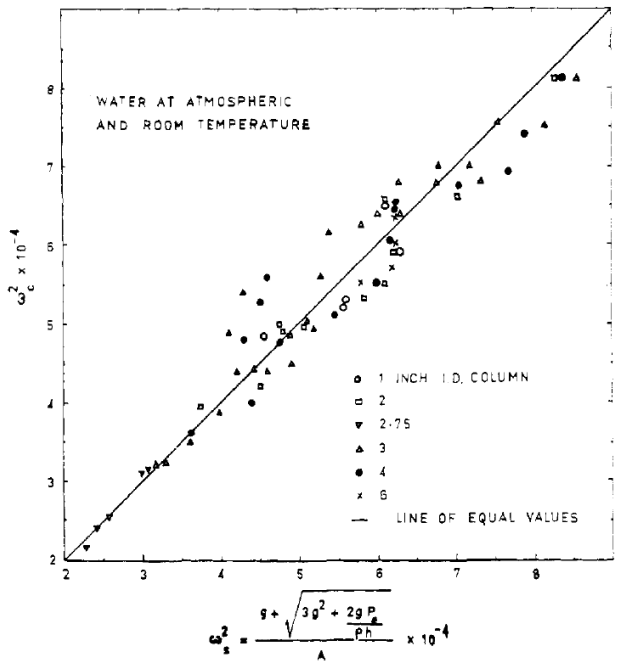

Figure 2.4: Cut-out frequency versus the stabilization frequency for a water column with air (Buchanan et al., 1962)

2.1.3. Baird and Coworkers

Around the same period as Harbaum, Houghton, and Buchanan et al.'s work M.H.I. Baird was investigating gas absorption by singularly rising CO_2 bubbles in a stationary BCR (Baird and Davidson, 1962). This early work indicated two important aspects of gas absorption (mass transfer) in a stationary liquid column, and they are influential to understanding the more complex situation in which vibration is applied. The first important point is that mass transfer coefficient (k_L) of smaller bubbles (d_{eq} < 25 mm) rising at a steady rate in a stationary water column is not readily time dependent as shown by the horizontal line in Figure 2.5, corresponding to d_{eq} < 2.13 cm.

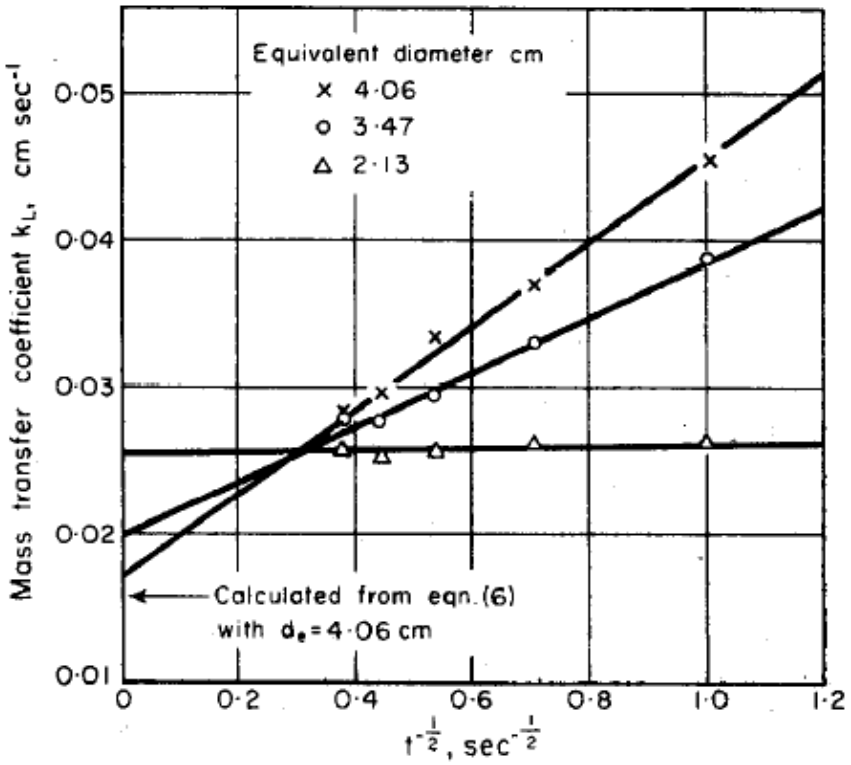

Figure 2.5: Mass transfer coefficient as a function of time for CO_2 bubbles in a quiescent water column (Baird and Davidson, 1962).

The second important aspect of Baird and Davidson's results is a corollary to the first. They proposed that circulation and renewal effects of wake behind a bubble may establish a

steady state through eddy diffusion. They noted that a stagnation layer was established for bubbles rising in n-hexanol and n-butanol solutions where surface tension between CO_2-solution was lower than CO_2-water. In essence, the reduction of a turbulent wake behind the spherical bubble due to surface tension "smoothing" at the interface reduces the concentration gradient. The gas phase is thus insulated from the liquid by a thin boundary layer of partially dissolved gas-solution. This principle was demonstrated in their work by noting the decrease in wake profile (bubble surface ripple) and subsequent decrease in k_L with the addition of the surfactant Lissipol (Figure 2.6). This theory could explain why k_La would increase with vibration as the boundary layer is sloughed off by the shearing effect of the vibration.

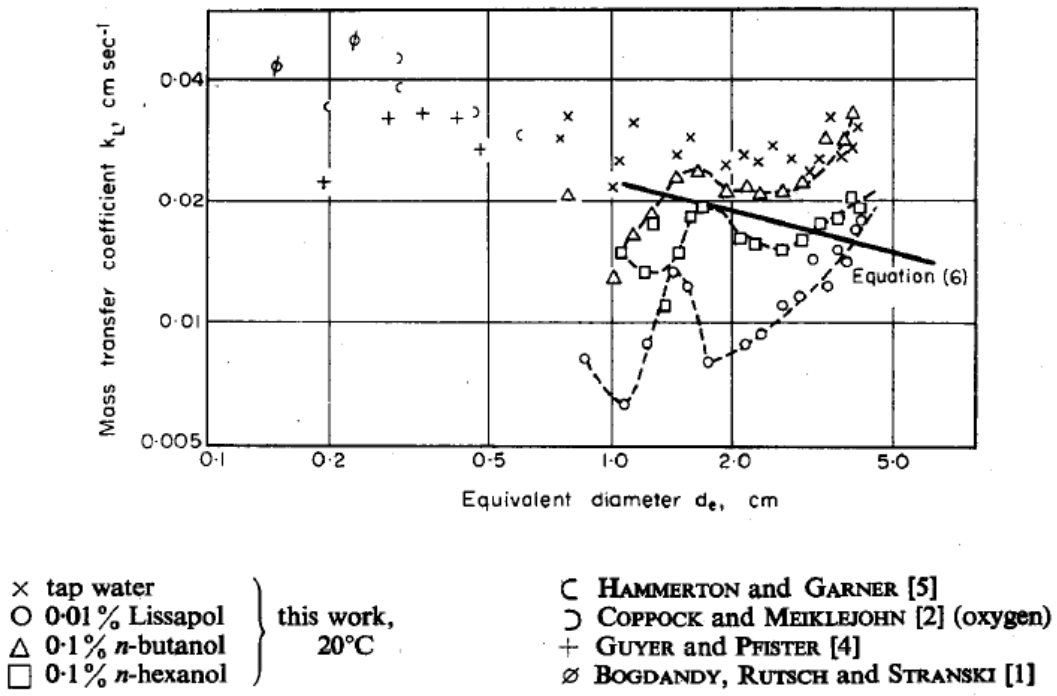

Figure 2.6: Effect of surface tension effects on mass transfer coefficient of CO_2 in solution (Baird and Davidson, 1962)

Baird (1963) turned to the problem of vibrating a BCR and focused on the measurement of size and resonant frequency of singular bubbles and slugs made stationary in a vibrating liquid column. In this work he examines the original equation for bubble resonant frequency offered by Minnaert (1933),

$$f = \frac{1}{2\pi r_0}\left(\frac{3\gamma p_e}{\rho}\right)^{1/2} \tag{2.29}$$

and offers a modification for bubbles,

$$f = \frac{1}{2\pi r_0}\left(\frac{3\gamma p_e}{\rho_l}\right)^{1/2}\left(1+\left(\frac{r_0}{R}\right)\left(\frac{4h}{R}-1\right)\right)^{-1/2} \tag{2.30}$$

where, r_0 is the mean radius of the bubble, γ is the specific weight of the liquid, p_e is the external pressure of a static system and R is the column radius. Equation (2.30) offers more reliability, and includes the effects of the containing vessel (column) and the depth of the bubble which Minnaert's formula did not. Two salient points are offered by this work. First, stroboscopic photography confirms that the bubbles do indeed reach a maximum volume at the top of the stroke giving credence to equation (2.25). Second, expansion amplitudes of the larger and more visible slugs were seen to be larger than the contraction amplitudes leading to an amplitude disparity. This disparity observed in the slug motion could be applied to smaller bubbles, and can be explained by Bjerknes (1906) who notes that "the light…body [bubble] will in the two extreme positions be in different masses of [liquid], and if these have not exactly the same motion, it will be subject in these two positions to kinetic buoyancies not exactly equal and not exactly opposite in direction."

2.1.4. Ellenberger, Krishna and Coworkers

The research into vibrating and pulsing BCR's is suspended for the most part until early into the 21st century when Krishna and Ellenberger (2002) began reexamining the measurement of void fraction and mass transfer in a vibrating BCR. Their early work showed a marked improvement in void fraction (ε) with vibration (Figure 2.7), and specifically ε showed maxima at specific "critical" frequencies (Figure 2.8).

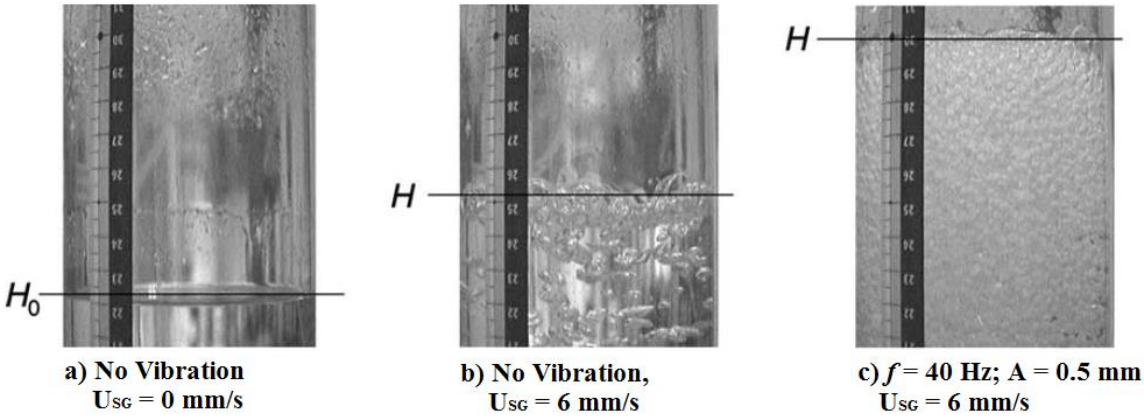

Figure 2.7: Improvement in void fraction with vibration (Krishna and Ellenberger, 2002)

Specific combinations of optimum frequency and maximum amplitude (determined by their set-up to be 0.5 mm) were found to double the void fraction as the gas superficial velocity was increased. However, the results showed that k_La increased 1.5-2 times greater than the void fraction (ε) alone (Figure 2.8), but contrary to Harbaum and Houghton (1962) Krishna and Ellenberger (2002) proposed that the mass transfer rate increase was not solely due to an increase in interfacial area (a) but rather an increase in mass transfer coefficient (k_L) attributed to an increase in turbulence. It should be noted that, Krishna and Ellenberger (2002) did not independently measure k_L and a as Harbaum and Houghton (1962) did to base their conclusions upon.

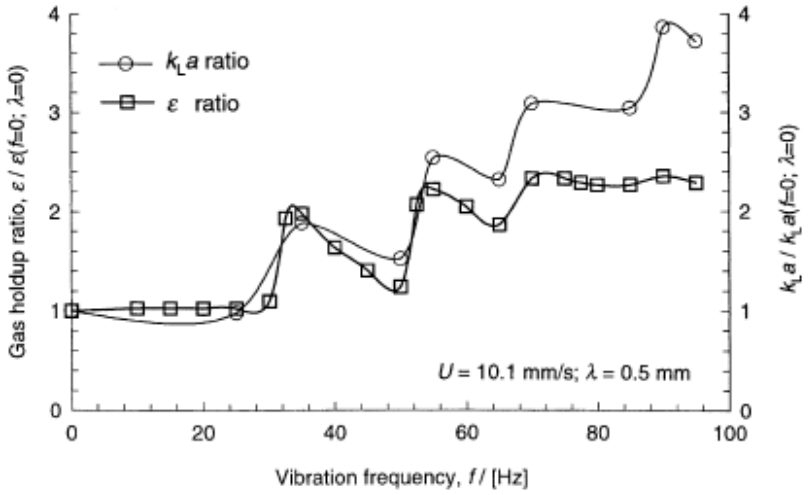

Figure 2.8: Improvement of volumetric mass transfer coefficient and void fraction (gas holdup) with vibration frequency (Krishna and Ellenberger, 2002)

Krishna and Ellenberger (2002) also attempted to distinguish between the effects of vibration frequency and the amplitude on void fraction. Their results show increased void fraction (ε) for both increasing frequency and amplitude, but the general trends differ in shape. It is easily seen from Figures 2.9a and b that increasing the amplitude of vibration has a more pronounced effect on the void fraction versus increasing frequency. For example, at f = 60 Hz and superficial gas velocity of 0.01 (m/s) a 50% increase in frequency gives a 17% rise in void fraction whereas a 50% increase in amplitude gives a 36% increase in void fraction. Since a rise in ε is expected to directly increase a it suggests a greater increase in k_La can be achieved through higher amplitude as well.

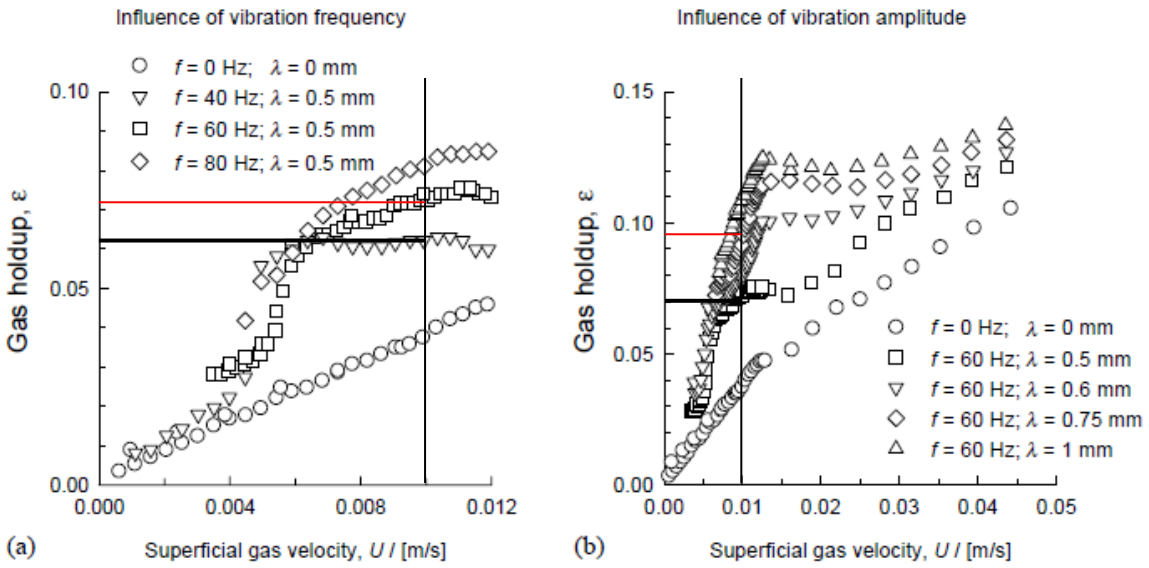

Figure 2.9: a) Influence of vibration frequency on void fraction for air in water, and b) Influence of vibration amplitude on void fraction for air in water (Ellenberger and Krishna, 2003)

Bubble rise velocities have also been found to be reduced by standing waves. By comparing the size of the bubbles at the opening of a single capillary tube to the (average) size of the bubbles in the column Ellenberger and Krishna (2003) noted that bubbles were reduced in size by up to 50%. Experiments relating amplitude of vibration with both void fraction (ε) and bubble velocity (U_{SG}) have shown an increase in ε and a decrease in bubble velocity with increasing amplitude (Figure 2.10). While both dependent parameters seem to show an

approaching plateau, the experimental setup used was limited to smaller amplitudes, and no results at higher amplitudes (A > 1.2 mm) were reported (Ellenberger and Krishna, 2003).

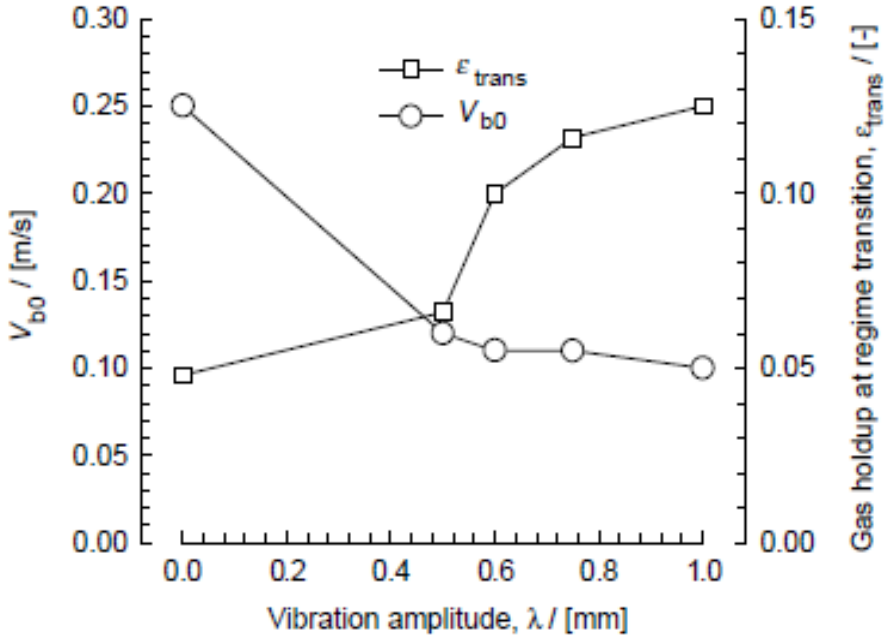

Figure 2.10: Effect of vibration amplitude on bubble velocity (rise) and void fraction (gas holdup) for a water column with air (Ellenberger and Krishna, 2003)

In a following study an attempt was made to theoretically determine the local void fraction and bubble velocity as a function of liquid column height by using the Rayleigh-Plesset equation (2.31) and a force balance on a bubble Eq. (2.32) (Ellenberger et al., 2005). The Rayleigh-Plesset equation describes the change in bubble radius (r) with time and height (z),

$$\frac{\partial^2 r}{\partial t^2} = -\frac{3}{2r}\frac{\partial r}{\partial t} + \left(\left(p_e + 2\frac{\sigma}{r_0} \right) \left(\frac{r_0}{r} \right)^3 - 2\frac{\sigma}{r} - 4\frac{\mu}{r}\frac{\partial r}{\partial t} - p_e - p(z,t) \right) \tag{2.31}$$

A force balance on a bubble is made on a bubble by including the Bjerknes force as a pressure gradient giving,

$$\frac{\partial U_b}{\partial t} = -V\frac{dp(z,t)}{dz} + (\rho - \rho_g)Vg - \frac{1}{2}C_D\rho_l |U_b| U_b \pi r^2 \tag{2.32}$$

It should be pointed out that equation (2.32) is not correct because of the missing mass term on the left hand side. This is easily seen if one does a quick check of the dimensions for each term. A modification of equation (2.32) is proposed to account for the missing mass,

$$\rho_g V \frac{\partial U_b}{\partial t} = -V \frac{dp(z,t)}{dz} + \Delta\rho V g - \frac{1}{2} C_D \rho_l |U_b| U_b \pi r^2 \tag{2.33}$$

where $\Delta\rho = \rho - \rho_g$. It is unclear whether the error was simply a misprint or if equation (2.32) was used in the subsequent calculations, but it should be treated with caution in either case. However, based on solutions to Eq. (2.31) and Eq. (2.32) local void fraction was predicted to increase at harmonic wavelengths (Figure 2.11). The local void fraction also showed particular increases at the pressure antinodes, especially at higher harmonic modes (Ellenberger et al., 2005).

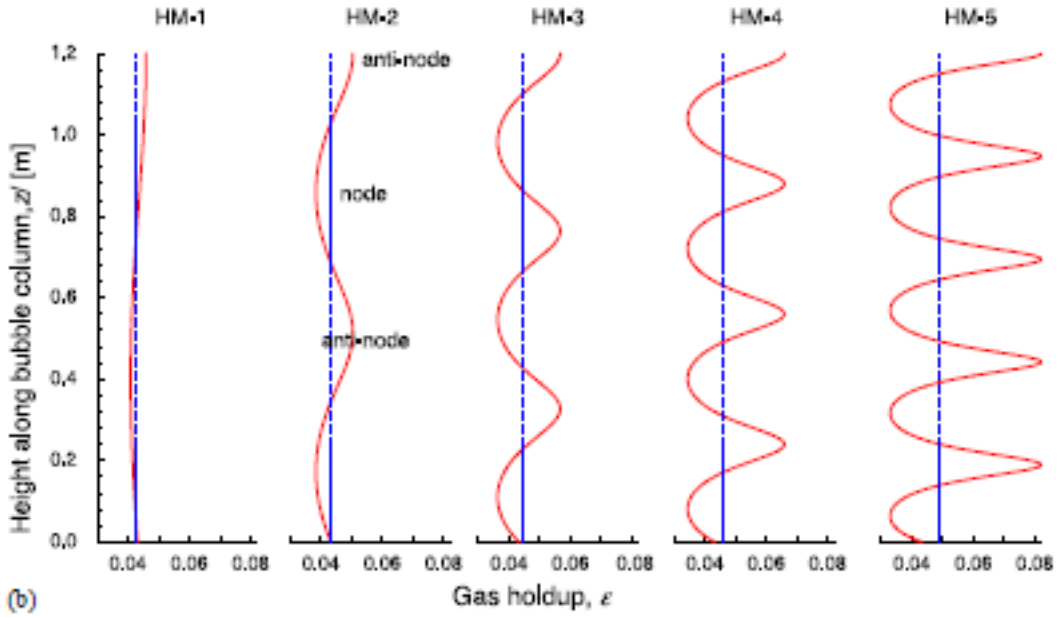

Figure 2.11: Theoretical influence of harmonic modes on local void fraction for a water column with air (Ellenberger et al., 2005)

The theoretical predictions were experimentally tested by using an electrical conductivity meter to detect local void fraction at specific heights along the liquid column marking the first

attempt in the literature to examine the variation of local gas hold-up along the column (Ellenberger et al., 2005). Examining the local void fraction as opposed to the global value gives the advantage of examining spatial effects, but the conductivity meter comes with certain disadvantages. Figures 2.12 a-f show that local gas holdup peaks at corresponding nodes for each harmonic mode (HM). There is some discrepancy between their experimental results (Figure 2.12) and the predicted values of equations (2.31) and (2.32) (Figure 2.11), especially concerning the slope of the axis of symmetry (roughly superimposed line).

The identification of the number of nodes for each result is striking. By roughly generalizing the axis of symmetry a decreasing trend in slope is seen, with a positive slope for HM1 and HM2, a nearly neutral slope at HM3, and decreasing in HM4 and HM5. This effect may be due to either experimental techniques or some unaccounted for physical effect, but would be interesting to investigate further.

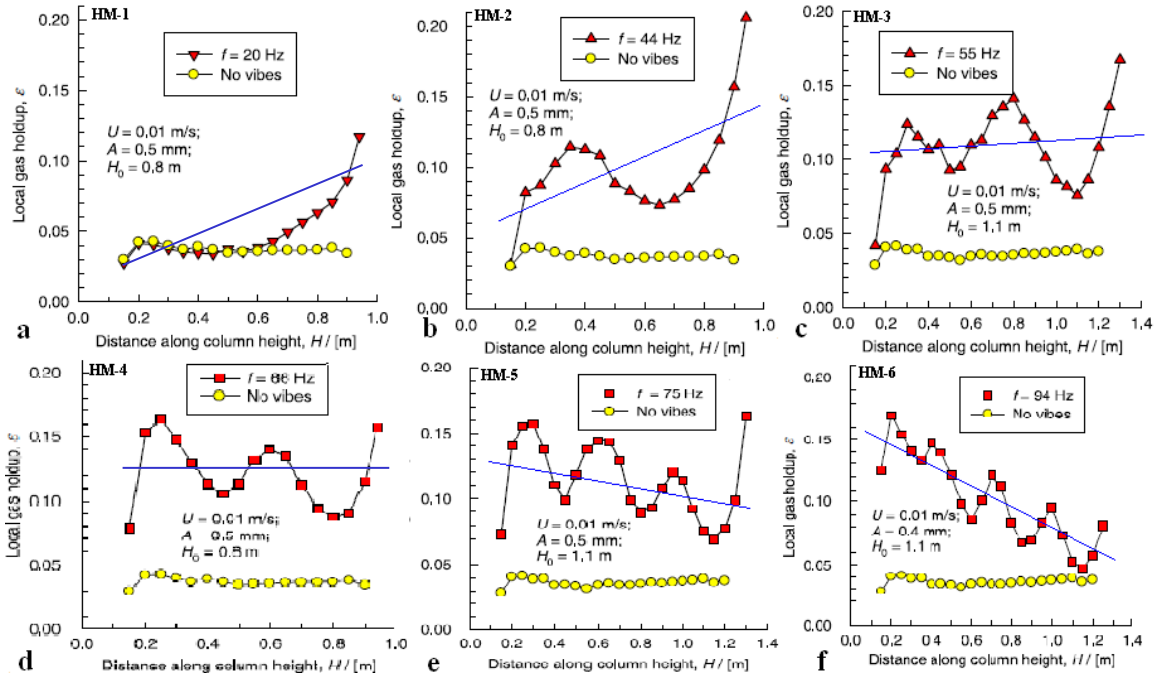

Figure 2.12: Experimental results for local void fraction with column height corresponding to harmonic modes (Ellenberger et al., 2005)

2.1.5. Waghmare and Coworkers

While the interest in vibrating BCR's has been reinvigorated recently, most of the research focus was on the effect of the frequency of vibration on mass transfer. Waghmare (2008) expanded the previous research in three areas which are relevant to this study. The first, was a unified model to predict void fraction and mass transfer coefficient based on correlations and theory which compared well to experimental results. The second, provided experimental results showing the effects of viscosity on $k_L a$, and a valuable theoretical relationship is presented which predicts the viscosity effects well. Finally, the third was a model to predict the bubble size distribution at varying column heights and vibration frequencies based on Population Balance Modeling and compared with experimental results with some success (Waghmare et al., 2007; Waghmare et al., 2008).

Waghmare et al. (2007) proposed a model to predict void fraction based largely upon breakage due to power input. Beginning where Buchanan et al (1962) left off, but assuming that static pressure at the column is greater than the sum of the hydrostatic pressure and vibration pressure Eq. (2.21) can be rewritten as,

$$\frac{\Delta V_{\max}}{V_0} = \frac{\rho h \omega^2 A}{p_e} \tag{2.34}$$

It is important to note at this point that the assumption used by Waghmare to derive Eq. (2.34) may be a source of error since the magnitude of the vibrational pressure for most test cases will be on the same order as the external (atmospheric) pressure. For example to make Waghmare's assumption valid the magnitude of external pressure should be greater than or much greater than the magnitude of the sum given by,

$$|p_e| >> |\rho g h - \rho h \omega^2 A| \tag{2.35}$$

For example, a typical test point for air in a 78 cm column of water at atmospheric pressure, frequency of 40 Hz and amplitude of 2.5 mm gives,

$$\left|\rho g h - \rho h \omega^2 A\right| = 115{,}000$$

and,

$$\frac{p_e}{\left|\rho g h - \rho h \omega^2 A\right|} \approx 1$$

As can be seen, vibration pressure is indeed a significant component of the total pressure. However, proceeding with the assumption Waghmare offers the following equation for void fraction based on the input parameters,

$$\langle \varepsilon \rangle = \frac{1}{H}\int_0^H \varepsilon(h)dh = 2.25\left[\frac{U_{SG}\left(gU_{SG} + 0.5\omega^3 A^2\right)^{2/5}}{\left(\frac{\sigma}{\rho}\right)^{3/5}\left(\frac{g}{\sqrt{\nu}}\right)^{2/3}}\right]E(Bj) \tag{2.36}$$

where,

$$E(Bj) = \frac{3}{Bj}\left[1-(1-Bj)^{1/3}\right] \tag{2.37}$$

and,

$$Bj = \frac{1}{2}\frac{\rho H \omega^4 A^2}{g p_e} \tag{2.38}$$

Furthermore, Waghmare uses Equation (2.36) and couples it with a modified penetration theory defined by,

$$k_L a = \sqrt{\frac{4\mathcal{D}}{\pi t_c}\left(\frac{6}{d_b}\varepsilon\right)} \tag{2.39}$$

where, $\mathcal{D}$ is the diffusivity of the species (cm^2/s).

The resulting equation for mass transfer is also a function of only input parameters,

$$\langle k_L a \rangle = \frac{1}{H}\int_0^H k_L a(h)dh = 4.58\left[\frac{j_G \sqrt{\mathcal{D}} P_m^{\,4/5}}{\left(\frac{\sigma}{\rho}\right)^{6/5}\left(\frac{g}{\sqrt{\nu}}\right)^{1/3}}\right] G(Bj) \tag{2.40}$$

where,

$$G(Bj) = \frac{3}{2}\left[\frac{1-(1-Bj)^{2/3}}{Bj}\right] \tag{2.41}$$

Both the results for Eq. (2.36) and Eq. (2.40) as derived are based upon the following assumptions (Waghmare et al., 2007):

1. gas concentration is dilute ($\varepsilon < 1$)
2. fluid amplitude is continuous
3. coalescence is small
4. bubble breakage occurs primarily through shear
5. bubble expansion and contraction has a negligible effect on mass transfer

Waghmare measured void fraction using a manometer with pressure taps at two locations on the column. Initial void fraction and mass transfer experiments were conducted using water and air in a cylindrical column at a liquid height of 78 cm. A piston was used to oscillate the fluid column from the base at amplitudes of 1.66 mm and 2.46 mm over a frequency range of 0 – 30 Hz. The frequencies tested by Waghmare were lower than most of the previous researchers

(Waghmare, 2008; Buchanan et al., 1962; Ellenberger et al., 2005). Air was injected from a 0.75 mm diameter stainless steel capillary tube at superficial gas velocities (U_{SG}) of 0.1, 0.25, 0.5, 0.75, 1.0, 1.25, 1.5 cm/s. A high speed camera and image processing software was used to find bubble number density and projected surface area from which the Sauter mean diameter was derived as described previously. Furthermore, in experiments the frequency and amplitude combinations were such that $Bj < 1$ to avoid flooding at the injector tip (Waghmare et al., 2007; Waghmare et al., 2008).

The experimental results for bubble diameter showed good agreement with Hinze's breakup model as a function of input power (Figure 2.13). The overall void fraction was presented as a function of bubble diameter for varying frequencies (Figure 2.14) and showed how bubble sizes are reduced and homogenized (distribution spikes) with increasing frequency.

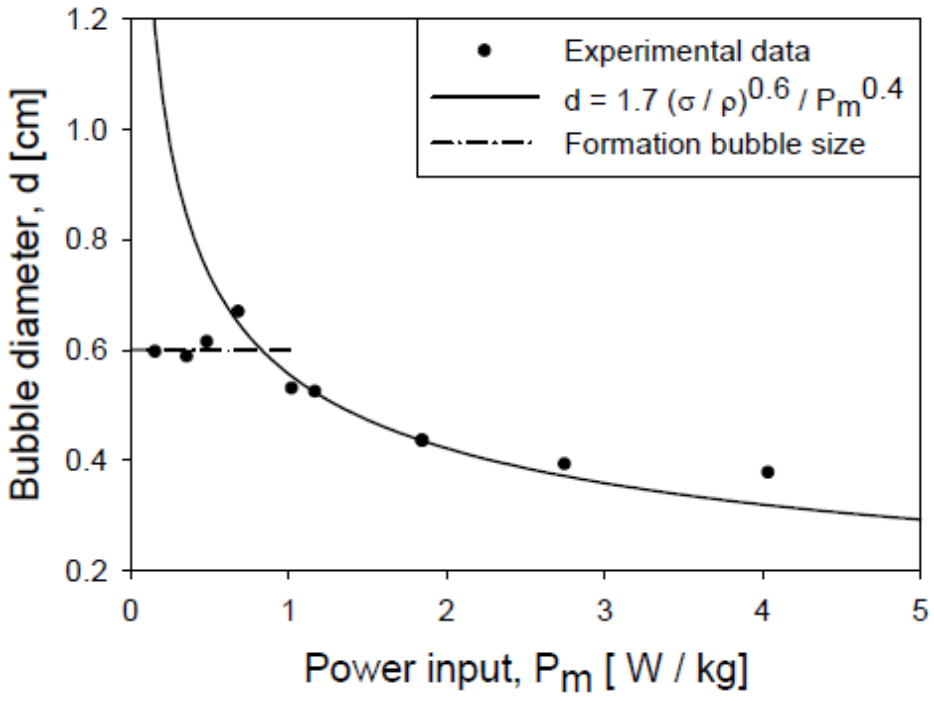

Figure 2.13: Experimental results showing agreement with Hinze (1955) correlation at column location z/H = 0.69 (Waghmare et al., 2007)

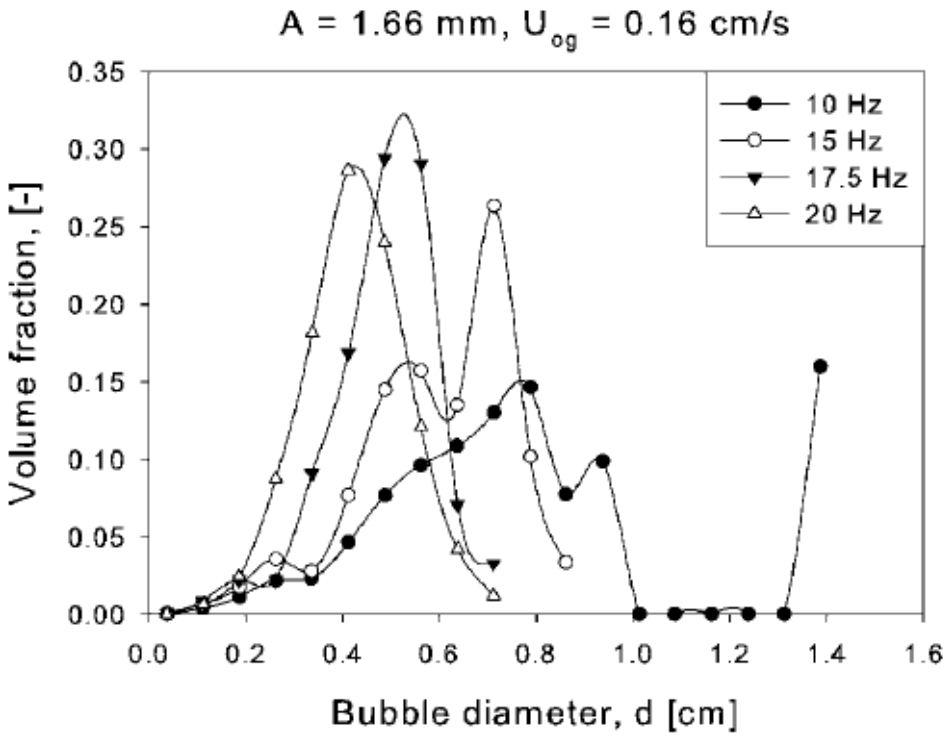

Figure 2.14: Experimental results for void fraction and bubble size distribution with varying frequency for a vibrating water column with air (Waghmare et al., 2007)

Experiments showed void fraction to be a function of superficial gas velocity (Figure 2.15) which agreed with the prediction of Eq. (2.36) for the specific test parameters of frequency, amplitude, and liquid properties. However, it would seem more appropriate and beneficial to show the void fraction plotted as a function of Bjerknes number or the frequency amplitude product ($\omega^4 A^2$) rather than superficial gas velocity since it is obvious that the void fraction should be dependent on the amount of gas being input into a batched system. Perhaps plotting the void fraction as a function of *Bj* would also show which parameters may be more influential. However, Waghmare's results show good agreement with equation (2.36) for void fraction as a function of input power (Figure 2.16). Specific power provides a more useful tool as an input parameter, since it takes into account all of the input parameters of a vibrating BCR: superficial gas velocity, frequency, and amplitude.

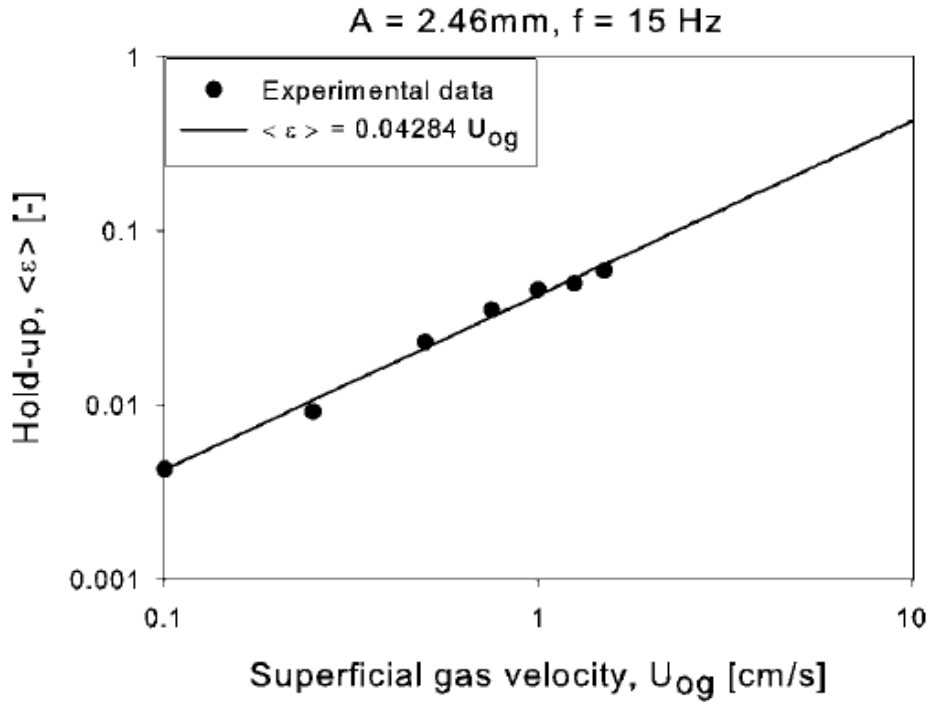

Figure 2.15: Experimental results of void fraction compared to predicted values of Eq. (2.36) with superficial velocity for a vibrating water column with air (Waghmare et al., 2007)

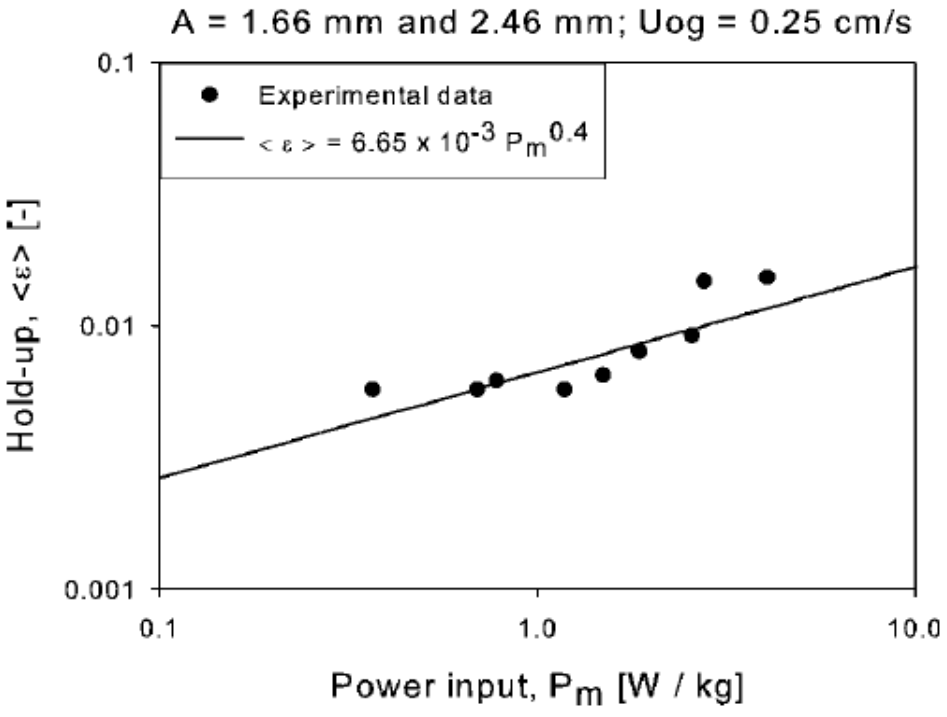

Figure 2.16: Experimental results of void fraction compared to predicted values of Eq. (2.36) with specific power input for a vibrating water column with air (Waghmare et al., 2007)

Waghmare's experimental results for mass transfer also showed good agreement between the predicted mass transfer rates of Eq. (2.40) as a function of superficial gas velocity (Figure 2.17) and specific power input (Figure 2.18). However, unlike the relationship between void fraction and superficial gas velocity the effect of U_{SG} on mass transfer is reported to be more significant. Here, if one was to suspect that improvement of k_La from superficial gas velocity was mostly due to an increase in a through void fraction, then the slope of the line in Figure 2.17 would be similar to Figure 2.15, but it is more than half. The variation in slope suggests that k_La is not necessarily increased by changes in a alone. In fact, the increased exponential dependence of k_La on P_m (Figure 2.18) versus that of ε (Figure 2.16) implies that vibration has an impact on k_L independent of a. Once again, perhaps studying the variation of k_La with the Bjerknes number would provide insight into which processes provides more benefit, vibration frequency/amplitude or superficial gas velocity.

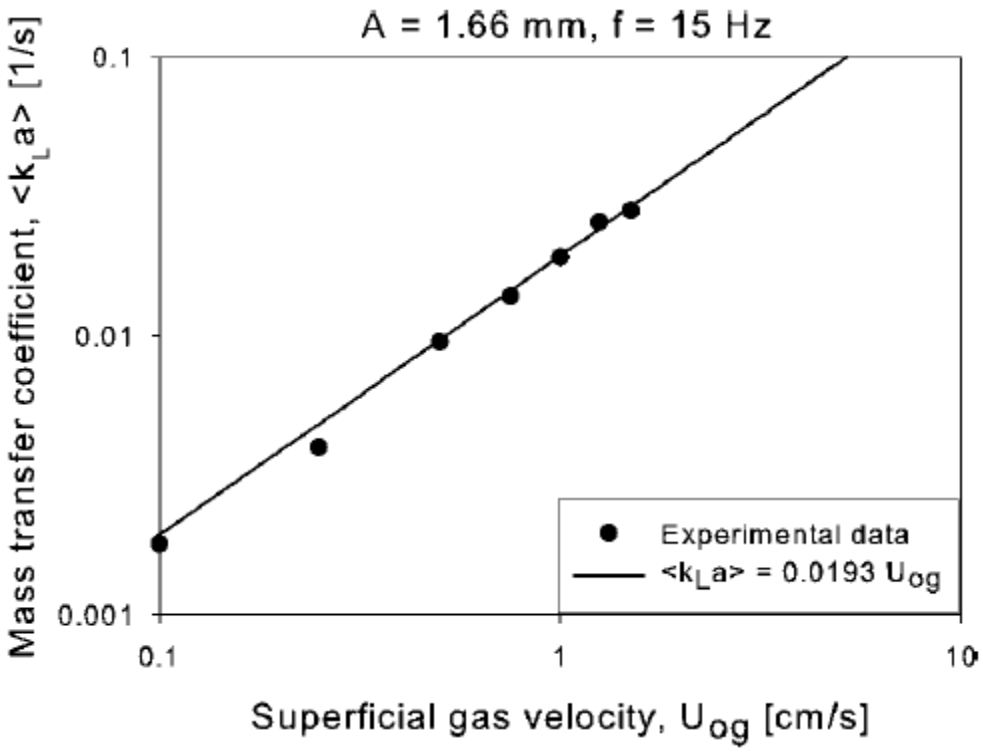

Figure 2.17: Experimental results of mass transfer compared to predicted values of Eq. (2.40) with superficial gas velocity for a vibrating water column with air (Waghmare et al., 2007)

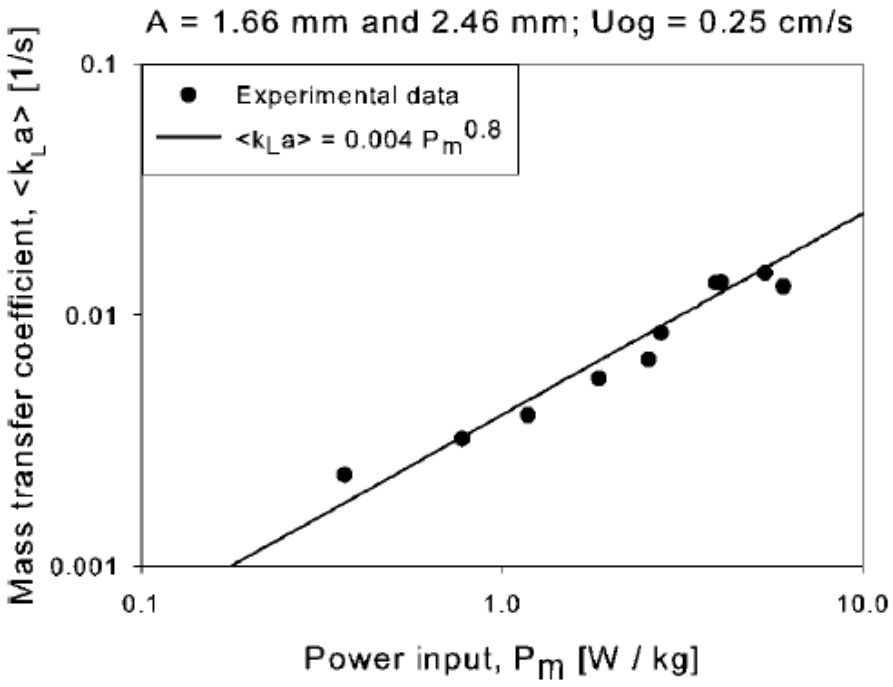

Figure 2.18: Experimental results of mass transfer compared to predicted values of (2.40) with specific power input for a vibrating water column with air (Waghmare et al., 2007)

An interesting result of Waghmare's model for predicting void fraction and mass transfer is the contribution of fluid properties. It should be noted that both equations (2.36) and (2.40) are inversely proportional to surface tension and directly proportional to kinematic viscosity and density of the surrounding fluid. While Buchanan et al. (1962) mentioned testing fluids other than water (including slurries) the reported results were limited. Additionally, only one other research group had investigated the effect of viscosity on bubbles in oscillating fluid columns, but the work was limited to a kinematic investigation of singular bubbles (Jameson and Davidson, 1966; Jameson, 1966). Furthermore, all of the previous research focusing on mass transfer in a vibrating BCR have used water as the continuous media, and no experimental results have been reported on the effects of liquid properties on void fraction (ε) or particularly, mass transfer (k_La) in vibrating BCR's**.**

The second product of Waghmare's research reveals a relatively powerful correlation for the determination of k_La based on fluid viscosity in a vibrating column reactor (Waghmare et al.,

2008). To develop the theory Waghmare makes use of the Einstein-Stokes theory at constant temperature given by,

$$\frac{\mathcal{D}_1}{\mathcal{D}_2} = \frac{\nu_2}{\nu_1} \tag{2.42}$$

Inserting (2.51) into (2.50) gives the following,

$$\langle k_l a \rangle = 2.6 \frac{U_{SG} \nu^{-1/3} \sqrt{\mathcal{D}_0 \nu_0} P_m^{4/5}}{g^{1/3} \left(\frac{\sigma}{\rho} \right)^{6/5}} \tag{2.43}$$

where $\mathcal{D}_0$ and ν_0 are the diffusivity and kinematic viscosity of a reference fluid, and in most cases these values are for water. The significance of Eq. (2.43) is that, based on a vibration profile, superficial gas velocity, and fluid properties, values of $k_L a$ can be predicted as being proportional to the viscosity by,

$$\langle k_l a \rangle \propto U_{SG} \nu^{-1/3} \tag{2.44}$$

Using the apparatus previously described water, a 2%wt solution of water and carboxy-methyl-cellulose (CMC), and a 3%wt CMC solution were tested which provided viscosities of 1, 11 and 62 cP (Waghmare et al., 2008). The results of the experiments agreed with the Einstein-Stokes theory showing that diffusivity which is inversely proportional to the viscosity has a direct effect on mass transfer. Therefore, as fluid viscosity is increased the mass transfer should show a decrease. Figure 2.19 shows that while increasing viscosity may dampen the curve the relative increase due to vibration is still exhibited in the same general form. Therefore, even in practical cases where the fluid is more viscous than water, a definite increase can be made in mass transfer through vibration. The experimental results showed good agreement with the proposed

correlation (Figure 2.20). Waghmare (2008) adds that results for Eq. (2.44) also match well with correlations proposed by Nakanoh and Yoshida (1980) for non-vibrating cases given by,

$$\langle k_l a \rangle \propto U_{SG} \nu^{-0.28} \tag{2.45}$$

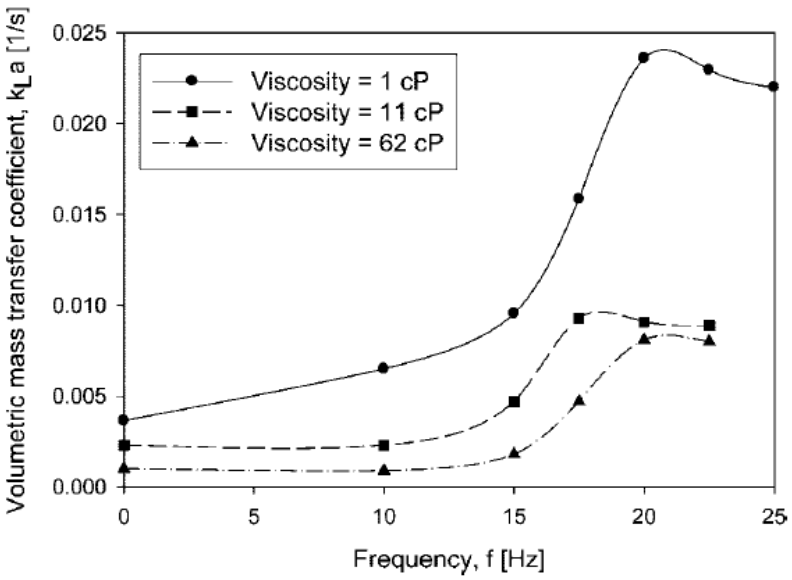

Figure 2.19: Experimental results of mass transfer in a vibrating BCR with increasing fluid viscosity for air-water, air-2%CMC sol., and air-3%CMC sol. (Waghmare et al., 2008)

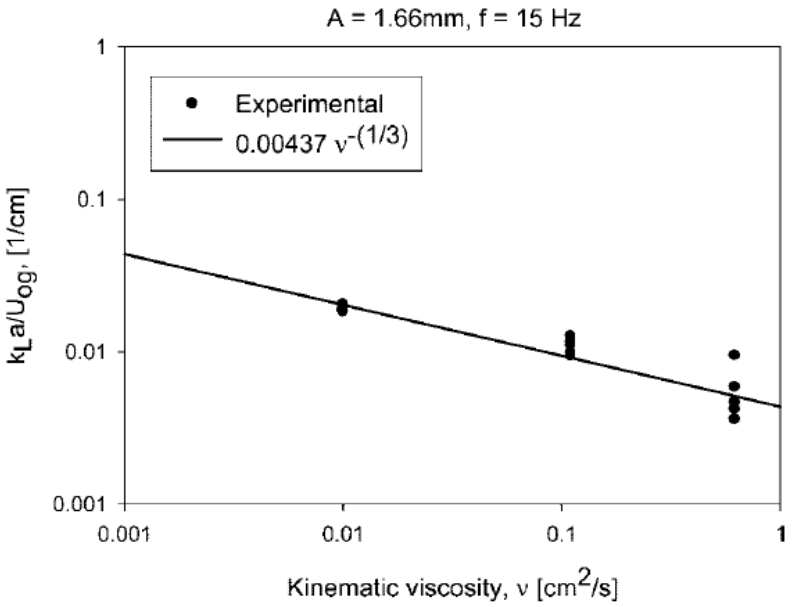

Figure 2.20: Experimental results in comparison with predicted values of Eq. (2.43) for a vibrating BCR with air-water, air-2%CMC sol., and air-3%CMC sol. (Waghmare et al., 2008)

The mechanism for increasing k_La arising from the "Bjerknes effect" does not seem to be hindered by viscosity which aligns with Jameson's (1966) conclusion that the motionless condition for a single bubble in an oscillating fluid is not affected by viscosity as long as the fluid is not extremely viscous. However, when comparing the experimental results in a unified fashion as a function of frequency there is still considerable scatter and ambiguity (Figures 2.21a and b). It is still difficult to distinguish viscous effects at higher frequencies or higher amplitudes than the experiments above could achieve. Further investigation and improvement of the relationships between mass transfer and viscosity in a vibrating BCR is certainly warranted, especially at higher amplitude, frequency, and pressure.

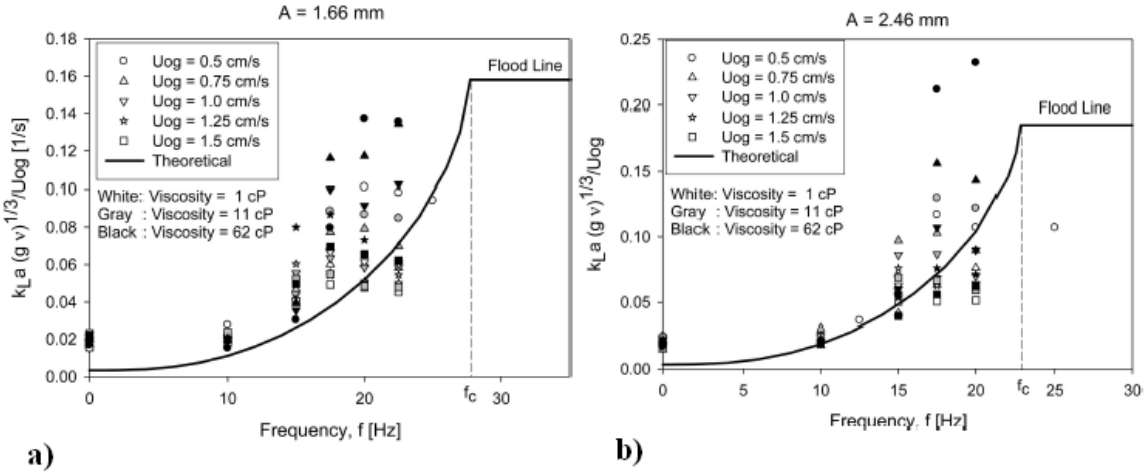

Figure 2.21: Comparison between experimental results and Eq (2.43) with frequency and superficial gas velocity in air-water, air-2%CMC sol., and air-3%CMC sol. at an amplitude of a) 1.66 mm and b) 2.46 mm (Waghmare et al., 2008)

2.2. Testing Procedures and Equipment

2.2.1. Measurement of Void Fraction (ε) and Bubble Size

Measurement of void fraction and bubble size has been a primary concern for investigators in determining the hydrodynamics of multiphase flow. Bubble size, shape and void fraction are important parameters in a regular BCR, and specifically in a vibrating BCR because of their combined relationship to the interfacial area (a). In most cases the research has been

concerned with volumetrically averaged void fraction because of the limitations in measuring local values. There have been exclusive experiments where local void fraction was determined by alternate methods in bubbly flows (George et al., 2000; Mudde and Saito, 2001; Cartellier, 2001) including one case in a vibrating BCR (Ellenberger et al., 2005). However, excluding the singular case (Ellenberger et al., 2005), all of the research to date in a vibrating BCR has relied on manometry or volume displacement to give a column averaged value. While the volumetric methods are easily applied they do not allow insight into height specific phenomena such as the Bjerknes force.

In manometry, two pressure taps are created in the column wall separated by a known column height (Figure 2.22).

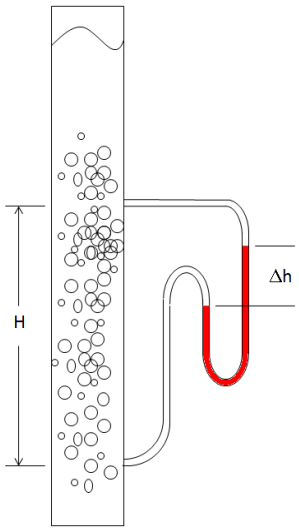

Figure 2.22: Illustration of the manometric void fraction method

A fluid such as Meriam Red 295 is used as the manometer fluid and the average volume fraction of the liquid height between the two pressure taps such as used by Waghmare et al. (2007),

$$\langle \varepsilon \rangle = \left(\frac{\rho_m - \rho}{\rho} \right) \frac{\Delta h}{H} \tag{2.46}$$

where ρ_m is the manometer fluid density.

One considerable drawback to this method when applied to a vibrating BCR is the pressure fluctuations across the column due to vibration. Pressure fluctuations in the fluid lead to erroneous readings at the manometer. This particular effect was noted as a significant source of error, particularly when frequency is high and in cases exhibiting "flooding" or aggregation of the bubble swarm at the injector site (Waghmare, 2008).

Another means of measuring void fraction in vibrating BCR's that has commonly been used is simply measuring the change in liquid height (Figure 2.7). Using a scale to measure the liquid height before vibration and during vibration gives a difference from which void fraction can be derived by,

$$\langle \varepsilon \rangle = 1 - \frac{H_0}{H} \tag{2.47}$$

where H_0 is the initial quiescent liquid height and H is the final mixture height under vibration. As can be seen from Eq. (2.47) this method is also volumetric in nature and can only describe the column averaged void fraction. Therefore, this method is also limited in its ability to capture local effects along the column which is a disadvantage to understanding the local development of the processes at work. Another difficulty in measuring void fraction using total liquid height arises from the interface. Determination of the liquid height can be difficult if the interface exhibits significant turbulence or sloshing. Therefore, a Styrofoam disk has been used by some to dampen the interface and make recording of liquid height during vibration easier (Knopf et al., 2005a; Waghmare et al., 2008).

There are other methods to measure void fraction for local cross section areas that have been used successfully in both vibrating and non-vibrating BCR's. A conductivity meter was used to measure local void fraction of column cross section at specific heights in a vibrating BCR by Ellenberger et al. (2005). The local void fraction was determined by,

$$\langle \varepsilon \rangle_{area} = 1 - \frac{\phi_U}{\phi_{U=0}} \tag{2.48}$$

where ϕ_U is the signal output of the conductivity meter at the flow condition and $\phi_{U=0}$ is the signal for the no flow (quiescent) condition at each location.

The conductivity meter utilizes two conductive rods separated by a known distance, and derives a signal based on the conductivity of the medium between the probes. Since the conductivity of air is less than that of water a maximum signal is expected at a no flow condition, and a decreased signal when air (bubbles) is present. Thus the ratio of flow signal to no-flow signal will always be less than unity and will depend directly on the amount of air between the probes. A disadvantage of the method requires the liquid to be electrically conductive. Resolution of the signal will also depend on the conductivity of the liquid. One can see that the application of this method is limited to conductive fluids, and cannot be applied to organic liquids which may be non-conductive or weakly conductive. Therefore the method is suitable for the lab where comparisons could be made indirectly based upon fluid properties alone, but not directly to field applications where a BCR is often used in a reaction process with organic liquids such as hydrogenation of coal-oil slurries in the Fisher-Tropsch process (Fan, 1989).

The results of the local void fraction measurement were crucial to locating specific heights in the column where void fraction increased dramatically. The local void fraction increases were found to significantly correspond with harmonic pressure node locations (Figure 2.23).

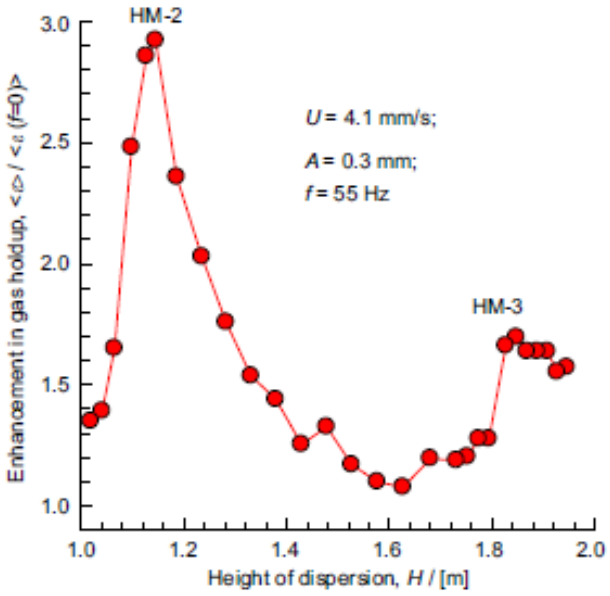

Figure 2.23: Experimental results of local void fraction along a column height using a conductivity meter (Ellenberger et al., 2005)

Some other novel methods to measure local void fraction in non-vibrating bubbly flows include electrical capacitance tomography (Huang et al., 2003), X-ray tomography or "Computed Tomography (CT) (Figure 2.24), and Computer Automated Radioactive Particle Tracking (CARPT) (Dudukovic et al., 1999). These methods are advantageous for imaging the flow and local void fraction in cases where the system excludes more visual or direct probe methods such as in high pressure or corrosive environments. However, tomography methods are generally computationally and cost prohibitive typically requiring complex algorithms and expensive analyzers and equipment.

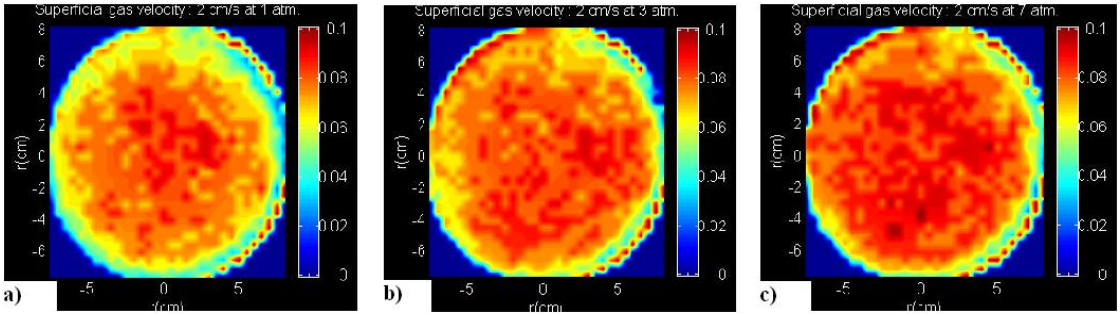

Figure 2.24: CT images showing local void fraction with superficial gas velocity at a) p_e = 1 atm, b) p_e = 3 atm, c) p_e = 7 atm (Dudukovic et al., 1999)

Examining the distribution of void fraction in a vibrating column is certainly beneficial to understanding the phenomena at work. Conductivity methods require altering the chemistry of the fluid medium which is restrictive. Additionally, no quantitative analysis was given to relate possible effects of altering the fluid chemistry on the mass transfer (k_La) measurements in these experiments (Ellenberger et al., 2005). Tomography methods using x-rays or electrical capacitance are computationally and fiscally expensive, and usually require considerable development time and expertise.

Single and dual point optical probes have been used to measure multiphase flow properties such as interfacial area, void fraction, bubble size and speed (Guet et al., 2003; Guet et al., 2005; Julia et al., 2005) Single and dual point probes are reported to be simple to produce and cost effective (Cartellier, 2001). Recently a 4 point optical probe has been used quite extensively to measure local void fraction in BCRs with better accuracy than the single and two point versions (Wu et al., 2008; Xue et al., 2008b). The Comparison of 4 point optical probe results and photographic methods show good agreement (Figure 2.25).

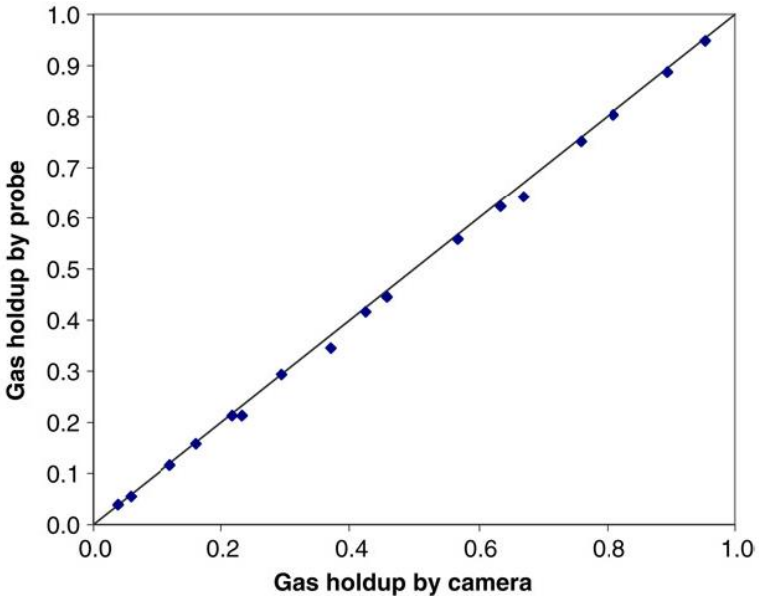

Figure 2.25: Comparison of experimental results of void fraction using 4 point optical probe and photographic methods (Xue et al., 2008b)

To the author's knowledge all of the previous research in vibrating BCR's has used photography or video to determine bubble size distributions. Current methods utilize charge coupled device (CCD) or complementary metal-oxide semiconductor (CMOS) "digital" cameras to capture images of a vertical column cross section (Figure 2.26).

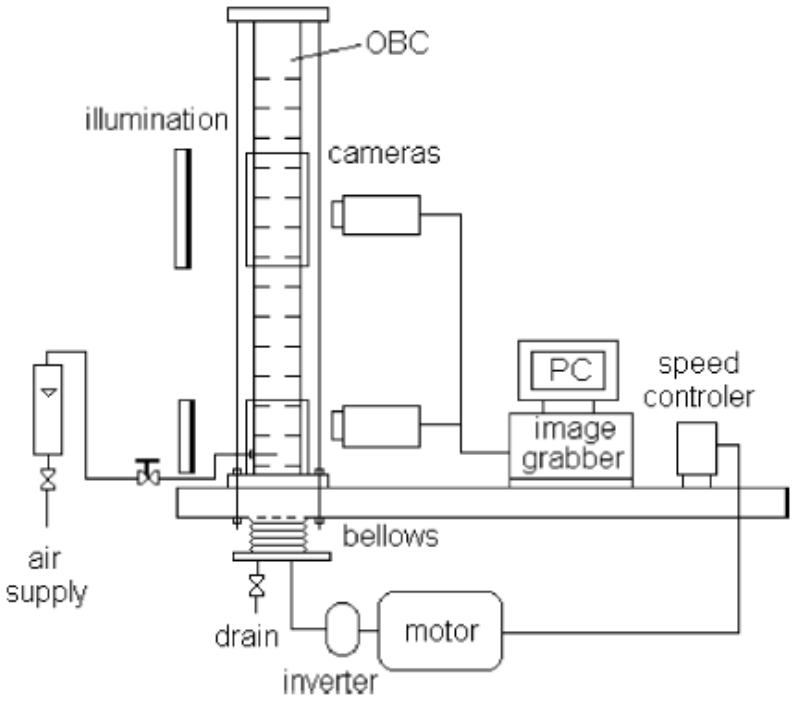

Figure 2.26: Schematic of a typical camera arrangement to capture bubble distribution images (Oliveira and Ni, 2001)

The two dimensional bubble images are typically processed by image software which calculates the projected area of each bubble (Figure 2.27). This method usually requires the assumption of a spherical bubble in order to ascribe an equivalent spherical bubble diameter to each recognized bubble. The Sauter mean diameter can then be readily obtained from equation (2.4). This process is described well by Oliveira and Ni (2001) for the case of a baffled vibrating BCR.

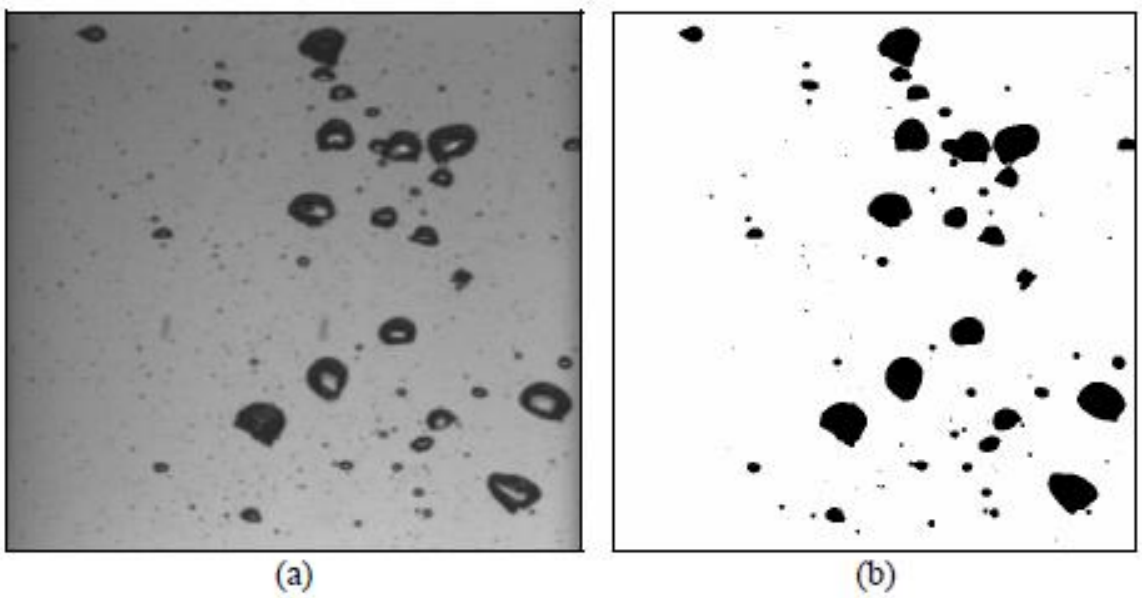

Figure 2.27: Photographic processing of the bubble distribution with software; a) Pre-processed image b) Post-processed image using ImageJ software (Waghmare, 2008)

The advantages of using photographic methods include: cost, availability, and versatility. Relatively low cost cameras are typically adequate to capture high resolution images needed for the calculation of the projected cross sectional area. The method is also versatile enough to capture bubble distributions at varying locations along the column height which gives qualitative insight to the mechanics of the flow (Waghmare et al., 2008). However, photographic techniques are limited to the focal area and depth of field, and as such can only capture images of areas in the vicinity of the column wall. The bubble size distribution results using photographic methods have been cause for concern since the method fails to capture the larger bubbles near the center of the column. Therefore the method is only inclusive for homogeneous flow or low superficial gas velocity (U_{SG} < 5 cm/s) (Shah et al., 1982). Water boxes have been used to decrease the distortion due to the change in refractive index for flow visualization (Oliveira and Ni, 2001; Waghmare et al., 2007; Zhu et al., 2001).

The 4-point optical probe has also been used to determine bubble size distributions as a function of chord length in slurry flows (Wu et al., 2008) and in a non-vibrating BCR with

internals (Youssef and Al-Dahhan, 2009) and without internals (Xue et al., 2008a; Xue et al. 2008b). The 4-point optical probe allows the measurement of bubbles flowing past an inspection point, and gives the chord length distribution as a probability distribution for a large sample size (Figure 2.28).

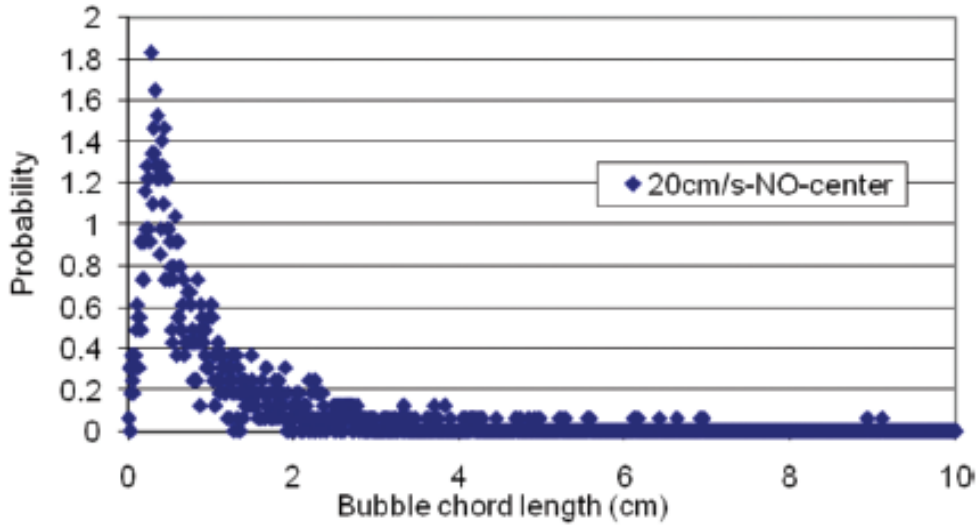

Figure 2.28: Example of bubble chord length distribution taken with 4 point optical probe (Youssef and Al-Dahhan, 2009)

2.2.2. Measurement of Volumetric Mass Transfer Coefficient (k_La)

The primary objective for most of the BCR research is driven by the chemical processing industry in order to optimize the mass transfer of one species to another typically through absorption of gas. Naturally, a majority of the previous research has focused on measurement of the volumetric mass transfer coefficient (k_La) as a reference for overall reaction efficiency and speed. The method to measure mass transfer (k_La) in a BCR involves determining the concentration of absorbed gas in solution. Prior to the invention and acceptance of the polarographic electrode dissolved oxygen (DO) probe this was done by completing the reaction of a sample through titration (Harbaum and Houghton, 1962). However, the DO probe is now a widely used and accepted form of measuring the mass transfer (absorption) of oxygen in aqueous

solutions (Baird and Garstang, 1972; Ellenberger and Krishna, 2003; Knopf et al., 2005a; Waghmare et al., 2008).

The DO probe works by measuring the current flow between two electrodes generated by an oxidation-reduction reaction. The measurements taken by the DO probe are representative of dissolved oxygen concentration in the sample at any time. The volumetric mass transfer (k_La) is determined by measuring the oxygen concentration and applying the concentration within a mass balance given by (Baird and Garstang, 1972),

$$\frac{dC}{dt} = k_L a(C^* - C) \tag{2.49}$$

where C^* is the oxygen saturation concentration and C is the instantaneous concentration. Integration of Eq. (2.49) with boundary conditions,

$$C(t=0) = C_0$$
$$\lim_{t\to\infty} C = C^*$$

gives,

$$\ln\left(\frac{C^* - C}{C^* - C_0}\right) = -k_L a t \tag{2.50}$$

Equation (2.50) can be manipulated to form the same expression as Eq. (2.1), given C_0 = 0. Note that this method is analogous to the lumped capacitance method for transient conduction heat transfer (Çengel and Ghajar, 2011). As for the case of the lumped capacitance method some assumptions must be made about the bulk fluid to qualify. The oxygen concentration of the fluid batch must be uniform at any instant. This assumption is generally appropriate for well mixed systems as in the case of a vibrating BCR with a high degree of turbulence. Additionally, the assumption that k_La is not a function of time is inherent in the integration. The accuracy of the

method requires that the probe be responsive, or that it does not suffer from a time lag. Benedek and Heideger (1970) and Baird and Garstang (1972) give a reasonable account of the sources of errors involved with using an oxygen probe in unsteady state measurements and report worst case error in k_La measurement to be 15%. Furthermore the polarographic probes used in the current literature are all of a similar type with similar response times and accuracies (Ellenberger and Krishna, 2003; Knof et al., 2005a; Waghmare et al. 2008).

The method of desorption can also be used to track the concentration of oxygen using the same method. In fact the process is just reversed, for example a fluid that is initially saturated with oxygen can be injected with nitrogen. Nitrogen causes oxygen to come out of solution decreasing the concentration. Fan and Cui (2005) use the desorption method by measuring the oxygen concentration using a novel optic method which measures the collision of oxygen molecules with the probe by energy transfer to give partial pressure of oxygen. The partial pressure can then be related to the oxygen concentration, presumably through Henry's Law (Tapley, 1990),

$$py_i = h_T x_i \tag{2.51}$$

where y_i and x_i are the mole fractions of the gas and liquid phase respectively, and h_T is Henry's constant which is a function of the temperature for a gas species *i*.

Interestingly another method to measure mass transfer rate of a reactive solution is by observing a color change of the solution with respect to time. This method typically uses an indicator similar to titration with starch and triiodide. Fan and Cui (2005) give an excellent example of this method by injecting ozone into a solution of potassium iodide producing the reaction,

$$2KI + O_3 + H_2O \rightarrow I_2 + 2KOH + O_2$$

The starch present in the solution acts as an indicator when it reacts with the iodine product turning purple. Analogous to the dissolved oxygen in water the color change indicates a concentration change of potassium hydroxide (dissolved oxygen in potassium solution), or conversely the absorption of ozone (bubbles) in solution. It can be seen that in the presence of vibration the rate of concentration change is faster (Figure 2.29b) than the quiescent reaction (Figure 2.29a).

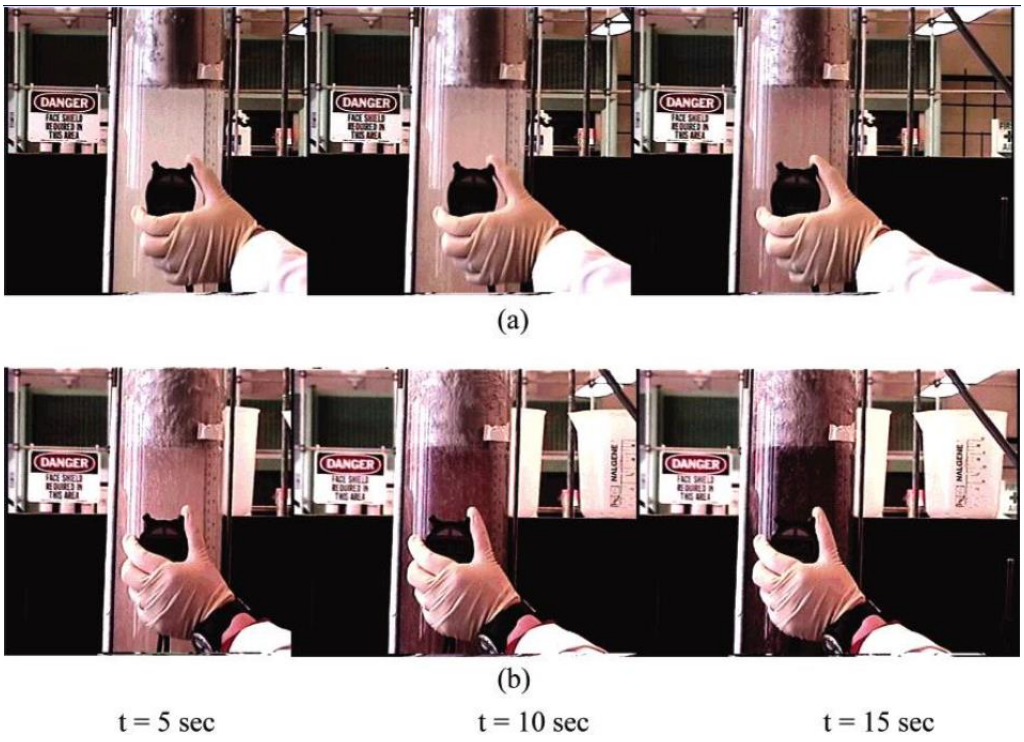

Figure 2.29: Observation of mass transfer using a color indication a) with no vibration and b) with vibration (Fan and Cui, 2005)

The primary disadvantage to both physical and visual titration methods are due to the need for chemical processing which is both more laborious and more difficult than DO probe "unsteady state" methods.

2.2.3. Measurement of Bubble Velocity (U_b)

Measurement of bubble velocity in the research has been confined to non-vibrating cases. Redfield and Houghton (1965) examined the mass transfer and drag coefficients for singular

bubbles rising in a quiescent fluid by measuring the rise velocity of the bubbles using a series of light beams and photocell detectors. Additionally, bubble rise velocity has been measured in bubbly flows and column reactors directly using 2-point conductivity probes (Lewis and Davidson, 1983), single point optical probes (Cartellier, 2001) and 4-point optical probes (Frijlink, 1987; Mudde and Saito, 2001; Guet et al., 2003, Luther et al., 2004; Bai et al., 2008). In all cases the reported uncertainty for measuring bubble velocity is less than 20%, and some methods are found to be more accurate than others.

Direct measurement of bubble velocity is important in the case of a vibrating BCR in order to better understand velocity profiles and the hydrodynamics of the column. The change in rise velocity is a distinct indicator of the forces at work, particularly the "Bjerknes force" which has already been qualitatively observed in the previous research. However, the previous research lacks quantitative measurement of these forces. Bubble velocity measurements in non-vibrating BCR's have led to considerable improvements in understanding the overall flow. Measuring the bubble velocity in a BCR with a 4-point optical probe has even given researchers the ability to relate reactor flows to bubbly pipe flows (Mudde and Saito, 2001). The literature shows that measurement of bubble velocity has been successful in non-vibrating columns, and suggests that there is a distinct need for bubble velocity measurements in vibrating BCR's to help better understand the physics of the flow.

2.2.4. Vibrating Apparati: advantages and disadvantages

There are generally two methods to provide oscillation to a bubble column that has been found in the research. The first method requires shaking the column vessel itself (Figure 2.30) (Rodgers and Hughes, 1960; Buchanan et al., 1962; Baird, 1963; Jameson and Davidson, 1966). The second method applies vibration directly to the fluid either through a piston type device (Figure 2.31) (Krishna and Ellenberger, 2002; Waghmare, 2008; Bretsznajder et al., 1963;

Oliveira and Ni, 2001), a resonating device placed in the fluid (Fan and Cui, 2005), or air pulsing (Baird and Garstang, 1967). There are advantages and disadvantages to using either method.

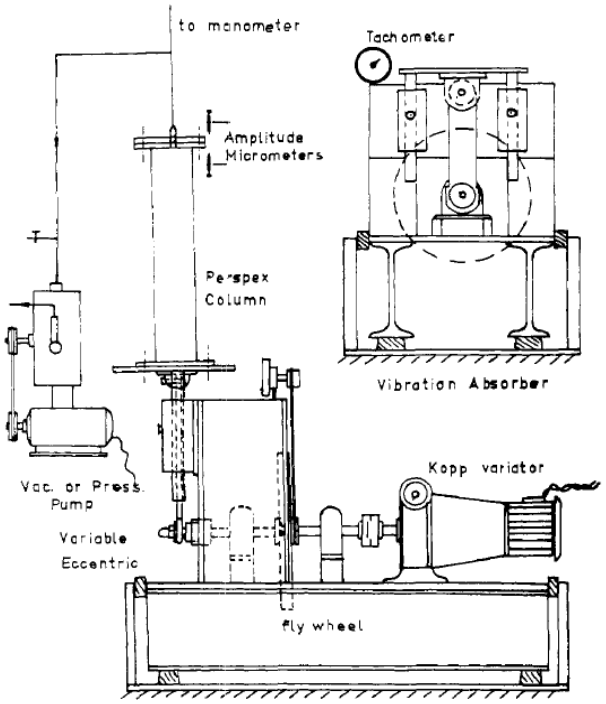

Figure 2.30: Schematic of device typical of "whole cylinder" shaking (Buchanan et al., 1962)

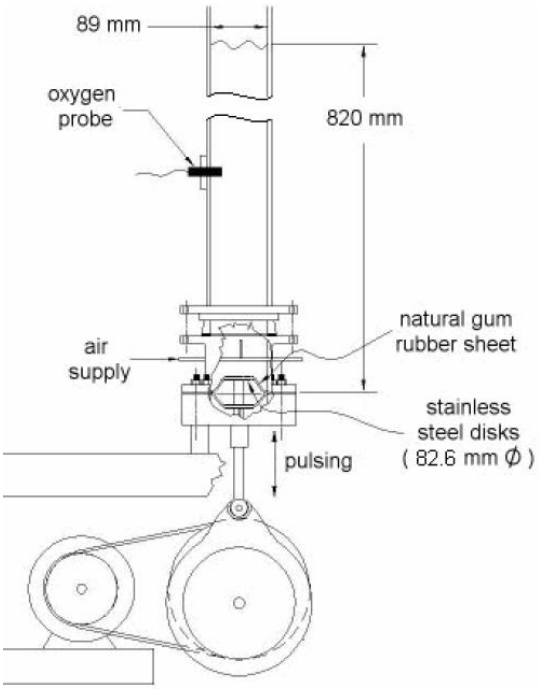

Figure 2.31: Schematic of device typical of "piston pulsing" (Waghmare et al., 2008)

Typically vibration of the entire column is preferable with respect to the "quality" of amplitude and frequency input. There is some skepticism as to whether piston inputs create unpredictable wall effects (Buchanan et al., 1962). One could argue that the pressure pulse being applied to the fluid column may not be uniform based solely on the geometric shape of the piston as it stretches (Figure 2.31). As a corollary, the velocity profiles developing in the liquid could have significantly different effects on the centerline of the column, or at the walls. The determination of the amplitude input for piston type vibration has already been noted as a cause for concern because of piston geometry. Fluid amplitude has been observed to be different from the mechanical amplitude based on the piston membrane thickness (Knopf et al., 2005a).

One obvious advantage to pulsing a liquid column is its lower power input and improved scalability. Pulsing provides better scalability for larger size systems since the fluid mass alone is being driven, and not the container or whole system mass as in the case of cylinder shaking. Because of the reduced mass driving requirements of piston pulsing, much higher frequencies can typically be achieved where mass transfer is greatly increased (Ellenberger et al., 2005). However, since amplitude and frequency have not been clearly disconnected in the previous mass transfer experiments it could be possible to generate higher mass transfer rates at lower frequency and higher amplitude leading to lower structural and power requirements.

2.3. Related Works

There are a few relevant works present in the literature which apply to this study that are not directly concerned with vibrating BCRs. However, the results offer insight into measurement methods, experimental conditions, and similar results which may be applicable and have not already been discussed.

One of the methods used to improve mixing in reactors has been to oscillate baffles inside the reactor (Baird and Garstang, 1972) or to oscillate the reactor with fixed baffles (Baird

and Garstang, 1967; Oliveira and Ni, 2001). The baffles impart turbulence to the flow through creation of vortices which enhance mixing. In both cases improvements in mass transfer have been observed in connection with the frequency and amplitude. Oliveira and Ni (2001) show that an oscillating baffled column reactor provides improvements in column averaged void fraction that are correlated directly to the specific power input similar to Waghmare et al. (2008). Using a photographic technique they correlate the Sauter mean diameter of the bubble distribution to power input (*P*) by,

$$d_{32} = kU_{SG}^{m}\left(P/V\right)^{n} \tag{2.52}$$

where k, m and n are all correlation variables for the specific experimental set up. In this particular case with a baffled column, P/V is defined as (Oliveira and Ni, 2001),

$$P/V = U_{SG}\rho g + \frac{2\rho N_b}{3\pi C_d^{\,2}}\frac{1-\alpha^2}{\alpha^2}A^3\omega^3 \tag{2.53}$$

Where N_b is the number of baffles per unit length (m^{-1}), α is the baffle free cross-sectional area and C_d is the discharge coefficient. It can be seen that the time averaged power density (P/V) (W/m^3) described by Eq. 2.53 varies somewhat from Waghmare et al. (2007) particularly in regard to the vibration and amplitude exponents.

The same method used for diameter is applied to void fraction, and using k = 0.175, m = 0.4, and n = -0.2gives (Oliveira and Ni, 2001),

$$\left\langle \varepsilon \right\rangle = 0.1U_{SG}^{0.4}\left(P/V\right)^{0.2} \tag{2.54}$$

As can be seen from Figure 2.32, prediction of Eq. 2.54 agrees with their experimental data.

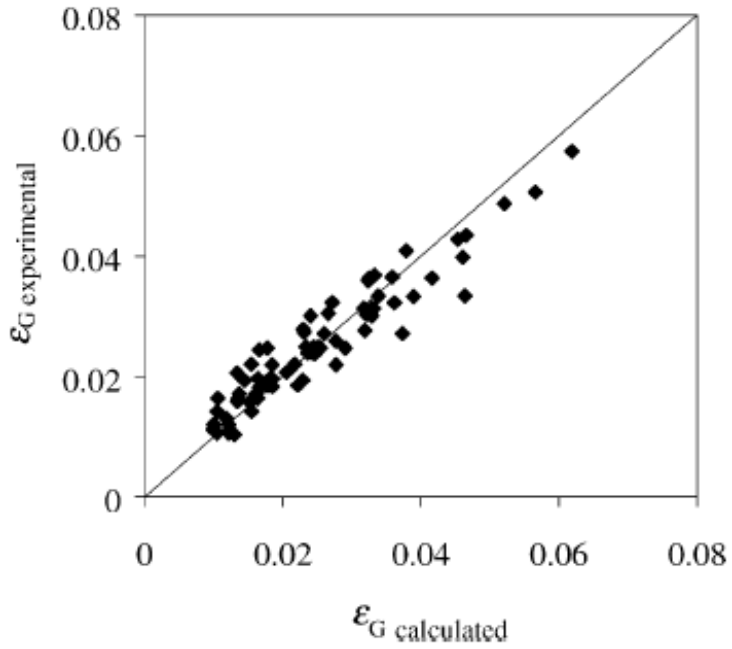

Figure 2.32: Experimental results for void fraction compared to Eq. (2.54) in an oscillating baffled column with air-water (Oliveira and Ni, 2001)

Finally, based on equations (2.53), (2.54) and a mass transfer correlation by Ni and Gao (1996) for a similar set-up, Oliveira and Ni (2001) propose that mass transfer in an oscillating baffled column reactor can be correlated simply to the Sauter mean diameter of the bubbles and the void fraction by,

$$k_L a = 0.284 \frac{\varepsilon^{1.5}}{d_{32}^{\ 0.6}} \tag{2.55}$$

Remarkably, Eq. 2.55 is a function of only two derived parameters: void fraction and bubble size which are in turn, functions of superficial gas velocity and volume specific power input. However, these results are derived from expressions specific to oscillating baffled columns, but it is important to see the similarity to the approach of Waghmare et al. (2008). Indeed, the advantage of relating two oscillating flows even separated by physical internals through an input power parameter may be a useful tool in relating all oscillating flows regardless of set up.

Another interesting example of research into the Bjerknes effect may be found in Fan and Cui (2005). Contrary to the bulk of the literature reporting Bjerknes type effects on bubble motion for low frequencies (f < 120 Hz), Fan and Cui (2005) present similar results but for ultrasonic frequencies ($\boldsymbol{f}$ = 16, 20 kHz). Using an oscillator placed inside the fluid at the top and bottom of the column they are able to show clearly the concentration of bubbles at the antinodes as reported by Ellenberger et al. (2005) (Figure 2.33).

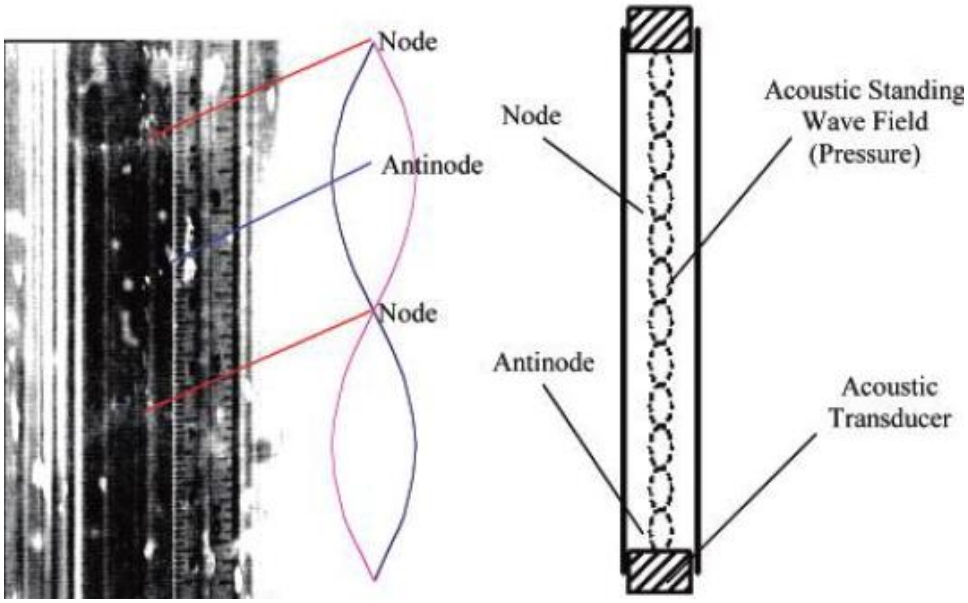

Figure 2.33: Images showing bubble grouping at pressure wave antinodes for nitrogen-oxygen saturated water at f = 16 kHz (Fan and Cui, 2005)

Experimental results showed the migration of bubbles opposite to the pressure field as predicted by Bjerknes (1906) which is indicated as a delay in the rise time or a decrease in the rise velocity of approximately 20% (Fan and Cui, 2005) (Figure 2.34).

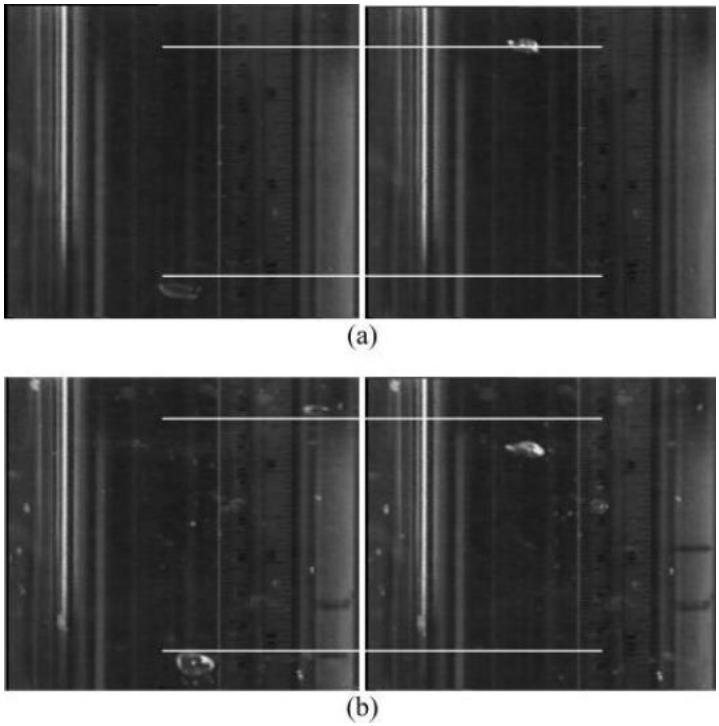

Figure 2.34: Image showing the effect of vibration on bubble rise time (velocity) for nitrogen-oxygen saturated water for a) no vibration and b) vibration at *f* = 16 kHz (Fan and Cui, 2005)

Bubbles were seen to cluster at the pressure node and to collect toward the axis of the funnel presumably by lift forces created from higher velocity profiles at the axis (Fan and Cui, 2005). However, as shown by the scale lines (funnel throat diameter) drawn on the picture, lift forces alone cannot account for the difference in cluster tightness since lift (generated by downward flow from funnel throat) should be equal for both pictures. For example the picture showing no vibration shows a bubble cluster approximately three scales wide and 6 scales high, whereas the picture showing the bubble cluster under the influence of vibration is approximately two scales wide and only 3 scales high. Opposite to Fan and Cui's interpretation of the results, Bjerknes (1906) predicts the mutual attraction of two pulsating bodies in the presence of an oscillating field if their pulsations are synchronous. This secondary Bjerknes force or "mutual attraction" would more accurately describe the bubble cluster that is occurring than lift forces would, especially since lift forces would only be apparent in the horizontal axis and not the vertical axis as is seen (Bjerknes 1906) (Figure 2.35).

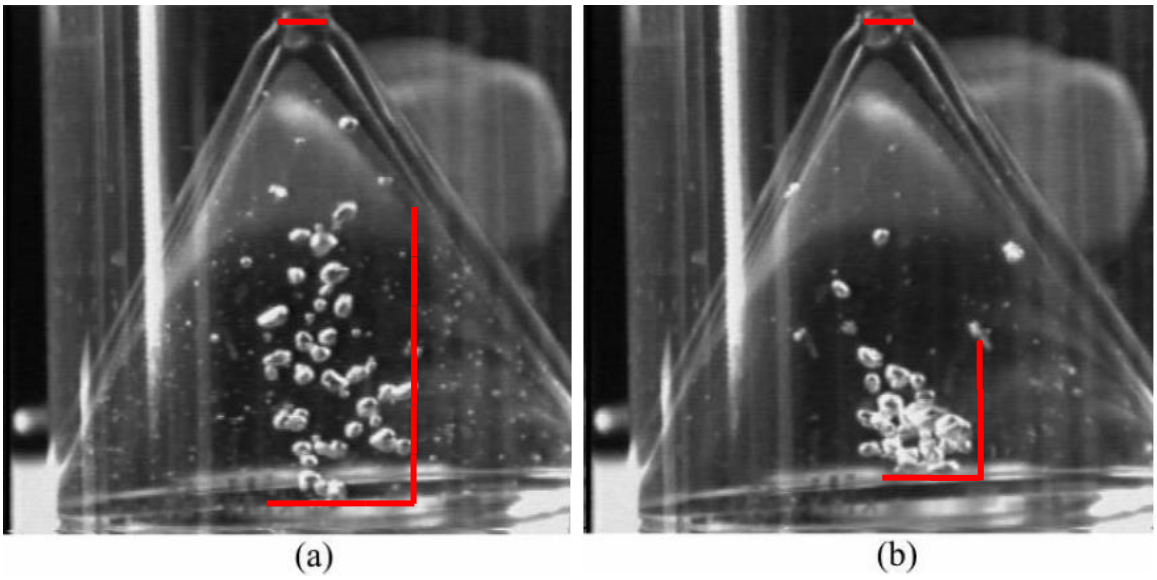

Figure 2.35: Images showing effect of vibration on bubble attraction for the case of a) no vibration and b) vibration at f = 16 kHz (Fan and Cui, 2005)

The results of Fan and Cui's (2005) mass transfer measurements at f = 16 kHz show improvements of 120%, slightly smaller than those found by Ellenberger et al. (2005) for f = 60 Hz. Figure 2.36 shows that mass transfer is increased with vibration especially at low gas rates, but more interestingly it is increased proportional to the input power and not necessarily the frequency. This last point is significant in that it agrees with the findings of both Waghmare et al. (2008) and Oliveira and Ni (2001) that mass transfer is strongly correlated to power input. However, Figure 2.36 also shows that the frequency component may not be contributing as much as the amplitude which has not been studied in great detail.

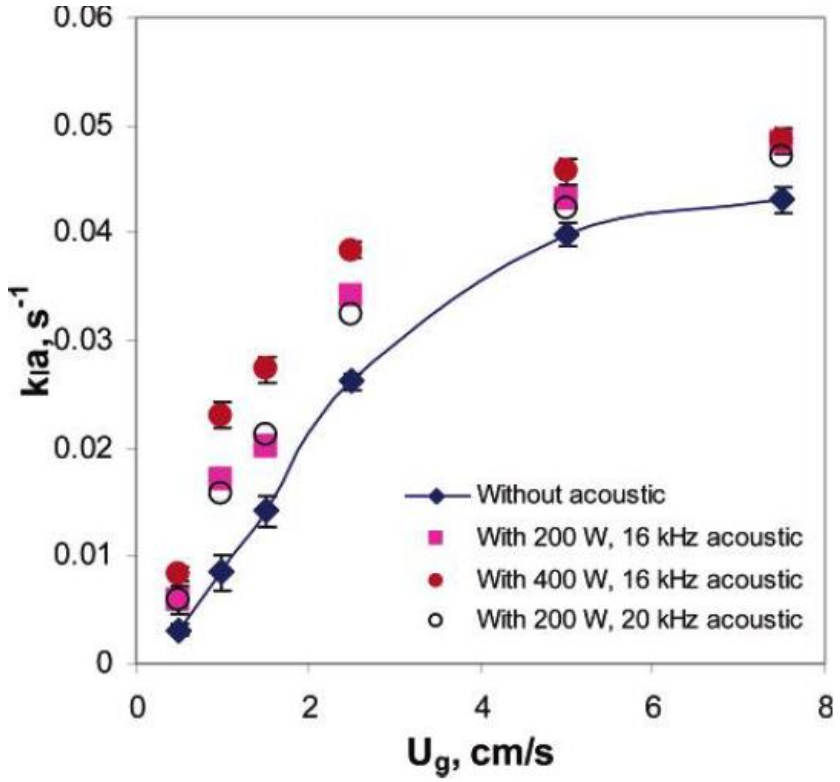

Figure 2.36: Experimental results for k_La showing improvement with superficial gas velocity and acoustic power for nitrogen-oxygen saturated water (Fan and Cui, 2005)

Fan and Cui (2005) provide excellent examples of mechanisms in the flow field which can be attributed to Bjerknes forces. The results give particular credence to the work presented by both Ellenberger et al. (2005) and Waghmare (2008). However, two similar results at such strikingly different frequency regimes elicits the question. What is the unifying parameter? The answer may be found in the power input, but furthermore what is the relationship that amplitude plays within the input power product compared to frequency?

Drag has been included as an important force in each analysis described above, and rightfully so as it opposes both the buoyancy and kinetic buoyancy "Bjerknes" forces. Only Houghton (1963) and Jameson (1966) have treated viscous forces with anything more complex than a simple drag model. In fact Jameson's results show that for small Reynolds numbers the drag on the rising bubble in an oscillating fluid must be negligible enough for the Bjerknes number (*Bj*), Eq. (2.46) to be 1, but for higher Reynolds numbers ($Re > 2$) *Bj* is greater than unity

(Figure 2.37). It should be noted however, that Jameson (1966) defines a "vibration" Reynolds number as,

$$\mathrm{Re}_{v} = \frac{\omega A r_0}{\nu} \tag{2.56}$$

where r_0 is the mean bubble radius (m) as noted previously.

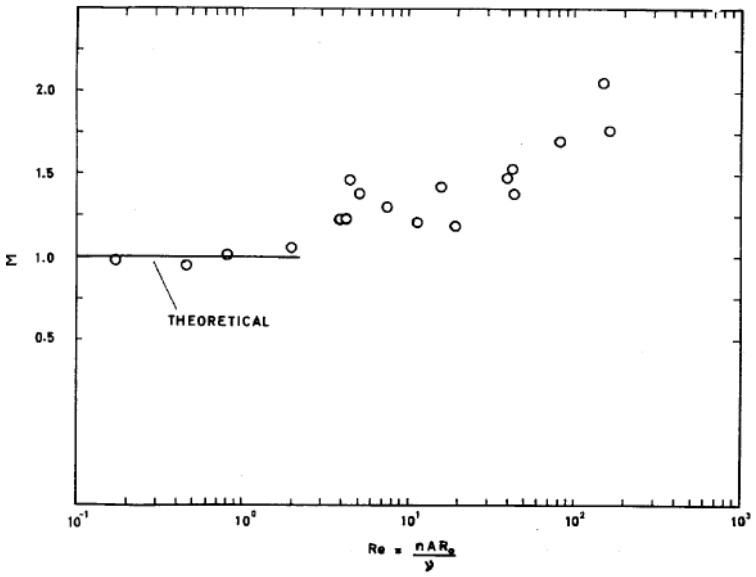

Figure 2.37: Experimental results with correlation between dimensionless parameter M (Bjerknes number (*Bj*)) and Reynolds number (Jameson, 1966)

Both Waghmare and Ellenberger use simple drag models to predict the outcomes of their experiments as previously described. However, both models use approximations for C_D that are applicable to homogeneous bubbly flows (Ellenberger et al., 2005) or fluidized solid beds (Waghmare et al., 2008). There are no published results for a vibrating BCR to date that have modeled drag applicable to spherical bodies in an oscillating field as would seem more appropriate. Additionally, and assuming that the Bjerknes force is well characterized, there has been no research to determine: the effect of drag on bubble velocity, the calculation of drag coefficients, or the effect bubble wake profiles have on mass transfer in a vibrating BCR. Flow visualization of bubble and fluid structures would also provide valuable insight.

2.4. Summary

The history of vibrating BCR research dates back to the 1960's with the early work of Harbaum and Houghton (1960) who found that mass transfer in a bubble column increased in the presence of vibration. Buchanan et al. (1962) studied the general motion of bubbles in a column of varying height, head pressure, frequency and amplitude noting a critical frequency at which bubble motion will stop relative to the fluid, and they ascribed this to an inviscid force balance relating kinetic buoyancy or "Bjerknes force" to natural buoyancy. Further study of the Bjerknes force and attempts to model it for a vibrating liquid column were carried out by Harbaum and Houghton (1962), Houghton (1963), Jameson and Davidson (1966), and Jameson (1966) with varying and conflicting results.

Ellenberger and Krishna (2003) returned to the subject of mass transfer in a vibrating BCR showing that particular frequency and amplitude combinations provided optimum mass transfer. Furthermore, an extended study of frequency effects ($0 < f < 100$) showed particular increases in local gas hold up corresponding to standing pressure wave nodes (Ellenberger et al., 2005). However, the results of both studies were limited to a single fluid (water), a single head pressure (atmospheric), and low amplitudes ($A \leq 1\,\text{mm}$). Knopf et al. (2005b), also studied the effects of vibration on a BCR and found that, contrary to Harbaum and Houghton (1962), amplitude had more of an impact on improving void fraction and mass transfer. Previous researchers have opted to apply piston pulsing to impart vibration to the fluid, but a distinct non-linearity has been found in the measured amplitude input based on the stiffness of the piston's rubber membrane raising doubt about the accuracy of the method (Knopf et al. 2005a). Furthermore, some of the previous research using piston pulsing was unable to fully separate frequency and amplitude based upon the use of an electro-dynamic shaker (Krishna and Ellenberger, 2002; Ellenberger and Krishna, 2003; Ellenberger et al., 2005).

Combining a bubble breakage theory by Hinze (1955), Stokes-Einstein relationship for viscosity and diffusivity, and penetration theory Waghmare et al. (2008) offers a semi-empirical correlation to predict void fraction and mass transfer of a vibrating BCR based upon fluid properties and power input. The correlation is shown to give moderately good results based on experiments performed with a low frequency piston pulsing set-up at two amplitudes with varying fluids at atmospheric pressure (Waghmare et al., 2008). A comprehensive comparison of experimental parameters and results is given in Tables 2.1 and 2.2.

Table 2.1: Summary of previous research parameters

Investigators	Frequency (Hz)	Amplitude (cm)	Column Diameter (cm)	Liquid Height (cm)	Mode of Pulsing	Liquid/Gas
1. Harbaum & Houghton (1962)	20 - 2000	0.1	7.6	61	piston-diaghragm	H_2O/CO_2
2. Buchanan et al. (1962)	20 - 48	0.05 - 1	5 - 15	15 - 100	whole column	Mercury, lube oil, glycerol, ethanol, butanol, slurry/air(?)
3. Bretsznajder et al. (1963)	5 - 67	0.05	20	84	piston-diaghragm	H_2O/CO_2
4. Baird (1963)	0 - 1050	-	5.1 / 6.4	23	whole column	H_20, glycerol, paint resin, hydroxy-ethyl cellulose/air
5. Baird and Garstang (1967; 1972)	0.9-1.4	0 - 15.2	7.6	305	air-pulse	H_2O/air
6. Jameson & Davidson (1966)	20 - 60	0.4 - 0.8	1.9	38.7 - 41.8	whole column	H_2O, dilute glycerol, glycerol/air
7. Nyborg & Rogers (1967)	25 - 200	0 - 0.3	2 x 0.3, 2 x 0.6*	12	whole column	dist. H_20 (w/ blue dye)/air
8. Oliveira & Ni (Baffled) (2001)	1 - 5	0.2 - 0.8	5	150	metal bellows	H_2O/air
9. Krishna & Ellenberger (2002)	10 - 100	0 - 0.12	10	200	piston-diaghragm	H_2O/air
10. Ellenberger et al. (2005)	10 - 100	0 - 0.12	10	200	piston-diaghragm	H_2O w/0.03%Wt NaCl/air
11. Fan & Cui (2005)	16000 - 20000	-	10.26	80	acoustic transducer	H_2O/N_2, H_20/O_2, KI/O_3
12. Knopf et al. (2005a; 2005b)	10 - 30	0.05 - 0.25	8.9	82	piston-diaghragm	DI H_2O/air
13. Waghmare et al. (2008)	10 - 30	0.05- 0.25	8.9	78	piston-diaghragm	H_2O, 2% CMC, 3% CMC/air

* - Nyborg and Rogers used two rectangular containers with dimensions of width x depth
(?) - Assumed gas phase

Table 2.2: Summary of previous research results

Investigators	μ (cP)	ρ (g/cm^3)	p_e (kPa)	U_{SG} (cm/s)	d_b (cm)	ε	k_La (s^{-1})
1. Harbaum & Houghton (1962)	1	1	93.9	0.13 - 1.4	0.11 - 0.22	0.05 - 0.25	0.035
2. Buchanan et al. (1962)	1.2 - 1490	0.79 - 1.33	13.3 - 226.6	-	-	-	-
3. Bretsznajder et al. (1963)	1	1	atm	-	-	-	-
4. Baird (1963)	1 - 3000	0.93 - 1.01	atm	-	-	-	-
5. Baird and Garstang (1967; 1972*)	1	1	atm[1]	1.6 - 2.6	0.2 - 0.3	0.05 - 0.14	0.05 - 0.15*
6. Jameson & Davidson (1966)	1 - 1000	1 - 1.22	atm	-	-	-	-
7. Nyborg & Rogers (1967)	-	-	atm	-	-	-	-
8. Oliveira & Ni (2001*)	1	1	atm	0.1 - .64	3 - 11	0.01 - 0.06	-
9. Krishna & Ellenberger (2002)	1	1	atm	0.1 - 1.4	1.6 - 3.7	0.01 - 0.13	0.02 - 0.07
10. Ellenberger et al. (2005)	1	1	atm	1	-	0.05 - 0.2	0.01 - 0.05
11. Fan & Cui (2005)	1	1	atm	0.5 - 7.5	3.5 - 5.5	-	0.005 - 0.05
12. Knopf et al. (2005a; 2005b)	1	1	atm	0.01 - 0.15	-	0.005 - 0.06	.003 - 0.014
13. Waghmare et al. (2008)	1 / 11 / 67	1/1/2001	atm	0.1 - 1.5	4 - 6	0.0021 - 0.0597	0.001 - 0.037

* - Investigators used baffled columns
1 - Investigators claim back pressure higher than atmospheric, but not quantified

2.4.1. Research Objectives

Based upon a review of the literature the results of the previous research are somewhat scattered and often conflicting. Various attempts to model the system have been complicated, and occasionally erroneous or contrived. There is a definite need to expand the study of amplitude effects on mass transfer by extending the magnitude beyond 2.5 mm, and divorcing the amplitude and frequency to study each effect individually in order to compare the individual response with the product. Additionally, there is some doubt as to the effect that piston pulsing has had on the experimental outcomes. Therefore the objectives of this research are threefold:

1. Fill the gaps in experimental results for void fraction, bubble velocity and size by observation of the hydrodynamics of the bubble column reactor at varying frequency,

amplitude, head pressure, column diameter and fluid combinations and to compare the results with previous research.

2. Determine the effects of amplitude on mass transfer by vibration of the whole cylinder with comparison to results found by piston pulsing.
3. Correlate the input parameters of the bubble column and the results of the previous objectives to facilitate prediction through physics based modeling and/or flow mapping.

2.4.2. Research Tools and Equipment

To meet the proposed research objectives some specific tools and equipment must first be designed, built and verified. Since much of the previous research has been focused on small amplitude vibration a review of the available shaker technology was necessary to determine if a commercial option was possible. Additionally, the desire to shake the entire column necessitated a slightly larger test weight. The commercial options reviewed either did not meet the testing requirements, or were cost prohibitive. Therefore a custom shaker was needed which would meet the testing requirements. In addition to experimentation, the scope of this research includes the following preliminary tasks:

1. Design and build 4 pressurized bubble columns with varying diameters capable of withstanding the vibration loads, and instrument them for mass transfer, void fraction, bubble size and velocity measurements.
2. Design, build and verify a shaker device capable of vibrating the bubble columns at amplitudes between 1-10 mm and frequencies of 0-60 Hz.

CHAPTER III

EXPERIMENTAL SETUP

The experimental setup is comprised of three components: bubble columns, shaker, and instrumentation. The bubble columns consist of the physical cylinders as well as the necessary components to mount them to the test base of the shaker including: flanges, top plate, and hardware. The bubble column reactor (BCR) must be designed to withstand the vibration profile necessary during testing while maintaining pressure. Instrumentation used during testing is also lumped under the bubble columns category since most of the measurements concern the reactor. The shaker is the key component of the testing. Commercial options for shakers were not viable due to the high amplitudes, high test mass, separation of amplitude and frequency, and cost which necessitated a custom shaker to be built. The design and construction of the components are described in the following sections.

3.1. Bubble Columns

Four bubble columns were made which vary in size from 1.0 in. inner diameter (ID) to 5.5 in. ID. The range of diameters was chosen to represent both a “small” diameter and a “large” diameter. The bubble columns are instrumented with pressure taps for differential pressure measurements, and a polarographic dissolved oxygen probe for mass transfer measurements. Compressed air is injected into the column through a single orifice injector and controlled/measured by a metering valve/mass flow meter. Each column is designed to be pressurized over a range of 0.3 – 5 atm.

3.1.1. Design and Construction

The main bodies of the bubble columns are cast acrylic cylinders purchased from www.eplastics.com. Cast acrylic provides better optical clarity and higher strength than extruded acrylic or polycarbonate (Lexan). There are 4 cylinders which have internal diameters of 1.0, 2.5, 4.0, and 5.5 inches, respectively. Each cylinder is similar in construction, but there are a few differences. The 4 in. cylinder is 48 inches tall while the 1.0, 2.5, and 5.5 inch cylinders are each only 24 inches tall. The 4 in. cylinder was chosen to be the tallest specifically to test effects of fluid height. Based on the review of the literature it was seen that both 4 in. diameter and 48 in. height are typical of the columns used by other researchers. However, Buchanan et al. (1962) notes that only 12 to 14 cm of liquid height is required to see the Bjerknes interaction. Therefore the other cylinders are made shorter both to reduce cost and to reduce the test loads. Thus the 4 in. cylinder will be tested first to validate the experimental set up since it is most similar to previous research, and the other columns will be used specifically for comparison of diameter effects.

Each cylinder is capped on each end with 7 in. diameter flanges to provide a mounting base and pressure seal. The top flange (Figure 3.1a) is bored through to fit around the outer diameter of the cylinder, and the bottom flange (Figure 3.1b) is counter bored 0.75 in. The flanges are drilled with a pattern of 8, 1/4 in. bolts which provide the mounting points for the column to attach to the test base of the shaker at the bottom and the pressure plate at the top. Both flanges for the 4 in. cylinder were machined from 1 in. thick, 7 in. square, acrylonitrile butadiene styrene (ABS) plate (www.interstateplastics.com).

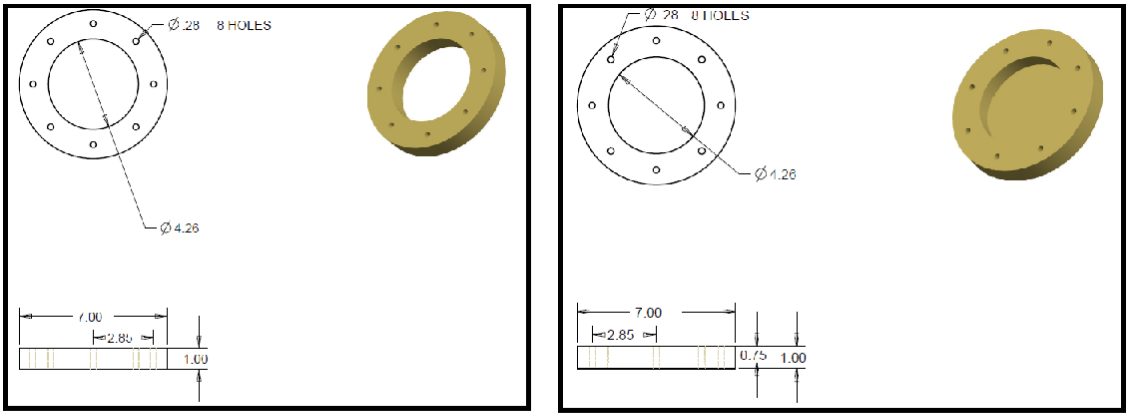

a) b)

Figure 3.1: a) Top and b) bottom flanges for 4 in. column

The flanges for the 1, 2 and 6 in. cylinders were machined from a 7 in. nominal diameter natural ultra-high molecular weight (UMHW) polyethylene rod purchased from (www.interstateplastics.com). Both ABS and UMHW are impact and chemical resistant and will bond to acrylic with the proper adhesive, but UMHW was available in a rod while ABS was only available in plate. Therefore, the switch was made from ABS to UMHW to facilitate faster manufacture. It was thought that by ordering the rod in a 7 in. diameter little to no working of the diameter would be necessary to fit the flange design, but unfortunately the tolerance limit for the UMHW rod diameter is very loose. The rod stock received was actually 7.38 in. in diameter and does not fit into the test base inset. It is recommended that future flange construction be reverted to ABS because it has a slightly better machinability and gives a superior bond with acrylic. The flanges are glued to the acrylic cylinder using IPS® Weld-On #10 cement. Weld-On #10 offers a high strength bond and adheres to a range of plastics including ABS and acrylic (Product Bulletin, 2008). Installing the flanges on the cylinder seals the bottom and allows the column to open at the top for filling (Figure 3.2).

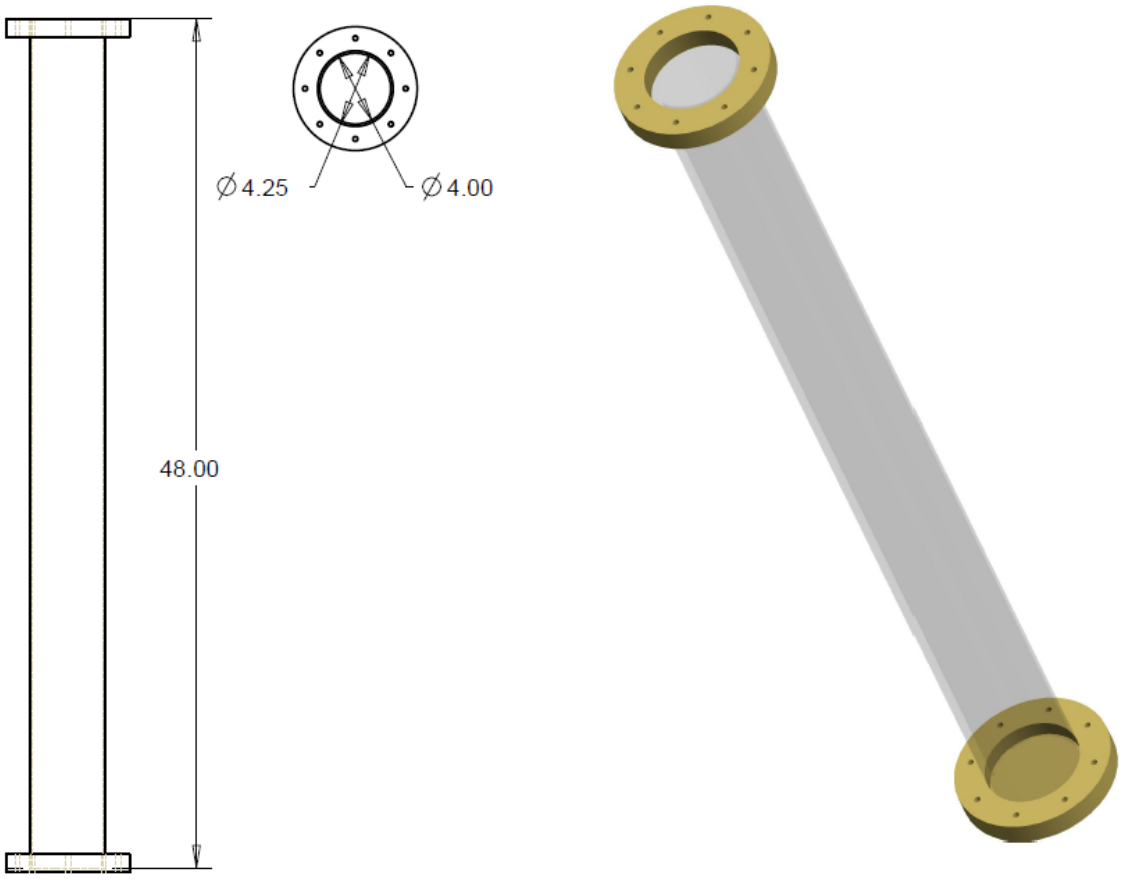

Figure 3.2: Bubble column design (units are in inches)

The bubble column is capped at the top by a 3/8 in. thick 9 in. square aluminum plate. The plate provides both a mechanical support of the bubble column and seals the column for pressurization. Similar to the shaker test base, the top plate is also machined with a 7 in. diameter inset for easier alignment with the bubble column and drilled with the 8 bolt hole pattern to match the flanges. A small 4.75 in. diameter notch is machined into the top plate inset and filled in with a ring of gasket sealer to create an integral pressure seal. When the top plate is mounted to the flange the column is airtight and supplied with external pressure through an air hose connected to the plate by the 1/4 in. male pipe thread fitting. The air hose connects the bubble column to the pressure manifold.

To reduce optical distortion due to the cylinder curvature a water box was designed for each cylinder. Originally, the 4 in. water box was constructed from 3, 1/8 in. thick polycarbonate plates glued together at the seams with 5 min. epoxy to form a C-channel. The C-channel was capped on each end by a short piece of polycarbonate with a 2.13 in. radius cut. When the caps are glued onto the channel it forms a half enclosure which mates to the radius of the cylinder at the top and bottom, and butts up to the centerline of the cylinder along the long edges. The water box was attached to the cylinder with 5 min. epoxy. Polycarbonate was chosen as the water box material over acrylic because it is easier to drill and cut without cracking. During testing, however, the water box was removed as will be described in section 3.2.2. No water box was designed for the 1.0, 2.5, or 5.5 in. cylinder either

3.1.2. Instrumentation

The majority of the measurements taken in the experiment are based around the column itself. Two pressure taps at 60 mm and 1000 mm from the top of the flange were drilled into the column with an 1/8 in. hole. The tap locations correspond to a fluid height of 79 and 1019 mm, respectively. The holes were de-burred to prevent obstruction and reduce losses. Two mounting blocks were machined from ABS which were glued to the cylinder with Weld-On #10 and align with the tap holes. The mounting blocks were drilled and tapped to allow a PVC 1/4 in. male pipe thread (MPT) to 1/4 in. compression coupling valve to be installed (Figure 3.3). Each valve is connected with a length of 1/4 in. outer diameter (OD) vinyl tubing which connects to a port on a Validyne differential pressure ΔP CD-15 transducer which has a frequency response of 1000 Hz. The differential pressure measurement will allow the differential pressure at the head and the base to be measured to account for any oscillating pressure fluctuation during cylinder vibration. For cases in which the column head is not pressurized the ΔP transducer will simply measure the hydrostatic pressure. During vibration with no column head pressure the hydrostatic pressure gives an indication of the pressure being applied within the fluid environment by the shaker.

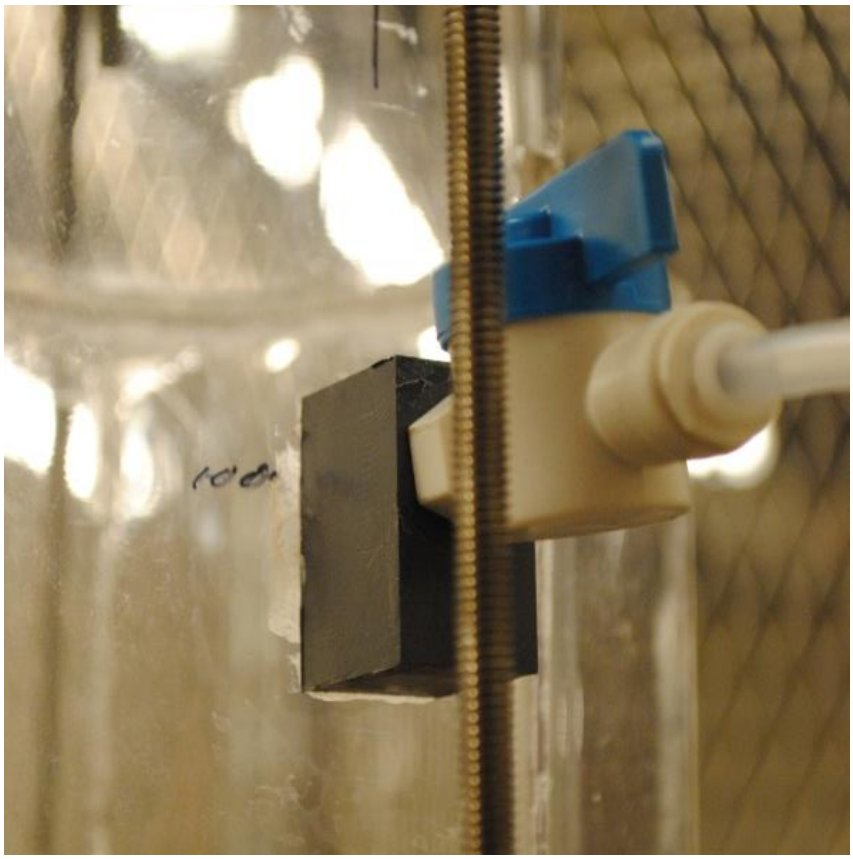

Figure 3.3: Upper pressure tap block and valve

The DO probe must be in contact with the test fluid to measure dissolved oxygen and must be installed on the cylinder. The DO probe is approximately 9 in. long and has a diameter of 0.498 in. A 1/2 in. hole was drilled into the cylinder at 3 column diameters or 12 in. (30.5 cm) from the tip of the injector to allow access to the probe. Based on previous research the DO probe was placed 3 column diameters away from the injector, and extends 0.10 column diameters into the fluid to allow a suitable mixing length and separation from the boundary layer for proper measurement (Rice et al., 1990; Clark et al., 1987). The probe also uses an electrolyte solution in the tip so the probe must be able to be removed, filled, and installed periodically for proper calibration and maintenance. To facilitate this requirement a two part mounting block was machined from ABS. The base consists of a 1.25 in. square block drilled through with a 1/2 in. hole, counter bored 0.045 in. with a 0.688 in. diameter to provide an inset for a Japanese

Industrial Standard (JIS) B 2501 P-12 rubber O-ring. The O-ring has an 11.8 mm (0.465 in.) ID and is 2.4 mm (0.094 in.) thick. The O-ring was glued in place with silicone to provide a positive seal against the body of the probe when installed while allowing flexibility during removal. The surface mounted to the cylinder was machined with a radius of 2.13 in. to match the curvature of the column's outer diameter. The base is aligned with the 1/2 in. hole drilled in the cylinder and cemented in place with Weld-On #10 (Figure 3.4).

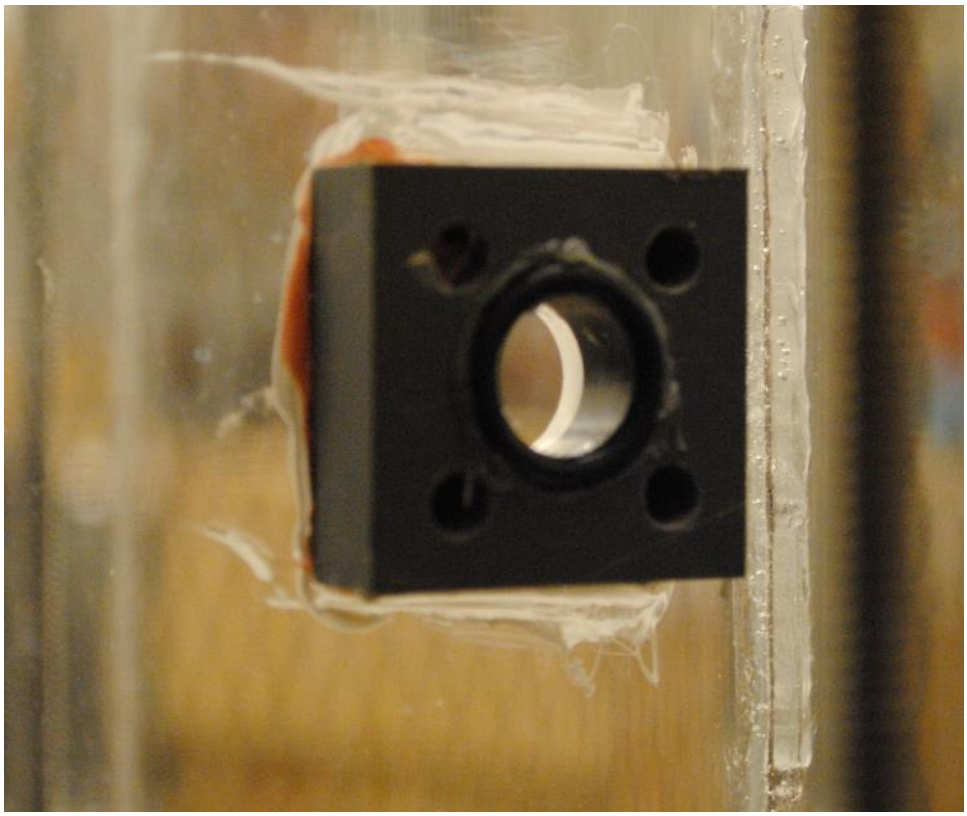

Figure 3.4: DO probe mounting block base

A corresponding cap piece was machined to match the base in which the probe will be installed with a low interference fit. The cap attaches to the base through 4, 10-32 thumb bolts mating the two pieces together. Another O-ring is installed over the probe once it is fit into the cap and the compression between the base and cap provided the seal (Figure 3.5).

Figure 3.5: DO probe installed on the cylinder

The final component directly mounted to the cylinders is the gas injector. The gas injector provides air injection to the cylinder. The injector tube is a 15 gauge, 316 stainless steel, hypodermic round tube with an internal diameter of 0.0625 in. (1.53 mm) and an outer diameter of 0.072 in. (1.82 mm) (www.smallparts.com). The tube is bent at a 90 degree angle in a manner as to not pinch the tube. The injector is mounted with a 1/8 in. compression to 1/4 in. MPT union using a special compression ferrule. The injector extends from the face of the compression nut through the cylinder wall and is aligned with the center of the cylinder (Figure 3.6). A small hole was drilled into the cylinder wall to allow the injector and filled in afterward with 5 min. epoxy and silicone. The adapter union containing the injector is installed into a mount machined from ABS which is attached by two 1/4 in. bolts to the flange. The injector mount has a 1/4 MPT x 1/4 ID barb fitting installed opposite to the injector which is inserted into a length of flexible vinyl tubing connected to the gas manifold (Figure 3.7). A schematic of the injector is provided in Figure 3.8 for reference.

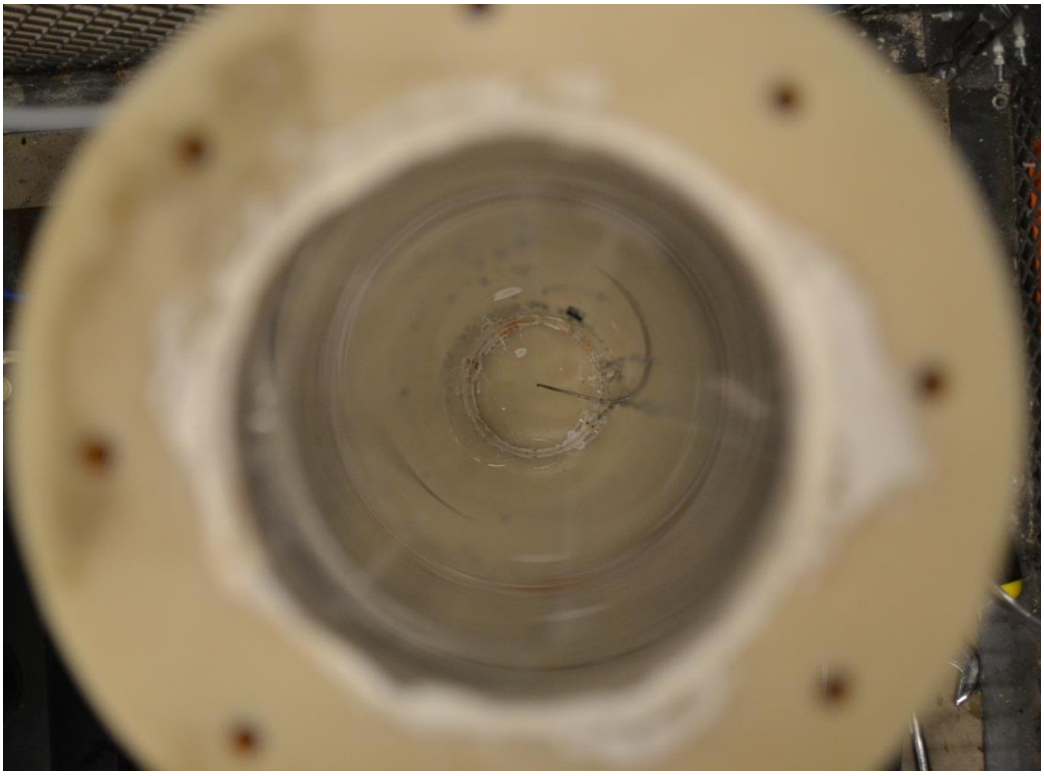

Figure 3.6: View from top of column showing the injector at the center of the bubble column

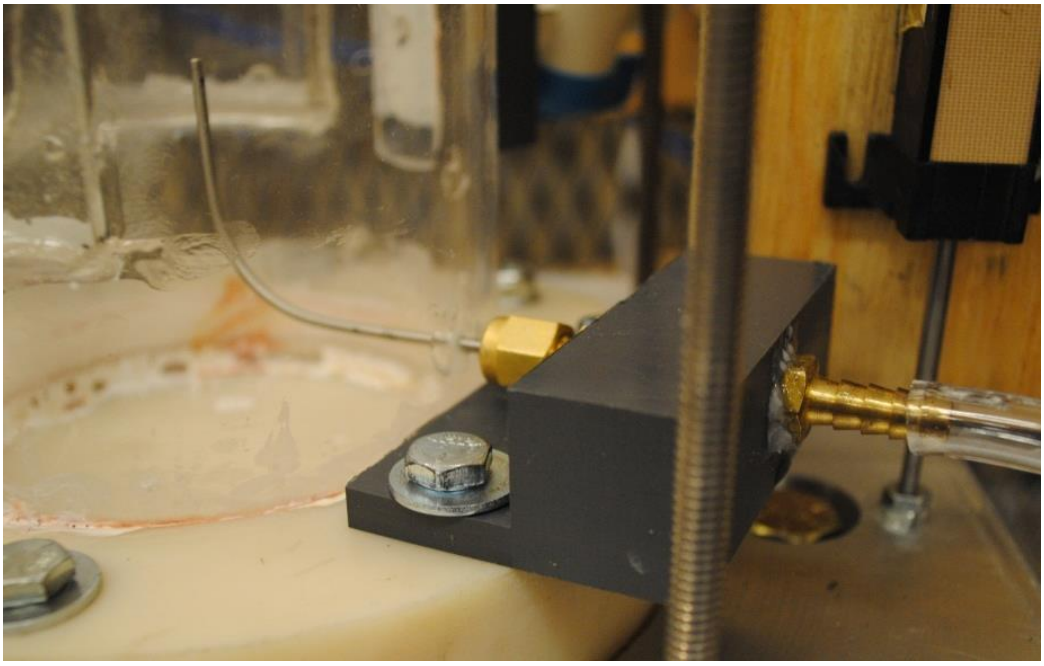

Figure 3.7: Gas injector unit connected to 4 in. column

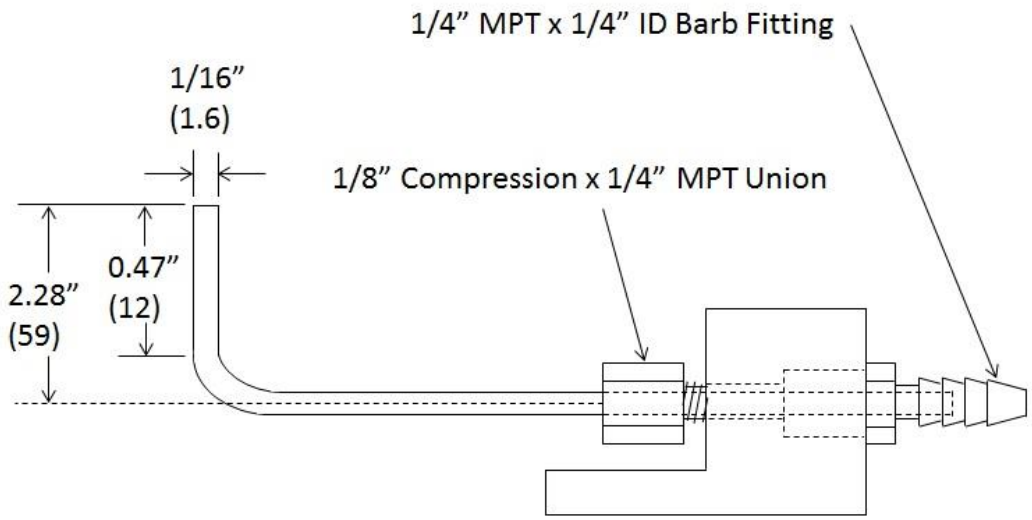

Figure 3.8: Gas injector schematic

Pressurized air supply to the injector is controlled by an ON/OFF globe valve on the gas manifold and regulated by both a coarse and fine metering valves on the flow meter manifold. There are two Micro Motion Elite series Coriolis mass flow meters with ranges of 0.0002 – 0.0062 kg/min and 0.0100 – 0.5000 kg/min which are connected from a supply to a distribution manifold (Cook, 2004). The mass flow meters have an uncertainty of ± 0.20% gas flow rate. The distribution manifold is installed with a coarse metering valve and a Parker Model 24NS 82(A)-V8LN-SS Needle Valve for fine adjustments of air flow. All of the gas inputs to the system are controlled at the pressure manifold (Figure 3.9). The pressure manifold controls compressed air going to the injector as well as air to pressurize the column. The column pressure is maintained at a constant value by ON/OFF globe values and a pressure regulator/bypass valve. Two globe valves are used to select from vacuum or compressed air pressure. The selected column pressure source is routed to a 25 ft., 1/4 in. ID coiled Nylon air hose which connects to the top plate on the column. The pressure is measured at the manifold by a gauge for convenience, and the pressure is maintained in the column during gas injection by an adjustable 0 – 100 psi pressure relief valve. Another globe valve is positioned downstream of the pressure relief valve to relieve excess pressure and to bypass the relief valve.

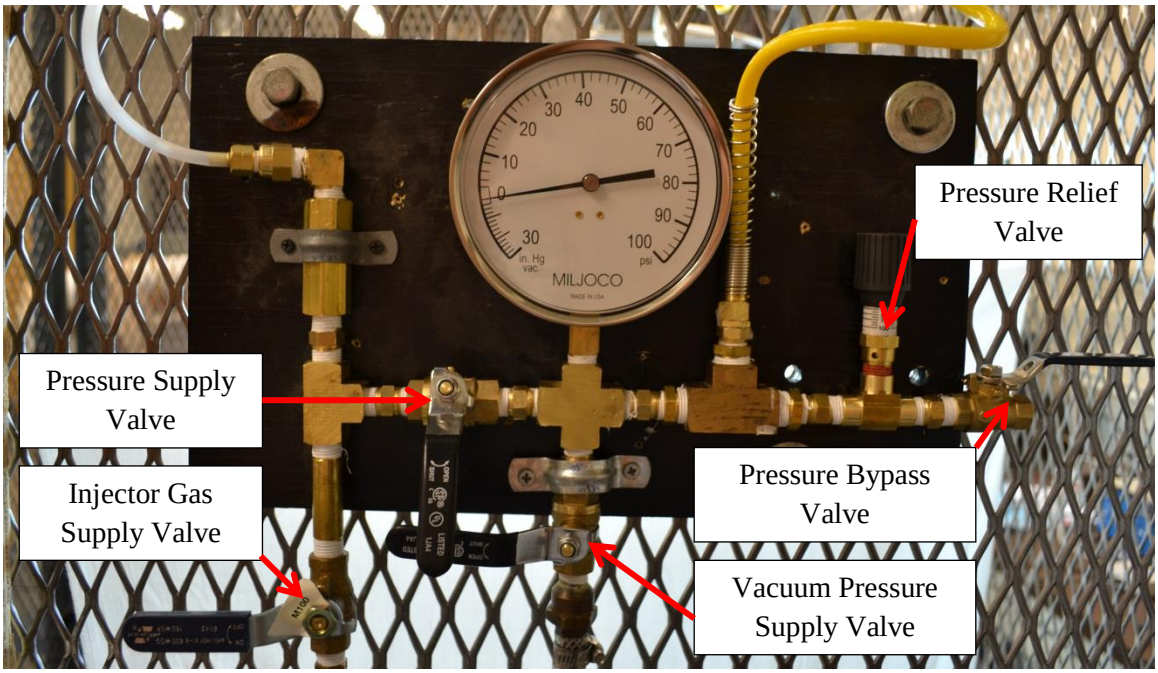

Figure 3.9: Pressure manifold

Vacuum pressure is supplied by a vacuum pump system. The system consists of a pump, inlet filter, ON/OFF switch, manifold, reservoirs and pressure control valve. The vacuum pressure can be adjusted by turning a small slotted screw on the pressure control valve. Clockwise decreases vacuum and counterclockwise increases vacuum to a maximum of 21 in. Hg. The pressure control valve automatically controls the pump operation to maintain the vacuum at ± 2 in. Hg (Figure 3.10). However, once selected vacuum pressure is achieved, closing the pressure feed valve at the manifold will maintain pressure in the column for an extended time.

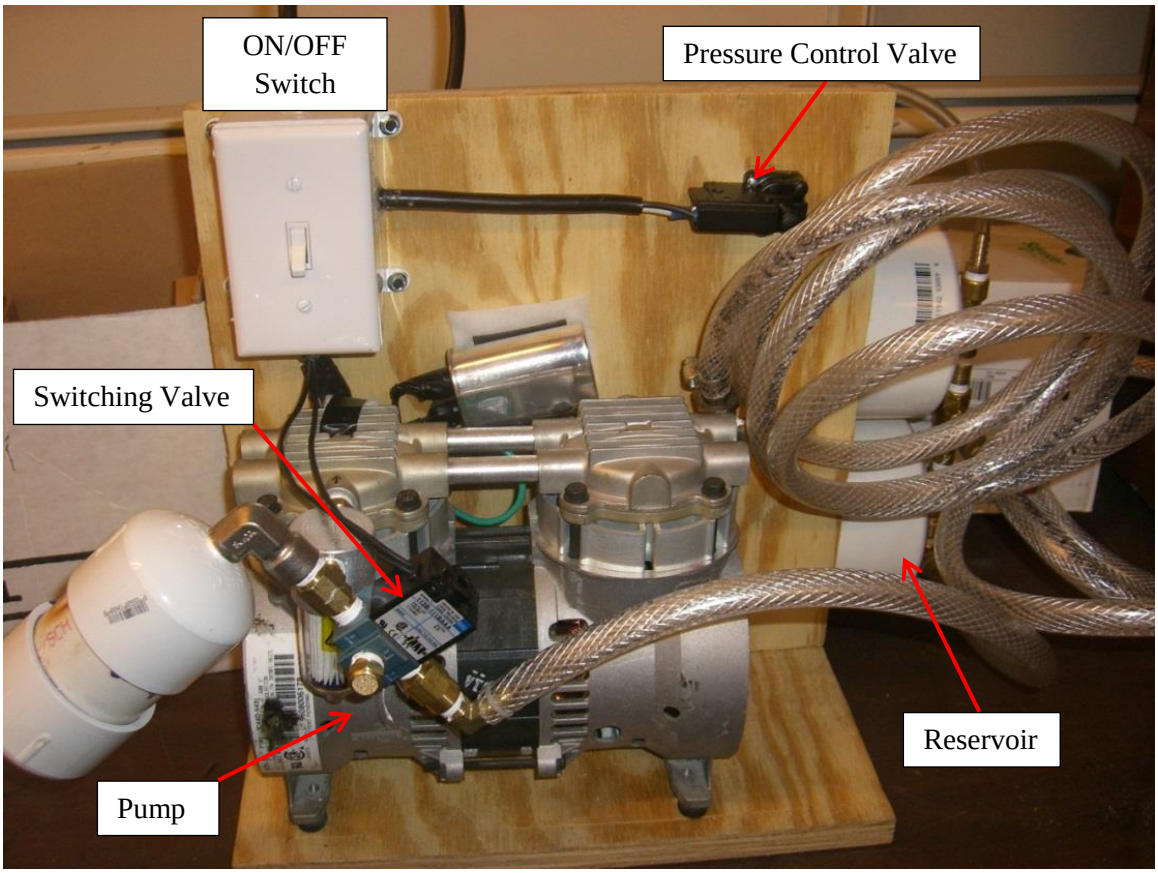

Figure 3.9: Vacuum pump system

Flow visualization of the column was taken to capture bubble sizes and motion. A Nikon D3100 was used to capture still images of the bubble column. The camera was set to a shutter speed of 4000 (s^{-1}) and provided 9.8 mega pixel monochrome images. A Casio Exilim EX-F1 camera was used in high speed mode at a rate of 300 frames per second to capture high speed video. Finally a Sony DCR-VX2000 video camera was used to capture traditional video at 30 frames per second. The frame rate of the high speed video was found to be the best compromise between speed and resolution.

3.2. Shaker Equipment

3.2.1. Design and Construction

The general design of the shaker follows a similar design to that of Buchanan et al. (1962) because both experimental ranges are similar. Initially, there were several concepts reviewed which would provide the necessary vertical motion while restricting lateral motion including a complicated Watt linkage design and a cantilevered beam concept. The purity of the vertical motion was an important consideration in the context of the experiment. A simple "paint can shaker" would simply introduce too many unknowns to the study of the Bjerknes forces. Since one of the experimental requirements was to examine higher amplitudes, the intent of the design was to focus on achieving maximum amplitudes of 10 mm which could be varied by quick and simple adjustments to the machine. Additionally the mechanism was to be simple in construction and yet versatile enough to be used or adapted easily to suit future research. However, it was still a requirement to achieve at least 40 Hz frequencies in order to compare the set up with the previous research. Therefore, the design of the entire shaking device can essentially be divided into two components: the motion and the drive.

The motion was the most complicated aspect to design. There are several ways to achieve an oscillatory motion, a couple of which have been mentioned already, but the easiest method to transform rotation into linear displacement is through what is typically called a 4-bar linkage. While there are traditional 4-bar linkages that will provide a straight line motion they are often limited to short lengths and are sometimes complicated. The Watt linkage mentioned previously does provide a long enough straight line to be considered, but the difficulty of machining the components with the precision required and the number of parts would necessarily make the design too complicated. A variation of the 4-bar sometimes called a "slider-crank" provided a better option. A piston and crankshaft is a common example of a slider crank. With

an appropriate restraining, sliding mechanism a shaker table could be driven by an offset linkage to give the required vertical motion needed (Figure 3.10).

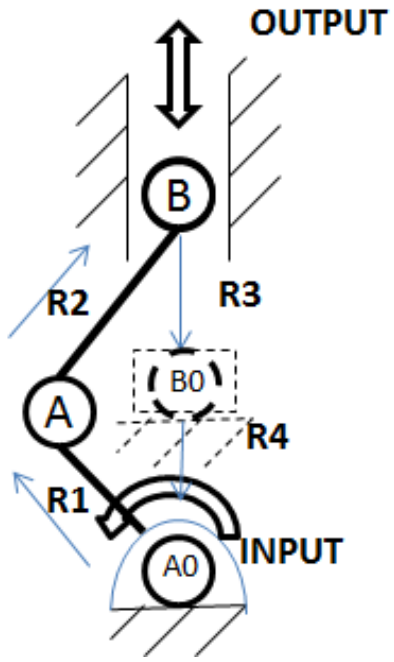

Figure 3.10: Schematic of slider-crank mechanism

The design for the "sliding" motion was originally composed of a single large cylinder and rod or "piston", but quickly evolved to two smaller pistons and cylinders in order to prevent rotation about the single cylinder. The linear sliding motion can be achieved using square forms such as with T peg or C channel designs, but circular rods were found to be more common in similar applications and materials were available locally. To prevent binding, the cylinder housing length was designed to be 4 times the diameter of the rod. Creating longer cylinder housings decreases the force required to offset any moment created by lateral reaction forces during rotation, and thus reduces the likelihood that rods will pinch or bind in the housings. The lateral forces encountered by both rods was expected to be high (Appendix A) so the rods (pistons) were made from 2, 12 in. lengths of 1.5 in. diameter chrome plated steel. The steel rods were selected to be 1.5 in. diameter in order to resist deflection and based upon material availability. The

chrome plating offers a hardened surface to resist abrasion and reduces sliding friction. Figure 3.11 shows the sliding rod (piston) fitting in the piston housing indicated by the arrows.

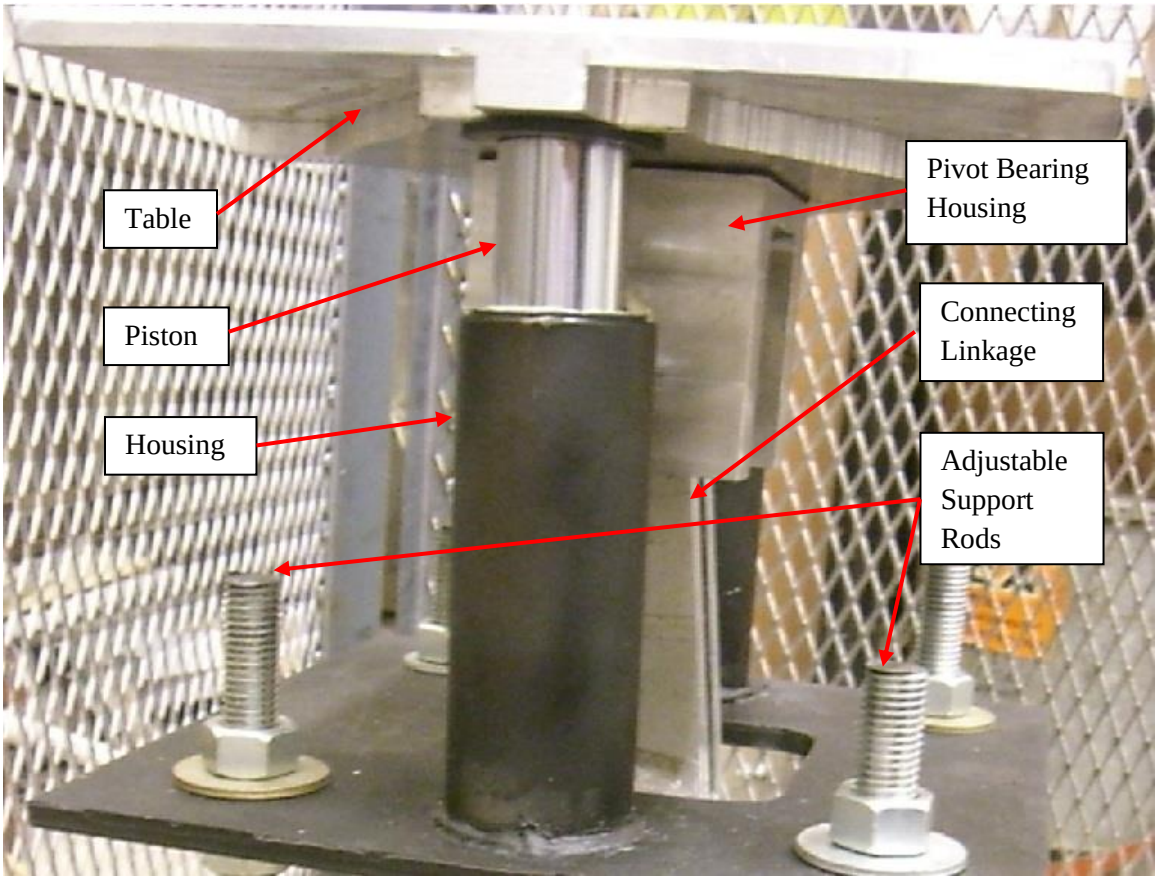

Figure 3.11: Shaker piston and housing

The drive for the shaker was designed based upon an analysis of the power required during operation. Starting with the equation of motion for the test article the acceleration can be determined by taking the derivative twice (Appendix A). Once the acceleration is known the force follows by Newton's 2nd Law giving,

$$F = -mA\omega^2 \sin \omega t \tag{3.1}$$

The force balance (Eq. 3.1) should include the force of gravity (weight), but weight has been neglected since it is insignificant in comparison to the dynamic forces. The power can be determined by multiplying force by the velocity to give,

$$P = mA^2\omega^3 \sin\omega t \cos\omega t \tag{3.2}$$

The minus sign in the power equation is dropped in favor of simplicity and by acknowledging that the power term is simply out of phase with the force (Figure 3.12). As can be seen the maximum conditions met by the shaker can be quite large. In fact to power the shaker with a 100 HP source is unrealistic in a lab setting.

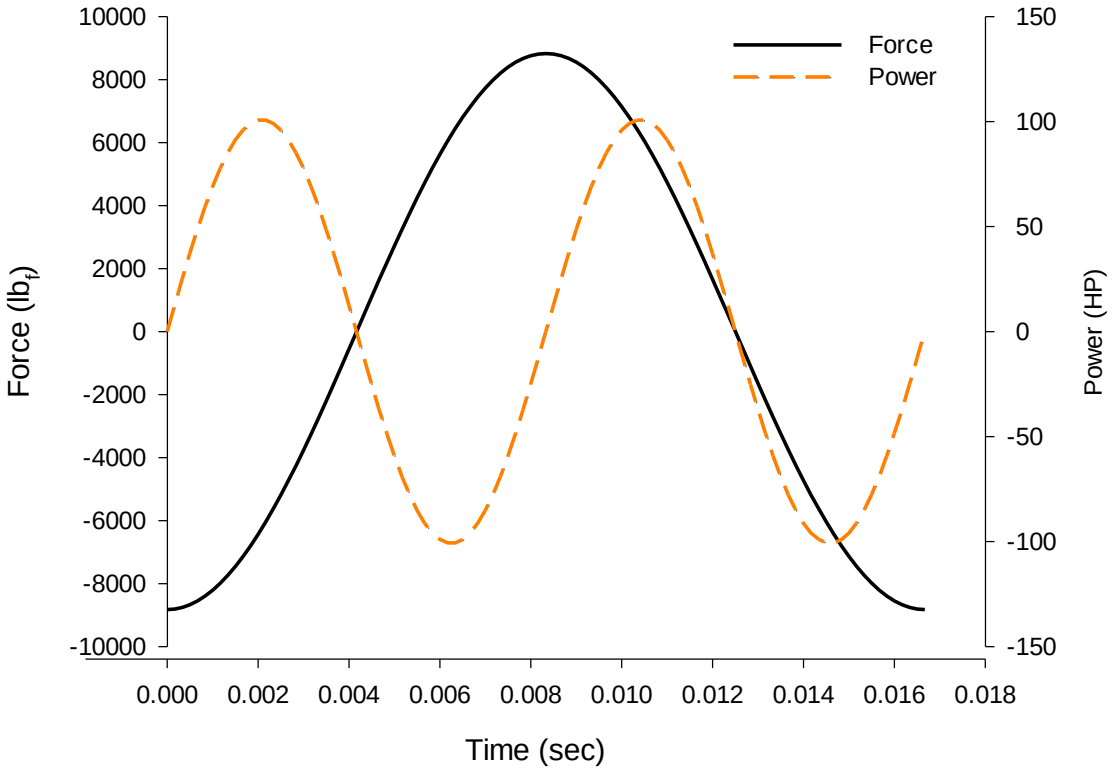

Figure 3.12: Force and Power for an oscillating 60 lb_m (27 kg) mass at f = 60 Hz and A = 0.5 in. (13 mm)

A unique advantage to an oscillating device is that the power requirement is cyclic. The energy to drive this device, being the integral of Power over one cycle, is actually zero. However, the analysis above did not include the effects of friction, and because friction will most certainly be present the energy will in fact not be zero. It is difficult to gauge or predict what the friction forces might be in order to predict the power requirements of the drive system, but it is easy to assume a certain energy loss attributed to friction which would be acceptable. A flywheel

can then be designed such that it will offset the frictional losses during steady state operation (Appendix A).

To offset the requirement of machining a flywheel, drive shaft and bearing supports from scratch a pre-made and available flywheel was sought which would fit the inertia profile of the design. The investigation into available flywheels led to the possibility of using a used 12 HP internal combustion engine (Tecumseh) purchased as scrap. The engine flywheel was found to be an appropriate mass and radius to fit the energy requirement, and the crankshaft, which was modeled in Pro-E to determine moments of inertia, provided additional energy storage to the system. The crankshaft could be supported by the engine case bearings and continually lubricated to reduce friction. Since the crankshaft was designed to provide rotation of the drive shaft from the 2.5 in. combustion stroke of the piston it was thought that a device could be designed which would adapt the 2.5 in. engine stroke to the 0.5 in. amplitude requirement of the experiment. The system would then operate in reverse by driving the engine shaft with an electric AC motor. The problem was that the engine stroke was not adjustable and so a mechanism would need to be designed which could convert the displacement of the crankshaft while being adjustable.

The rocker beam (RB) design evolved from the desire to use pre-existing IC engine components. The design is both part drive and part motion, and consists of a single beam which connects by linkage the crankshaft of the motor at one end to the base of the shaker table at the other. The RB is essentially a lever arm, but unique to the design is an adjustable pivot point or "slider" which changes the static amplitude of the engine crankshaft to an infinitely adjustable range of amplitude at the shaker table. The combination of parts can be analyzed as two 4 bar linkage systems with a common pivot, or an 8 bar linkage system. Preliminary analysis of the system was performed using a program written in Mathcad. A schematic of the 8 bar linkage is given in Figure 3.13.

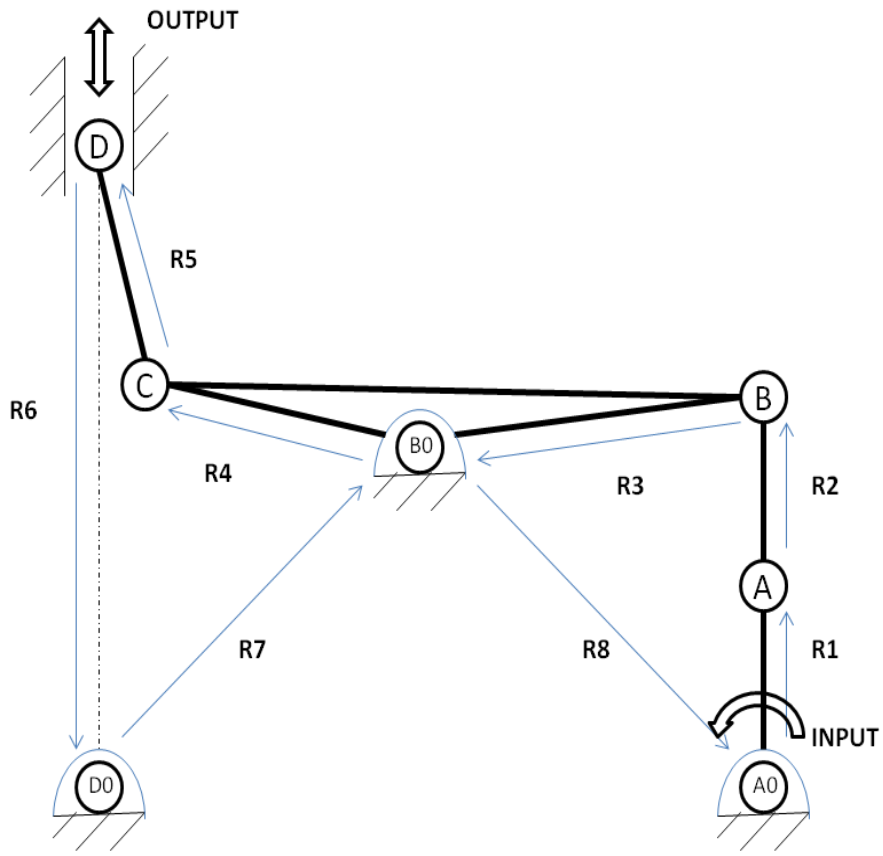

Figure 3.13: Schematic of Rocker Beam (RB) design as an 8 bar linkage

The preliminary analysis in Mathcad was followed by modeling in Pro/Engineer (Pro-E). Pro-E is a 3D modeling software which provides a set of analysis packages which are well established and used by many agencies to design and analyze products. Components were designed and assembled in Pro-E using the Mechanism analysis package. Mechanism analysis allows the components to be virtually assembled as the parts would be in real life, and predictions of motion and reaction forces can be produced by "running" the assembled machine (Figure 3.14).

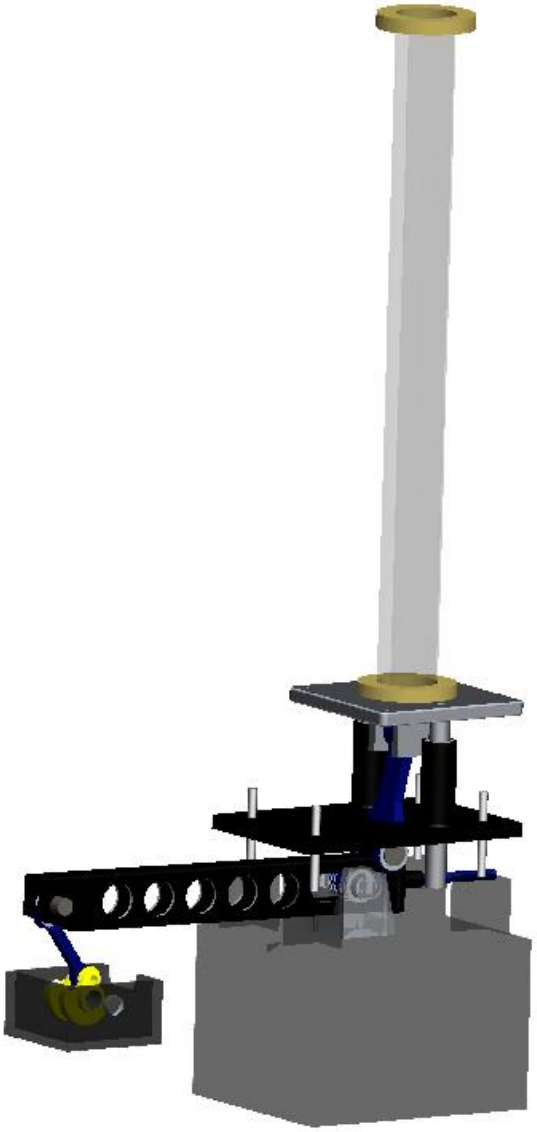

Figure 3.14: RB shaker assembled in Pro-E Mechanism

Using a virtual motor operating and different speeds the frequency of the machine could be altered. Changing the position of the pivot slider within the rocker beam allowed the amplitude to be adjusted. Running the virtual machine at different amplitude and frequency combinations in Pro-E showed that the displacement results were typical and agreed with both simple rotational motion and the predictions of Mathcad based on a 4 bar analysis (Figures 3.15 and 3.16). Acceleration profiles and reaction forces at the each of the bearing locations were analyzed in a similar manner.

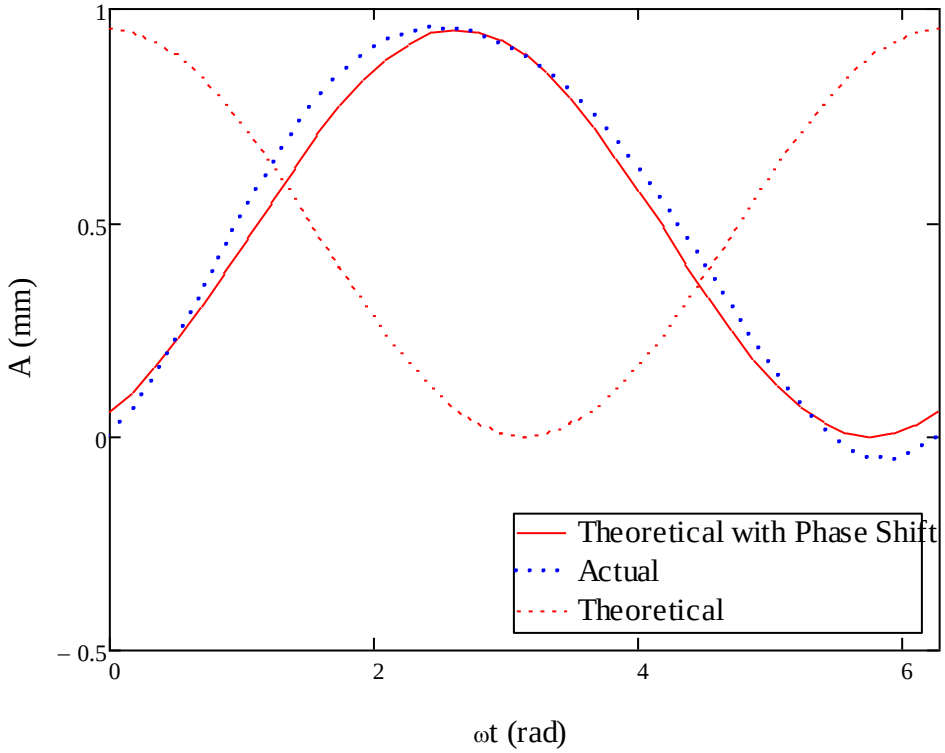

Figure 3.15: RB design displacement prediction vs. theoretical sine wave

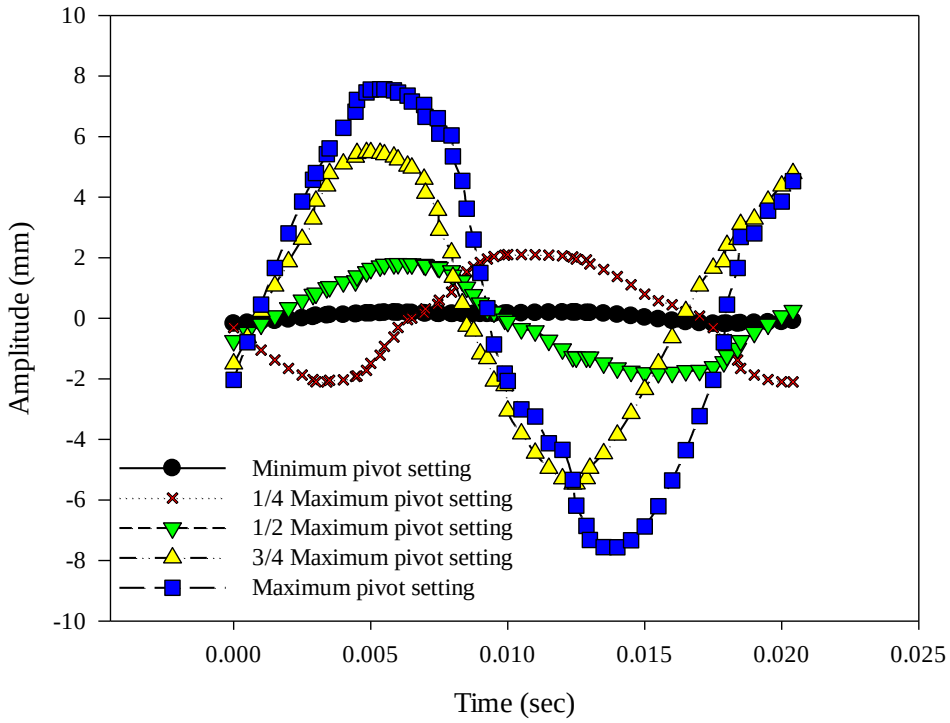

Figure 3.16: RB design displacement predictions using Pro-E at varying pivot adjustments

Surprisingly, the results showed the reaction forces at the bearings to have an unusual response. The reaction forces present at the shaker table end were typical and comparable to rotational motion, but the bearing forces at the crankshaft end were 2 to 3 times higher than expected being nearly half of the forces seen at the table (Figure 3.17). Furthermore, the profiles showed a flattening at the peak of the cycle and a sharp curve at the trough.

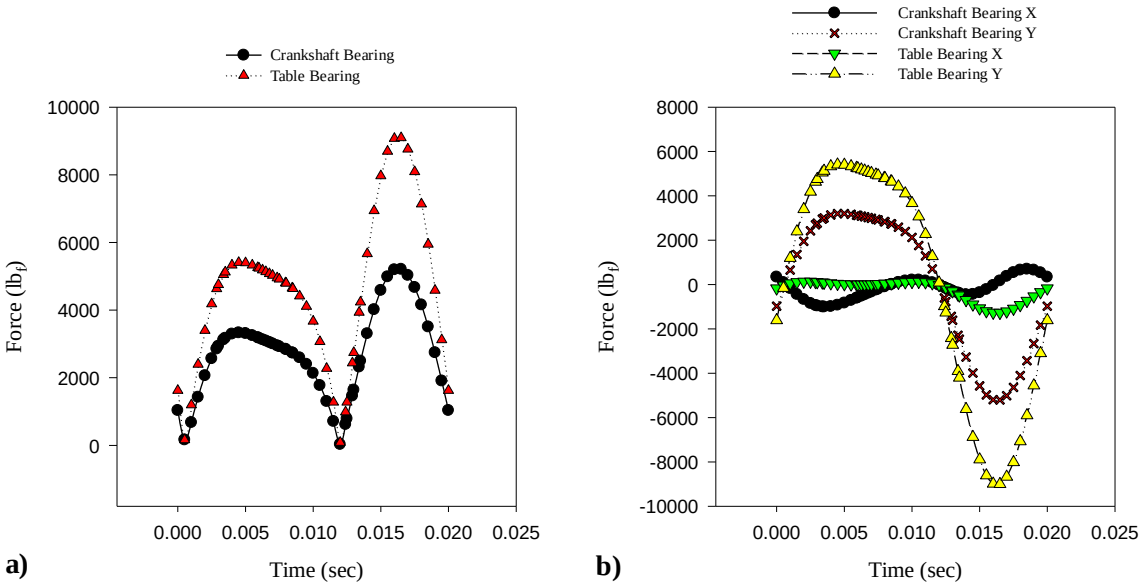

Figure 3.17: a) Bearing reaction force magnitudes and b) bearing reaction force components

Examining the reaction forces statically one would first suspect that the reaction at the crankshaft would be reduced in proportion to the mechanical advantage provided by the lever arm which is about 1/5. However, when the system is in motion the lever arm contains a significant amount of inertia based on its geometry and mass. Since the portion of the RB that extends from the pivot to the crankshaft is much longer than the portion extending to the shaker table, the bearing and linkage at the crankshaft actually maintains higher reaction forces due to the increased mass moment of inertia (Figure 3.18).

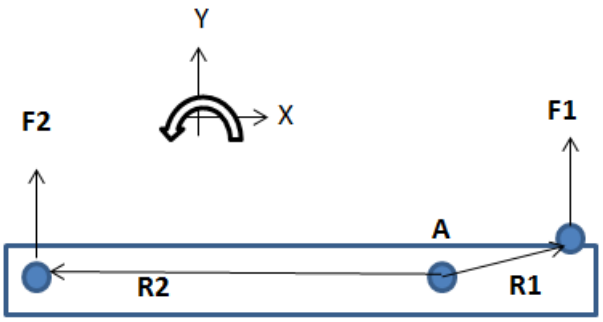

Figure 3.18: Moment diagram of dynamic reaction forces

A simple moment balance taken about the point A reveals the impact of the beam's inertia given by,

$$\sum \mathbf{M_A} = \mathbf{R}_1 \times \mathbf{F}_1 + \mathbf{R}_2 \times \mathbf{F}_2 = I\boldsymbol{\alpha} \tag{3.3}$$

To illustrate the effect of the mass moment of inertia (I) more simply the forces can be assumed to be perpendicular to the radii. To be clear, this is not the case in actuality but it is an approximation which shows the relationships simply.

$$R_1F_1 + R_2F_2 = I\alpha \tag{3.4}$$

The equation can be arranged to show,

$$F_2 = \frac{I\alpha - R_1F_1}{R_2} \tag{3.5}$$

Thus it is seen that the mass moment of inertia plays a direct role in increasing F_2 by the direct magnification of the rotational acceleration. Therefore, when viewed in the light of a dynamic system the RB design becomes handicapped by the rotational speed.

The analysis of the RB discredited it as a viable design to provide the experimental profile needed, but it raised an important question which has until now not been addressed. In what manner does the acceleration profile affect the hydrodynamics of the flow, the Bjerknes

effect, and/or the mass transfer rates? Based on Bjerknes (1909) the action of kinetic buoyancy is dependent on the pressure field established in the fluid. The pressure field is established based on the acceleration profile of the shaking device, and the RB design certainly produces an unconventional acceleration profile (Figure 3.19).

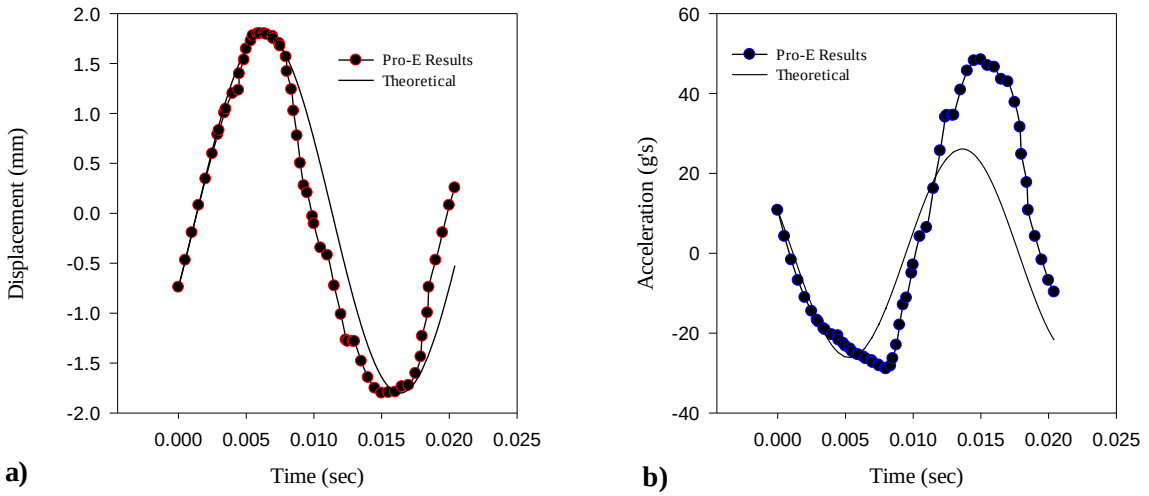

Figure 3.19: Pro-E results for a) displacement and b) acceleration vs. theoretical sine wave input for *f* = 60 Hz at 1/2 maximum pivot bearing position

Previous research has exclusively used sinusoidal inputs for simplicity, but if it were possible to establish a pressure field that is periodic (not necessarily symmetric) could it be shaped such that the motion of bubbles could be controlled? Furthermore, would an asymmetric pressure profile improve bubble breakage and thereby improve mass transfer? For example could a waveform such as that produced by the RB cause bubbles to move down faster, stay down longer, etc.? These questions are valid enough to be studied, and so it was decided to proceed with construction of the RB design to study these effects at lower frequencies.

Another drive mechanism design was necessary, however, which could provide the full range of amplitude and frequency needed for the study. A simple eccentric and link was designed capable of integrating into the overall shaker design which includes the table and sliding mechanism, base and drive system. The eccentric drive mechanism (EDM) consists of a hollow

cylinder which is positioned around and parallel to the main axis of a power transmission shaft. The steel cylinder is attached with two 5/8-11 bolts threaded through the transmission shaft. The center of the cylinder is offset from the transmission shaft center (zero) by adjusting both bolts (Figure 3.20). The transmission shaft is made from 1.5 in. diameter chrome hardened steel rod.

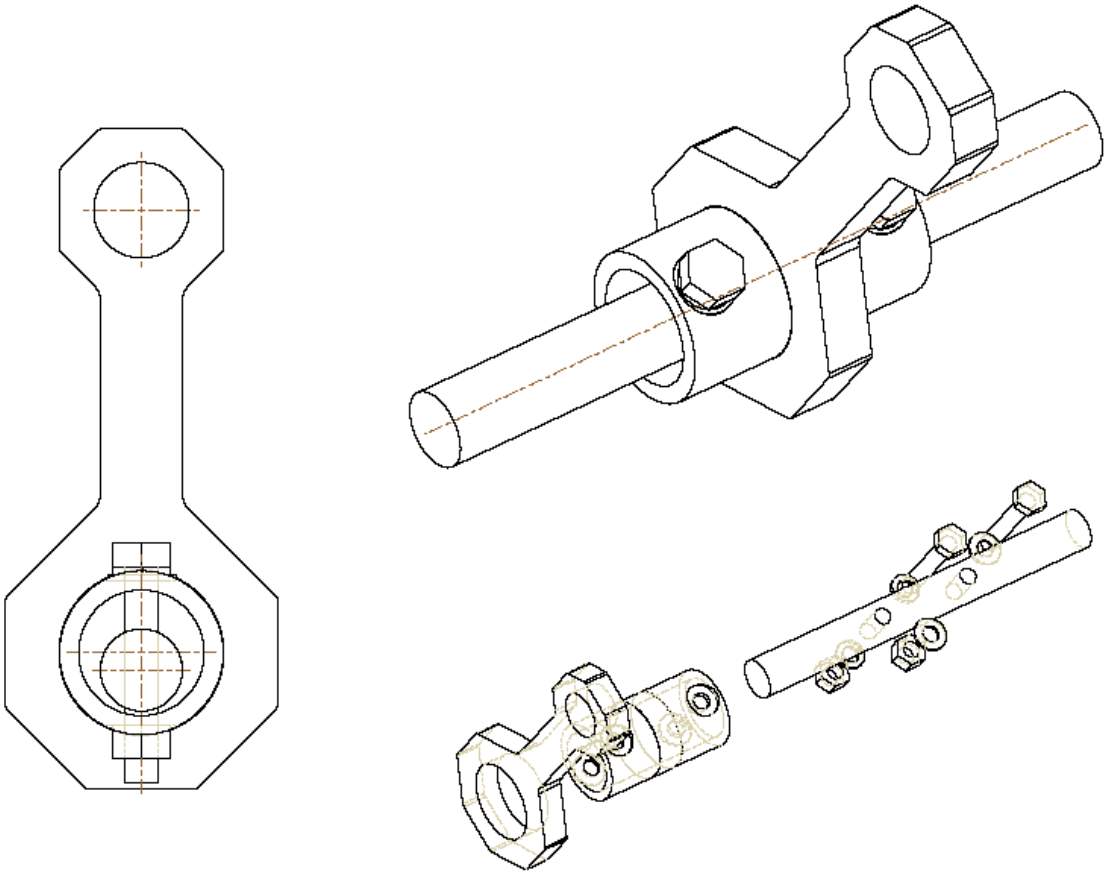

Figure 3.20: Schematic of eccentric drive mechanism (EDM)

The cylinder rotates within a ball bearing inset into a link machined from Al 6061. The link attaches to the shaker table with a 1.75 in. steel shear pin (Figure 3.21). Since any mass added to the system above the eccentric detracts from the overall test mass, aluminum was chosen because it provides similar strength properties to steel but is much lighter.

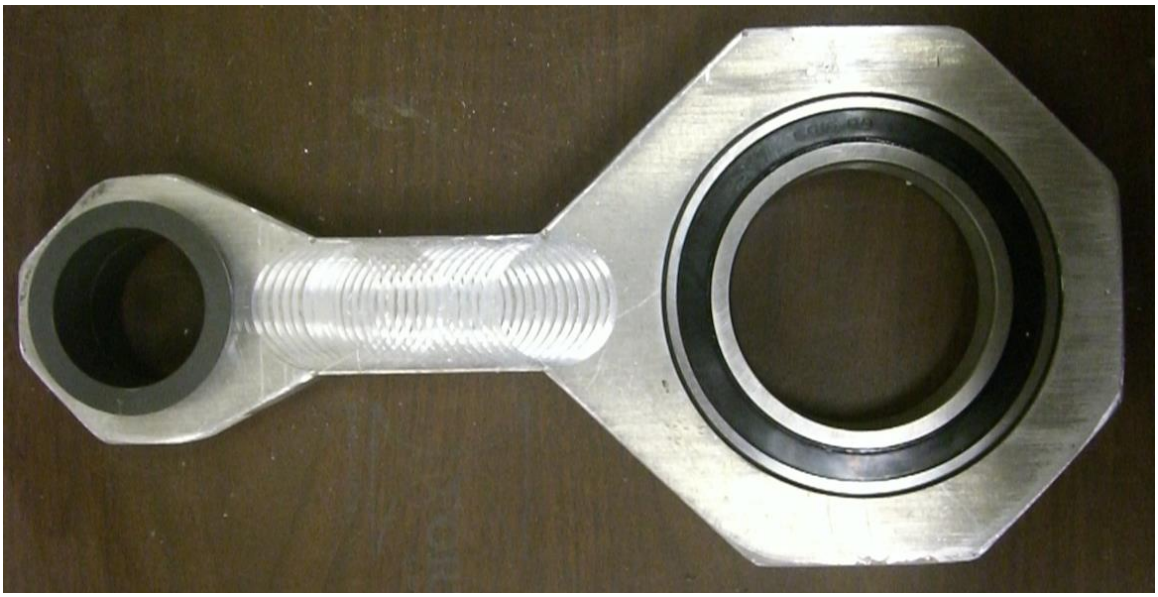

Figure 3.21: EDM link

Adjusting the bolts equally directly changes the amplitude of the shaker from 0 mm (axes aligned) to 10 mm (transmission shaft surface touches the inside surface of the cylinder). This design provides a simple and effective means to adjust the amplitude to nearly any measure needed with relatively few moving parts or complications.

To analyze the shaker system using the EDM design Pro-E was once again used to model parts and assemble them into a virtual machine. The machine was run at varying motor speeds (frequencies) and eccentric displacements (amplitudes) to derive the reaction forces, accelerations and displacements at the shaker table. The acceleration and displacement profiles were as expected and comparable to a sinusoidal input (Figure 3.22).

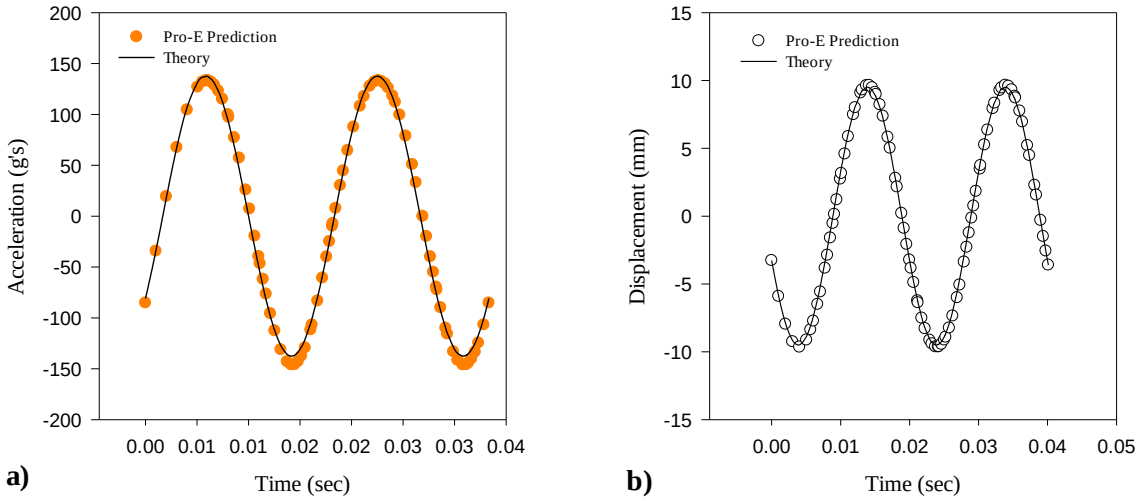

Figure 3.22: Predicted results for a) displacement and b) acceleration of the EDM shaker compared with theoretical sine wave at f = 50 Hz and A = 9.5 mm

The reaction forces found during the mechanism analysis were then used within Pro-E Mechanica to analyze the stresses and strains of critical components. Pro-E Mechanica produces stress and strain predictions based upon a finite element method (FEM) (Figure 3.23).

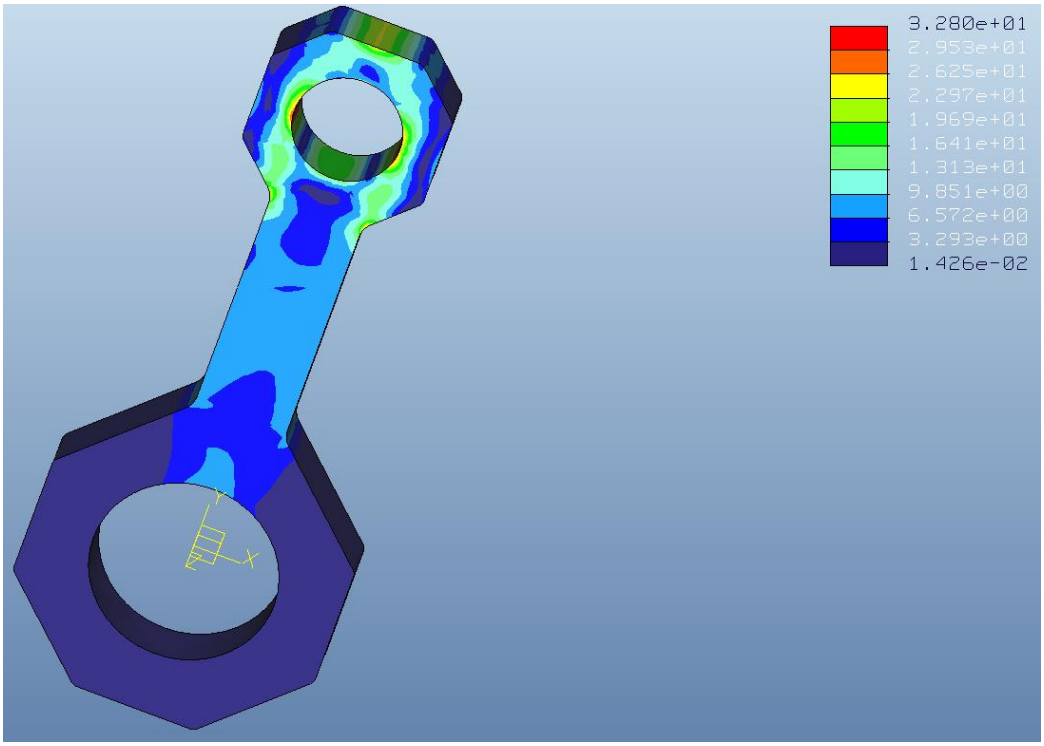

Figure 3.23: Stress analysis results (von Mises) of the max reaction forces on the EDM link using Pro-E Mechanica (units are ksi)

One distinct advantage of using Pro-E to analyze the design of the shaker was the 'all-in-one' package offering the ability to quickly and seamlessly trade material properties and component geometry in order to optimize the design. Using this optimization process the materials and geometry were selected for the eccentric cylinder and link. The final design of the shaker will primarily use the EDM drive to facilitate testing.

The limiting factor for the EDM drive was the linkage bearing. The RB design primarily used journal bearings lined with IGUS iGlide 300 polymer bushings because the dynamic loading (P*V) was not as extreme due to the limited travel (pivoting) encountered. The EDM uses an eccentric which rotates continually and thus the dynamic loading is higher. Initial selection of the link bearing was based on maximum load (~10,000 lbs) and rotation speed (3600 RPM). Figure 3.24 demonstrates the need to move to a roller bearing between 2 and 5 in. diameter for the EDM link.

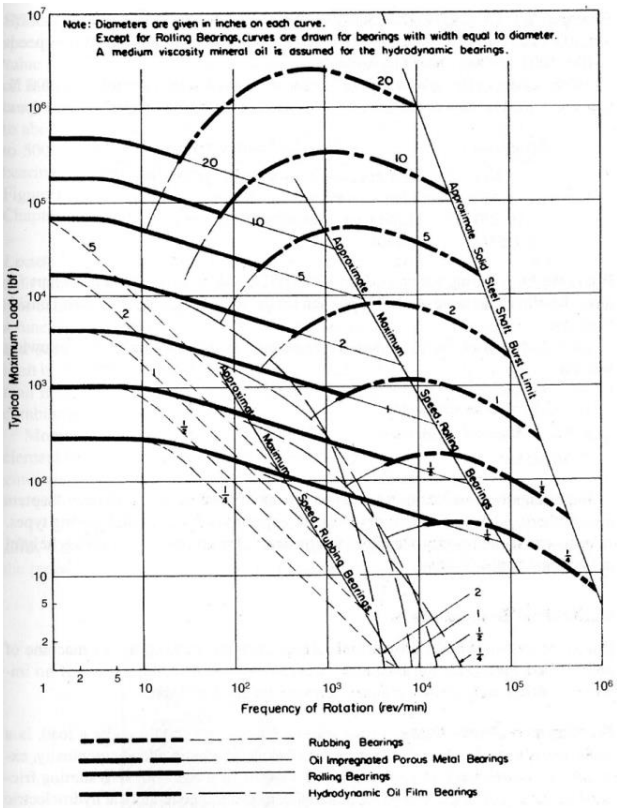

Figure 3.24: Bearing selection chart (Khonsari and Booser, 2001)

The final selection of a double sealed 75x115x20 mm sealed deep groove radial ball bearing (VXB 6015-2RS) provided the necessary dynamic load rating at an appropriate cost. The final dynamic load rating for the bearing is rated at 39,500 N (8880 lb). The maximum speed of the bearing is 3400 RPM (f = 56 Hz). A slight decrease in the rotation speed was accepted in lieu of lower cost and availability when compared to higher end bearings. The loss of 4 Hz from the ultimate design goal of 60 Hz was seen as a beneficial trade. The geometry of the EDM followed the geometry of the bearing since it was the limiting factor, and the full experimental range of the shaker is restricted to experimental frequencies of f = 50 Hz for safety.

Based on the power requirements and the inertial properties of the flywheel and crankshaft a 3 phase, 3HP, 208-230 VAC motor (WEG P/N: 00336ES3EF56C) was selected to drive the shaker (Appendix A). The AC motor is driven by a 3HP, 10A, 230 V, 1 phase variable frequency drive "speed controller" (Schneider Electric P/N: ATV12HU22M2). The speed controller converts single phase 220-240V line voltage to a 3 phase 230 V output for the motor while controlling the speed of the motor by regulating the carrier frequency.

A carriage was designed to mount and align both the AC motor and the crankshaft. The crankshaft is kept within the original case and rests on two journal bearings at the front and the back. The case is sealed and can be filled with any medium weight oil such as 10W-30 to provide lubrication during operation. The RB was designed to connect to the crankshaft via linkage which extends through the original cylinder opening of the motor while the EDM design couples to the remaining crankshaft at the flywheel end. Therefore, the carriage serves both designs simply by rotating the carriage 90° and changing the drive mechanism (Figure 3.25).

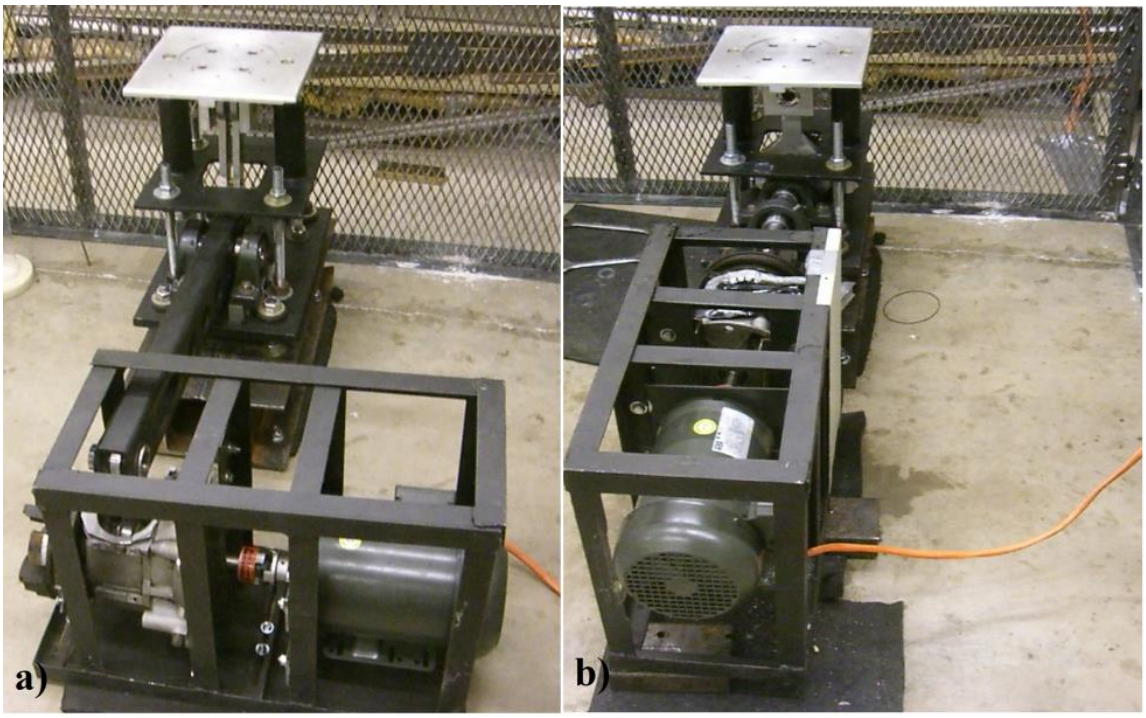

Figure 3.25: Motor carriage mounted in a) RB configuration and b) EDM configuration

The front of the crankshaft carries the flywheel and the AC motor connects to the back of the crankshaft with a jaw type coupler. The carriage has holes drilled in the base which allow it to be mounted to the cement floor in either configuration using 4, 3/8 in. concrete anchor bolts (Red Head wedge type) (Figure 3.26).

The jaw type coupler consists of two aluminum coupler bodies (Lovejoy) which slide over the 1-1/2 in. diameter crankshaft and 5/8" diameter AC motor shaft and remain in place by a key and set screw. The couplers each have three prongs, a common 2 -1/2 in. outer diameter and couple together using a rubber "spider". The spider (Lovejoy, Buna-N, A/L075) transmits the torque from the AC motor to the crankshaft and serves as both a safety device to prevent the AC motor from over torque and to align both shafts to within 1° angular and 0.015 in. parallel. The spider is rated for a maximum torque of 90 in-lbs. and rated for 5 HP at 3600 RPM.

The crankshaft is mounted with a flywheel on the side opposite the AC motor. An adapter shaft was machined to fit the 5/8-18 threaded crankshaft end. The adapter provides the locking feature of a nut to keep the flywheel in place while providing a similar 1.5 in. diameter to couple with the drive shaft of the EDM. The adapter and drive shaft are coupled using a stiff rubber sleeve held in place by band clamps. The rubber provides the coupling enough flexibility to account for misalignment in the shafts.

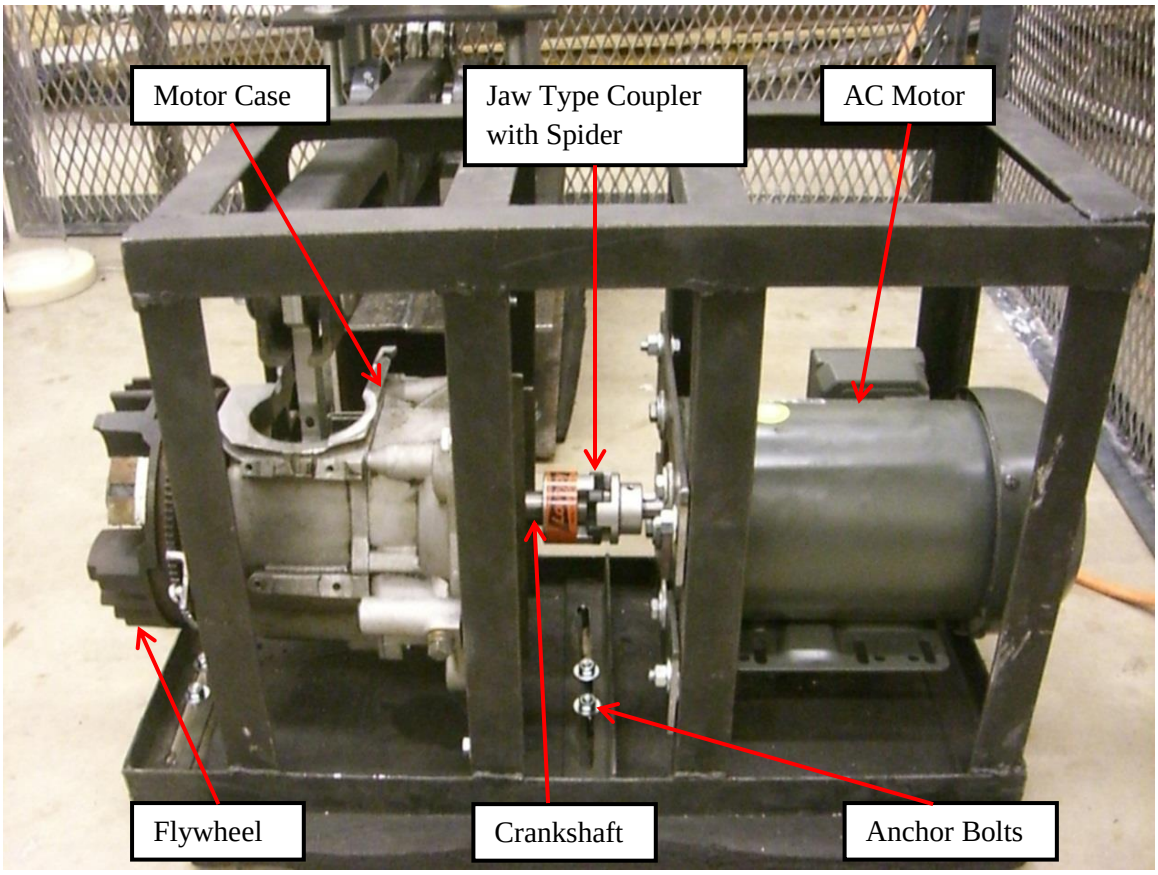

Figure 3.26: Motor carriage and components

Both drive designs use a common base for mounting. The base consists of two 24 in. long 6 in. 15 pound I-beams welded together at the seam (sub-base). The sub-base is attached to the ground by 4 5/8 in. cement anchor bolts (Red Head wedge type). The combined bolt pullout strength is rated at 26,500 lbs. for un-cracked concrete. Assuming a concrete failure mode in tension the bolts still provide 15, 900 lbs. of tensile load which far surpasses the design loads. A foam rubber mat is placed between the metal base and the concrete to dampen the vibration imparted to the floor. A 1/2 in., 12 x 18 in. steel plate is mounted to the sub-base using 4, 6 in. X 3/4-10 threaded rods fastened with rubber pads, washers and nuts. The pads, washers and nuts provide a vibration isolation "sandwich" for each surface (Figure 3.27).

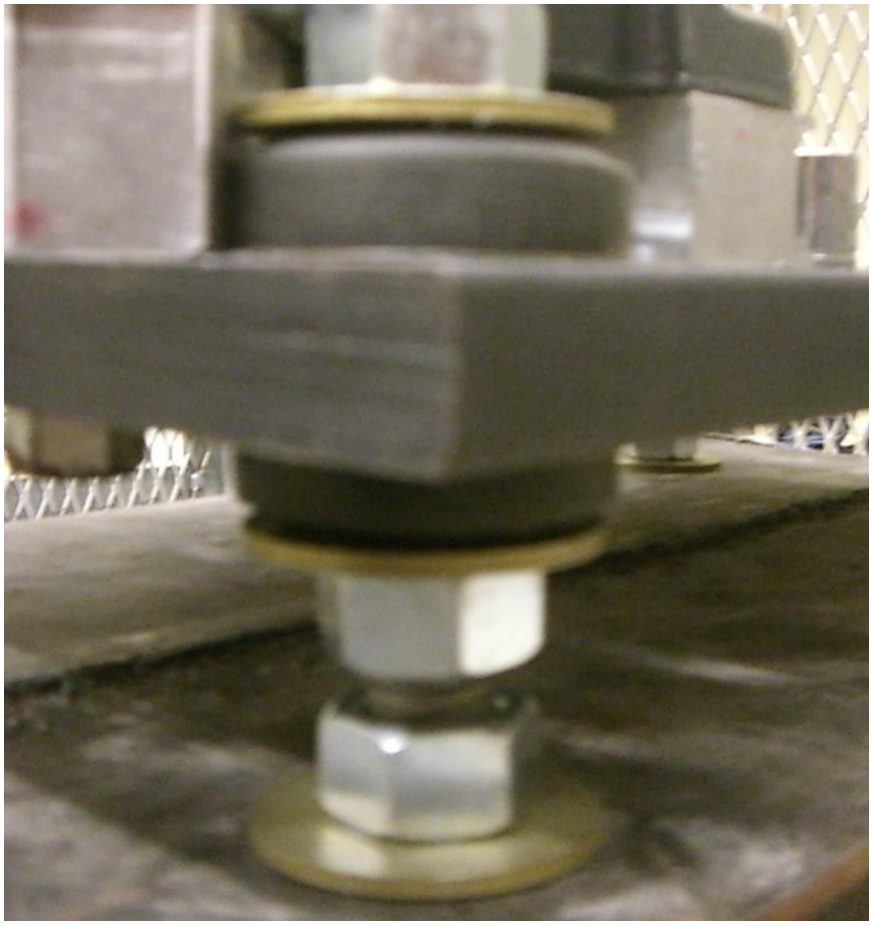

Figure 3.27: Vibration isolation mounts

The steel plate provides the primary attachment point for both drive systems and the piston housing. The piston housing is mounted above the plate using 4, 18 in. 3/4 – 11 threaded rods and attached with washers and nuts. The threaded rod provides the capability to adjust the height of the piston housing to suit either drive design, and also allows the piston housing to be leveled independently of the base structure.

3.2.2. Initial Testing and Troubleshooting

Early testing of both mechanisms revealed both problems that were predicted during analysis and that were unexpected. The RB design was tested by running the machine at low frequencies (2 – 5 Hz) to ensure smooth operation. The speed was increased to a maximum of 20 Hz. At 20 Hz the RB design was found to impart too many transverse loads to the motor carriage causing significant rocking and vibration to the carriage and components. Furthermore the carriage was observed to have shifted slightly at the mount location with the floor causing a slight misalignment of the crankshaft link and the rocker beam. While the shift of the carriage was not large enough to cause considerable problems it was large enough to consider termination of testing at higher frequencies and for longer durations than 5 min. As predicted by the analysis the RB design's suitability is only for lower frequencies ($f < 20$ Hz). Other aspects of the design tested well in operation including the motion of the table and the adjustment of the pivot bearing to alter amplitude.

The EDM design was tested in the same manner as the RB with the speed being increased incrementally and for longer intervals. The EDM design tested much better at higher frequencies than the RB design as expected and has since been used in tests at $f = 34.9$ Hz for durations of 5 min. (length of experiment). However, typical issues occurring in vibrating systems were observed including: attachment bolts loosening, eccentric adjustment bolts loosening, component wear, and noise. One significant problem encountered was the tendency for the EDM link to

"walk" towards one end of the outer cylinder. The cylinder was machined with a slightly larger diameter past the mount location of the link to prevent the bearing from traveling. However, it is suspected that during operation the thermal and mechanical relaxation of the inner ring of the roller bearing was enough to overcome the tolerance of the larger diameter. The bearing being situated at the larger diameter induces a higher preload on the bearing which increases fatigue and reduces the bearing life. Thus the shaker assembly was disassembled and the link remounted in the design position. To prevent future travel two compression pins were installed in the cylinder to provide a mechanical stop (Figure 3.28).

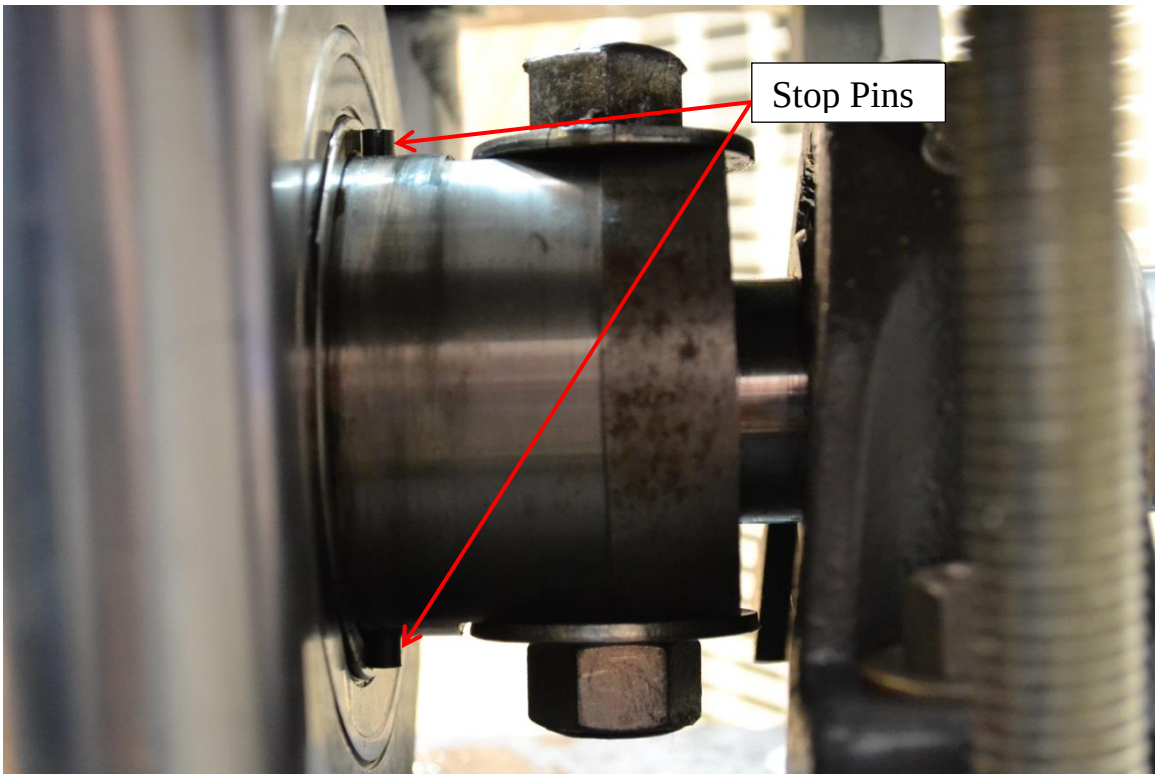

Figure 3.28: EDM cylinder with stop pins

The adjustment bolts of the eccentric also had a tendency to loosen and therefore cause the amplitude of the shaker to change during the test. Initially the natural friction between the bolt and drive shaft threads was enough. However, as lubricants seeped into the bolt threads and as the machine was run the washers and nuts were loosened and the natural friction was no longer

sufficient to restrain the bolts. A solution was needed which would provide the ability to adjust the bolts while still maintaining a "fixed" position during the run. The eccentric was disassembled to fix the problem and new bolts were installed with locking nuts. The lock nuts use a nylon insert to keep the bolt from loosening. Therefore, the lock nuts can be tightened to maintain a higher tension on the bolt washer thus increasing the friction at the washer and cylinder interface to prevent the bolt from moving during vibration.

Aside from some minor leaks at the glued joints the cylinder responded well during testing, and required no further troubleshooting or redesign. The water box on the 4 in. column was more problematic. During testing the seams of the box connecting the viewing face to the side plates failed and leaked. An attempt was made simply to reseal the box seams using a flexible adhesive like silicone, but the pressures exerted on the panel were too large. The primary issue was the flexibility of the front pane which was observed to flex out and in with the corresponding vibration. The continual flexing of the pane caused the premature fatigue of the seams. The water box was removed from the 4 in. column with no observable loss of optical clarity. An analysis of error involved in bubble area measurements was performed on a system with and without a water box. The results showed that optical techniques used to measure bubble size distributions and flow phenomena are inherently erroneous away from the cylinder centerline anyway due to the curvature of the tube, regardless of the use of a water box. No water box was installed on the 1.0, 2.5, 5.5 in. columns.

3.3. Data Acquisition

The data acquisition system used to collect the data for this work consists of a PC and Vernier SensorDAQ. The data acquisition system is responsible for collecting and managing the measured signals coming from the accelerometer, the differential pressure transducer and the DO probe. The Vernier SensorDAQ is a 13 Bit analog to digital converter which connects directly to

the computer via a USB 2.0 cable. The DAQ has a maximum sampling rate of 10 kHz. One of the advantages to using the Vernier DO probe and the Vernier SensorDAQ is that they are completely compatible and are made specifically for each other. The differential pressure transducer and the accelerometer signals were taken using the ±10 V analog voltage leads which also connect to the SensorDAQ. The differential pressure transducer voltage is measured from the CD15 carrier demodulator box used in conjunction with the transducer, while the accelerometer voltage is measured from a differential voltage pin-coaxial cable connected to the "analog out" source of a Vishay Model P3 Strain Indicator and Recorder.

The data is acquired and stored on a CPU using Data Logger Lite software. Data Logger Lite provided all the functionality required for initial validation tests and experiments. However, the SensorDAQ is completely compatible with National Instruments LabVIEW software as well.

3.4. Summary

Table 3.1 presents the final design capabilities and the tested capabilities to date. The final shaker construction is presented in Figure 3.29.

Table 3.1: Final shaker design and tested capabilities

Properties	Max	Ranges	Tested
Amplitude (in/[cm])	0.37/[1.0]	0.04 - 0.39/[0.10 - 1.0]	[0.15 - 0.95]
Frequency (Hz)	60	5 - 60	7.5 - 39.4
Test Mass (Maximum Conditions) (lbm/[kg])	20/[9]	5 - 20	5 - 15
Column Diameter (in/[cm])	5.5/[14]	1 - 5.5/[2.5 - 14]	4.0
Liquid Height (in/[cm])	44/[110]	0 - 44/[0 - 110]	[40 - 85]
Column Pressure (atm)	5	0.3 - 5	0.3 - 2

Figure 3.29: Final constructed shaker design with test column

CHAPTER IV

CALIBRATION AND EXPERIMENTAL PROCEDURE

The experimental setup involves the use of measurement tools which require calibration at regular intervals including: differential pressure transducers, accelerometers, DO probes, shaker frequency and amplitude, and photographic measurements. The calibration steps and results are included. A series of experimental tests are run using the set up for comparison with previous research results and to validate the experimental set up. The uncertainty of the measurements was analyzed and the comparison to previous research is presented and discussed. Finally an experimental procedure is outlined for the operation of the experimental set up in order to perform a typical test.

4.1. Calibration

The calibration of the experimental set up and measurement devices is described in the following sections including: pressure transducer, DO probe, accelerometers, and photographic measurements.

4.1.1. Pressure Transducer

Calibration of the Validyne DP-15 differential pressure (ΔP) transducer is performed by a series of simple steps. The first step is to zero the output. The ΔP transducer signal is measured by taking the differential voltage output from the demodulator box which processes the signal from the transducer itself. The demodulator includes two controls which are the zero and the

span. The ΔP output must be zeroed by ensuring the voltage reading from the demodulator reads zero at ΔP = 0 which is obtained when both + and – ports are open to the atmosphere. By turning the zero control, the voltage output can be lowered or raised until it reaches approximately zero.

The second step is to set the span. The span is controlled in a similar manner as the zero, however, the span voltage is set to the maximum reading required. Calibration of the ΔP transducer was performed by setting the span to approximately 4 V at 100% of the ΔP diaphragm value. This value allows enough output voltage range of the demodulator (max ~ 8.1 V) to encompass 200% diaphragm value (maximum safety factor). The voltage range was set to allow 200% diaphragm value to prevent signal chopping during cases in which the pressure may slightly exceed the range. The 4 V span also allows enough voltage resolution to match the resolution of the pressure transducer.

The third step is to take a series of measurements of the voltage output with corresponding known pressures. The voltage at a given pressure is measured at a sampling rate of 1 sample/second for 40-100 seconds. The data is then placed into an excel sheet and averaged. The average voltages for each pressure set were plotted. Enough data points should be taken to ensure a high degree of linearity. The equation generated by the linear regression of the calibration points is used within the data acquisition program to convert the voltage reading into a differential pressure measurement (psi). An example of the calibration curve is given in Figure 4.1.

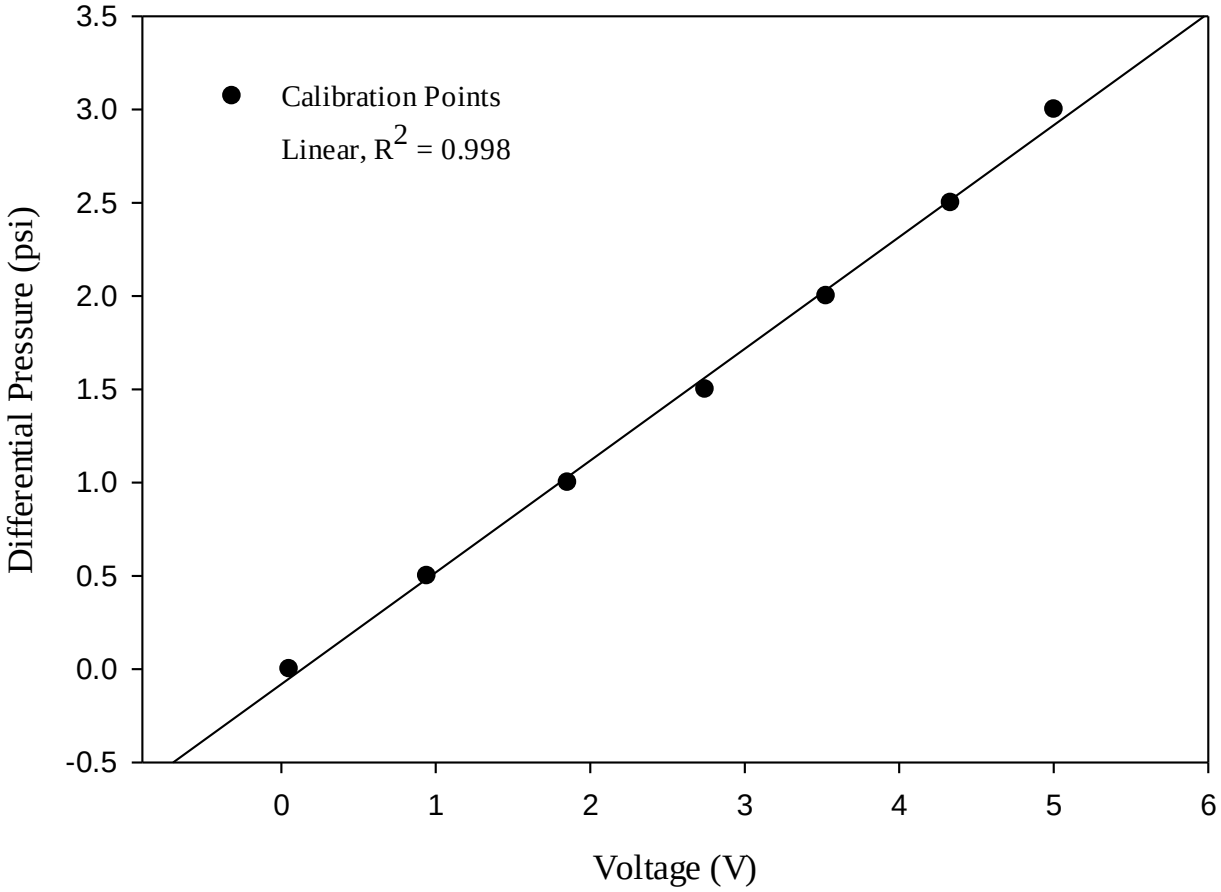

Figure 4.1: Calibration curve of Validyne differential pressure transducer

A range of pressure diaphragms were used in the course of the experiments performed. The 3-32 (2.0 psi) and 3-36 (5.0 psi) diaphragms offered sufficient range to cover the pressures occurring in the column for low frequency low amplitude combinations ($A \leq 2.5$ mm, $f \leq 10$ Hz). However, higher frequency, higher amplitude combinations required the 3-38 (8.0 psi) to 3-42 (20.0 psi) diaphragms to be used to prevent damage to the diaphragm. For each calibration, the pressure supplied to the + port of the transducer was generated using a Si Pressure Instruments hand pump while the – port was open to the atmosphere. The hand pump output was connected in parallel to a SPER Scientific model 840081 digital manometer with a range of 0-15 psi. The pressure supplied to the + port of the transducer was determined by the manometer reading which has an accuracy of ± 0.3% full scale and a resolution of 0.01 psi.

4.1.2. DO Probe

Calibration of the DO probe is not necessarily required for mass transfer measurements since only the change in values is recorded as an "unsteady state" measurement. Additionally, the Vernier DO probe comes supplied with an internal calibration curve given by,

$$C = 3.27s - 0.327 \tag{4.1}$$

where C is the oxygen concentration (mg/L) and s is the voltage signal (V).

The DO probe can be calibrated to become more specific and accurate to the system being measured. To calibrate the probe a two point calibration is performed with a zero scale and full scale reading. The zero scale reading is taken by placing the probe tip into a Sodium Sulfite Calibration Solution provided by the manufacturer. The solution is chemically devoid of oxygen and therefore causes the voltage signal of the probe to drop. After allowing the signal to stabilize, the lowest voltage corresponds to an oxygen concentration $C = 0$ (mg/L).

The full scale reading is taken in a similar manner. The probe tip is rinsed in distilled water after being removed from the calibration solution and placed into a small bottle. The small bottle has approximately 1/4 in. of distilled water at room temperature in the bottom. The probe is inserted about 1/2 in. into the bottle and held in place by a rubber grommet integrated into the lid of the bottle. The voltage output is allowed to stabilize at a maximum value which corresponds to the known value of dissolved oxygen in distilled water. The maximum value of dissolved oxygen in distilled water is also the same value as that of moist air at the same pressure and temperature. The maximum value can be determined based upon a table provided in the manufacturer's user manual or derived from several equations which can be integrated into Excel for easy calculation (Appendix A) (Water on the Web, 2007). A typical response for the DO probe in the calibration solution and in the calibration bottle corresponding to the zero and full scale readings respectively is given in Figure 4.2.

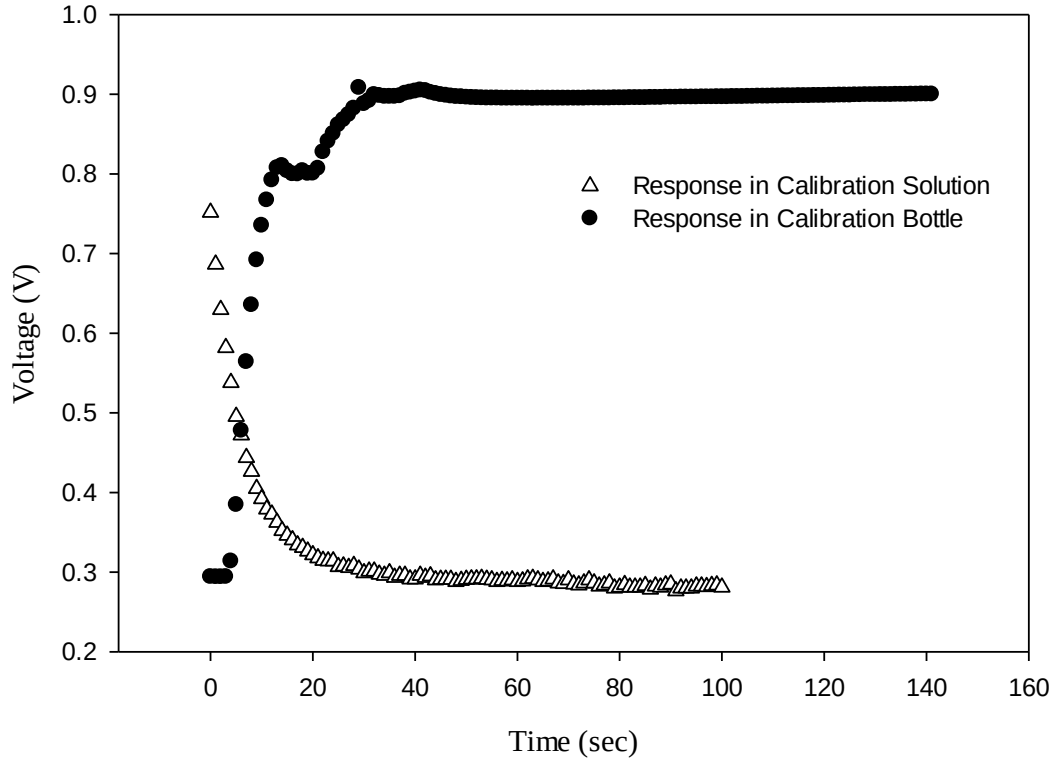

Figure 4.2: Typical DO Probe response for zero and full scale calibration points

Two calibration points are used to form the linear equation which is then used within the data acquisition program to convert the probe signal to dissolved oxygen concentrations (mg/L). The uncertainty of the probe is ± 0.2 mg/L and the resolution is 0.007 mg/L.

4.1.3. Accelerometers

A ± 50 g strain gauge type accelerometer was used to measure the acceleration profile of the shaker during operation. A bridge amplifier was used to convert the accelerometer signal into a voltage output which was read by the data acquisition system. Calibration of the accelerometer requires three steps. With the accelerometer in the upright position the strain box is used to balance the accelerometer bridge. After the accelerometer has been balanced the next step is to record the voltage with the accelerometer still in the upright position. The voltage at this position corresponds to a reading of 0 g's. The accelerometer is internally adjusted to be zero in the upright position, i.e. it has an internal value of -1 g to offset gravity.

The third step is to flip the accelerometer upside down and record the voltage. The voltage at this position corresponds to a value of 2 g's (one g due to gravity and one g due to the internal reference). The corresponding voltage levels for 0 and 2 g's is used to form the linear equation which is then used by the data acquisition program to convert the voltage from the strain box into accelerations (g's). This "static" calibration is good for the entire range of the vibration frequency used in this research (Lowery, 2012).

There was no documentation provided with the accelerometer, but similar models claim a linearity of ± 0.75% full scale at f < 100 Hz. Applying this to the accelerometer in use would give an uncertainty of ± 0.38 g's in the experimental frequency range. This value corresponds well with the values and variation provided by the bridge amplifier display. Furthermore the values measured during testing (Figure 3.30) also matched well to the theoretical response except for particular values which can be associated with the mechanical system.

4.1.4. Photographic Measurements

The photographic measurements of the bubble size distributions at specific locations along the column were used to determine the Sauter mean diameter. Calibration of the system involves associating photograph pixels with a known length scale. The analysis of the photographs was performed using ImageJ software, which is a free image processing program written in Java. The output of the "Analyze Particles" routine provides information about the cell (bubble) size distribution in terms of pixels. The number of pixels per length scale was determined by associating a known length within the picture to the number of pixels between two points. In the analysis performed for this research each picture includes a reference length of 5 cm which was physically transcribed to the cylinder using a precision rule with a resolution of 0.25 mm.

There are generally two methods to translating pixels into a physical distance using the ImageJ Software. The first method is to take a picture of an object with a known dimension. For example a picture can be taken of a ruler with known scale. The picture of the ruler is then opened in ImageJ and a line is drawn between the two scale marks (Figure 4.3). The line is then measured by selecting Analyze → Measure which outputs the length in pixels. Several lines and measurements can be made to ensure a representative sample and averaged to give a pixel to length scaling factor. The scaling factor can then be manually applied later in an Excel document or other processing routine to convert the raw pixel data into a physical scale. The other method is to use the scale inherent to ImageJ by selecting the Analyze → Set Scale function. To use this function a line must be drawn on a representative photo and then set. ImageJ will automatically apply the scale to all subsequent analyses. The scale can also be set as a global scale if necessary.

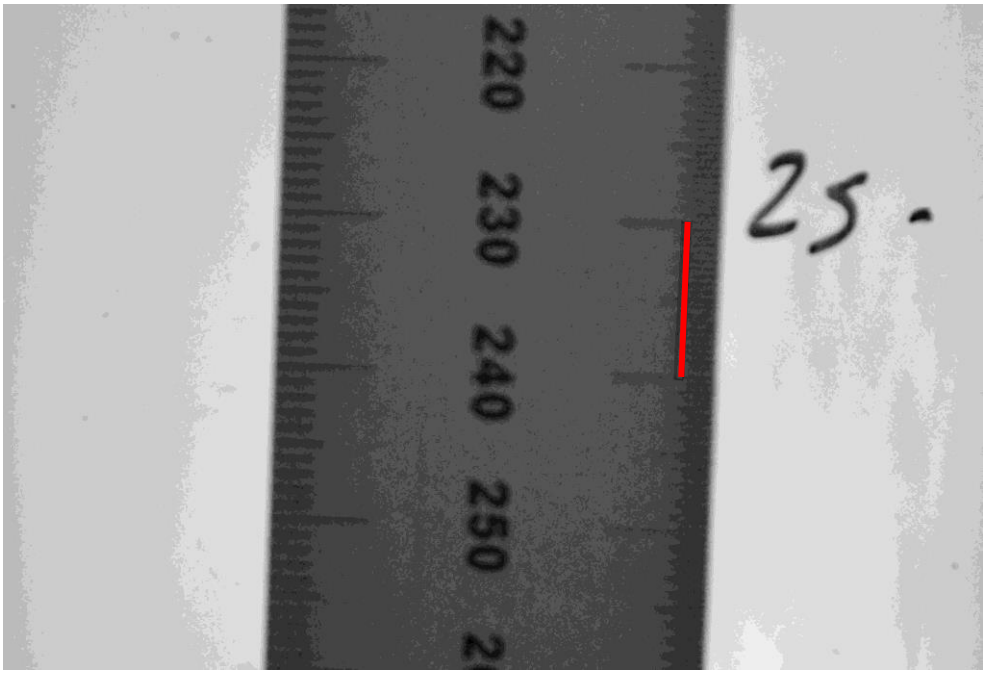

Figure 4.3: Scale factor processing Method 1 using ImageJ software

There are advantages and disadvantages to using both methods. The first method is more absolute and statistically valid since you have a number of reference measurements from which you can take a mean. However, the first method requires that the camera be fixed in the same

position with the same focal length and viewing area for every shot being analyzed or the scaling factor will be erroneous. The second method is much easier and can be applied to each picture being processed which takes the error out of changing camera position. However, there is only one representative measurement from which the scale for the picture is derived so the error in the scaling factor can be highly systematic due to bias (Figure 4.4). A discussion of photograph processing using ImageJ will follow in § 4.2.1 and a discussion of measurement uncertainty can be found in Appendix B.

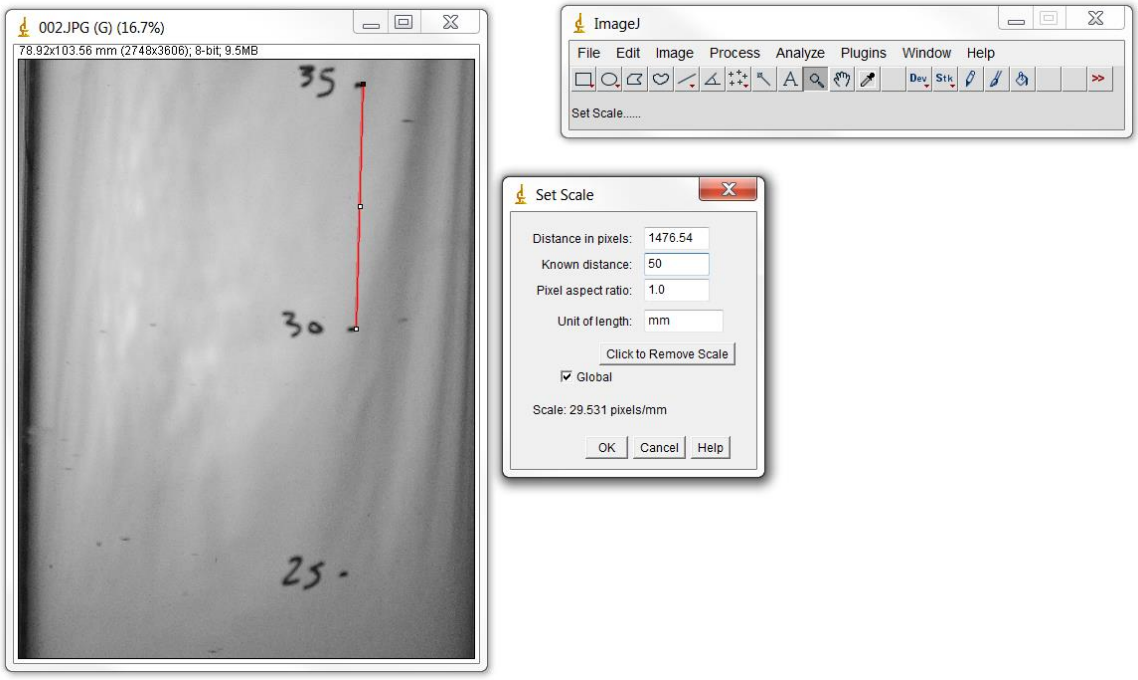

Figure 4.4: Scale factor processing Method 2 using ImageJ software

4.2. Experimental Procedure

The following sections outline the general use of the experimental set up including operation of the shaker and the measurement techniques used in the validation tests and experiments performed during this work. The majority of the techniques are related to acquiring measurements including processing of DO measurements to produce volumetric mass transfer rate (k_La), shaker amplitude and frequency, photograph processing for bubble size and void

fraction measurements, and determination of superficial gas velocity for air injection. A final summary of tests performed is included in Table 4.1.

4.2.1. Pre-Operation and Warm Up

To ensure the safety of the personnel working in and around the shaker and the proper operation of the equipment a series of checks should be performed prior to use each day.

1. Inspect the shaker for loose, missing, or broken hardware including: motor carriage hardware, anchor bolts, couplers, drive shafts, flywheels, linkages, and base hardware.
2. Inspect the column and mounting hardware to ensure that there are no leaks, or loose components.
3. Ensure the pressure tap valves are open.
4. Turn on the camera, and ensure: a memory card is installed, the lens cap is removed, the remote shutter receiver is installed and ON (if necessary).
5. Turn on/Wake the PC and access the data acquisition program.
6. Turn on the ΔP transducer demodulator, bridge amplifier, and power transformer.
7. Allow the DO probe, ΔP transducer and accelerometer to warm up for at least 10 minutes.
8. Turn on and position the backlight lamps if flow visualization is required.
9. Ensure the Pressure Bypass Valve on the Pressure Manifold is OPEN (Figure 3.8).
10. Ensure the pressure supply valve on the Pressure Manifold is OPEN (Figure 3.8).
11. Turn on the mass flow meters.
12. Ensure compressor supply valve is CLOSED.
13. Turn on compressor.

4.2.2. Setting Shaker Amplitude and Frequency

The amplitude and frequency of the shaker are important parameters associated with the vibration input for each test. Proper adjustment of the EDM is essential to ensuring the amplitude of vibration is correct. Furthermore, setting the frequency and operating the speed controller is necessary to running the shaker. The following steps are used to operate the shaker.

The amplitude of the shaker is changed by "tightening" or "loosening" the two bolts on the EDM using a 15/16 in. open end wrench (Figure 3.28). The following procedure is recommended.

1. Measure the current amplitude setting:
    a. Cycle the shaker to either the top of stroke (TOS) of bottom of stroke (BOS) by rotating the flywheel counter clockwise. The bolts will be in a vertical position at TOS/BOS.
    b. Place metal ruler flat side against the right hand side of the shaker so that it rests against the piston housing and base plate edges. The ruler should be in a vertical orientation so that it slightly touches the shaker table edge.
    c. Align ruler mark with bottom edge while holding ruler near the base. While holding the ruler in place slowly rotate the flywheel counter clockwise until the BOS/TOS is reached which is indicated by the momentary halt and change of direction.
    d. Divide the measured displacement between TOS and BOS by half to determine amplitude.

       Note: The steel ruler has smallest increments of 0.5 mm so a resolution of 0.25 mm can be obtained with an uncertainty of ± 0.25 mm.

2. Change the amplitude.

    a. Loosen the nylon lock nuts on both EDM bolts using a 15/16 in. open end wrench.

    b. Adjust the bolts by tightening (clockwise rotation) or loosening (counter clockwise) the heads. The bolts should be adjusted in quarter turns alternately to avoid cocking the drive.

    c. Measure the displacement of the outer cylinder axis from the drive axis using the depth gauge end of a caliper. The displacement or "eccentricity" of the drive is measured by placing the flat end of the caliper on the flat machined surface centered with reference to the bolt head. The caliper depth gauge is extended until it strikes the drive shaft. Alternately, it may be easier to extend the depth gauge first to a larger length then touched to the drive shaft and reduced or closed until the flat end of the caliper arm is flush with the flat machined surface. The eccentricity measurement gives reference to how far the axis centers are apart and should be equal.

        Note: There are two locations the outer cylinder axis can have relative to the drive shaft and the bolt heads. For example the drive can be adjusted "over center" where the outer cylinder axis is farther than the drive shaft axis, or "under center" where the outer cylinder axis is closer than the drive shaft axis relative to the bolt heads. If the condition is "over center" the larger the eccentricity the larger the amplitude will be. The drive is currently in an "under center" configuration so smaller displacements give larger amplitudes and vice versa. It should be noted that while the EDM can technically be cocked so that the axes of the shaft and the cylinder are not parallel it is very hard to do so. The effort required to turn one bolt or another increases greatly once the axes become slightly misaligned, and therefore hard to turn bolts are an indication that the axes

are misaligned. The eccentricity should be measured if the bolts become overly hard to turn and the lagging bolt adjusted to match.

d. Check the amplitude (See Steps 1a-1d) and repeat Steps (2b-2c) until desired value is reached.

e. Retighten the nylon lock nuts.

f. Check the final amplitude and make small adjustments to suit (Step 2d).

3. Remove all tools from the area and make a final clearance check of the drive by rotating the shaker through one cycle. Do not proceed if any binding occurs. Flywheel should rotate easily by hand and any undue force will cause the transmission coupling to fail in shear as a safety.

The frequency of the shaker is set using the dial on the speed controller (Figure 4.5). The minimum frequency change is 0.1 Hz and the dial will increase by that increment unless turned quickly. The speed controller has a red LED display which indicates the frequency setting. Once the frequency is set the shaker is run by pressing the green RUN button. It is important to ensure that there are no loose hardware, tools or other objects in or around the motor carriage, drive or shaker table that would bind or jam the device, and that the area is clear of personnel before running the machine. To stop the shaker the red STOP button is pressed.

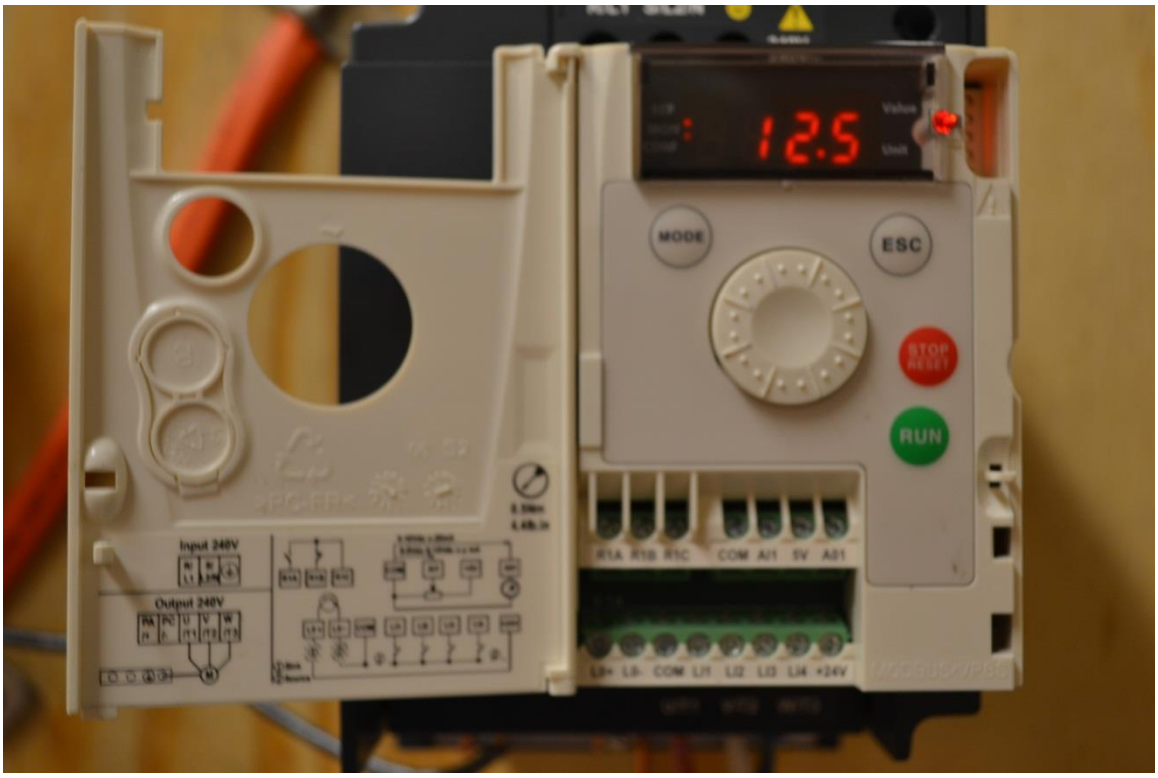

Figure 4.5: Motor speed controller

4.2.3. Mass Transfer Measurement

The dissolved oxygen, differential pressure and accelerometer measurements can be taken simultaneously using the data acquisition system. However, due to the differences in sampling rates it is necessary to separate the mass transfer measurement from the acceleration measurements. The mass transfer measurement primarily concerns the use of the DO probe, but depending on the frequency of vibration and the sampling rate the differential pressure and acceleration outputs may provide some value. The DO measurement is taken over a period of 250 – 1500 seconds, depending on the mass transfer rate, at a sampling rate of 1-4 samples/second. A sampling rate of 4 samples/second was found to be the best for cases where vibration frequency is greater than 15 Hz due to the fluctuation of the signal. In cases where the signal fluctuated the samples were time averaged which is discussed in greater detail in §5.2.1.

The DO probe requires a 10 minute warm up to generate reliable data as per the manufacturer's recommendation. Therefore, it is critical that the Pre-Operation checks have been performed as previously described. It was found that by setting the data acquisition system to collect data for 600 seconds the necessary warm up time would elapse, and a measure of probe responsiveness could be gauged. One disadvantage to all DO probes is the use of a gas permeable membrane to separate the test fluid from the cathode, anode and filling solution. Any defect in the probe membrane will result in unresponsive, unrealistic or sporadic output from the probe. If the probe is responding in such a manner it is best to remove the probe, replace the membrane, recalibrate and reinstall. Fortunately the membranes for the Vernier DO probe are easily replaced by simply unscrewing the old membrane cap and replacing it with a new one. Membrane caps are inexpensive and can be reordered through the Vernier website (www.vernier.com/products/accessories/mem).

Removal and installation of the probe into the cylinder is fairly common. Since it is not recommended to leave the probe out of use for more than 24 hours it must be removed from the cylinder and used. To store the probe the membrane cap the following is recommended:

1. Remove the membrane cap by unscrewing from the DO Probe body.
2. Empty the membrane cap of filling solution and rinse with distilled water. Place the cap on a disposable shop towel to dry.
3. Rinse the inner probe tip with distilled water and gently blot dry with a disposable shop towel.
4. Screw a dry membrane cap halfway onto the DO probe body so that the inner probe tip is covered, but does not press against the membrane cap membrane.
5. Place back in storage box away from traffic so that it is not damaged.

To prepare the probe for use the opposite instruction is followed.

1. Remove DO probe from storage box and remove membrane cap.
2. Fill membrane cap with ~ 1 mL of filling solution using the plastic pipette.
3. Screw membrane cap onto DO probe body.
4. Plug probe into the SensorDAQ and place the probe tip into water.
5. Allow 10 minutes for probe warm up.
6. Calibrate (See §4.1.2).
7. Unplug probe from the SensorDAQ.
8. Install the probe into the probe mounting plate.
9. Install rubber O-ring around probe and position against the mounting plate inset. The inset should face the probe tip (away from wire lead).
10. Install the probe into the cylinder.

It is easiest to install the probe in the cylinder when the cylinder is empty of fluid. However, it is possible to install the probe with the cylinder full by placing the column under a vacuum. To remove the probe while the column is filled the following procedure is recommended. Installation follows the same but oppositely.

1. Close the Pressure Supply, Injector Gas Supply, and Pressure Bypass valves on the Pressure Manifold (Figure 3.8).
2. Open the Vacuum Supply valve.
3. Turn on the Vacuum System by placing the switch to ON (Figure 3.9).
4. Adjust the vacuum by turning the regulator adjustment screw clockwise (decrease) or counter clockwise (increase). A vacuum of ~ 15 in Hg is recommended.
5. Allow the system to come to the vacuum selected by monitoring the gauge on the Pressure Manifold.

6. Remove the thumb screws from the DO probe mounting block and grasp the mounting plate to remove the probe. A slight resistance will be felt due to the vacuum and air will begin to enter the column. The pump may also turn on automatically to readjust pressure.
7. As the probe is removed with one hand, install the rubber stopper into the open port of the mounting block. A small amount of water may be lost as the probe and stopper are switched depending on the speed of the exchange.

The DO probe measures the absorbed oxygen content present in the liquid, and is sampled continuously over a set time interval to record the unsteady mass transfer of oxygen from the air to the liquid. The probe operates by taking a small amount of the oxygen in the test fluid (see §2.2.2.), and therefore the measured response of the probe will appear to decrease when left in stagnant water for a period longer than 1 minute. Therefore fluid must be flowing past the probe for an accurate measurement. A short wait period of approximately 30 seconds after initiation of gas injection was found to be more than adequate to give a reliable measurement (indicated by the jump in Figure 4.6).

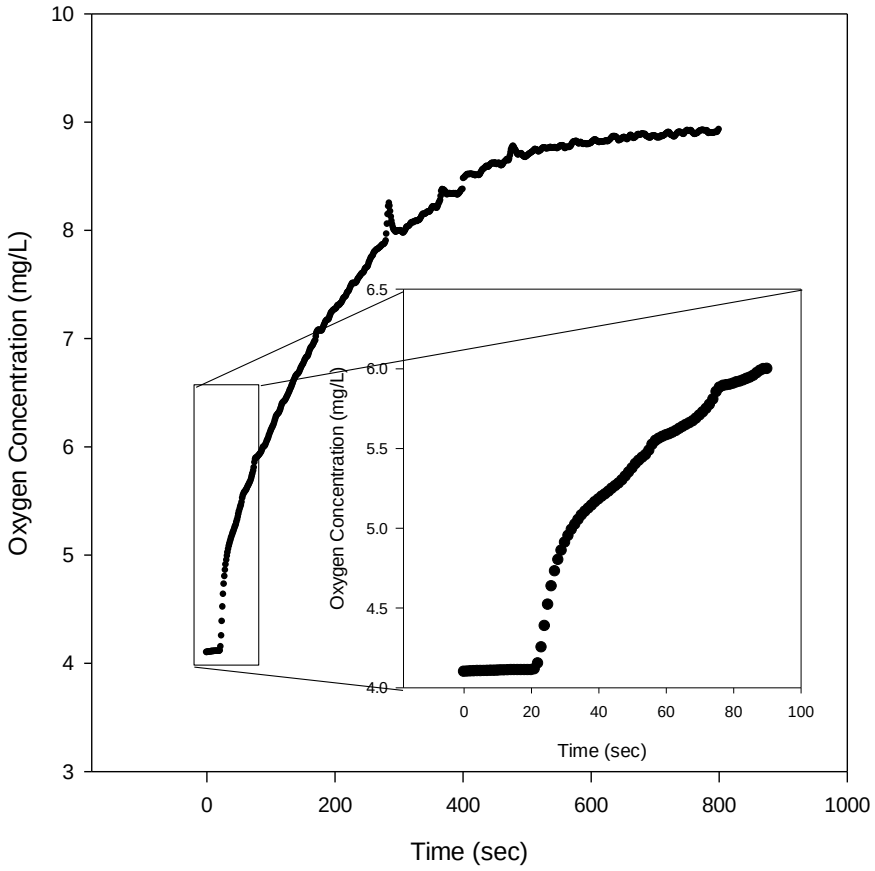

Figure 4.6: Dissolved oxygen concentration over time

The amount of time required for a mass transfer measurement depends on the mass transfer rate which is being sought. Therefore, some prior knowledge of the mass transfer rate is useful in determining the length of time an experiment will take, but it is not necessarily required to perform the measurement. Typically the oxygen concentration curve for a non-vibration or a vibration run at f < 10 Hz will trend to a nearly constant value which is close to, but not necessarily, the saturated oxygen concentration value that is used during the calibration. Often in dynamic systems which model a similar exponential rise or decay a time equivalent to 5τ is used as a cut-off reference, where τ is the time constant of the system defined by,

$$\tau = \frac{1}{k_L a} \tag{4.2}$$

A time of 5τ would correspond to less than 1% change in the response. However, in the case of mass transfer it was found that a time equivalent to 3τ (95% complete) was sufficient to determine a reliable volumetric mass transfer coefficient considering the accuracy of the probe and the saturation concentration. If prior knowledge of the mass transfer rate is known then the sampling time can be truncated appropriately, but in cases where the mass transfer rate cannot be predicted in advance it is best to collect overly many points. During analysis of the data the extraneous terms can be discarded.

Post processing of the data is relatively simple to perform manually using an Excel sheet or other software package capable of statistical regression tools. To derive volumetric mass transfer (k_La) from the collected oxygen concentration data, the data must be linearized. The actual absorption of oxygen follows Equation 2.59 which is a logarithmic function of the oxygen concentration, volumetric mass transfer rate, and time. The two constants C_0 and C^* must be fixed. It is beneficial to have the largest separation possible between the two, but both values can be determined from the data set by applying a min and max function to determine the C_0 and C^* values respectively. A new equation can be written as,

$$-\ln(C') = k_L a t \tag{4.3}$$

where,

$$C' = \frac{C^* - C}{C^* - C_0} \tag{4.4}$$

The mass transfer rate (k_La) can thus be determined by the slope of a linear regression of Equation 4.3 plotted as a linear transformation following Y = mX where,

$$Y = -\ln(C')$$
$$X = t$$

Some iteration between the number of samples used to predict the slope of the regression line is recommended since the natural log function becomes increasing ill-conditioned as C approaches the maximum value. The algorithm suggested for use in MS Excel is:

1. Select the range of X values (N samples) corresponding to $t = 0$ to $t = C^* - \Delta t$. For example, C^* is occurs at $t = 917$ seconds with a $\Delta t = 1$ second. The values in the X range should consist of $t = 0$ to $t = 916$ seconds.
2. Select the range of Y values corresponding to the selected X values by using the CTRL button so that both ranges are selected.
3. Plot the selection using Scatter Plot.
4. Select the data points on the graph and select Add Trendline. Select all three boxes Set Intercept = 0, Display Equation on chart, and Display R-squared value on chart.
5. In another cell write the equation = $3/[k_La]$ where $[k_La]$ is the slope of the trendline. The cell will calculate the time step required to reach 3τ assuming the value of C^* is the oxygen concentration as $t \rightarrow \infty$.
6. Select the linearized concentration plot with the trendline and change the X and Y ranges to match the result of Step 5. The regression slope will be recalculated accordingly. Change the value in the 3τ calculation cell and check to see if the X and Y ranges match the result.
7. Check the result of the new calculation with the X and Y ranges and iterate until they are within 5%. The R^2 value should increase as you perform this iteration.

Note: for a more precise result of the slope of the regression line it is recommended that the Regression Analysis Tool of the Data Analysis Add-In be used with the ranges found through the algorithm above.

Alternatively, the exponential regression tool provided in Excel could be used provided the Equation 4.4 is manipulated into a different form, but the process above was preferred. Figure 4.7 provides a graphical example of the linear transformation of C and determination of k_La from the DO data.

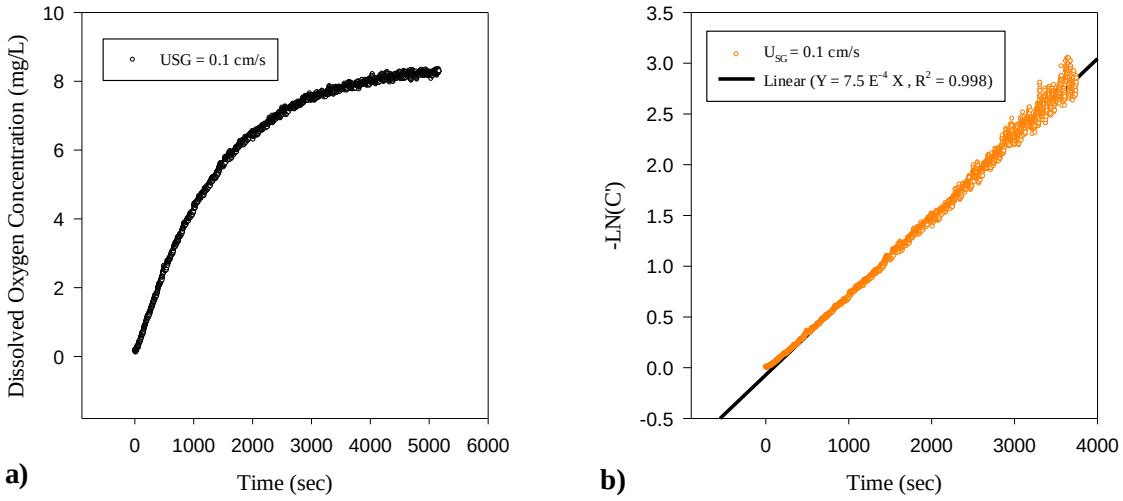

Figure 4.7: a) Dissolved oxygen concentration vs. time and b) linearization and regression analysis to determine k_La for f = 0, U_{SG} = 0.1 cm/s ($\dot{m}$ = 0.0006 kg/min), p_e = 1 atm

An example mass transfer run is detailed in the following steps:

1. Perform Pre-Operation and Warm Up
2. Set Shaker Amplitude and Frequency
3. De-aerate the column fluid:
    a. Ensure the compressor valve is CLOSED
    b. OPEN the Nitrogen supply valve on the bottle and increase pressure to 100-110 psi
    c. OPEN the supply valve on the Two Phase Flow Set Up which is connected to the Nitrogen supply
    d. OPEN the supply valve to the mass flow meter

e. Set the mass flow meter supply (suggested: 0.0100 kg/min)

f. OPEN the Injector Gas Supply valve and CLOSE the Pressure Supply valve on the Pressure Manifold (Figure 3.8). Keep the Bypass/Relief valve OPEN.

g. The Nitrogen should begin bubbling through the column. Monitor the DO Concentration on the data acquisition meter or track the concentration by selecting START on the data acquisition system until the DO Concentration is 0 ± 0.2 mg/L.

h. Turn off the Nitrogen supply by closing the supply valve on the bottle, and CLOSE the supply valve to the Two Phase Set Up gas manifold.

4. OPEN Pressure Supply valve on the Pressure Manifold and CLOSE Injector Gas Supply valve. Injector bubbling should cease.
5. OPEN compressor valve
6. Adjust airflow on the mass flow meter to desired level and record.
7. OPEN Injector Gas Supply and CLOSE Pressure Supply valves on the Pressure Manifold. Air should begin bubbling through the column.
8. For a run with vibration: push the green RUN button on the motor speed controller.
9. Begin data collection. For mass transfer runs with vibration no wait time is necessary before initiation of data collection, but a wait of 20 – 30 seconds should be implemented during static measurements to ensure sufficient flow past the DO probe.
10. For a run with vibration: push the red STOP button to stop the shaker.
11. CLOSE Gas Injector Supply and OPEN Pressure Supply valves on Pressure Manifold to cease bubbling in the column.
12. CLOSE compressor valve. Residual air pressure will bleed out through the Bypass/Relief valve to decrease strain on the system.

4.2.4. Differential Pressure and Acceleration Measurements

The differential pressure and accelerometer data is measured over a period of 3 cycles of the shaker in order to analyze the shaker input per cycle. The analysis of this form captures the transient harmonics that may be apparent in the system, and capturing 3 cycles gives an indication of repeatability. To ensure that higher frequency modes are captured the accelerometer and ΔP data are best if measured over 3 periods at a sampling rate of 2000 samples/second. This sampling rate provides a Nyquist frequency of 1000 Hz which ensures that harmonic frequencies up to 1000 Hz can be accurately sampled. The Nyquist frequency is defined as,

$$f_{Nyq} = \frac{f_s}{2} \tag{4.5}$$

Data was collected for both ΔP and accelerometer measurements during vibration experiments both with and without injected air. Measurement of the acceleration was recorded in all three axes by gluing the accelerometer to the shaker test table with 5 minute two-part epoxy. A 2 g calibration was performed on a level surface verified by spirit level before remounting the accelerometer. The accelerometer was mounted such that the device axis was aligned with the table axis by ensuring the flat surface of the accelerometer bottom was flush with a machined table surface perpendicular to the axis to be tested (Figure 4.8). Care was taken to fix the accelerometer with as little misalignment as possible until the epoxy had set. At least 12 hours were allowed for the epoxy to cure before operation of the shaker.

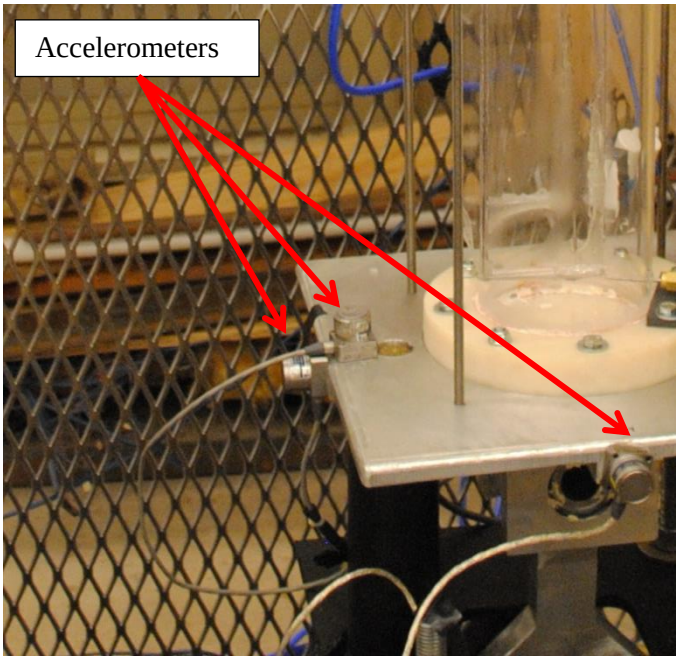

Figure 4.8: Accelerometer placement

The ΔP transducer was calibrated at the beginning of each measurement session, or if the transducer signal became erratic or erroneous during the session. A quick measurement of the transducer error was made by changing the position of the transducer. When the column is static the transducer measures the hydrostatic pressure corresponding to the liquid height above the transducer port. Simply changing the height of the transducer will give an output that can be compared to the theoretical hydrostatic pressure corresponding to the displacement. This is a quick method to determine if the transducer is working properly, or if it requires a new calibration. All differential pressure measurements taken with the ΔP transducer were taken simultaneously with the acceleration measurements.

An example of accelerometer and ΔP measurements is provided in the following steps with a typical output of form 1 (Figure 4.9):

1. Reset the sampling parameters of the data acquisition system. After mass transfer data collection is completed but before shut down (e.g. between Steps 9 and 10 of mass

transfer measurement example) the data collection system is reset to record a sample time of 3 periods. For example a vibration run with f = 15 Hz would be set to a sample time of $3/f$ = 0.2 seconds. The sample rate is set to 2000 samples/second.

2. Record a data set and store to memory. Repeat as necessary or desired.
3. Reset data acquisition sampling parameters. The sample time is set to 120 seconds and the sampling rate set to $4f$.
4. Record a data set and store to memory. Repeat as necessary or desired.
5. Shut down shaker and gas injection following mass transfer measurement example steps 10-12.
6. Save or export data file to CPU and/or flash drive.

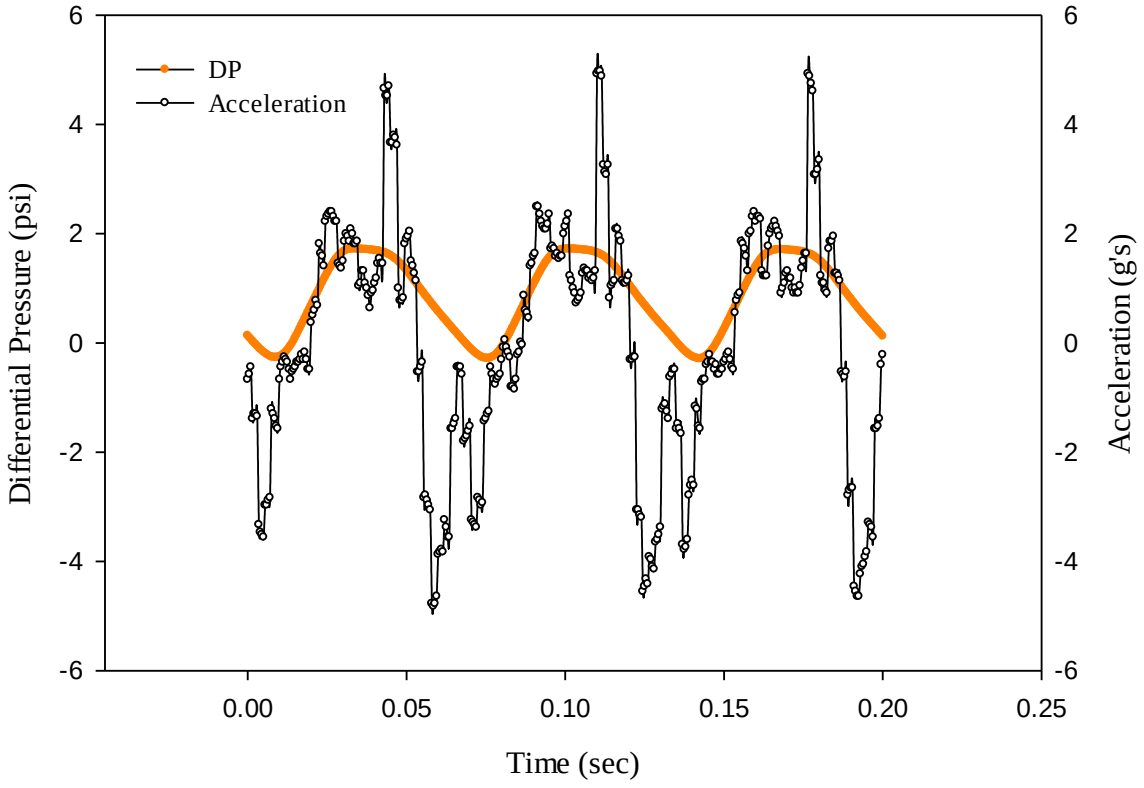

Figure 4.9: Accelerometer and Differential Pressure measurements for f = 15 Hz, A = 2.5 mm, U_{SG} = 0.25 cm/s at p_e = 1 atm with no air injection

4.2.5. Flow Visualization

Flow visualization was carried out on the column to facilitate calculation of void fraction from photographic measurement of the liquid interface, calculation of bubble size and distribution, and to capture the dynamic motion of bubbles at stabilization frequency. Monochrome still photographs were taken of bubbles within the column at 3 locations corresponding to column heights: H = 30 cm, H = 45 cm, and H = 60 cm with total liquid height of 85 cm. Monochrome still photographs were also taken of the liquid-air interface in order to measure mixture height to determine void fraction. A high speed camera was used to capture video of bubble motion.

The lighting configuration for both the still photographs and flow visualization are different. The lighting was provided by two halogen light stands. A series of lighting arrangements were tested to determine the best configuration to produce the still images which would process most accurately in ImageJ. The best configuration for the still images consists of both light stands in a backlight arrangement with one stand at approximately 30º with the camera, placed behind a white muslin backdrop, and the other stand at approximately 45º, placed outside the safety cage. The camera was placed outside the safety cage on an adjustable tripod and angled slightly with respect to the viewing pane (Figure 4.10). Each light stand was arranged with both light pods in a vertical configuration at a height of approximately 4 ft. The resulting lighting and camera configuration resulted in images of bubbles that are sharply contrasted with the fluid medium (background), but do not have glare points or reflections. The still photographs must capture bubbles with solid boundaries that contrast with the background so that the processing routine performed in ImageJ will produce binary images representative of the true bubbles in order to determine bubble sizes (areas).

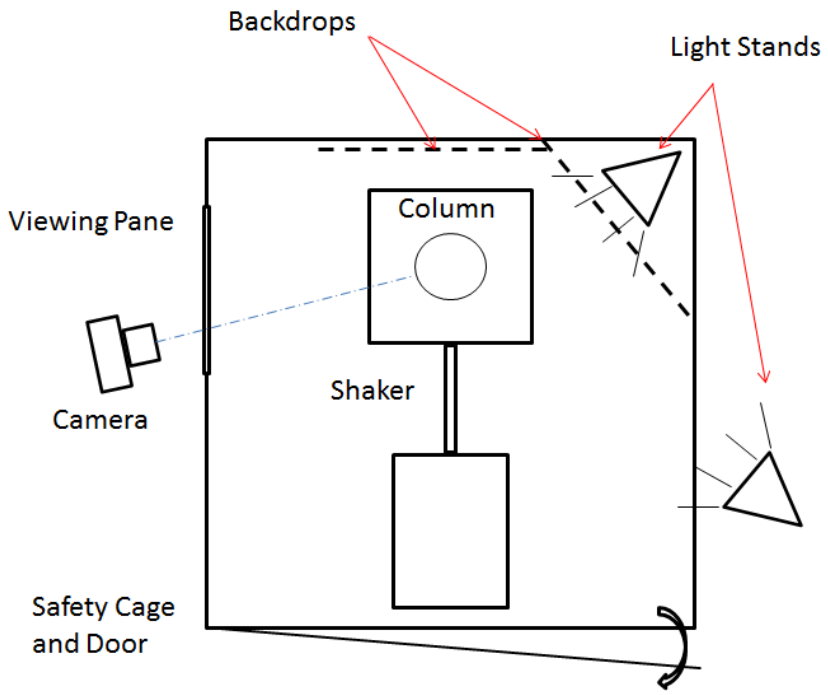

Figure 4.10: Schematic of lighting and camera arrangement for still images

Photographs of the liquid-air interface were also taken using the same lighting arrangement as the bubble images. However, the camera was removed from the tripod and the pictures taken by hand. The interface images must be captured by holding the camera so that the proper height and zoom can be reset. For instance, during higher frequency mass transfer runs the interface could be reach 100 cm or more, which surpasses the height adjustment of the tripod. The camera zoom may also need to be adjusted to capture the interface with respect to the scale reference marked on the column.

Slow motion and real time video were captured using a separate lighting arrangement. The lighting configuration was chosen such that one stand was behind the column for backlighting and one stand was outside the safety cage opposite to the backlight to illuminate the front features of the bubbles. Illumination of the bubble surfaces was important in capturing bubble coalescence and breakup phenomena whereas the backlight only configuration did not lend itself to providing qualitative images as well. However, the lighting arrangement of the

video capture was not as crucial as that of the still images of bubble size and air-water interface so long as the light quantity was sufficient. Both the Sony video camera and the Casio Exilim camera were arranged on a tripod in a manner similar to the still photographs. The zoom and the height of the video camera were adjusted as needed for each shot.

Post processing of the still images of bubbles and the air-water interface was performed using ImageJ software. Two separate routines were used to calculate the bubble size distributions and the mixture height based from still images of bubbles at different column heights and air-water interface respectively. The bubble size distribution is given by performing the following routine:

1. Calibrate scale using method 1 (see §.4.1.4). Thirty scale measurements were taken and then averaged to produce an average scale factor.
2. Open picture file in ImageJ using File → Open (Figure 4.11).

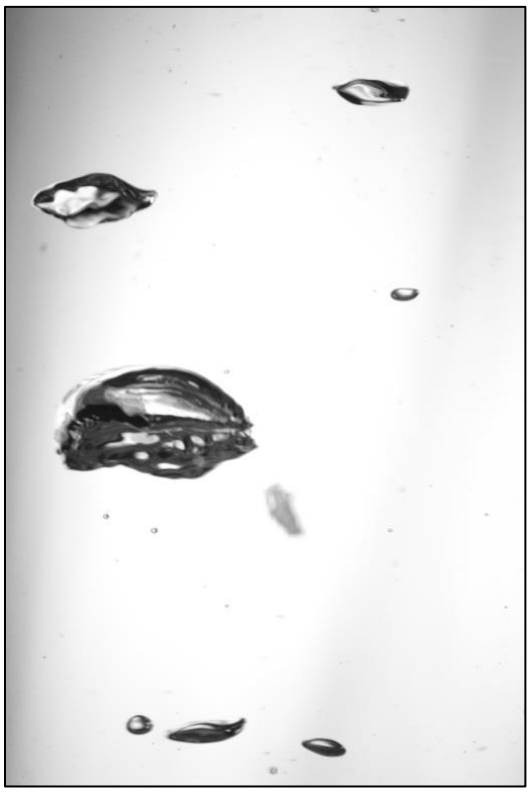

Figure 4.11: Original bubble image

3. Remove background using Process → Subtract Background. The rolling ball radius was set to 80 pixels with the "Light background" and "Sliding paraboloid" boxes checked. Select OK (Figure 4.12).

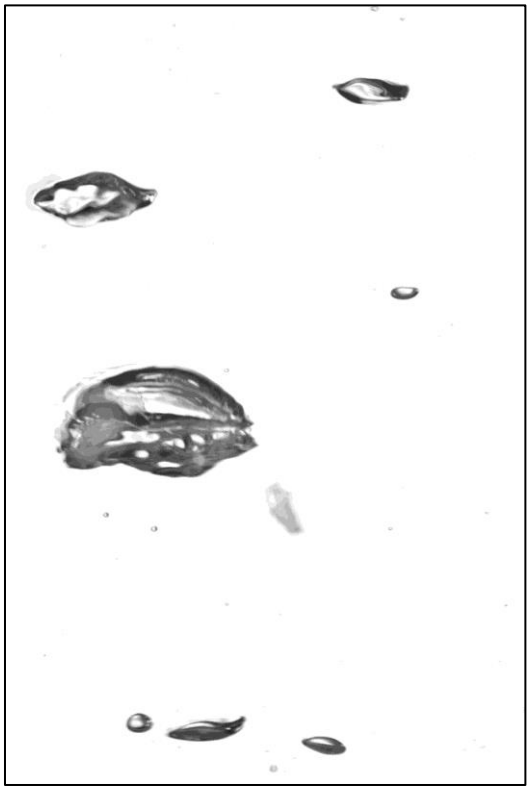

Figure 4.12: Bubble image with background subtracted

4. Adjust the threshold by selecting Image → Adjust → Threshold… or Ctrl + Shift + T. An automatic threshold is set by the software, but the threshold is adjusted to 240. The threshold function creates a binary picture by reducing all pixels with grayscale values lower than the threshold to white (0) and those above to black (255). A higher threshold will "complete" more bubbles that may have broken outlines, but more noise may be introduced and so a balance must be sought that represents the true image. Selecting Apply causes the picture to become a binary image for processing (Figure 4.13).

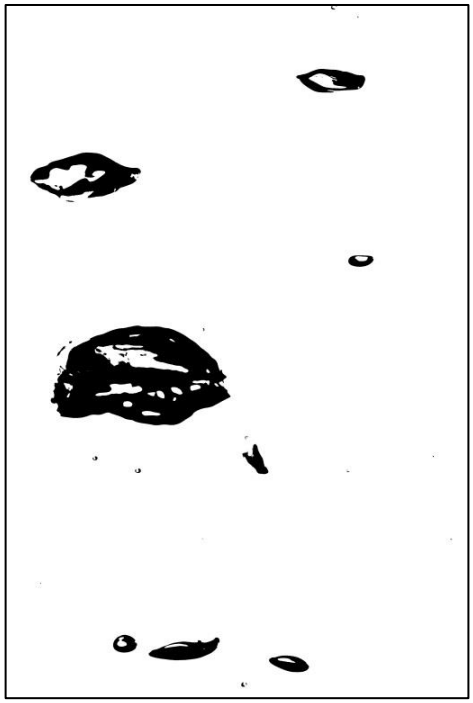

Figure 4.13: Bubble image after thresholding

5. Fill holes by selecting Process → Binary → Fill Holes. Any voids left in the bubble image after processing will be filled (Figure 4.14).

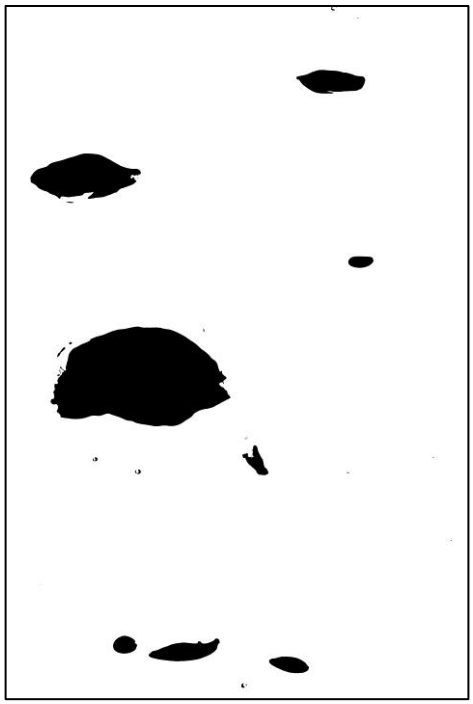

Figure 4.14: Bubble image with filled holes

6. Analyze the bubble areas by selecting Analyze→Analyze Particles. The Size is set to include actual bubbles and not any remaining fragments or rogue pixels. A simple examination of the original image will confirm what are and are not bubbles. Setting Area to "1.0 – Infinity" discriminates the analysis to only accepting "real" bubbles and rejects noise such as speckling produced during the thresholding process. Setting Circularity to 0.1 also discriminates the fragments or flotsam from obvious bubbles. Selecting "Outlines" from the Show drop-down menu will produce a copy of the original image with outlined overlays of objects that were analyzed (Figure 4.15). Select "Display Results", "Exclude on edges" and "in situ Show" boxes. Click OK.

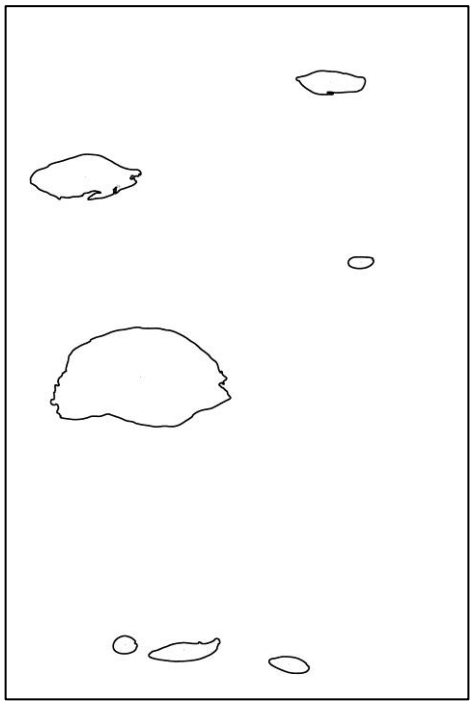

Figure 4.15: Analyzed image of outlined and measured bubbles

It is important to note at this point that there are some valuable data lost during processing. For instance the smaller satellite bubbles in this picture did not make the cut during processing because they did not have solid outlines. This is unfortunate, but several pictures are analyzed in this way and to be objective precedence must be made and observed for all pictures in

a particular stack. One should note also that while some of the real bubbles were lost during processing some of the "fictional" bubbles were also cut as should be. Notice that the irregular flotsam to the right of the bubble was not included in the analysis. Furthermore, the tiny bubbles apparent in the original at the top and bottom of the frame were also excluded. These bubbles were simply stuck to the wall of the column and did not represent the true nature of the flow. Therefore they should have been cut as such. It can be seen then, that while some data is lost, other erroneous data is also filtered and so it is seen to be appropriate. Another important fact is that this method cannot be used accurately in cases where the bubbles are overlapping to any degree. As such, there are certain column heights and experimental conditions which produce frothier flows and can be analyzed by this method but should be subject to skepticism. Several pictures (10+) are used for each vibration condition, at each column height making for a lengthy analysis if done step by step. Therefore, a macro was written to speed the process which produces steps 2 – 6 with one keystroke (Appendix A.7). The analysis results are saved as a text file for later manipulation in Excel.

Post processing of the air-water interface images was also performed using ImageJ. The height of the interface was measured relative to a scale marker in the picture. Several photographs of the interface were captured, measured, and averaged to give the mean interface height. The interface height was used in conjunction with the original liquid height measured prior to the experiment to calculate the volume averaged void fraction per Equation 2.46. The uncertainty of each measurement is given by the standard deviation of the mean for the sample measurements. To decrease systematic error, each image scale was calibrated prior to measurement using the known scale of 50 mm between two measured marks on the column present in the picture. A measurement is made from the bottom of the float to the reference mark on the column parallel to the column walls. Measurements were made from each individual image in a similar manner unless the bottom of the float could not be seen, or the bottom of the

float was below the reference. In the case where the float could not be seen a best approximation of the actual air-water interface was used. For the case where the bottom of the float was below the reference mark the sample picture was not measured. A sample interface height measurement is given as follows:

1. Open image in ImageJ using File→Open.
2. Calibrate the pixel scale. Draw a line parallel to the column wall from one column scale mark to the other mark using the "Straight" line tool (Figure 4.16a). Set the scale by selecting Analyze→Set Scale. Enter the "Known distance" (e.g. 50). Enter the "Unit of length" (e.g. mm). Click OK.
3. Measure interface height. Draw a line parallel to the column wall from the interface reference (e.g. bottom of float) to fixed reference (e.g. 85 cm mark) (Figure 4.16b).

a) 

b) 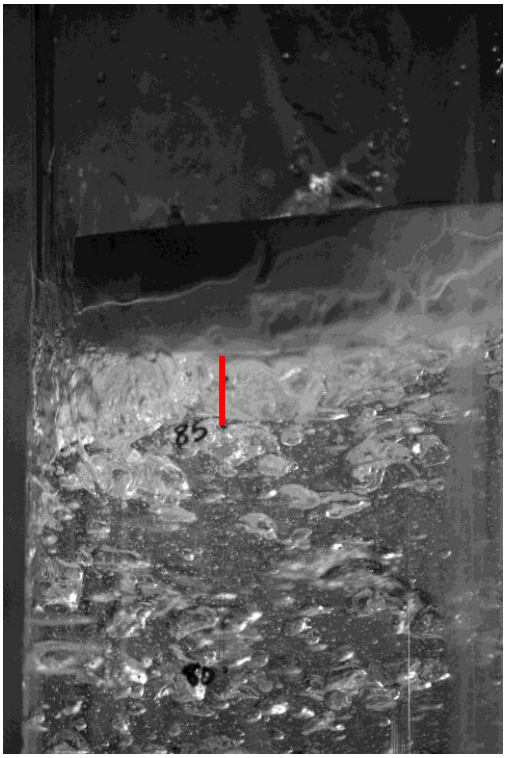

Figure 4.16: a) Scale calibration and b) measurement of interface height

4.3. Summary

The operation of the shaker equipment and experimental procedure has been outlined in a step by step fashion for reference to future users. The Pre-Operation and Warm Up procedure should always be performed at the beginning of any experimental session to ensure the safety of personnel and proper operation of equipment. The shaker amplitude is adjusted manually using the procedure described and physically measured using a precision metric ruler. Frequency of the shaker is automatically monitored by the speed controller and adjusted at the console. Mass transfer measurements are taken using the Dissolved Oxygen probe and the data acquisition program. Sufficient time of measurement must be allowed to ensure enough data points are available and representative of at least a 3τ period. It is always best to collect too many data points than too few. Differential pressure and acceleration measurements of the column and shaker table were taken using a differential pressure transducer and an accelerometer respectively. It is important to ensure that the differential pressure transducer is of the appropriate range and has been calibrated prior to each experimental session. Accelerometer readings were taken in all three table axes for both un-weighted and weighted conditions in order to characterize the shaker acceleration profile. Finally, flow visualization was performed using both still photography and real time/slow motion video. Monochrome images of the bubbles and air-water interface were taken using a backlighting configuration which was found to produce the best images for processing in ImageJ. The photographs were processed in ImageJ using a reduction process and analysis routine in order to determine bubble areas, numbers, and interface height for void fraction calculations. Video was used to capture qualitative information of the flow phenomena at varying vibration frequencies and amplitudes. A summary of tests performed during the course of this work are presented in Tables 4.1 and 4.2 with the results and discussion following in Chapter 5.

Table 4.1: Test Matrix

Test	Description	Inputs	Output	Required Measurements	Optional Measurements
0-1	Qualitative Analysis of Bubble Motion based on frequency and amplitude	f, A, p_e = 1 atm, H2O	Bubble Motion	video/photo, freq., A, accel.	ΔP, T
1	Verification of previous results: critical frequency	f, A, p_e = 1 atm, H2O	critical frequency, location of stationary bubble(s)	video/photo, f, A, accel.	ΔP, T
2	Static Column Testing	f, A,p_e = 1 atm, H2O, gas flow rate	ε, k_La, d_{32}	video/photo, gas flow rate	ΔP, T
3	Verification of previous results: ε and K_La	f, A,p_e = 1 atm, H2O, gas flow rate	ε, k_La, d_{32}	video/photo, gas flow rate, DO, f, A	ΔP, T
4	Response to vibration: variable frequency	constant gas flow rate, p_e = 1 atm, H2O	ε, k_La, d_{32}	video/photo, gas flow rate, DO, f, A	ΔP, T
5	Response to vibration: variable amplitude	constant gas flow rate, P0 = atm, H2O	ε, k_La, d_{32}	video/photo, gas flow rate, DO, f, A	ΔP, T

Table 4.2: Test Conditions

Test	Parameters	Range						
1	f	0.0	0.0	0.0	0.0	0.0	0.0	
	A	2.5	2.5	2.5	2.5	2.5	2.5	
	p_e	0.3	0.3	0.5	0.6	0.8	1.0	
2	f	0.0	0.0	0.0	0.0	0.0		
	A	-	-	-	-	-		
	U_{SG}	1.0	2.5	5.0	7.5	10.0		
	p_e	1.0	1.0	1.0	1.0	1.0		
3	f	10.0	15.0	17.5	20.0	22.5		
	A	1.5	1.5	1.5	1.5	1.5		
	U_{SG}	2.5	2.5	2.5	2.5	2.5		
	U_{SG}	5.0	5.0	5.0	5.0	5.0		
	p_e	1.0	1.0	1.0	1.0	1.0		
4	f	10.0	12.5	12.5	15.0	17.5	20.0	22.5
	A	2.5	2.5	2.5	2.5	2.5	2.5	2.5
	U_{SG}	5.0	5.0	5.0	5.0	5.0	5.0	5.0
	p_e	1.0	1.0	1.0	1.0	1.0	1.0	1.0
5	f	7.50	10.00	12.50	15.00	17.50	20.00	22.50
	A	1.50	1.50	1.50	1.50	1.50	1.50	1.50
	A	2.50	2.50	2.50	2.50	2.50	2.50	2.50
	A	4.50	4.50	4.50	4.50	4.50	4.50	4.50
	A	6.50	6.50	6.50	6.50	6.50	6.50	6.50
	A	9.50	9.50	9.50	9.50	9.50	9.50	9.50
	U_{SG}	5.00	5.00	5.00	5.00	5.00	5.00	5.00
	p_e	1.00	1.00	1.00	1.00	1.00	1.00	1.00

CHAPTER V

RESULTS AND DISCUSSION

5.1. Validation of the Test Set Up

Data was collected for static conditions to determine the accuracy of the measurement system and validate the data collection routine. Results of void fraction, mass transfer and to some extent bubble size for static conditions ensures that the instrumentation and the column functions as a system before vibration is applied to it by the shaker. The shaker was measured using an accelerometer to measure the machine response in comparison to the inputs. The vibration frequency and amplitude combine to give the total acceleration input into the system which can be measured by the accelerometer. Differential pressure measurements are used to confirm the response wave form. Mass transfer, void fraction, and bubble size distributions are recorded for a range of frequencies and amplitude that closely model the research of Waghmare (2008) which provides void fraction and mass transfer data. In this regard, there is no need to extrapolate from graphical data presented by other researchers which could be subject to interpretation error. The data provided by Waghmare (2008) is the only data known to be available for comparison with this research.

5.1.1. Shaker Vibration Frequency and Amplitude

Measurement of vibration frequency is critical to describing the input to the test system. Fortunately, the frequency is determined and controlled by the motor speed controller. The motor speed controller has an LED display which gives the frequency of the motor (Hz) with a resolution of 0.1 Hz. The speed controller is also very stable and actively monitors and controls

the frequency of the motor by controlling the input power carrier frequency. Because of the stability of the speed controller, the motor speed and therefore the shaker frequency is nearly constant and requires no additional monitoring or measurement. However, it has been observed that the frequency will modulate during operation at very low frequencies (f < 5 Hz) or during operation of the shaker at large power requirements (high frequency, high amplitude). In both cases the frequency was seen to vary by a maximum of +/- 0.2 Hz. For very low frequency vibration this difference can account for up to 10% variation, but the shaker was not designed to be operated at frequencies less than 5 Hz. For very high power requirements the frequency variations account for 0.4% variation which contributes to an overall error of 3.3% in the expected acceleration input (g's).

An accelerometer was mounted in three locations along the table to measure accelerations in all three table axes. The results show that the actual measured acceleration in the z-axis have profiles that match well with a sinusoidal wave (Figure 5.1) The accelerometer measurements in the x and y axis showed relatively low noise in comparison to the z axis with the y axis noise being the highest in magnitude and most coherent in comparison to the x axis noise (Figure 5.2).

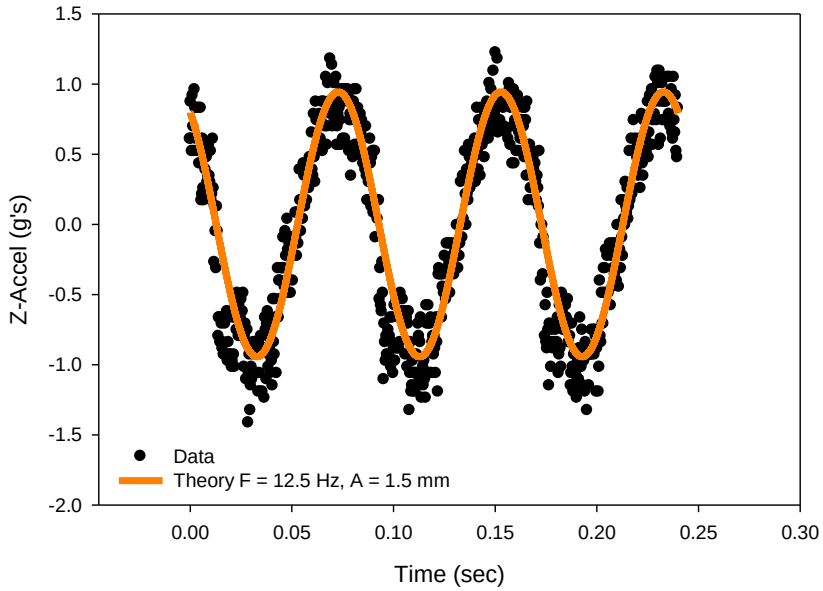

Figure 5.1: Comparison of measured z-axis acceleration vs. sine wave for f = 12.5 Hz, A = 1.5 mm.

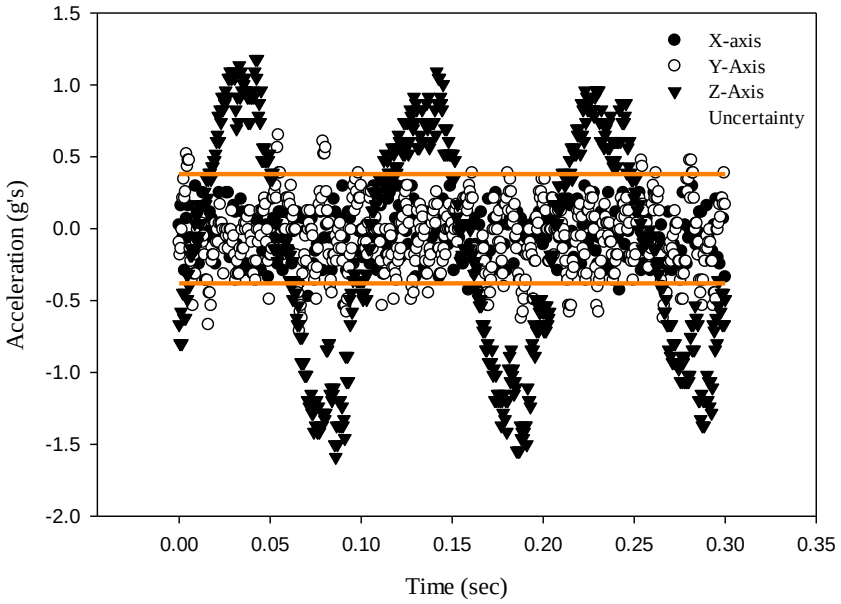

Figure 5.2: X-Y-Z Acceleration profiles for *f*=10 Hz, *A* = 2.5 mm

Several vibration test points were analyzed for frequency spectra using a fast Fourier transform. The resolution of the frequency spectrum is limited by the sample rate, but the results show that the noise ratio decreases at higher amplitude (Figure 5.3) but not necessarily higher frequency (Figure 5.4). It is interesting to note that the highest peak always occurs at 40 Hz for the y axis spectra. This may indicate that the y axis noise carries some resonance phenomena associated with the mechanical structure.

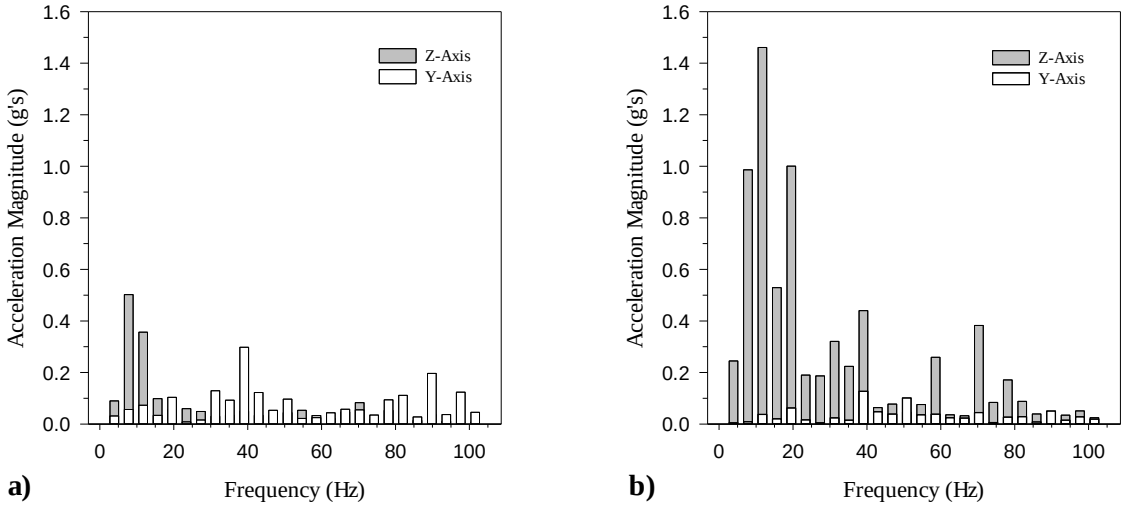

Figure 5.3: Frequency spectrum for a) *f* = 10 Hz, *A* = 1.5 mm and b) *f* = 10 Hz, *A* = 4.5 mm

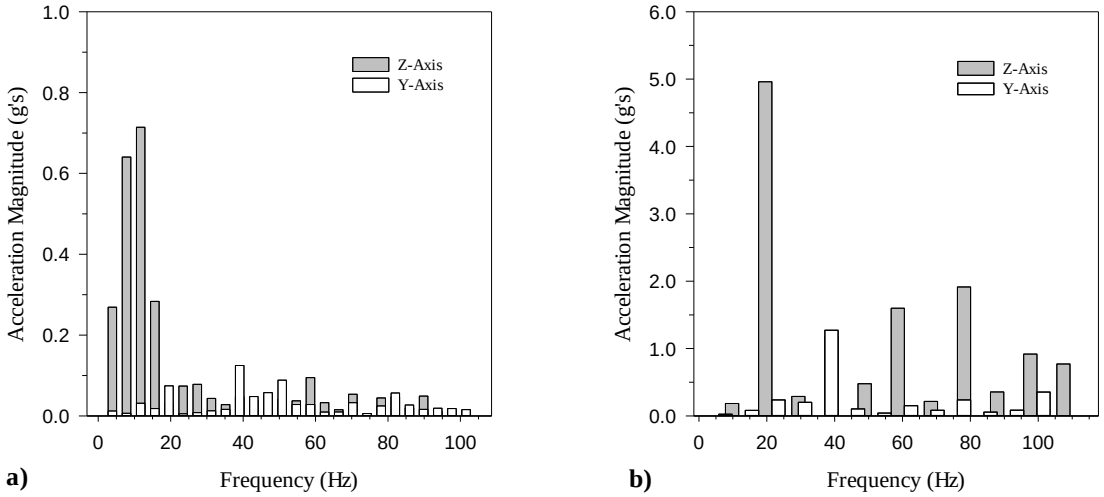

Figure 5.4: Frequency spectrum for a) f = 10 Hz, A = 2.5 mm and b) f = 20 Hz, A = 2.5 mm

The noise at the peak of the sine wave as noise is typical for rotary machines of this type. Unless the armature length of the slider crank is much larger than the radius of the rotary arm there appears to be resonance or "fuzz" at the top and bottom of the stroke (Lowery, 2012). There is also evidence of some sharp peaks that occur near the top and bottom of the stroke which may be caused by mechanical tolerance stack-up for accelerations greater than 1 g. For instance the small clearance between the eccentric adjustment bolts and the bolt holes in the cylinder can cause a very slight rocking motion which when rotating at high speeds could produce the overshoot.

It was noticed during a bolt change that the bolt threads themselves had been crushed in the area where they contacted the holes during operation. The additional space made by the thread material loss could cause an increased rocking effect. When the new bolts were installed a silicon RTV gasket sealer was pressed into the gaps between the bolts and cylinder holes to try and mitigate this effect or dampen the rocking. The new bolts and silicon smoothed the operation considerably and it is relatively simple to change the bolts if needed. The measured response of the shaker is not ideal, but the noise appears to be typical and of the machine type. It should also be mentioned that the actual vibration input has never been reported in the literature, and it is

likely that while the piston pulsing systems may show a "cleaner" response if measured they are likely to exhibit noise as well, simply due to mechanical relaxation (strain) or modal excitation of the materials. It is also be important to realize that the environment in the column does not necessarily "see" the noise due simply to viscous damping of the fluid. As evidence, the differential pressure of the system was measured concurrently with acceleration over time for an acceleration profile (~1g) showing a smooth pressure profile. Since the column was open to the atmosphere, differential pressure measures the hydrostatic pressure at H = 7.6 cm. Figure 5.5 indicates that the fluid pressure pulses being recorded are not necessarily dependent on any of the transient accelerations or noise imparted by the shaker itself.

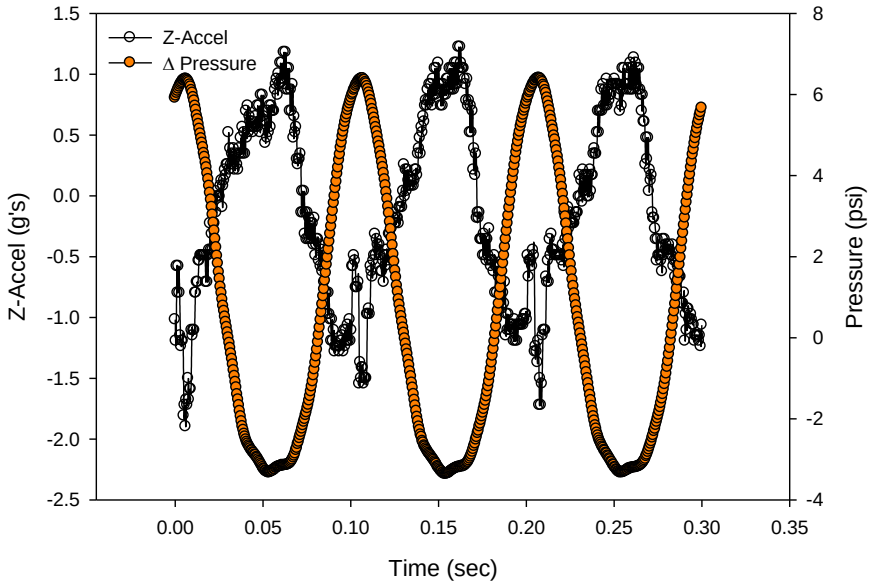

Figure 5.5: Differential pressure and acceleration measurement of column at *f* = 10 Hz and *A* = 2.5 mm

However, there are cases at large amplitude and/or large frequency combinations when the differential pressure has been seen to exhibit some resonance as well.

5.1.2. Flow Visualization

Flow visualization was used throughout the experiments to provide visual documentation of the phenomena occurring in the column. The photographs were processed to provide some physical data such as void fraction and bubble size distribution. However, in validating the set up the concern was to try and repeat the reported observations by previous researchers. Most notably the observations made by Buchanan et al. (1962) provides a reference for the "stabilization frequency". It was observed in this research that stabilization of the bubbles is not a steady phenomenon, nor is it easy to capture. An attempt was made to use the model Buchanan et al. provides for stabilization frequency to produce stable bubbles given the inputs of head pressure, column liquid height, frequency, and amplitude. It was observed that the model is fairly accurate in describing locations were bubbles are seen to exhibit less upward or downward movement, but that pseudo-stability would be a more accurate term. The model was actually used to determine stability locations at pressures ranging from 0.3 – 1 atm. Vacuum pressures of 0.3-1.0 atm were applied and a corresponding stabilization frequency was calculated using Eq 2.27 for A = 2.5 mm and the liquid height above the stabilization point of interest, h = 45 cm. The model predicts stability based upon the total liquid height above the point of stability. Therefore, with a total liquid height, H = 65 cm and liquid head above the point of stability, h = 45 cm, was expected to be the 25 cm column mark. Video and still photography was focused on this point, but included the range of 20 – 30 cm column marks. Using this procedure, the expected stabilization frequency was set and run and video and photographs taken to document the stability at the point of interest. The observed results showed agreement with the model at atmospheric pressure confirming the test set up captures the phenomena associated with previous research. Additionally, these points of stability studies showed that not only did bubble motion slow down or oscillate around zero as expected, but secondary Bjerknes forces were also observed, especially at these stability points in the form of mutual attraction or aggregation of

separate bubbles into clusters. It was also common to see the clusters attach to the walls of the column, and in some cases the cluster would remain stable long enough to gather quite a mass before being overcome by buoyancy (Figure 5.6).

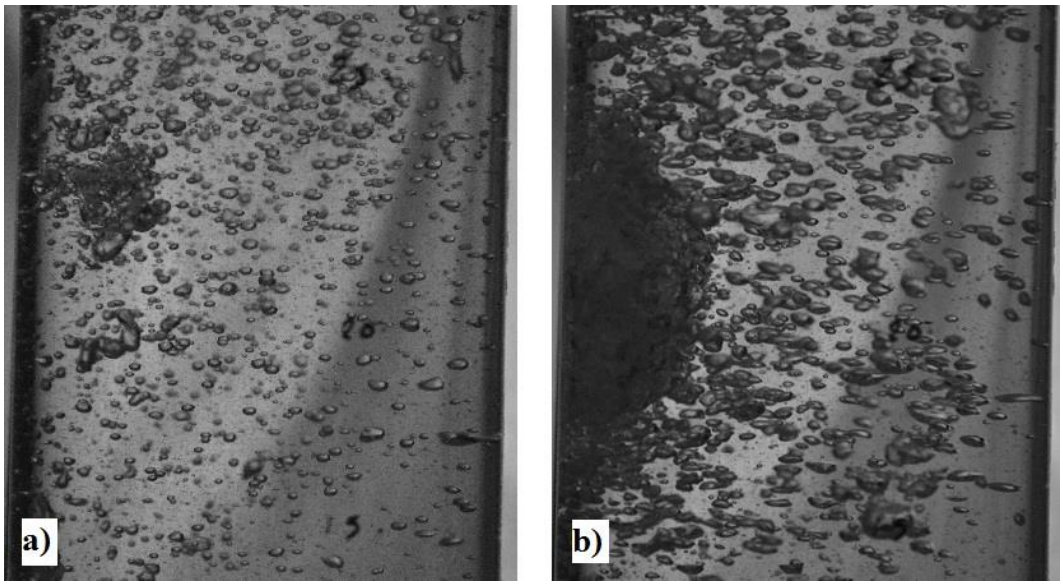

Figure 5.6: Photograph of a) bubble aggregation and b) large cluster attached to wall around the stability location of 20 cm for f = 23 Hz, A = 2.5 mm, p_e = 0.33 atm

In the research of Ellenberger et al. (2005) it was noted that void fraction increased at specific points along the column. Observations during this research agree with the findings of Ellenberger et al. (2005). Video and photographs captured areas of increased voidage apparent as dense bubble clouds and areas of relatively low bubble density along the column height (Figure 5.7).

As with Buchanan et al. (1962), Ellenberger et al.'s research implies that these locations of higher void fraction are stable and specific to a column height according to the vibration inputs. However, it was observed in this research that these areas of higher bubble density, which often appeared as bands of froth, would migrate up and down the column (Figure 5.8). Generally, the froth bands would form from bubbles accumulated at the bottom of the column and then

migrate up towards the interface. Occasionally the bands were seen to move slower, stop, or even reverse momentarily before reaching the interface where they would "pop" at the surface.

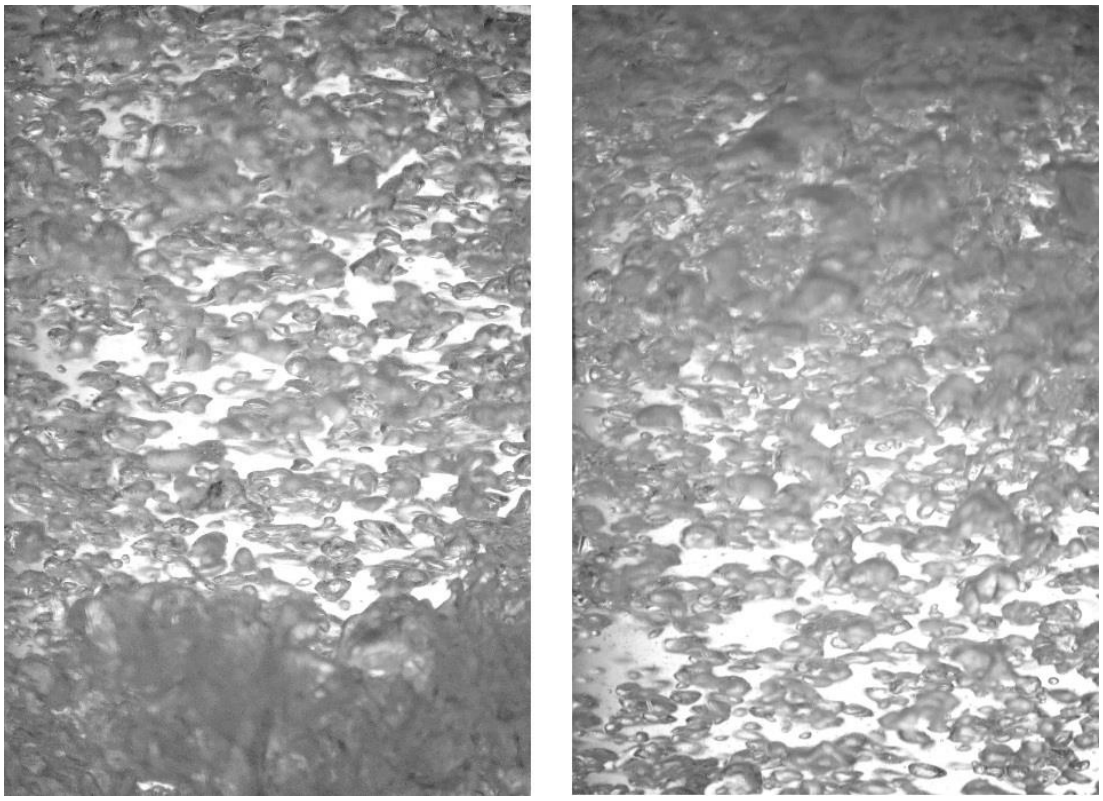

Figure 5.7: Photographs of high bubble density (high voidage) adjacent to a relatively clear zone for f = 19 Hz, A = 2.5 mm at H = 60 cm and p_e = 1 atm

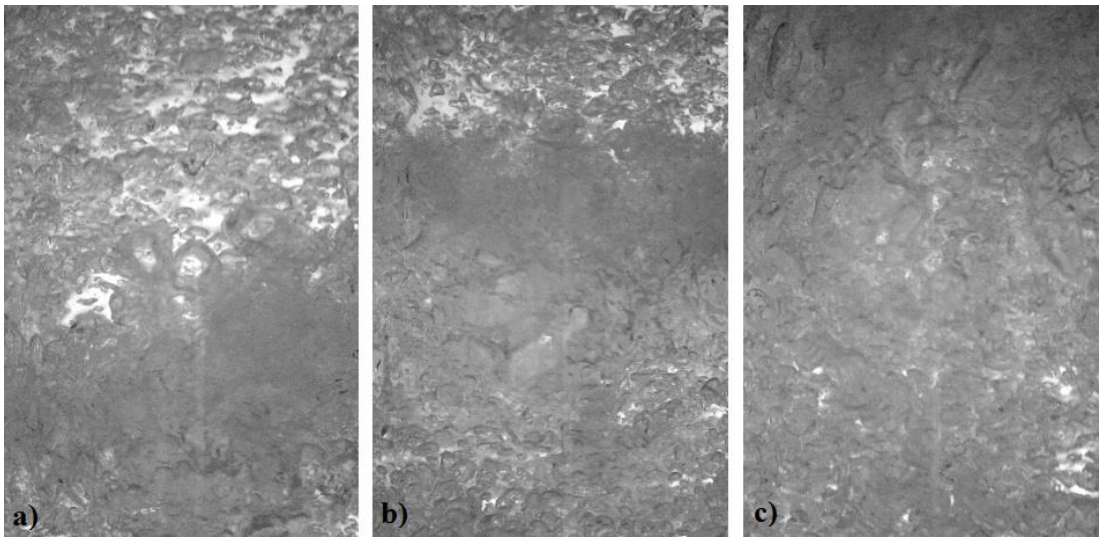

Figure 5.8: Succession of photographs showing a) frame 1 location of frothy band at column height, $H \approx$ 55 cm, b) frame 2 of the same frothy band at different column height, $H \approx$ 60 cm, and c) frame 3 of the same band at column height, $H \approx$ 65 cm (Frames are approximately 2 sec apart)

The froth bands would form and move to the surface in cycles but generally would only be one band in the column, per cycle. Each cycle of formation, movement, and surfacing was associated with a distinct change in the shaker, noticeable by a difference in the sound of the machine. Differential pressure and acceleration measurements were taken during the course of this cycling event and show that a distinct pressure rise and sharp acceleration occur during the formation of each band. For instance, Figure 5.9 shows the pressure and acceleration rise at the initiation of the froth band at $t \approx 26$ seconds while Figure 5.10 shows the repeating occurrence at t $\approx$ 18, 30, 35, 45, and 55 seconds.

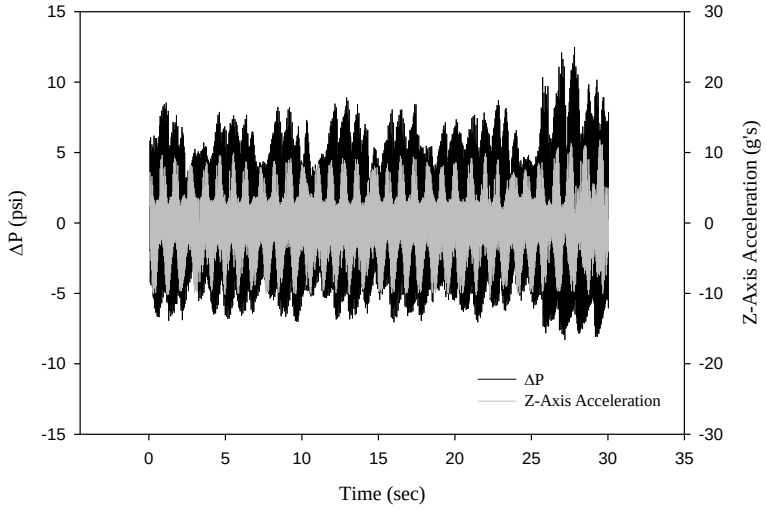

Figure 5.9: Acceleration and differential pressure profiles at the beginning of a froth band cycle event for f = 22.5 Hz, A = 2.5 mm, U_{SG} = 5.0 mm/s

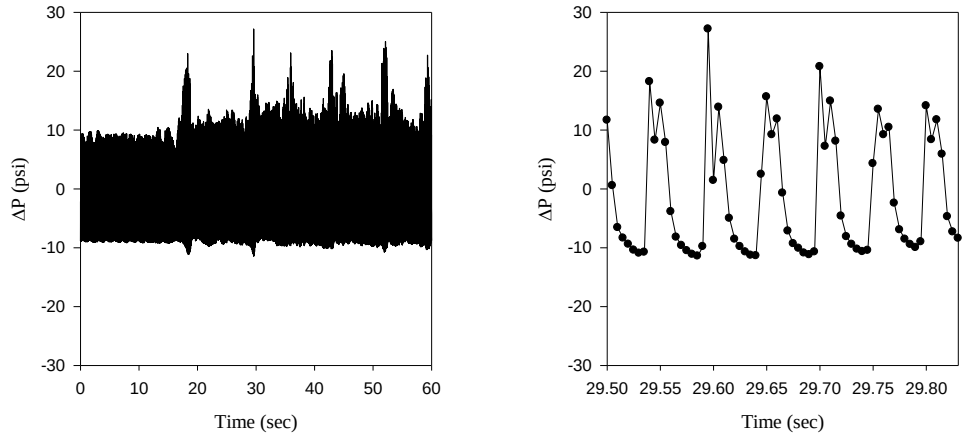

Figure 5.10: Differential pressure time history for a) several cycles of formation and b) zoomed-view of individual pressure spikes for f = 20 Hz, A = 4.5 mm and U_{SG} = 5.0 mm/s

The froth band appeared to be a collection of much larger bubbles or even a major slug that, when formed, caused a momentary cushion at the bottom of the liquid column. This cushion causes the bulk liquid to disconnect from the bottom of the column creating a large liquid plug which has a hammering effect on the froth band and displaces it to begin its motion. The general motion of the froth bands seems to align with the description of the cyclic process in Buchanan et al. (1962), but could also increase local void fraction at specific heights in the column, similar to the results of Ellenberger et al. (2005).

Both observations of bubble stability and high voidage zones at specific liquid heights help to validate the test set-up, and the ability to use the set-up to qualitatively capture the phenomena observed in previous research.

5.1.3. Mass Transfer

A series of mass transfer points were taken for vibration frequencies of 0, 10, 12.5, 15, 17.5, 20 and 22.5 Hz and amplitudes of 1.5 and 2.5 mm which closely follows the conditions tested by Waghmare (2008). The results of the mass transfer data collected using this test platform were compared to Waghmare's (2008) data with good results.

Mass transfer coefficients were first determined for a zero vibration condition at superficial gas velocities of 1.0, 2.5, 5.0, 7.5, and 10.0 mm/s with a liquid height of 85 cm in the 4 in. diameter column. Comparison of the data with Waghmare's results for similar conditions shows good agreement (Figure 5.11). Waghmare's data consists of two points for each no vibe condition so both points were averaged to give a representative value with error bars representing the uncertainty between them. The data shows a strongly linear trend ($R^2 = 0.999$) as expected. However, there is a slight shift in slope that appears to be either a property of the bubble size, or the method of calculating U_{SG}.

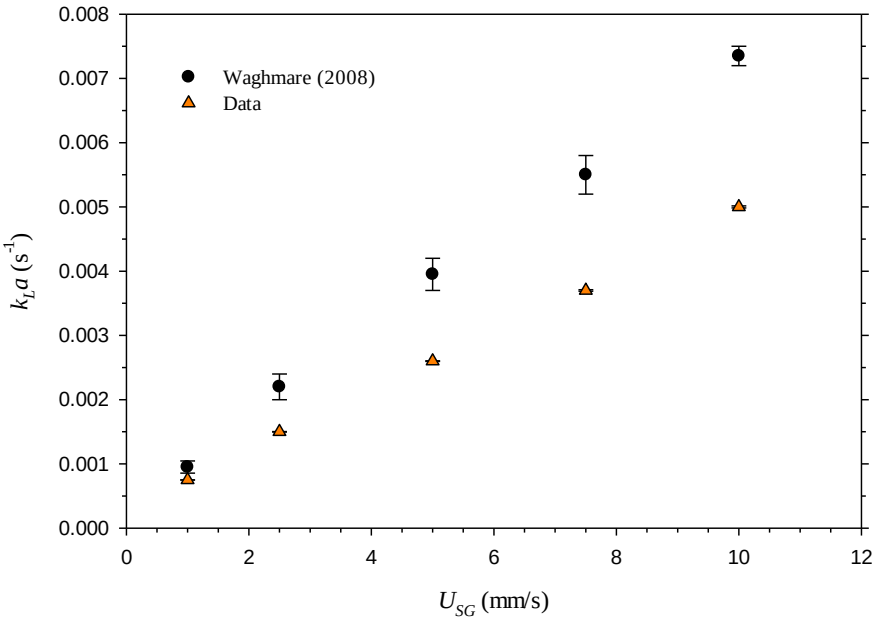

Figure 5.11: Comparison of k_La vs U_{SG} with Waghmare (2008) for no vibe condition

Both bubble diameter and superficial gas velocity effects were investigated to determine what could be the root cause of the difference in slope. It is evident from previous research, including Waghmare (2008), that U_{SG} was derived by the measured gas flow rate, Q (cm^3/s) using a volumetric gas flow meter divided by the column cross section area based upon the nominal tube inner diameter (Eq 2.6). The method used to determine superficial gas flow in this set up was derived from gas mass flow rates and the gas density by the following:

$$U_{SG} = \frac{\dot{m}_G}{\rho_G A_{cs}} \tag{5.1}$$

Where ρ_G is determined using the ideal gas law and average gas temperature and pressure. The average gas temperature is taken as the average of the measured gas temperature and fluid temperature (ambient). The average column pressure is taken as the static pressure at the mid point of the fluid height. The primary difference between the methods is the determination of and division by the gas density. However, a significant difference in density could easily lead to a U_{SG} value different than Waghmare. As an example, altering the density to 2.0 (kg/m^3) modifies

the superficial gas velocity based upon the raw mass flow measurement, and the data is recast to suit the comparison with excellent results (Figure 5.12).

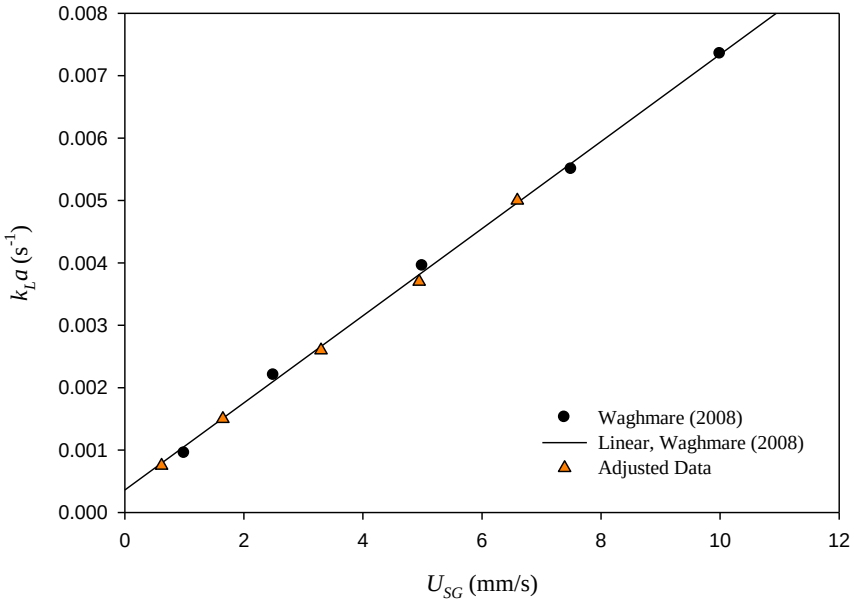

Figure 5.12: Comparison of k_La vs. modified U_{SG} data with Waghmare (2008) for static conditions

Another possible explanation for the data shift compared to Waghmare (2008) may be due to larger average bubble size. The inner diameter of the injector tip used in this study is roughly twice that used in Waghmare (2008). This would cause the average size of the bubbles to be smaller in Waghmare's experiment, with greater surface area per volume, and therefore could account for the increased k_La at the respective superficial gas velocities. If this is the reason for the difference then a comparison of the equivalent bubble size would indicate the shift, but a better marker would be the mass transfer coefficients at equivalent vibration conditions. Vibration has been noted in the literature to homogenize the bubble size, one could expect bubble sizes to be fairly uniform and roughly equivalent at similar vibration conditions. Equivalent kLa values at similar vibration conditions would either confirm or reject the bubble diameter as a leading cause of the data shift for the no vibe condition. It is seen in Figure 5.13 that the mass transfer coefficients match well with Waghmare (2008), especially at f = 10 Hz and f = 17.5 Hz when U_{SG} = 2.5 mm/s and f = 10 Hz and f = 15 Hz when U_{SG} = 5.0 mm/s. This would indicate that the data shift for no vibe condition is more likely caused by the initial bubble sizes due to the larger injector rather than the difference in U_{SG} measurement.

Mass transfer measurements were also taken for vibration cases at conditions similar to Waghmare (2008). The results show that while the associated peaks are appropriate the values for k_La are slightly different (Figures 5.13 and 5.14). A uniform error of 10% is given to Waghmare's data, since no measurement uncertainty was given, in order to illustrate any variations. One can see that the trends between both data sets match well, but the magnitude is off, especially for frequencies above 15 Hz when Waghmare's data becomes larger.

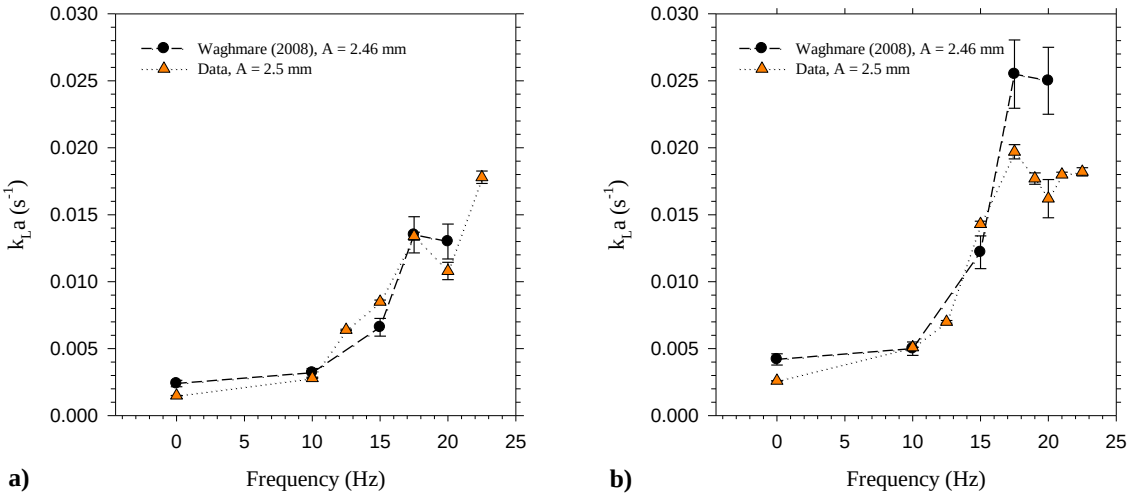

Figure 5.13: Comparison of mass transfer coefficient vs. frequency with Waghmare (2008) for similar vibration conditions at a) U_{SG} = 2.5 mm/s and b) U_{SG} = 5.0 mm/s

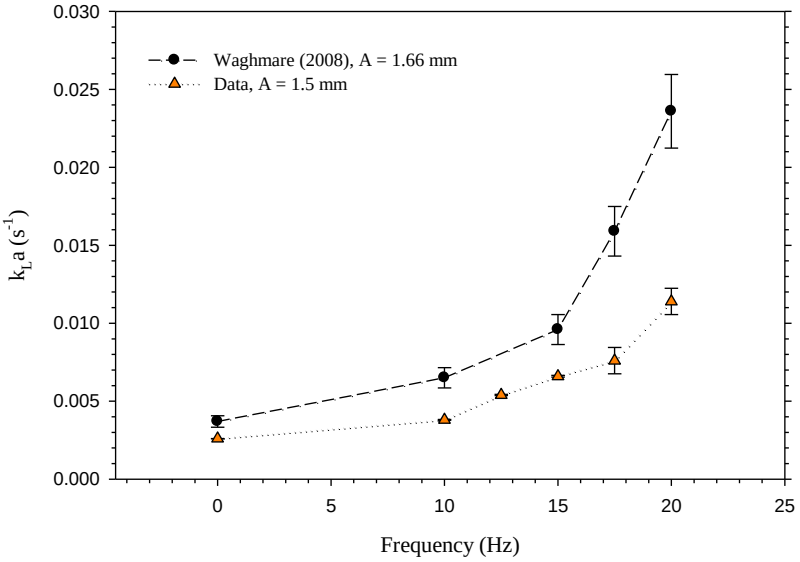

Figure 5.14: Comparison of mass transfer coefficient (k_La) vs. frequency with Waghmare (2008) for similar vibration conditions and superficial gas velocity

The similarity of trends in the mass transfer data during vibration implies that the physical phenomena are being captured by the set up. However, the difference in mass transfer coefficient magnitude is not surprising considering the disparity between reported outcomes from other research. The difference between the data magnitudes is likely due to the set up itself, either through the difference in injector size, the column diameter, method of shaking (whole cylinder vs. piston pulsing), or DO probe itself. Interestingly, a comparison of mass transfer improvement shows that this research produces more improvement, but still carries the same trend (Figure 5.15).

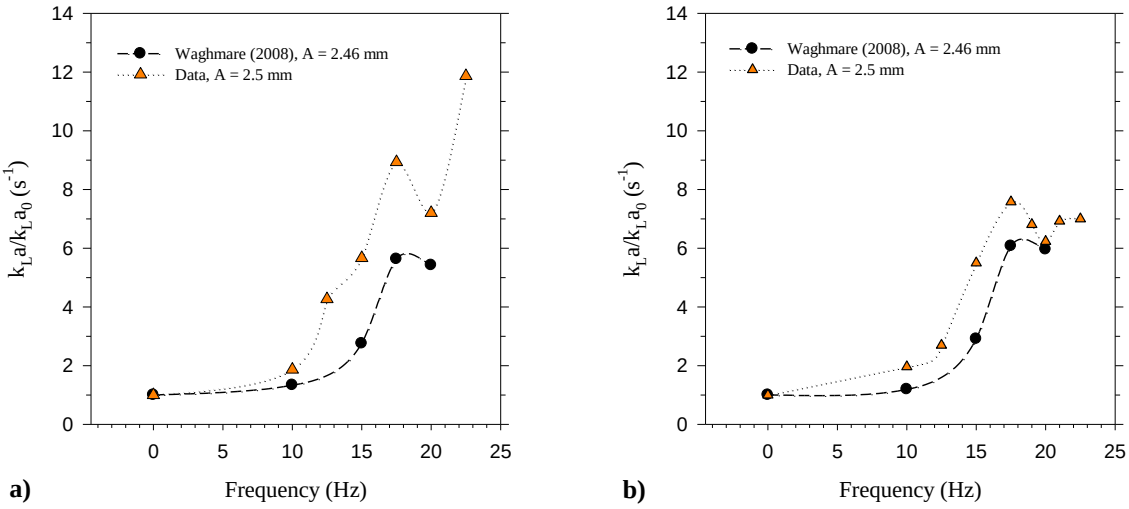

Figure 5.15: Comparison of mass transfer improvement (k_La/k_La_0) vs. frequency with Waghmare (2008) for similar vibration conditions at a) U_{SG} = 2.5 mm/s and b) U_{SG} = 5.0 mm/s

5.1.4. Void Fraction and Bubble Size

Void fraction and bubble size measurements were also taken at similar conditions to Waghmare (2008) for comparison. Data was taken for void fraction and bubble size for frequencies of 0 – 22.5 Hz, amplitudes of 1.5 and 2.5 mm and superficial gas velocities of 1.0 – 10.0 mm/s. The results show similar agreement to that found for mass transfer.

Void fraction measurements were first taken at a no vibration condition to establish a baseline and verify the set up. However, the method used to measure void fraction in this research differed from that of Waghmare (2008), but the results are comparable within the range of uncertainty (Figure 5.16). The uncertainty in void fraction is more severe at the lower superficial gas velocities because of the low void fraction values. As before, Waghmare offers two data points which are averaged to give the values shown in Figure 5.16 with the error bars representing the difference between the measured values and the average. Since Waghmare did not report uncertainty this is an attempt to show some representative estimate although it is probably underestimated as an uncertainty.

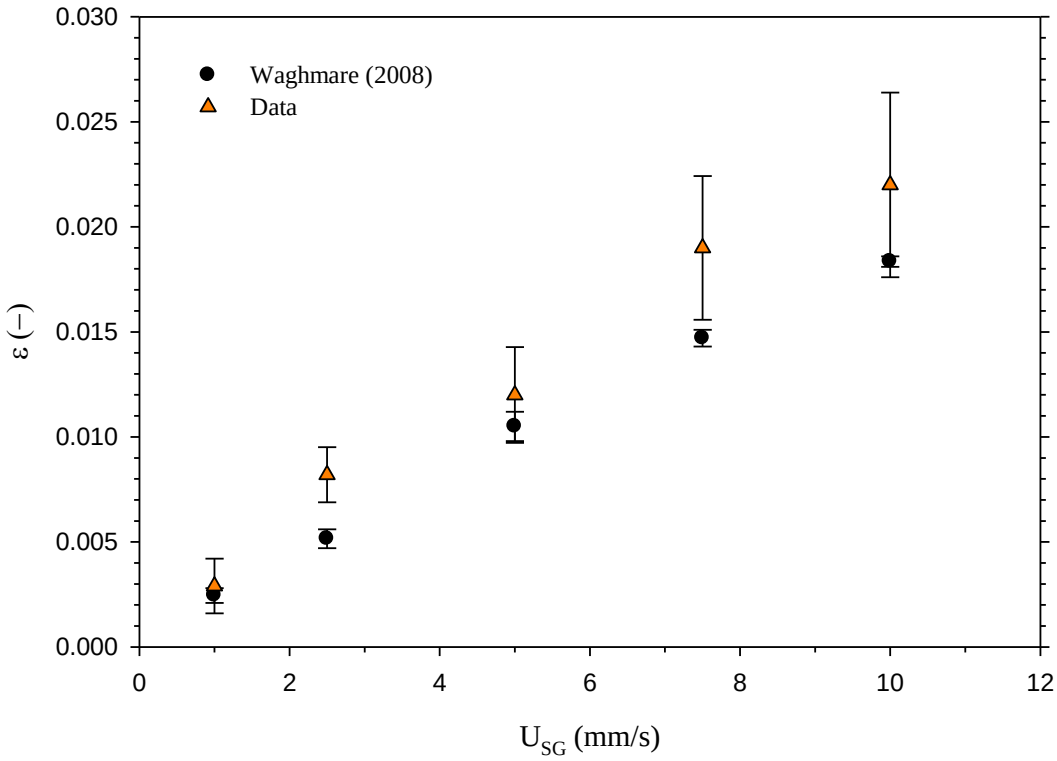

Figure 5.16: Comparison of void fraction vs. superficial gas velocity with Waghmare (2008) for static conditions

In the case of void fraction the resulting trend is similar to Waghmare (2008) and fairly linear (R^2 = 0.98) as expected from theory. Applying a trendline to both equations shows some (17%) difference in slope, but a much larger intercept indicative of a systematic error. The source

of the error is probably caused by the measurement technique which suffers more from human bias than Waghmare's manometric method. However, the results show that within the uncertainty of the measurements most of the data agrees well.

Void fraction data was also collected for frequencies range of 0-22.5 Hz and amplitudes of 1.5 and 2.5 mm each with superficial gas velocities of 2.5 mm/s and 5.0 mm/s. The results show a comparison with mass transfer data in that the trends are similar, but the magnitudes are not. There is considerable agreement for values below f = 15 Hz. For values above 15 Hz the increases in void fraction far surpass Waghmare. In fact the increase in void fraction at U_{SG} = 2.5 mm/s is even greater than the improvement at U_{SG} = 5.0 mm/s (Figure 5.17), probably due to the coupling of associated error at low void fraction.

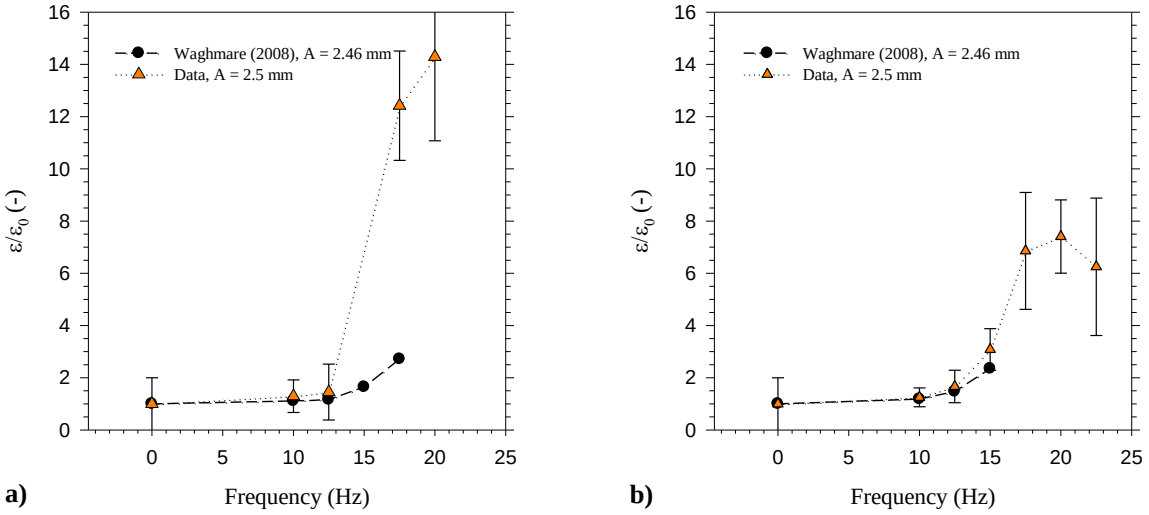

Figure 5.17: Comparison of void fraction improvement ($\varepsilon/\varepsilon_0$) vs. frequency with Waghmare (2008) for a) U_{SG} = 2.5 mm/s and b) U_{SG} = 5.0 mm/s

The large increase in void fraction at higher frequency may be due to the method used to determine ε which relies on photographic measurements of the interface height. The interface at such frequencies becomes highly unstable and it is difficult to reference a single point on the interface which is representative of the interface height (Figure 5.18). Because of the difficulty in determining what constitutes a representative interface a float was used (see §4.2.5 and Fig. 4.18).

However, even with the float there were occasions when the surface was not represented well by the float, and even instances when the float was submerged by the chaotic interface (Figure 5.19).

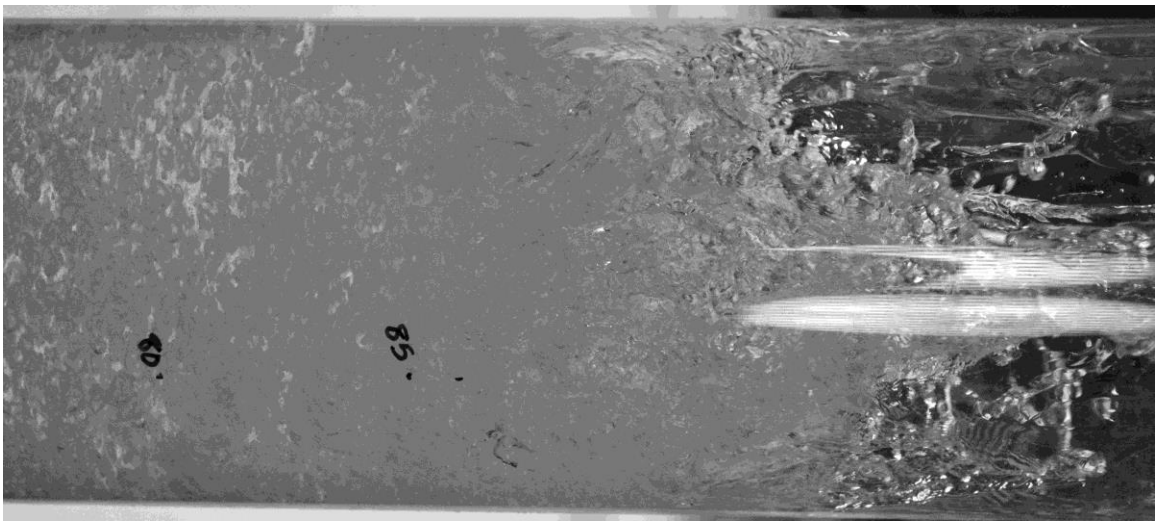

Figure 5.18: Column air-water interface at f = 17.5 Hz, A = 2.5 mm, U_{SG} = 2.5 mm/s

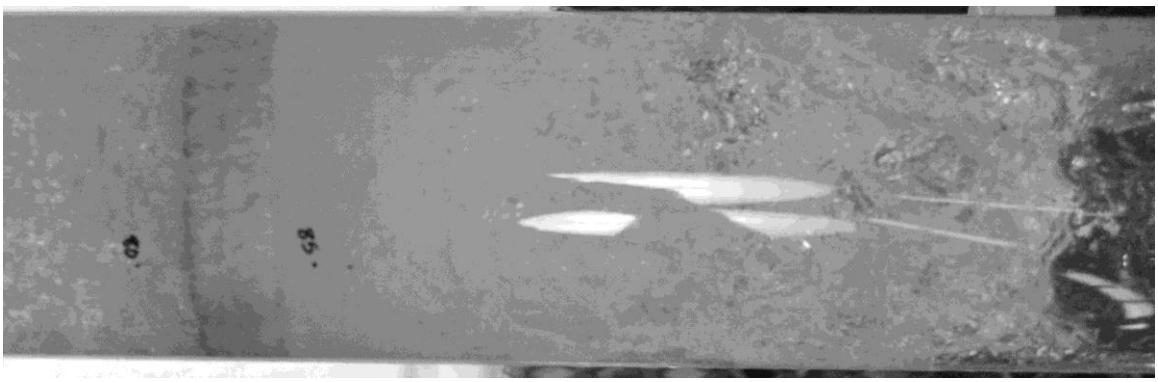

Figure 5.19: Submerged float during test at f = 15 Hz, A = 6.5 mm, U_{SG} = 5.0 mm/s

Bubble size distributions were collected from photographs taken at three separate column heights of H = 30 cm, H = 45 cm, and H = 60 cm. The size distributions were collected for all vibration conditions including no vibe condition. The Sauter mean diameter, d_{32}, produced by the distributions shows a decreasing trend for most vibration cases which agrees with the results found by Waghmare (2008) (Figure 5.20). However, at f = 15 Hz, d_{32} actually increases from H = 30 cm to H = 45 cm and decreases again at H = 60 cm.

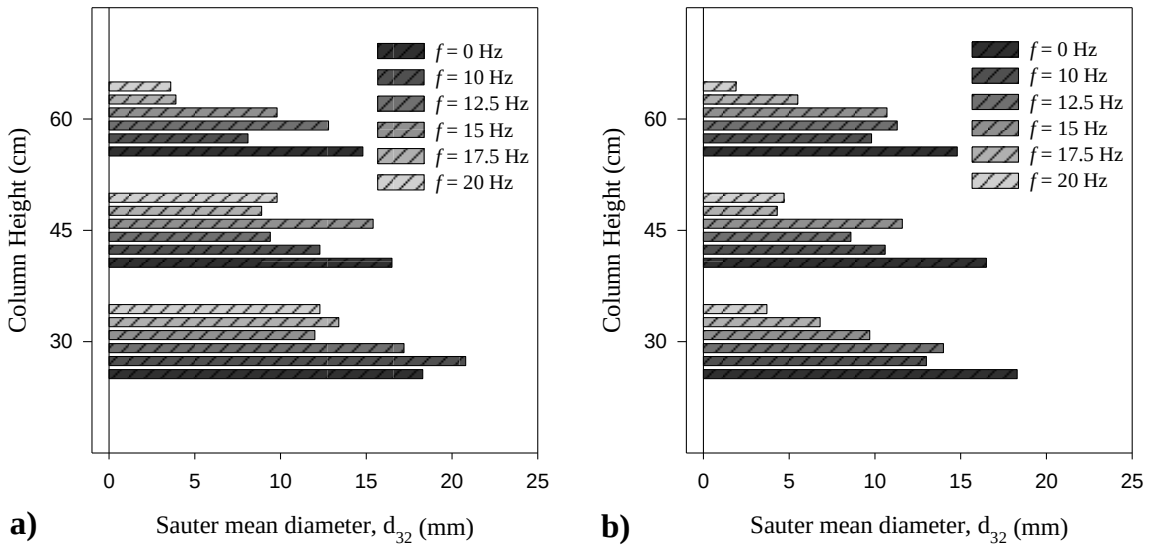

Figure 5.20: Bubble size (d_{32}) vs. column height for varying frequencies at a) A = 1.5 mm and b) A = 2.5 mm with U_{SG} = 5.0 mm/s

A possibility for the increase in void fraction at H = 45 cm specific to f = 15 Hz may be partially due to the presence of localized voidage increases as discussed in §5.1.2. The method to determine d_{32} relies on a distribution taken from the analysis of several photographs. It is likely that the analysis methodology misrepresents the distribution because of a high occurrence of overlapping bubbles. For example, multiple smaller bubbles appearing close together can be and usually are misrepresented as a large bubble by the analysis routine. This is a systematic bias that has been observed in this research, but has not been readily reported by previous researchers. Additionally, the uncertainty associated with calculating the mean diameter in this case (34%) encompasses the measurement difference. A better measurement technique would be recommended to determine if the size variation along the column length for particular conditions are based on the vibration inputs or is an artifact of the measurement error.

The photographic method has been found to be insufficiently accurate as a tool to describe bubble distributions at locations with tightly packed bubbles. Tightly packed bubbles have been noticed at most of the experimental points where frequency and amplitude exceed 15

Hz and 2.5 mm respectively. For the purpose of this research the method will be used to describe bubble distributions in comparison with previous research.

5.2. Effect of Vibration Amplitude

Additional experiments were conducted using the test set-up to measure the influence of amplitude on k_La, ε, and d_{32}. Amplitudes of 4.5, 6.5, 9.5 mm were tested over a frequency range of 7.5 – 17.5 Hz in addition to the data collected for comparison in §5.1.

5.2.1. Mass Transfer

The results of the mass transfer experiments show the same modal similarities as observed at lower amplitude. The values reached for k_La were also higher than those for lower amplitudes (Figure 5.21), but the increase ratio, k_La/k_La_0 appeared to stall when the non-dimensional amplitude (amplitude / internal injector diameter) $A/d_i > 4$ as seen in Figure 5.22. However, even with the improvement maxima mass transfer coefficients can be found at f = 12.5 Hz and A = 4.5 mm nearly equivalent to that found at f = 22.5 Hz and A = 2.5 mm within 5%. What this represents is a 50% increase in amplitude traded for a 44% reduction in frequency. Considering that power is proportional to $A^2\omega^3$ these changes lead to a total reduction of power by 44% for an equivalent output.

However, increasing amplitude alone to gain higher mass transfer does not always pay off. Upon examining the k_La values at f = 15 Hz for A = 2.5 mm and A = 6.5 mm on would expect a large mass transfer improvement for the power trade, but this point actually leads to a 500% increase in power for a mass transfer improvement of 1.8. This example leads to an important conclusion that agrees with the previous research. Mass transfer reaches optimum values at specific frequency and amplitude combinations, but the power requirements of those combinations must be weighed by the improvement in mass transfer itself.

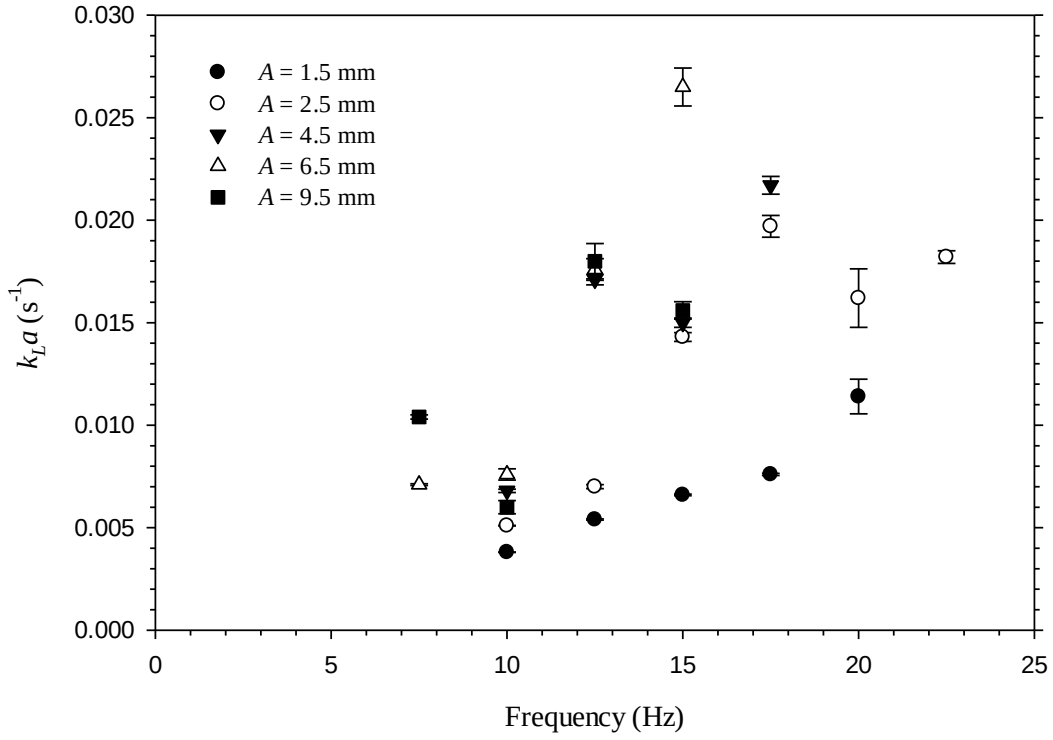

Figure 5.21: $k_L a$ vs. frequency for A = 1.5 – 9.5 mm

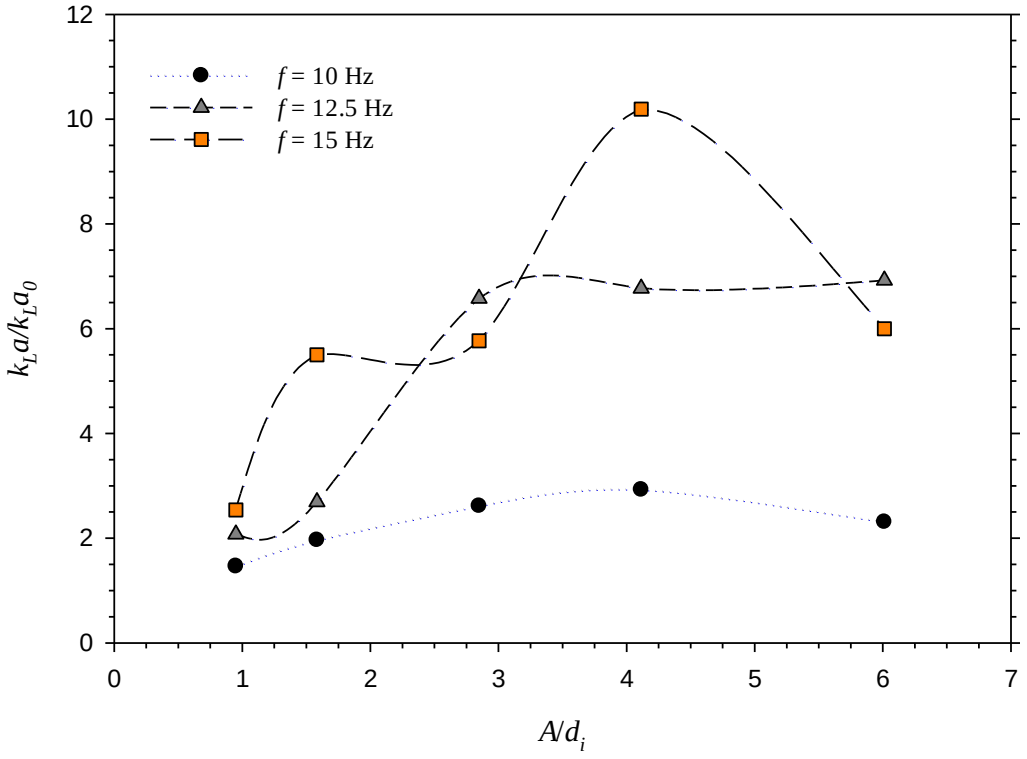

Figure 5.22: Mass transfer improvement with increasing non-dimensional amplitude at f = 10, 12.5, and 15 Hz

Connecting the data points shows a general trend of rotating the mass transfer lines counter clockwise and thereby shifts the frequency optimums to the left (Figure 5.23). It is also observed that there may be an optimum achieved at higher amplitude but at lower frequencies than previously observed, indicated by the trends for A = 6.5, 9.5 mm, and possibly 4.5 mm.

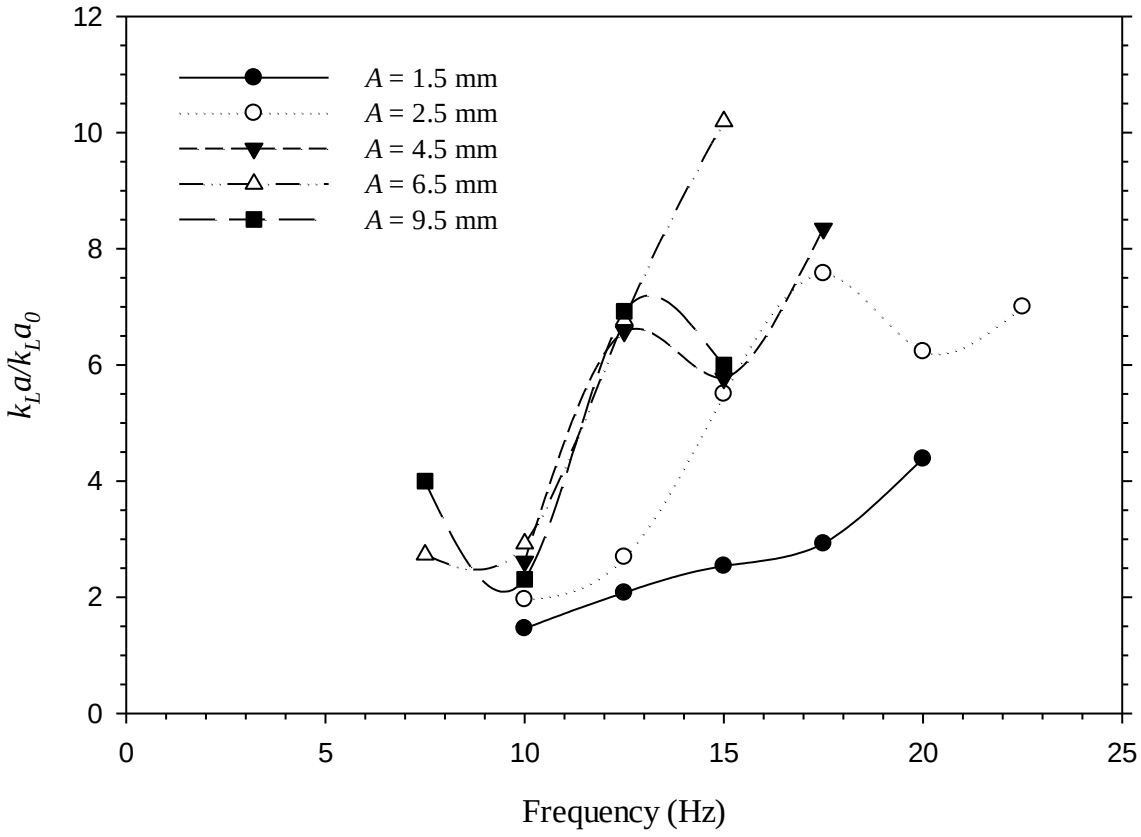

Figure 5.23: Effect of increasing amplitude on mass transfer maxima

It is interesting to develop anecdotal conclusions concerning the relationships between frequency and amplitude, and it is important to take into consideration the error associated with each data point in doing so. Therefore, it is prudent to examine causes of error before proceeding. During the course of the experiments it was noted that the oxygen concentration signals recorded during vibration were subject to noise, especially at the saturated oxygen condition (Figure 5.24).

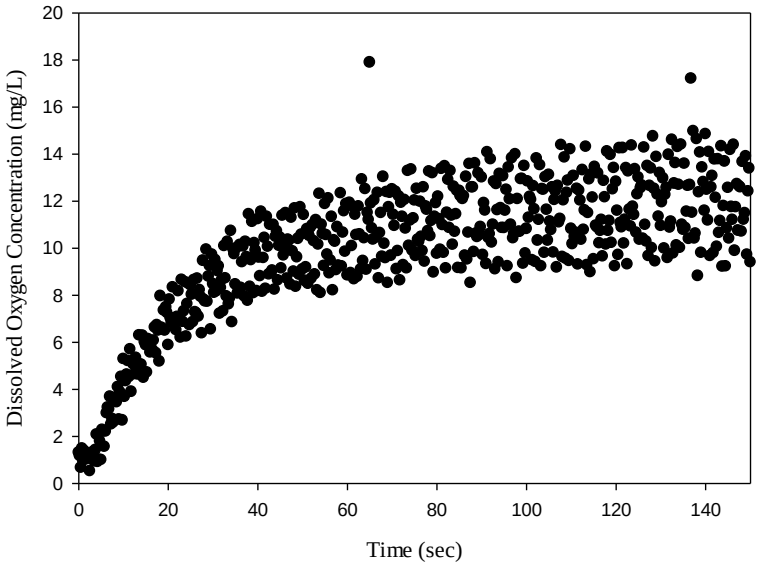

Figure 5.24: Example of dissolved oxygen noise for a signal at f = 17.5 Hz, A = 4.5 mm, U_{SG} = 5.0 mm/s, p_e = 1 atm

The noise was found to be especially large at higher frequency and it is suspected to be caused by the instrument reaction to the vibration condition imposed. The oxygen sensors while designed to be robust were still subject to 10's of g's during some test conditions. Therefore, it was necessary to follow a reduction process to filter the data to establish a mean within the signal. A routine was written in Excel VBA to gather a set number of data points and average them. An equivalent mean value for dissolved oxygen concentration was then output for the specific time interval based on the number of points to be averaged and the sampling rate (Figure 5.25). This effect was the driver for a reduction in sampling rate to 4 samples per second for higher frequency as mentioned in §4.2.3. The filtered signal was then linearly transformed and regressed to derive the k_La value. Similar filtering routines have been utilized in previous research. Unfortunately, there were not enough repeated samples of each condition to evaluate any kind of systematic error. The only error that can be offered is based solely on the regression statistics. A lack of understanding of the error associated with k_La based on these kind of measurements is also apparent in the literature. It would be worthwhile to perform a unique series of repeatability tests for a variety of conditions in order to better quantify the total

uncertainty associated with k_La for a given measurement. These results would be beneficial in drawing more accurate conclusions from these results and the research of others.

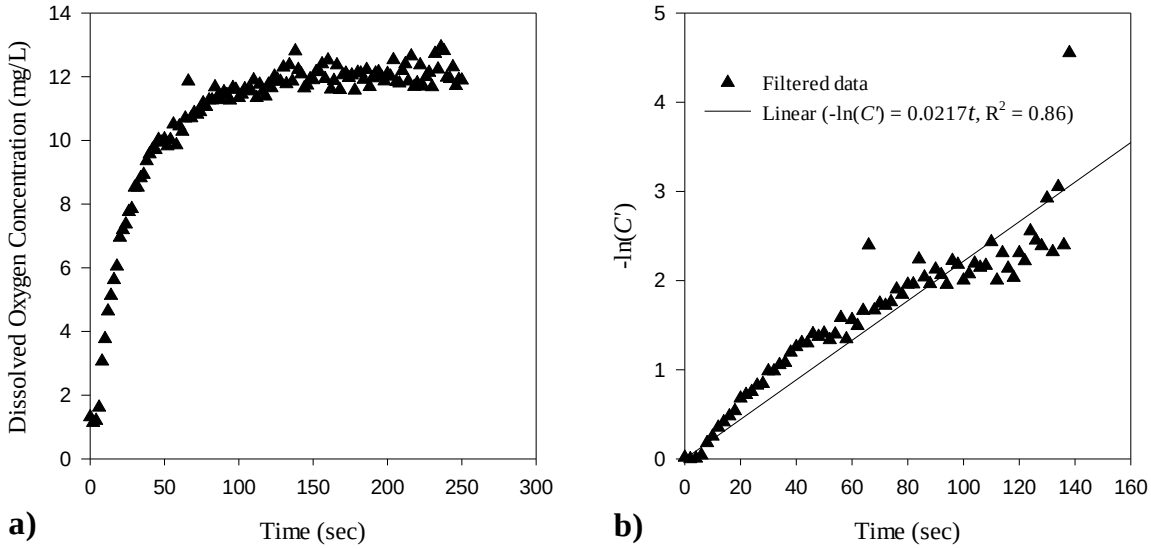

Figure 5.25: a) Filtered dissolved oxygen data and b) transformed and regressed data to derived k_La

It is important to reduce the complex relationship between frequency and amplitude to a unifying parameter in order to make design predictions. Previous research has suggested that mass transfer is proportional to both the specific power and superficial gas velocity. Waghmare (2008) suggests,

$$k_L a \propto P_m^{0.8} U_{SG} \tag{5.2}$$

A study of the data and its relationship to combinations of amplitude and frequency shows which terms have more impact from a modeling perspective. The results show that combinations of $A\omega^2$ and $A^2\omega^3$ are more significant than $A\omega$ alone (Figure 5.26). High amplitude data also conforms well to the relationship between specific power, P_m, which is a function of U_{SG} and the $A^2\omega^3$ product. The association between the results and P_m improves when both data for U_{SG} = 2.5 mm/s and U_{SG} = 5.0 mm/s is used. This confirms that the effect of U_{SG} remains an important factor even for larger specific power inputs. Waghmare's research suggests that both

the experimental results and theory predict a linear relationship between U_{SG} and k_La. One could expect that the effect of U_{SG}, for the most part, is a superimposed effect, and it aligns with a physical explanation of the condition, since U_{SG} is merely a gas (mass) input dimensionalized by cross section area.

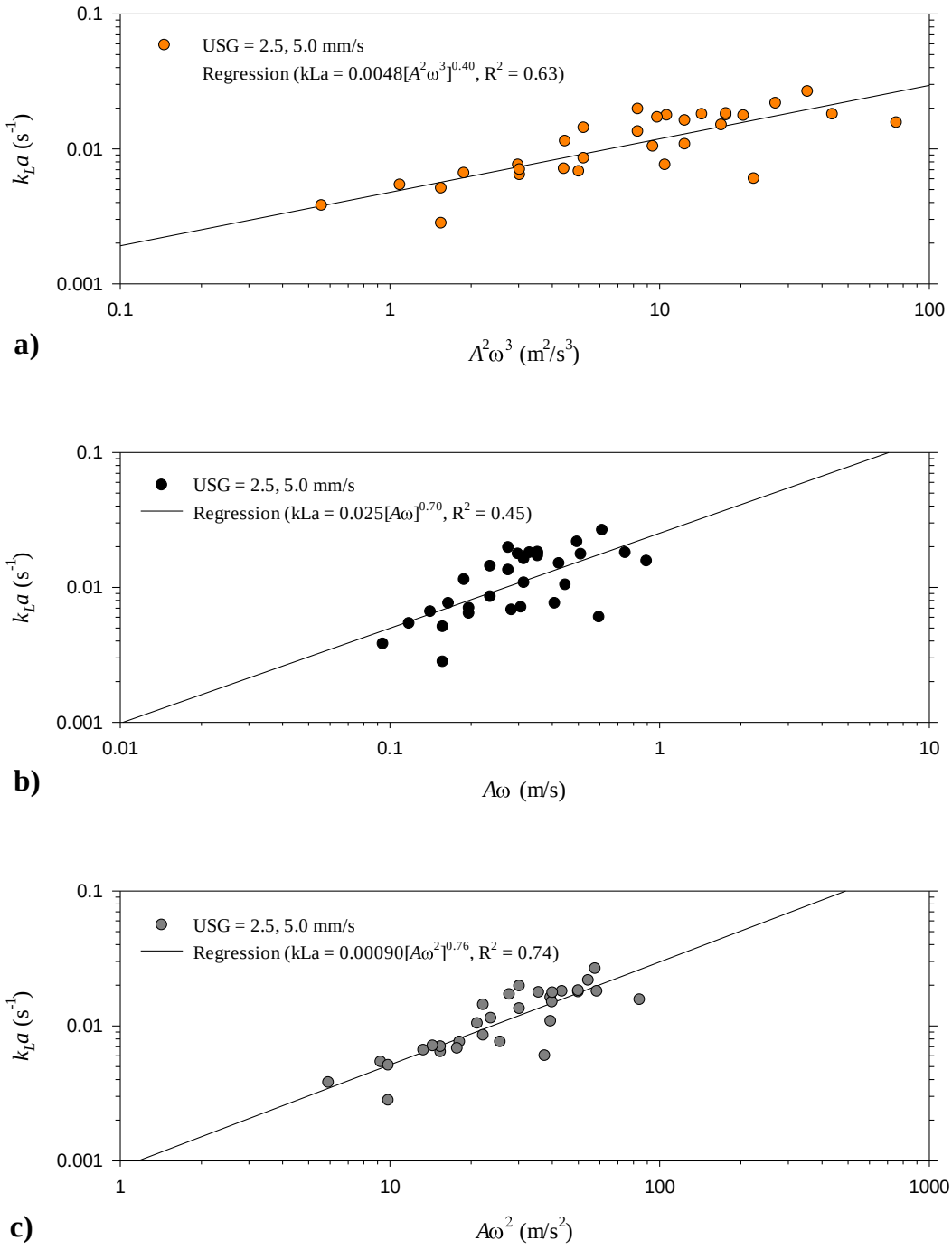

Figure 5.26: Correlation between k_La and a) $A\omega^2$, b) $A\omega$, and c) $A^2\omega^3$

In order to determine causal relationships from the data available, Minitab was used to perform a general, linear analysis of variance (ANOVA) on Waghmare's data with ln(k_La) as the response and ln(P_m), ln(U_{SG}) and the coupling of the two factors as inputs. ANOVA is a well known statistical method used to determine relational factors among input and response variables. ANOVA is especially useful in determining relationships within complex interactions. The analysis results show a fairly linear model ($R^2_{adjusted}$ = 0.905). Additionally the analysis shows U_{SG} to be nearly linear with a strong influence (F = 416) compared to the influence of ln(P_m) (F = 65.9) or the coupled effect (F = 0.83) on mass transfer. The model is provided below and the analyzed residuals are provided in Figure 5.27.

$$\ln k_L a = 0.898 \ln U_{SG} + 0.616 \ln P_m - 6.30937 \tag{5.3}$$

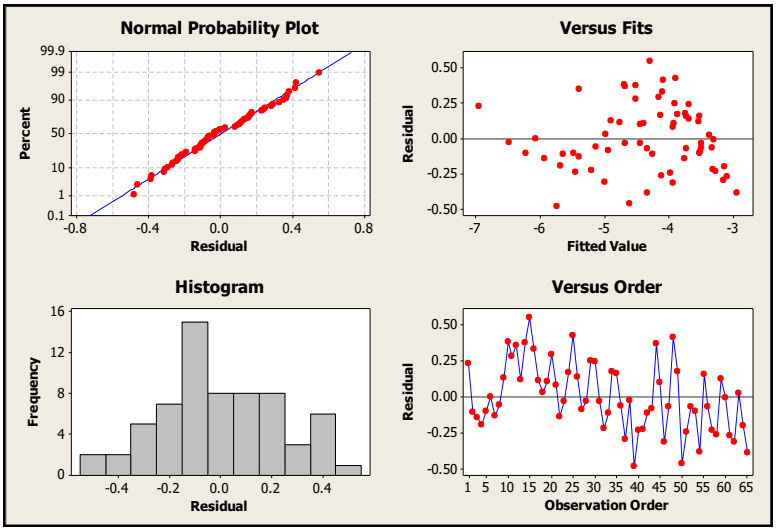

Figure 5.27: Residual plots for a general linear ANOVA model from Waghmare (2008) k_La data

Further inspection of the ANOVA model shows that Waghmare's data does not conform to the theoretical model he predicted for k_La (Figure 5.28). Performing a simple hypothesis test (t-test) on the exponents of the P_m terms in comparison with the theoretical value of 0.8 shows that none of the results for Waghmare's data are statistically equal. Thus, while Waghmare has claimed his results conform to his theory (Figure 2.16), they in fact do not pass a rigorous examination. This is cause to re-examine the data for associations that may be more applicable.

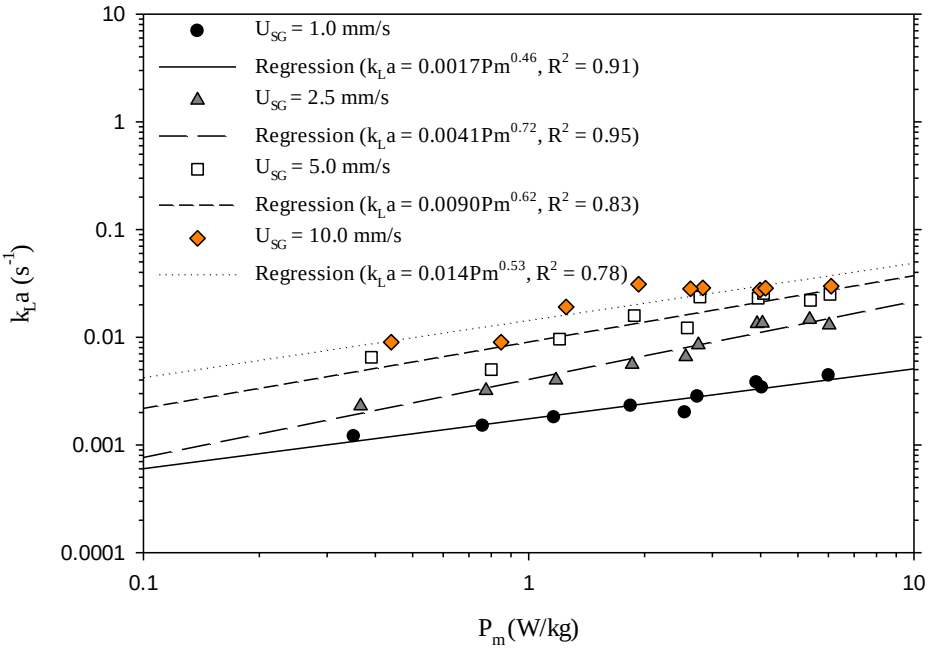

Figure 5.28: Regression of Waghmare (2008) k_La data for U_{SG} = 1.0, 2.5, 5.0, 10.0 mm/s

The associations made with data from this research show an effect of Bjerknes number (proportional to $A\omega^2$) to be as significant as P_m (proportional to $A^2\omega^3$) (Figure 5.29). It would appear that Bj is a better factor to use than P_m in this case. However, Bj cannot account for the effects of U_{SG} like P_m can, especially for no vibration conditions when Bj = 0.

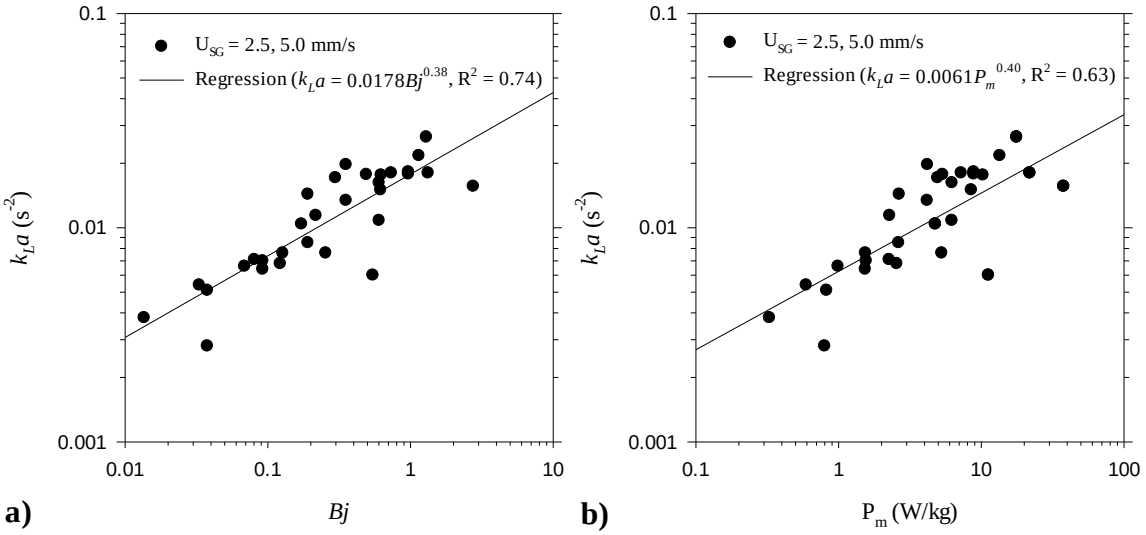

Figure 5.29: Effect of a) Bj and b) P_m on k_La for U_{SG} = 2.5 and 5.0 mm/s

Therefore, assuming that U_{SG} is a nearly linear contribution that can be superimposed, a closer examination using only U_{SG} = 5.0 mm/s shows that there is good agreement between both the results of this research and the results of Waghmare's data for U_{SG} = 2.5 and 5.0 mm/s (Figure 5.30). Both superficial gas velocities are included for Waghmare because there is evidence of an apparent disconnect between the values of U_{SG} reported for this research and the corresponding values in Waghmare's data. Therefore, both data sets provide a relative margin for reference. Additionally, examining the overall effect with all the data provided in this research (U_{SG} = 2.5 – 5.0 mm/s) and provided by Waghmare (U_{SG} = 1.0 – 15 mm/s) shows a surprising result. The regression slopes of ln(k_La) vs. ln(Bj) are statistically equivalent, and are only offset by a constant (Figure 5.31). It can be seen that Waghmare's data is highly dependent on U_{SG}, but that the results of this research are not. This may be in part due to the experimental set-up and in how the superficial gas velocity is calculated between the two, but the difference in U_{SG} effect could also be due to the nature in which the two columns are vibrated. Furthermore, only a few values of kLa were recorded for U_{SG} = 2.5 mm/s such that the lack of data would be unable to show a distinct relationship in the analysis.

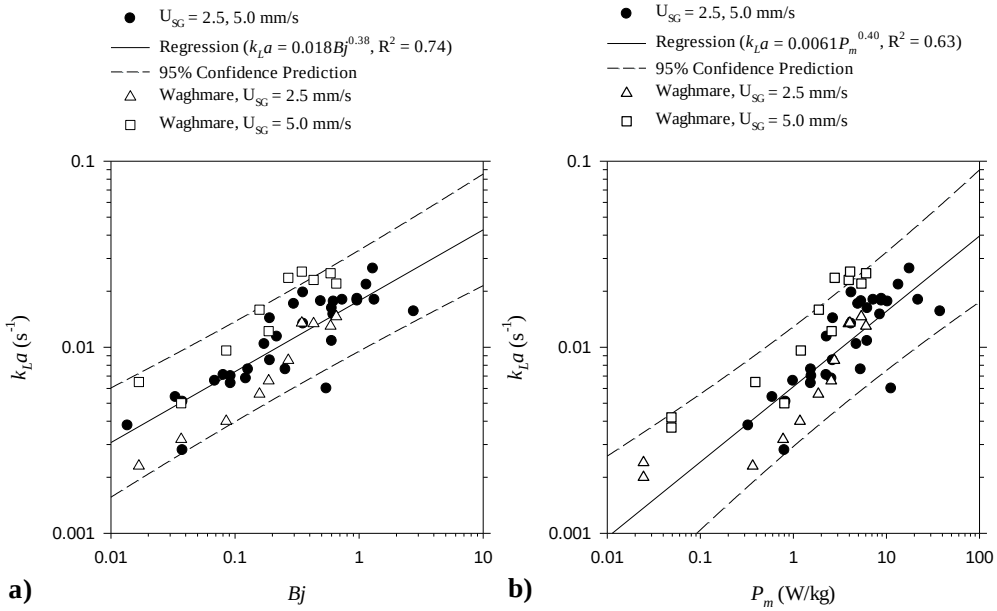

Figure 5.30: Effect of a) *Bj* and b) P_m on k_La for research results and Waghmare (2008)

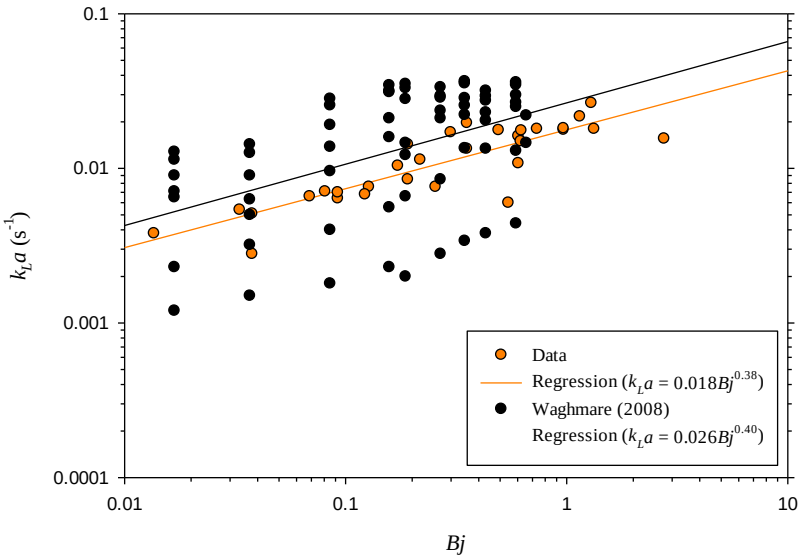

Figure 5.31: Comparison of ln(k_La) vs. ln(Bj) for research results (U_{SG} = 2.5 – 5.0 mm/s) and Waghmare (2008) (U_{SG} = 1.0 – 15 mm/s)

The same comparisons can be made for P_m, noting that the vertical scatter in Waghmare's data is once again due entirely to the absence of U_{SG} in the regression model (Figure 5.32). A better association of the dependency of U_{SG} on k_La can be seen by the 3D scatter plot of both data sets. Most notably, both data sets are seen to collapse when viewed from a perspective that includes both the effects of U_{SG} and ln(P_m). A similar 3D plot is shown for ln (Bj) (Figure 5.33).

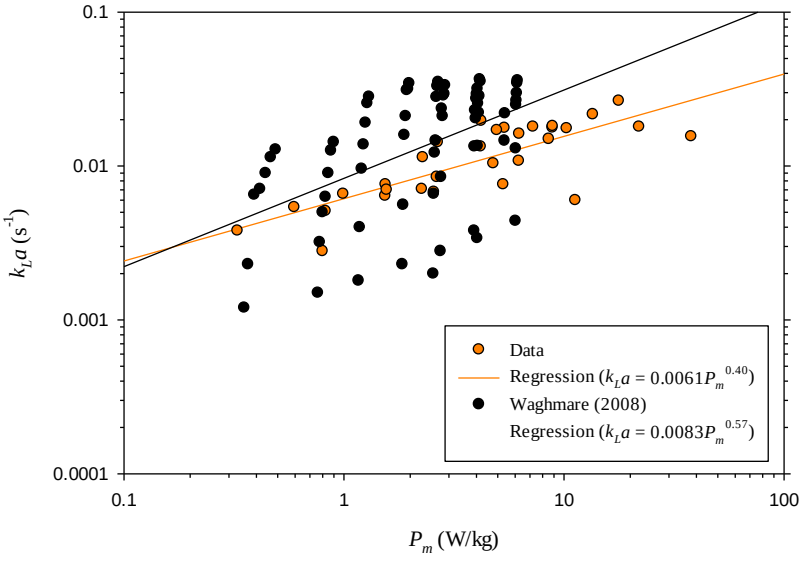

Figure 5.32: Comparison of ln(k_La) vs. ln(P_m) for research results (U_{SG} = 2.5 – 5.0 mm/s) and Waghmare (2008) (U_{SG} = 1.0 – 15 mm/s)

a) 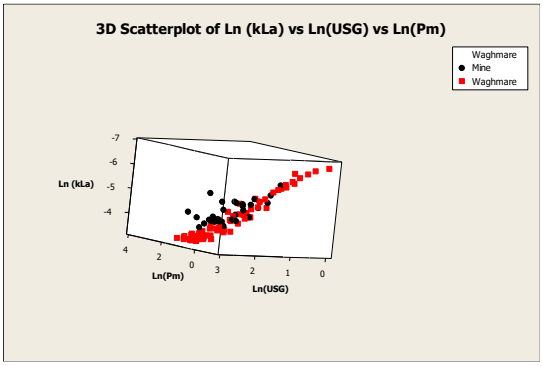

b) 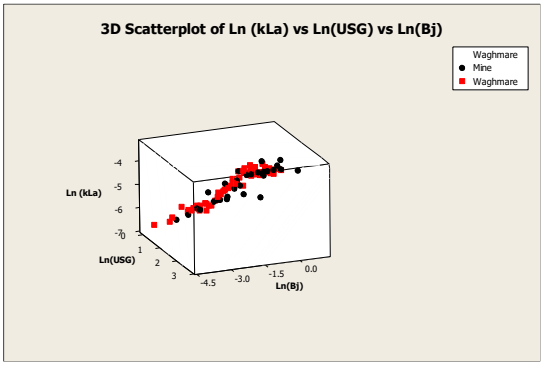

Figure 5.33: Adjusted view comparison of 3D scatter plot of both data sets for a) ln(k_La) vs. ln(U_{SG}) vs. ln(P_m), and b) ln(k_La) vs. ln(U_{SG}) vs. ln(Bj)

While the data taken from this research conforms more closely to a dependence on *Bj*, there is equal evidence that it could fit the model proposed by Waghmare (2008). There is certainly more association with the results of this data with *Bj* and analysis of all the data for Waghmare and this research shows a better match. However, the model proposed by Waghmare (2008) also accounts for an interaction with *Bj*. Performing another general linear ANOVA with ln(U_{SG}), ln(*Bj*) and ln(P_m) as factors and co-variants using Waghmare's data shows an even better correlation than just ln(*Bj*) or ln(P_m) ($R^2_{adjusted}$) = 0.947). What is remarkable is that *Bj* is seen to have a more significant impact (F = 13.9) than P_m (F = 2.82) on the mass transfer response. The model and the plot of residuals (Figure 5.34) is given below for reference. This analysis result also lends credibility that the Bjerknes number may be a better parameter to use when predicting mass transfer response.

$$\ln k_L a = 0.91 \ln U_{SG} + 0.74 \ln Bj - 0.46 \ln P_m \tag{5.4}$$

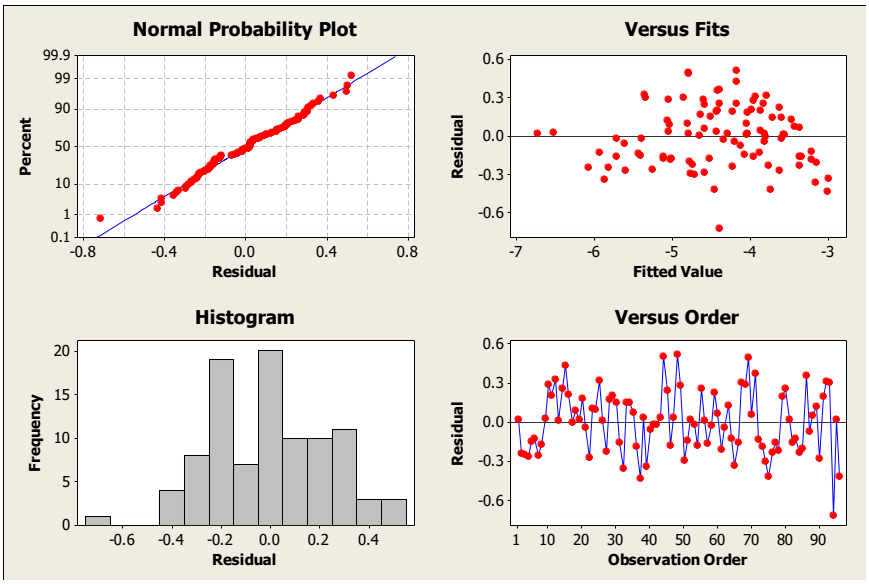

Figure 5.34: Residual plots for general linear ANOVA model of ln(k_La) with ln(U_{SG}), ln(Bj) and ln(P_m) for both Waghmare (2008) and present research data

Mass transfer data was taken from experimental runs made with larger amplitudes than previous research at lower frequency ranges (f = 7.5 – 20 Hz). The results show that at larger amplitudes optimum modes of mass transfer exist at specific amplitude and frequency combinations, and the effect of increasing amplitude tends to shift the modes to the left up to a certain extent. Additionally, the results suggest an optimum amplitude exists, independent of the frequency for the frequency range tested. A rigorous statistical examination and comparison of the results with Waghmare (2008) show that neither the results of this experiment or that of Waghmare conforms to the proposed theory (Eq. 5.2).

A general linear ANOVA was performed on the combined both data sets which showed that there was actually an effect of all three factors namely, U_{SG}, Bj, P_m on k_La in order of influence. However, performing regressions on previously collected data to discover causality is suspect to error. Therefore, additional data must be gathered from other sources, and preferably from well designed, statistically orthogonal experiments in order to accurately determine the association of k_La with U_{SG}, Bj, and P_m or any strong coupling that may exist. Additionally, the ANOVA suggests that Waghmare's theoretical prediction based on physical principles is not

entirely inaccurate, simply that some aspects or assumptions may need to be modified to suit the relationships and their individual strengths appropriately.

5.2.2. Void Fraction and Bubble Size

Void fraction and bubble size measurements were taken for increased amplitude similar to mass transfer experiments. The results of void fraction (ε) show improvements similar to mass transfer. The presence of optima occurs in the void fraction data similar to k_La, although the improvements in void fraction with increasing amplitude and frequency are greater than those of mass transfer. This is likely due to both the very small values of void fraction for no vibration conditions and the very large values found during high amplitude, high frequency cases, as discussed previously. Some of the statistical error accounts for this fluctuation, but there is likely a systematic error that is of equal magnitude that could not be quantified or included in the presentation of this data (Appendix B.3). However, for comparison the respective raw values and improvements are presented (Figure 5.35).

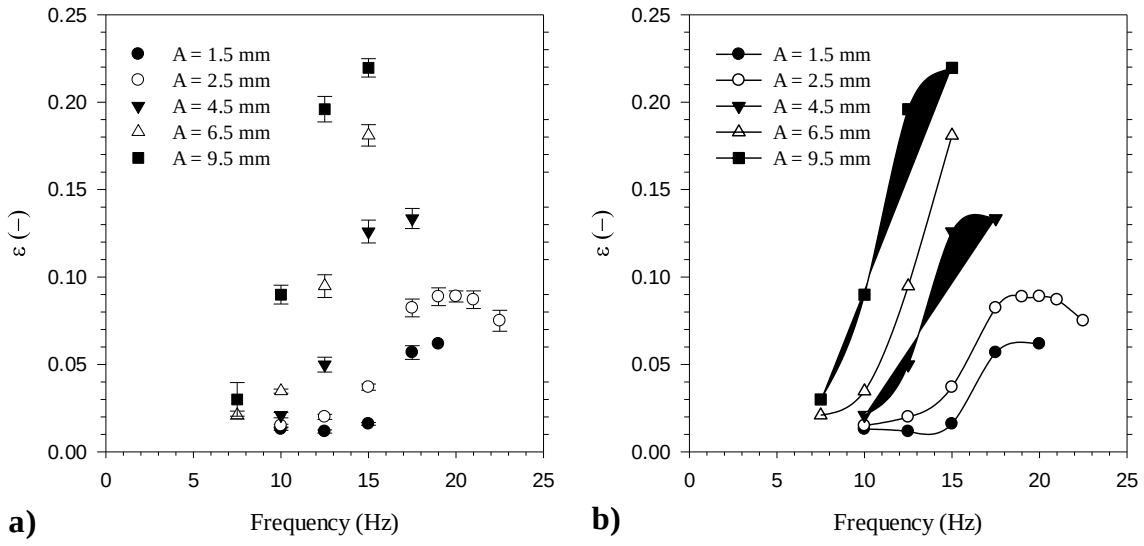

Figure 5.35: a) Void fraction vs. frequency for increasing amplitudes and b) void fraction improvement vs. frequency for increasing amplitudes

The results show that for the range of frequency tested there is typically only one optimum per amplitude. Similar to the mass transfer results, there appears an increase in amplitude which has a linear rotation effect to moves the maxima to the left on the frequency range. Unlike the mass transfer results, however, these shifts are completely ordered from high to low, whereas the mass transfer results showed some variability. This steady rise in void fraction with non-dimensional amplitude is more clearly seen in Figure 5.36.

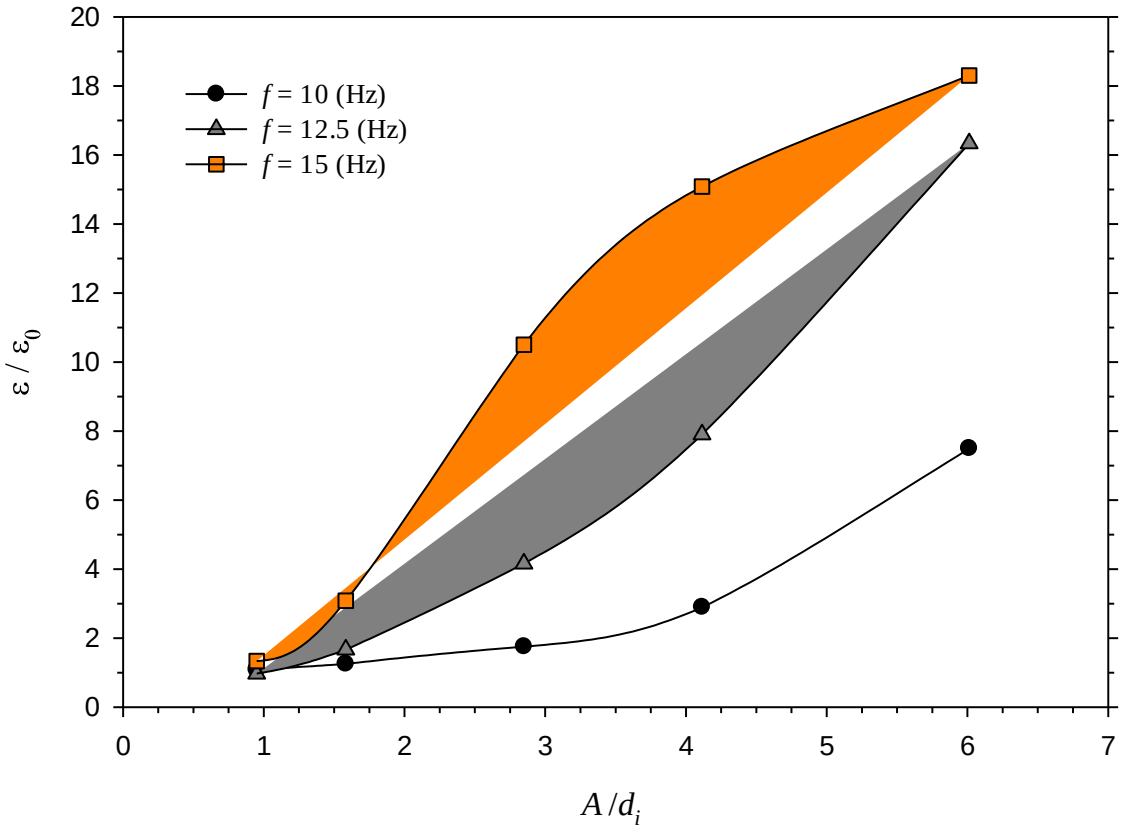

Figure 5.36: Effect of increasing non-dimensional amplitude on void fraction

As with the mass transfer results, a systematic study of vibration parameters and their combinations were reviewed for their respective influence on ε. The analysis shows that there is a strong void fraction dependence on $A\omega^2$, and again some dependence on $A^2\omega^3$. However, unlike the case of k_La, ε the correlation shows a much larger separation between the two parameters, and the regression fit is of higher quality (Figure 5.37).

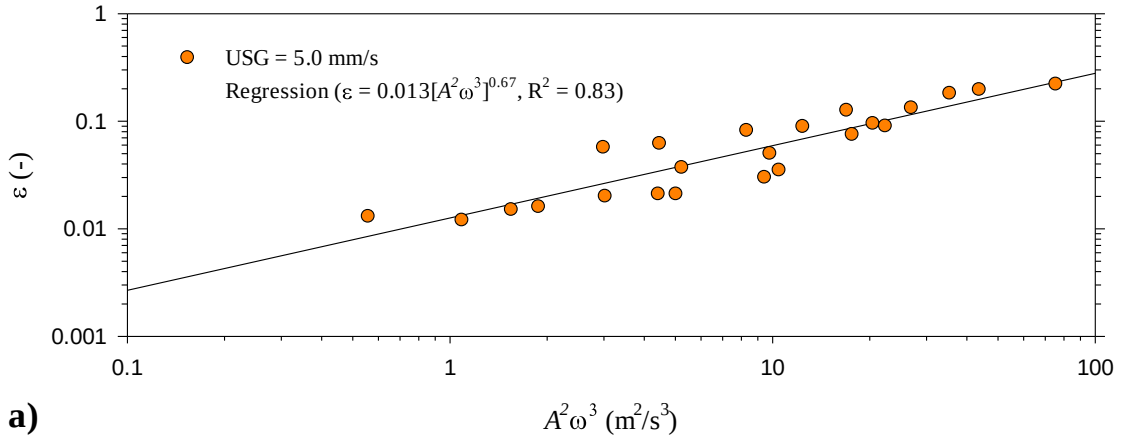

a)

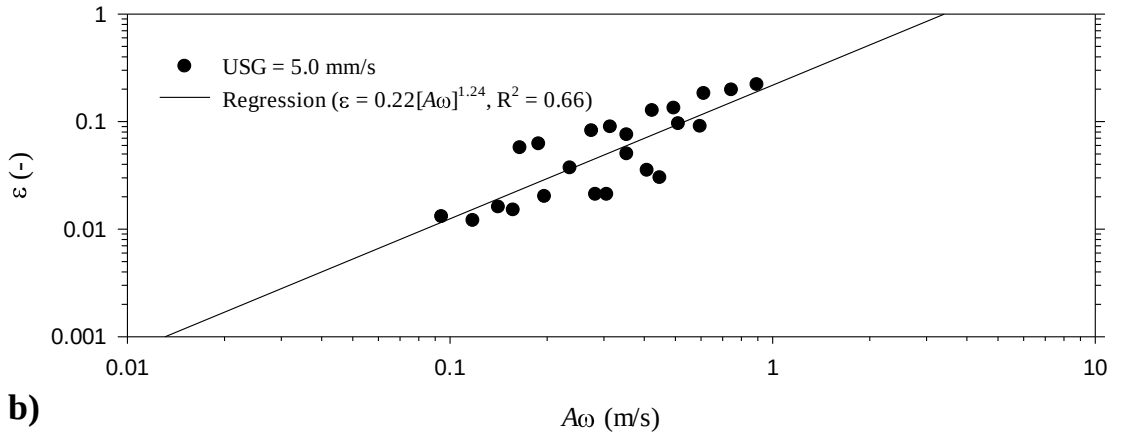

b)

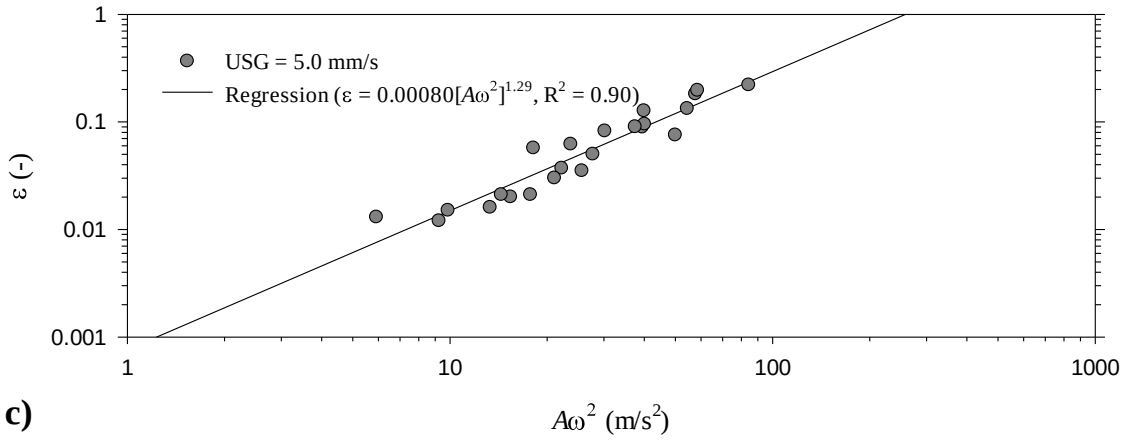

c)

Figure 5.37: Correlation between ε and a) $A\omega$, b) $A\omega^2$, and c) $A^2\omega^3$

Similar to mass transfer, the relationship between the void fraction and the Bjerknes number, *Bj* and the specific power input, P_m is significant. Due to the experimental conditions, not as many data points could be taken for U_{SG} = 2.5 mm/s so an analysis of the differences are not significant enough to warrant comment. It is evident from the previous research that void fraction is also linearly dependent on U_{SG} as well. However, a plot of the data shows that the relationship between ε and *Bj* is stronger than that for P_m (Figure 5.38). Oddly, the data shows a much clearer polynomial relationship with P_m which cannot be described or accounted for.

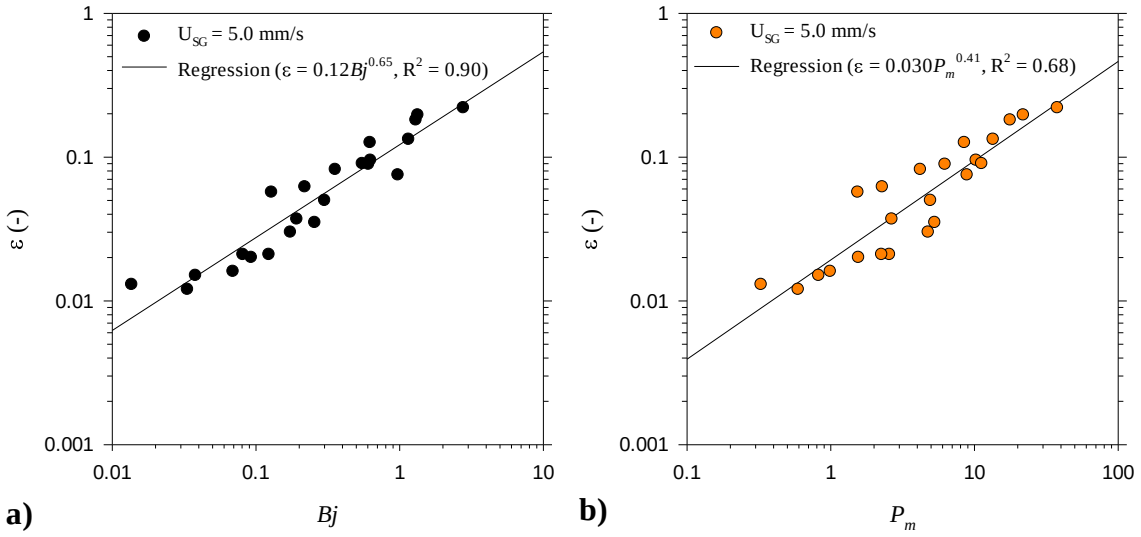

Figure 5.38: Effect of a) *Bj* and b) P_m on ε for U_{SG} = 5.0 mm/s

Minitab was used again to perform a general linear ANOVA in order to determine the statistical relationships between the log-transformed input parameters, ln(U_{SG}), ln(*Bj*), and ln(P_m) on the log-transformed output ln(ε). The analysis results using Waghmare's data shows a relationship similar to mass transfer in that ln(U_{SG}) is the most significant contribution (F = 210) with ln(P_m) following with a slight influence (F = 6.20). ln(*Bj*) was not seen to be a significant factor (F = 0.15). Taking the analysis of Waghmare's data further by refining the inputs to exclude ln(*Bj*) shows a relationship that is very similar to the predicted theory, namely,

$$\varepsilon \propto P_m^{0.4} U_{SG} \tag{5.5}$$

The general linear ANOVA model and the regression plots (Figure 5.39) are given below.

$$\varepsilon = KP_m^{0.45}U_{SG} \tag{5.6}$$

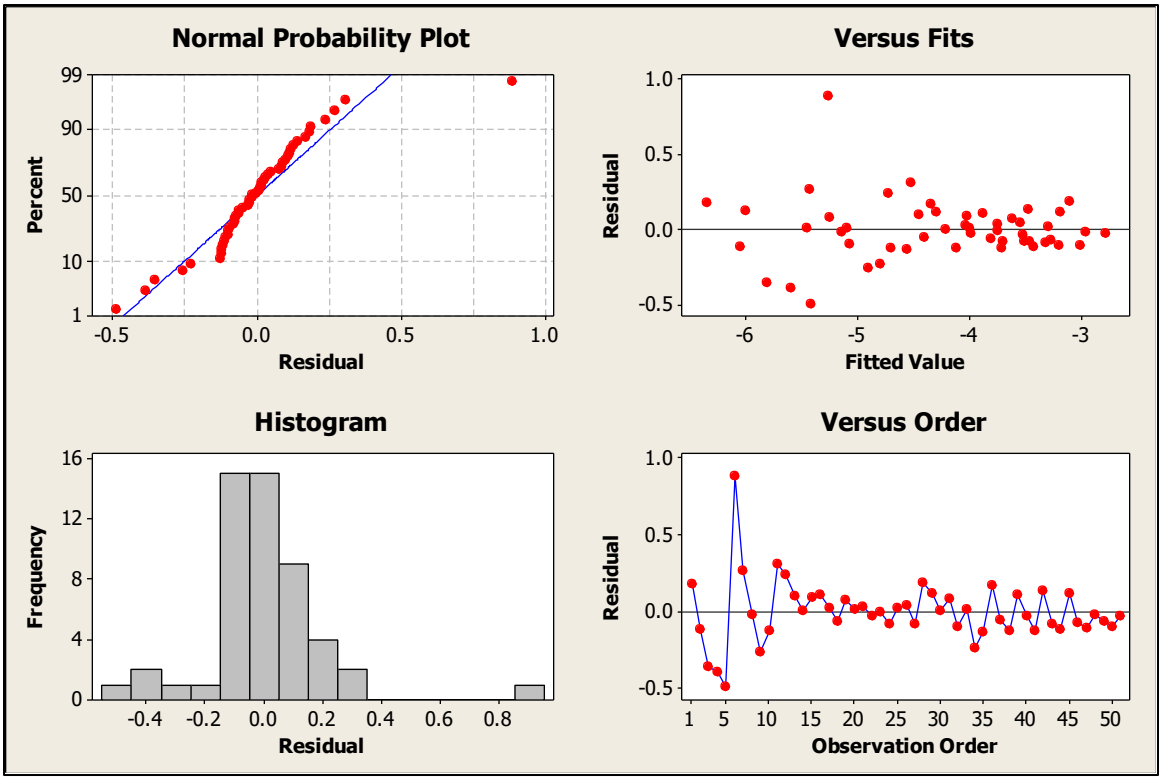

Figure 5.39: Residual plots for a general linear ANOVA model for Waghmare (2008) ε data

One can see that the residuals show a slight skew in early measurements indicated by the residuals vs. the observation order, but the residuals vs. fitted values sub-plot shows a fairly tight and uniform scatter. These plots indicate the model does a fair job at associating the effect of P_m on ε for Waghmare's data. However, it should be noted that while the analysis predicts exponential values similar to theory, they are not actually statistically equivalent due to the error associated with the regression coefficients. The take-away is that Waghmare's model does a better job at predicting void fraction when compared to his experimental results than it does for mass transfer. Therefore assuming the theoretical model to be somewhat accurate a review of the data from this research is appropriate as a comparison.

Analyzing the void fraction results from this research using ANOVA in a similar manner as previously, shows that void fraction is influenced more by *Bj* (F = 17.11) than by P_m (F = 1.55) or U_{SG} (F = 0.36). This is strikingly different from Waghmare (2008). In fact, the lack of influence of U_{SG} is suspect, primarily because one would expect at least a moderate contribution that is seen in no vibe cases. However, this can be partially explained by the limited number of levels (2) and the samples at each level (4 U_{SG} = 2.5 mm/s, 23 U_{SG} = 5.0 mm/s) which would skew the results. The difference in primary influences between Waghmare and this research is harder to justify, but there are two possible explanations to account for the shift. The model and the regression plots (Figure 5.40) for the general linear ANOVA are given below.

$$\varepsilon = K \frac{Bj^{0.97} U_{SG}^{\ 0.16}}{P_m^{\ 0.33}} \tag{5.7}$$

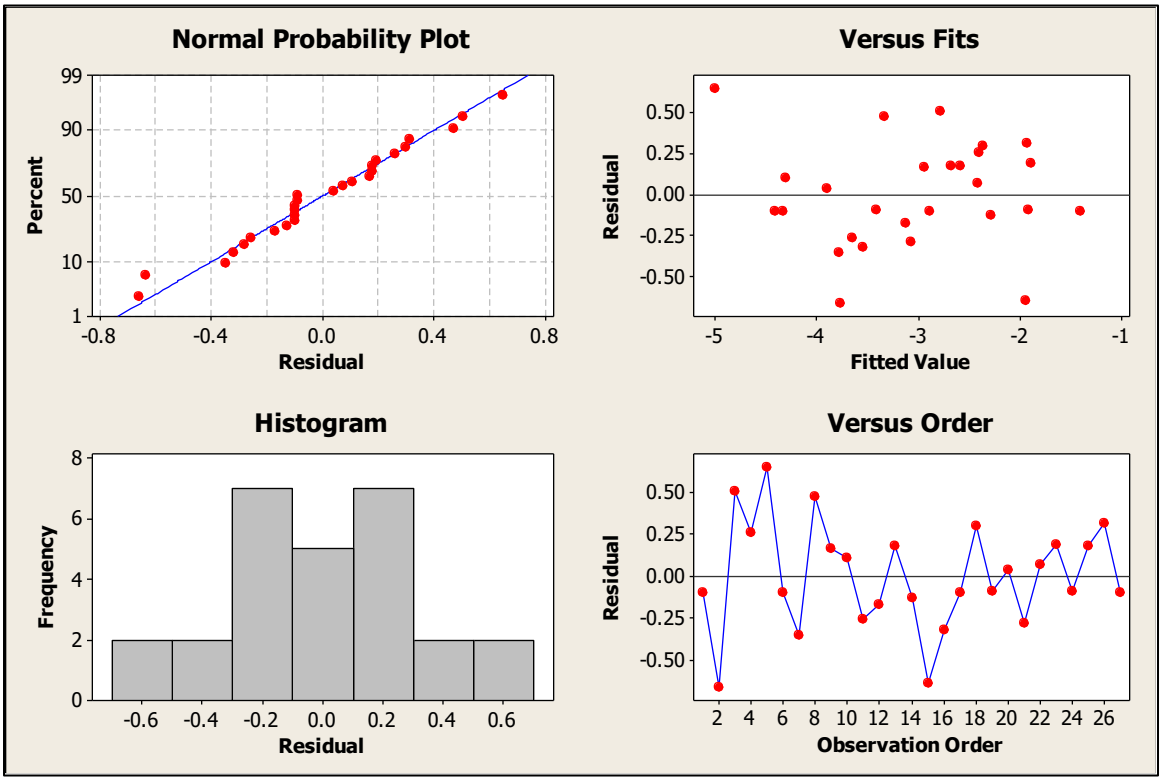

Figure 5.40: Residual plots for a general linear ANOVA model for ε vs. *Bj*, P_m, and U_{SG}

The first possibility for the difference in greater effect of *Bj* on the void fraction data in this research vs. the effect of P_m found in Waghmare (2008) is due to the set-up itself. Waghmare's set-up consists of a pulsed column where the vibration input is carried out at the bottom of the column through a flexible membrane or piston. The research performed with this set-up is fundamentally different in that it vibrates the entire column with the fluid inside. Therefore, one would expect to find different flow patterns established in each. For instance one could expect the pulses from the bottom being damped along the column height, whereas in whole cylinder shaking the presence of the wall shearing would induce a periodic velocity gradient in the fluid. This method in which the motion is imparted to the fluid could be the reason for a shift from an acceleration centered Bjerknes influence over that of a power centered P_m term.

The second possibility for the difference may be in the systematic error involved in the void fraction measurements themselves. For instance, the majority of Waghmare's data was taken for low amplitude vibration conditions, and $Bj < 1$. Therefore, conditions where the bubbles stalled at the bottom, coalesced and rose to the surface as observed in this research should not have been present in Waghmare's. Additionally, the methods used to evaluate ε were different. Waghmare used a manometer to take differential pressure measurements, but his measurements suffered from the instability inherent in the oscillating pressure environment. Conversely, this research utilized photographic measurements of the interface, which at times could be violent and/or un-identifiable. The interface photograph method is fraught with its own flaws and uncertainty. The addition of higher amplitudes could and very often were the cause of the interface instabilities and it is possible that the higher values of void fraction and increased improvement over Waghmare's own data were caused by the interface instability producing exaggerated results. This effect was previously mentioned in §5.1.4 in comparison with Waghmare (2008).

Void fraction measurements were taken for a range of higher amplitudes with a frequency range of f = 7.5 – 17.5 Hz. The results show that void fraction increases are higher than previous research, but show similar trends. Additionally, the void fraction data suggests that there are not as many optima for frequency and amplitude combinations, and there does not seem to be a frequency independent optimum for amplitude such as those found for k_La. An ANOVA was performed on Waghmare's data which showed void fraction to more closely resemble his theoretical model compared to the results of the mass transfer data. However, the data for this research shows a stronger influence from Bj as opposed to Waghmare's P_m. The difference in influential parameters is likely due to either the method used to determine ε, or the method to apply vibration to the fluid and cylinder. A model to determine ε as a function of Bj, P_m and U_{SG} is suggested based upon a general linear ANOVA for the data taken.

Results for bubble size show that the Sauter mean diameter, d_{32} decreases with amplitude. The effect of increasing amplitude causes a general clockwise rotation of the trend with frequency resulting in a d_{32} shift to the left on the frequency scale. Connecting the data with a spline indicates there may be local maxima at certain frequency and amplitude combinations. However, the error associated with the values wash out any definite observation of variation (Figure 5.41). The error associated with d_{32} is approximately 34% and is derived from the error associated with processing the bubble photographs. A more accurate method to evaluate bubble size is recommended. One possible method to achieve better results for bubble size distribution is the use of 4 point fiber optic probe which has been developed, used, and demonstrated to provide more accurate information about bubble size distributions in non vibrating BCRs. Coincidentally, the 4 point optical probe has been used to measure void fraction in BCR and could be avalid replacement to the method used in this research.

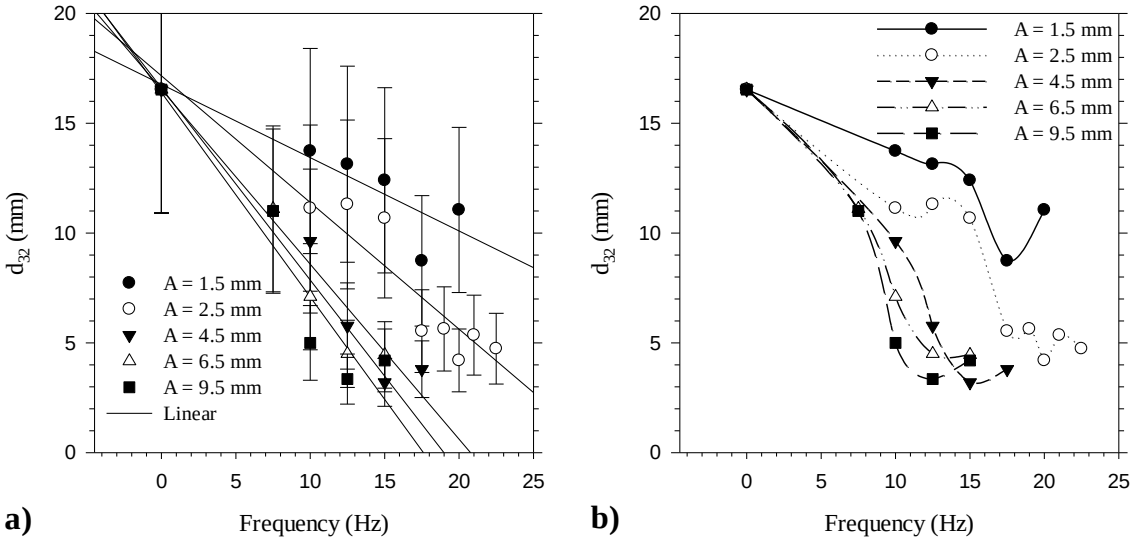

Figure 5.41: Sauter mean diameter vs. frequency for A = 1.5 – 9.5 mm with a) error bars and linear regression, and b) possible frequency/amplitude local maxima

The mean diameter also shows a steady decrease with amplitude suggesting that there are no optimum amplitudes independent of frequency for the range tested (Figure 5.42).

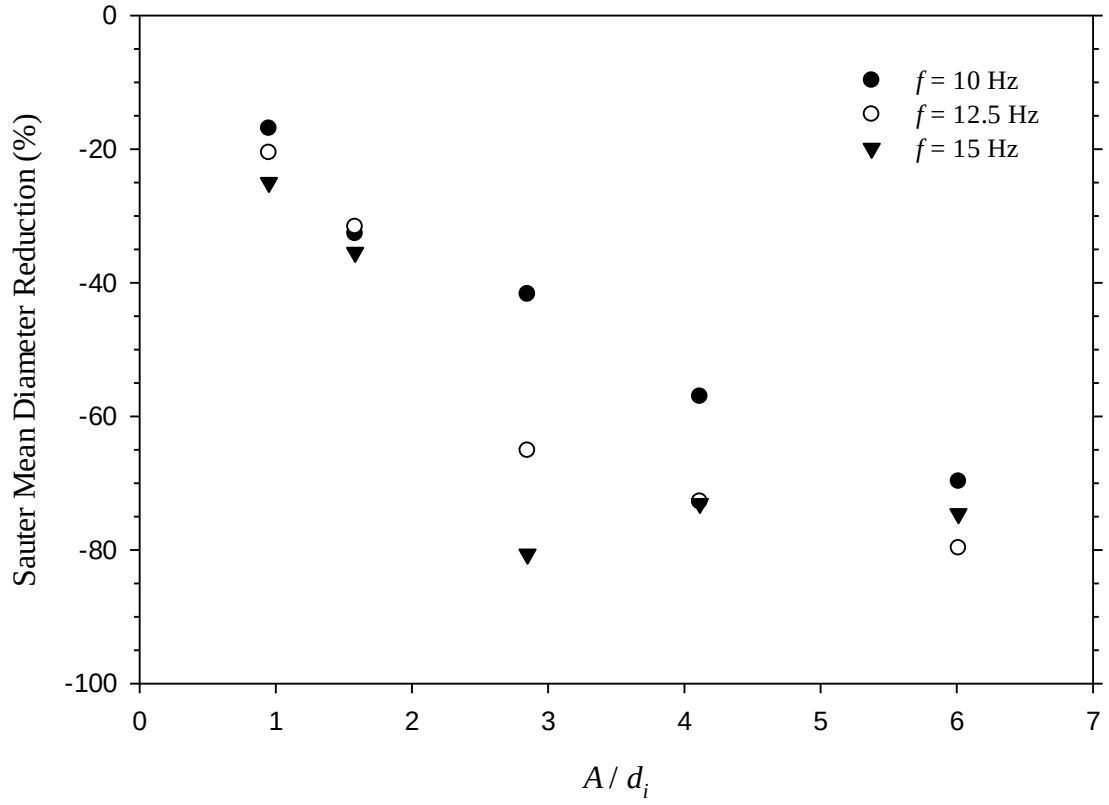

Figure 5.42: Sauter mean diameter reduction vs. non-dimensional amplitude for f = 10, 12.5, 15 Hz

During the analysis of the bubble distributions an interesting result was found. In previous research the bubble distributions taken from photographs were reported to take on a normal distribution. However, in this research the majority of the distributions were more representative of an exponential distribution rather than a normal one (Figure 5.43). These results would concur with the general distribution of samples taken with the 4 point optical probe for static BCRs such as that found in Figure 2.28.

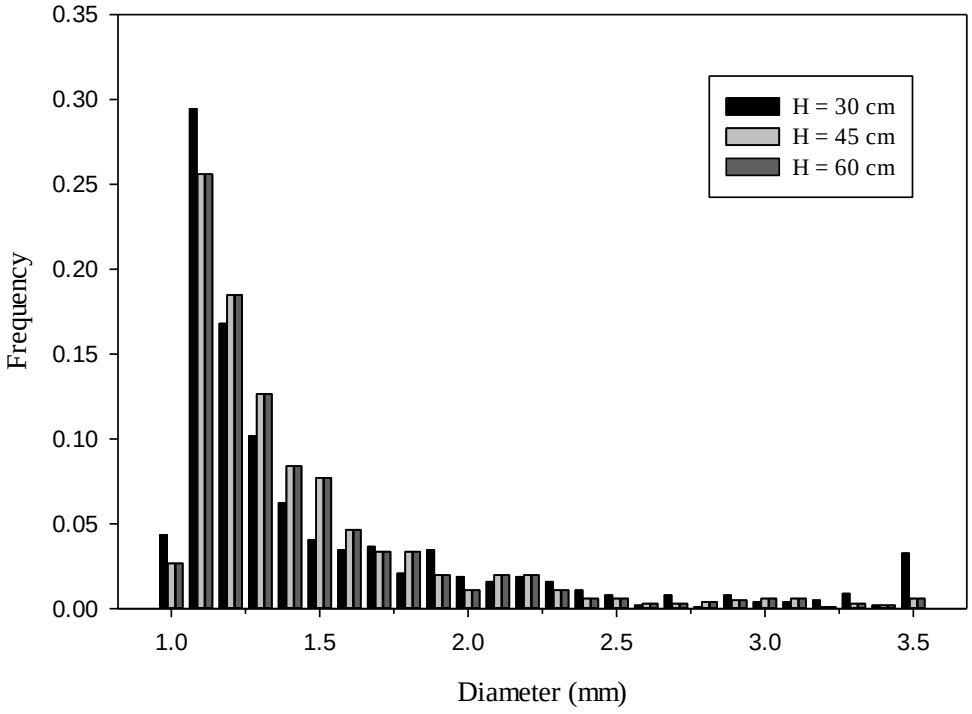

Figure 5.43: Bubble diameter distribution as a function of column height for f = 12.5 Hz, A = 4.5 mm, U_{SG} = 5.0 mm/s, p_e = 1 atm

Plotting the log-normal distribution of non-dimensional bubble size (bubble diameter / injector internal diameter) on log-probability coordinates shows a strong linearity (Figure 5.44). This linearity would imply that the distributions conform to an exponential distribution. There is some deviation from the linear trend, especially for smaller bubble sizes. The appearance of deviation from the trend shown in Figure 5.44 also agrees with a minimum bubble size suggested by Figure 5.42. Therefore, there is an expected "cliff" in the distribution where very few bubbles

are seen to be smaller than the median value which must be close to the size limit imposed by surface tension.

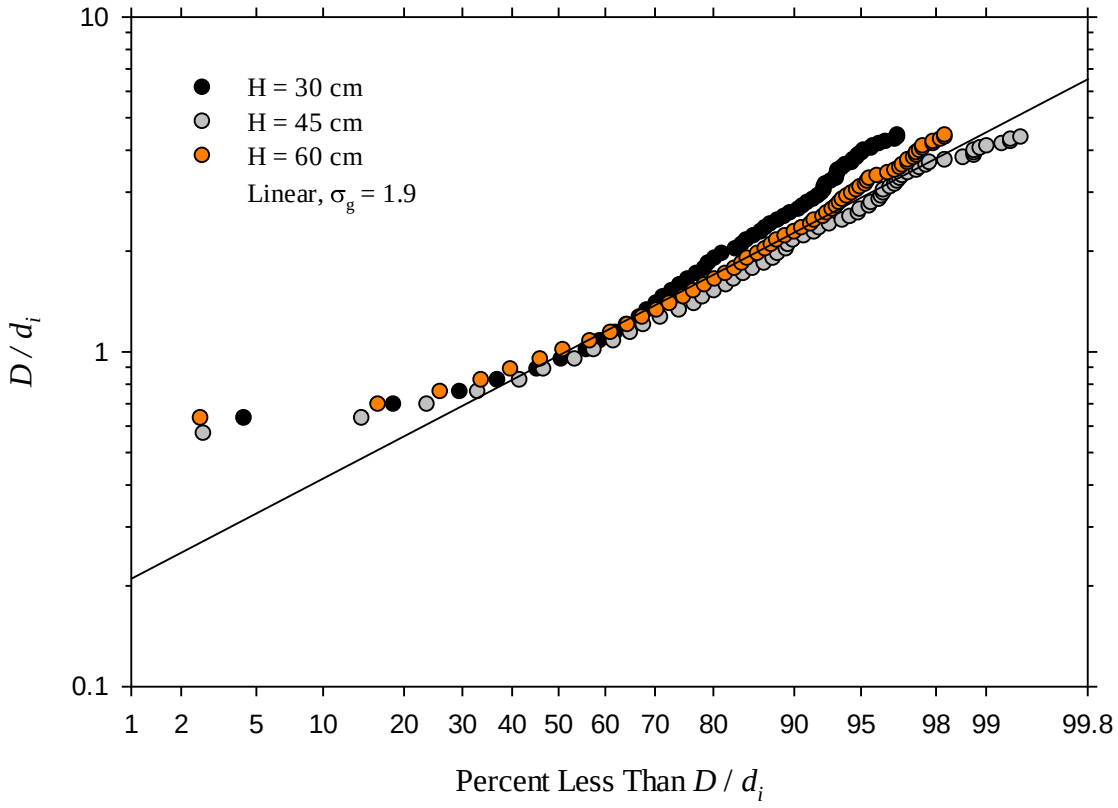

Figure 5.44: Log-normal distribution of non-dimensional bubble size

The photographic processing method was examined to determine if the influence of any parameters would skew the distribution results. The analysis showed that by changing a variety of parameters over a wide range of levels, similar exponential distributions (Figure 5.45). It was determined that a defined set of parameters be adjusted to meet any optimum result that was available and then applied to all processing routines in order to remain uniform. As an example, the rolling ball radius was varied and the Sauter mean diameter was calculated from the distribution. An optimum value of d_{32} was found to exist at a rolling ball radius (RBR) of 80 which was applied to the rest of the processing routines (Figure 5.46).

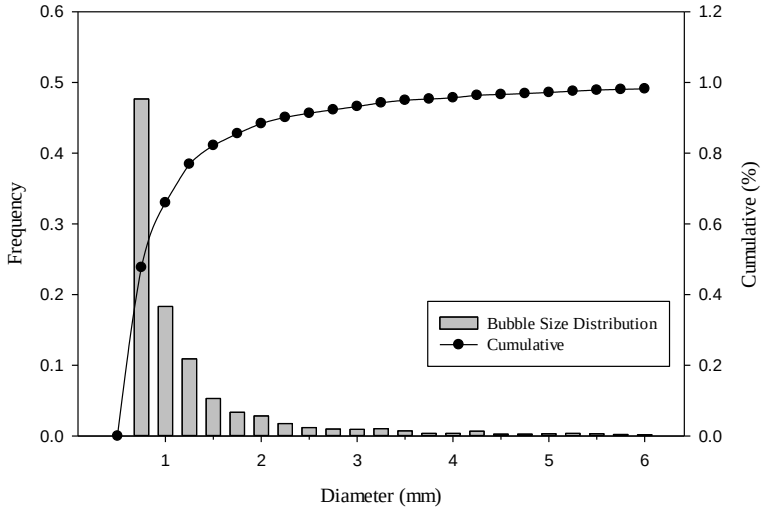

Figure 5.45: Bubble size frequency and cumulative distribution for RBR = 80

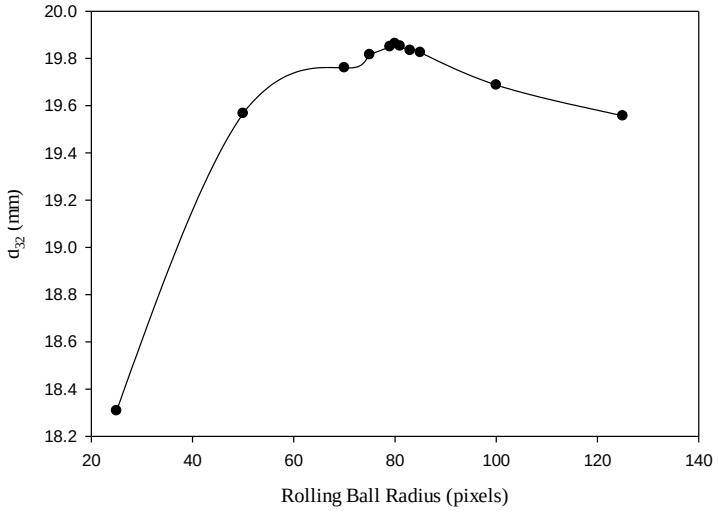

Figure 5.46: RBR optimization for bubble photograph processing

The results of the log-normal bubble size distribution found in this research cast doubt on the normal distribution results reported by Waghmare (2008). The method to determine accurate or representative bubble size distributions is also susceptible to processing constraints. It was observed during processing that the presence of clustered bubbles tended to misrepresent the results for individual bubble sizes. During an attempt to gauge uncertainty of the method it was discovered on numerous occasions that the area measurement of known objects were inflated by local bubbles that were clustered close by and assumed as the object during processing (Appendix

B.4). It is indeterminate whether size distributions processed in the presence of high clustering density is truly representative of the actual bubble sizes.

5.3. Summary

A series of experiments were performed first to validate the test set up, and second to extend the knowledge about the effect of amplitude on mass transfer, void fraction and bubble size. The shaker itself was tested using accelerometer and Δp pressure sensor to measure the difference between the actual shaker output and the expected theoretical sine wave. The results showed that shaker exhibits noise at the peaks and troughs of the cyle that is typical for the type of machine. Additionally, measurements from the Δp sensors show that the column pressure environment is relatively free from the influence of the noise present in the machine output. The shaker is therefore seen to meet the requirements of the experiment and performs to expectation.

The set-up was also tested for observations of bubble stability, column height specific void fraction increases, and increased bubble breakage from previous research. Video and photographic evidence show that there are specific pressure, frequency and amplitude combinations that will provide an ideal column height location where bubbles were seen to stabilize. The stability is better termed pseudo-stability as the bubbles were not seen to exhibit zero movement indefinitely due to instabilities present in the set-up. Secondary Bjerknes forces were also observed which are suggested to be the cause of the bubble aggregation or clustering seen in the experiments. This has only previously been reported for higher frequencies. The stability frequency model suggested by Buchanan et al. (1962) was also extended to include vacuum pressures which were observed to give the same stability at the specific height locations, but for lower frequency requirements. Cyclic migration of large bubble masses and froth bands were observed which agreed with the literature. The presence of the same observable phenomena

in this research lends credibility to the set-up by its ability to reproduce results previously seen in other research.

Mass transfer was measured for static conditions to demonstrate the capability of the DO sensor, and the method. k_La data obtained at frequency and amplitude regimes similar to Waghmare (2008) show good agreement. There exist a few irregularities at higher frequencies which may be based on the set-up itself. The experimental set up was used to extend the current state of research to include mass transfer coefficients at larger amplitudes (A = 4.5, 6.5, 9.5 mm) over a frequency range of 7.5 – 22.5 Hz. The results were compared to existing data provided by Waghmare (2008) and show some interesting results. Regression of the k_La data shows stronger dependency on Bj than P_m. Waghmare's data was re-analyzed to determine if a similar dependency on Bj also existed. The analysis shows that Waghmare's k_La data did not meet the theoretical model he predicted, as reported by him. However, a general linear ANOVA performed on both data sets showed that his model predicts the relationships between P_m, Bj and U_{SG} well, but the strength of the dependencies were inaccurate. Therefore, Waghmare's model should be considered a good starting point for predicting mass transfer from a physics based approach, but some assumptions should be reconsidered to determine if the model can be adjusted to match the experimental results. Furthermore, a series of statistically designed experiments is recommended to better determine causal relationships among the independent parameters of P_m, Bj, U_{SG} or others, and help build a better understanding of the physics involved.

Void fraction and bubble size distributions were recorded using photographs and computer processing routines. A similar comparison of void fraction data was made with the data published by Waghmare (2008). The data shows a marked increase in void fraction improvement, $\varepsilon/\varepsilon_0$, especially at higher frequency and amplitude combinations. This is likely due to the methodology in determining void fraction from photographic measurements of the liquid-air interface, which at higher frequency and amplitude combinations were seen to be highly

unstable. A regression analysis was also performed on the data to show the relationships between specific power input (P_m), Bjerknes number (Bj), and superficial gas velocity (U_{SG}). The results showed a distinct difference from Waghmare (2008). Waghmare's data agreed fairly well with his theory in showing the relationship between void fraction, Pm and USG, but the data from this study showed a very high dependency on Bj and less on U_{SG}. The difference in column vibration (pulsing vs. whole column shaking), the difference in void fraction measurement methodology (manometric vs. photographic), or an unaccounted for error or bias present in the void fraction data collected may be the cause. It is recommended that a different method be used to measure void fraction for future research using this set up, especially for vibration conditions that impart large accelerations or loads on the column.

Bubble size distributions seemed to suffer from the same flaw in using photographic methods. All of the previous research in vibrating BCRs have used this method to describe the bubble sizes, but it was seen during the course of this research to be flawed. The processing routine used to measure bubbles from photographs is a powerful tool, but it can only safely be used when bubbles are not very near each other. For most of the conditions present during this work the bubbles were seen to be homogenized by the vibration, and indeed in some cases were clustered together due to the vibration. Therefore, the processing routine could not accurately separate many smaller bubbles, and there were several instances when several smaller bubbles were "measured" to be one large bubble. This processing method is obviously not suggested as a means to accurately describe the bubble sizes. The distributions produced by processing these photographs indicate distributions that are non-normal, and tend to be exponential in appearance which does not agree with previous research, except for one case. However, accepting the error in the measurements the results of the d_{32} data shows a decreasing trend with increasing amplitude which conforms with the power based bubble breakage theory. Future research should utilize a different measurement methodology to obtain more reliable bubble size results.

CHAPTER VI

CONCLUSIONS AND RECOMMENDATIONS

6.1. Conclusions

The purpose of this research is to design, build, and validate an experimental set up, and to conduct experiments with the set up that increase the understanding of multiphase flow in a vibrating bubble column reactor. The research objective was accomplished in part by designing, building and validating an experimental set-up that was capable of testing the multiphase response to vibration, pressure, and gas flow inputs for specific liquid properties and heights. The experimental set up consists of a shaker device and an instrumented bubble column reactor. The shaker was designed to provide a vibration environment containing a frequency range of 5 – 40 Hz and an amplitude range of 1.0 – 10 mm. The shaker amplitude is controlled by adjusting bolts on the eccentric, and the frequency was controlled by the motor through a frequency modulated speed controller. Shaker table response was measured using an accelerometer. The bubble column reactor was designed from a clear cast acrylic tube with a nominal internal diameter of 4 in. to allow for flow visualization. 4 different diameter columns were prepared including a 1.0 in., 2.5 in., 4.0 in. and 5.5 in., but only the 4 in. diameter was used for the purposes of validation and experiments in this work. The bubble column reactor was instrumented with pressure taps, and a dissolved oxygen sensor in order to measure differential pressure across the column and dissolved oxygen concentration in the fluid. A 1.5 mm diameter single orifice gas injector was used to inject compressed air into the fluid. The injected air was controlled by a series of valves and measured using a coriolis mass flow meter. The bubble column was designed to be a

pressure controlled system and was tested over a range of 0.3 – 2 atm. A personal computer was combined with a SensorDAQ data acquisition card to record signals generated by the DO probe, accelerometers, and differential pressure transducers. The data was collected and analyzed for validation testing and experimentation.

The experimental set up was validated by comparison of data taken from a series of tests with previous research results. Accelerometer data from the shaker was taken during experimental runs and compared with theory from the known inputs of frequency and amplitude. The accelerometer signals show a sinusoidal wave that has a small amount of noise at the peaks and trough typical of similar machine types. Comparison of the z axis accelerometer data with signals measured at the x and y axis show good signal to noise ratio. Differential pressure transducer data taken with a liquid filled column also show a typical sinusoidal response which would indicate the shaker performs as expected and validates the final design. Mass transfer coefficients (k_La) were determined from DO measurements taken with a static, water filled bubble column injected with compressed, filtered air over a superficial gas velocity range of 1.0 – 10.0 mm/s. The coefficients showed a highly linear response vs. U_{SG} as expected from theory, and the values were similar in magnitude to data reported in the literature. A linear regression of the data showed the slope to be slightly different from that reported in literature, but is likely due to either a difference in gas injector size or determination of U_{SG}. Historically, k_La values reported in literature have been widely ranging. Similar experiments were performed at static conditions for void fraction and mass transfer with similar results showing good agreement with previous research. These comparison provide verification of the bubble column sensor operation and validity.

Mass transfer, void fraction, and bubble size measurements were also taken for frequencies of 10.0 – 22.5 at amplitudes of 1.5 mm and 2.5 mm. The mass transfer results showed good agreement with Waghmare (2008) for similar vibration conditions, especially concerning the trends of the data with frequency. The values of the mass transfer coefficients and

void fraction measurements were different for some values from those of Waghmare (2008) especially at higher frequency. However, the difference in data points are not extreme and are predicted to be due to the difference in experimental set up. Video and photographs were taken for "stability frequency" experiments similar to those of Buchanan et al. (1962) which show pseudo-stabilization of bubble velocity at predicted column locations for the associated column pressure and vibration conditions. The stabilization frequency model of Buchanan et al. was seen to be applicable even for vacuum pressures, thereby extending the model to regime previously untested. The results from these experiments showed the experimental set up's capability to reproduce data and observable phenomena indicated in the literature. The experimental set-up was seen to be validated, and was used in conducting additional experiments to advance the knowledge of the field.

The second objective of the research was met by performing an experiment to determine the effect of amplitude on mass transfer, void fraction and bubble size, especially at higher amplitudes than previously tested. Therefore, void fraction, mass transfer, and bubble size data was collected for amplitudes of 4.5, 6.5, and 9.5 mm at frequency ranges of 7.5 – 22.5 Hz. The vibration conditions at higher amplitudes have not been tested in previous work and the experiments were performed to determine if there was any separate influence on k_La, ε, and d_{32}. The results showed special cases exist where mass transfer improvement is achieved for a reduced power requirement when a frequency trade was accomplished. Frequency maxima were apparent in the high amplitude data which was similar to that for low frequency found in this research and in the literature. Additionally, a maximum amplitude was observed to exist for k_La data, but not for ε. The data was analyzed using statistical methods and ANOVA to determine if a unifying parameter existed that could predict void fraction and mass transfer. The results show that mass transfer can be predicted by a combination of superficial gas velocity (U_{SG}), specific power input (P_m), and Bjerknes number (Bj). The model predicted for mass transfer is similar to that proposed by Waghmare (2008) but with different exponential values, especially for P_m which

showed a reduced influence than the theory. Upon closer inspection of the data provided by Waghmare showed that the reported results were not statistically equivalent to the theory suggested by him. A combined data set consisting of data from this research and that of Waghmare (2008) was modeled using a general linear ANOVA which predicts mass transfer based upon the actual experimental results. A similar analysis performed for ε, showed Waghmare's data to be influenced primarily by U_{SG} and P_m predicted by his theory. However, data from this research was highly influenced by Bj. The difference in results is not well known, but may be due to the method of vibrating the column, or the method to determine void fraction.

Bubble size distributions were determined from photographs taken at three column heights during vibration and static conditions. The results showed that d_{32} decreased with increasing frequency as expected, and increasing amplitude caused a shift to the left on the frequency scale. The size distributions were found to be non-normal as suggested in the research performed for vibrating columns, but rather showed to be log-normal. However, similar log-normal distributions have been reported for bubble sizes directly measured by optical probe in static BCRs. The photographic processing method was determined to be susceptible to error due to processing bias and bubble clustering which is common during most vibration cases. Sauter mean diameter did not appear to exhibit a minimum in the frequency range tested, but the smallest values (A ~ 2 mm) were obtained at high frequency and amplitude combinations. The additional data provided by this research is determined to be beneficial as a contribution to the overall research effort and the experimental set up can be used to provide valuable data for future use. However, there are a few recommendations that are suggested.

6.2. Recommendations

A number of issues arose throughout this research which should be addressed and/or changed before other research should proceed. Additionally, there are a variety of recommendations that can be made for the future use of the experimental set up in part or as a

whole including modifications to the set up and new experiments. A list and short description of recommendations is provided, but these recommendations are by no means inclusive. The list is divided by recommendations concerning the experimental set up or hardware, and concerning new/future research.

6.2.1. Experimental Setup

- Modification of the current shaker: Slight modification of the current shaker could be made to improve the baseline design, including modifying the components to reduce mechanical tolerances if desired.
- Modification to DO probe: A more robust probe could be used for future vibration testing. Additionally, the method of sampling could be changed as well, which places the sensor at a stable location and drives a sample to the probe. An example would be to create a tapped column, similar to pressure taps, which would feed a small, low turbulence, sealed pump to deliver a column averaged fluid sample past a DO probe at the appropriate flow velocity. This would be similar to how they conduct in line sampling in processing plants.
- Data Acquisition & Interactive Control: A simple data acquisition unit was used to suit the purposes of validation and simple testing. A more robust system should be used in order to gather more sensor data in a unified system. A LabView program could be written to collect and analyze the data as the experiment occurs. Additionally, the speed controller is capable of being monitored and controlled electronically, which could also being integrated into a I/O data acquisition module and controlled by the same LabView routine. This single point experimental monitor and control would provide much more efficiency to the experimental set up and increase data fidelity and reliability.

- Void Fraction Measurement: A better void fraction measurement technique is suggested over the method used in this research. The possibility exists to use a manometry method, but the results show that is subject to flaws as well.
- Bubble Size Measurement: A better method to determine bubble sizes is needed, or the scope of the measurements should be limited to conditions where bubble separation is enough to ensure the processing routine does not overestimate overlapping bubbles.
- Superficial Gas Velocity Measurement: The current method to determine U_{SG} from mass flow meter data and the gas density is not equivalent to that of previous research and the reliance on gas volumetric flow meter data. It is important to determine which method is more correct or appropriate and establish compatibility or equivalency between the two so that data could be cross correlated more accurately.

6.2.2. Future Research

- Flow Visualization: Little has been done to properly visualize the flow to understand the flow properties as they relate to the two phases in the vibration environment. One example is to determine by seeding the flow with dye or particulates to determine the relative fluid motion, velocity gradients, etc. compared to the gas motion. Another example would be to use laser Doppler or laser particle tracking type technologies to measure the velocity vectors for each phase.
- Direct Probes: 4 point optical probes have been found to work well in providing bubble size, velocity, and void fraction data. This technology could be developed and implemented on the column as a means of re-measuring some of the responses found during this work or separate works concerning vibration BCR. Additionally, electrical probes of a similar design could also be used.
- Effect of Column Size and Fluid Properties: This work prepared an experimental set up and some tools needed to perform experiments with different size/height columns as well

as fluid properties. Additionally the effect of injector size on mass transfer could easily be implemented to determine the cause of the trend slope deficiency of this research when compared to Waghmare.

- Bubble breakage mechanisms and Entry Length: It was observed during this research that unique bubble breakage phenomena exist within the vibrating BCR. It would be an interesting study to use flow visualization to determine the phenomenological sources behind the bubble breakage mechanism. This research could directly feed into and from Waghmare's model to predict void fraction and mass transfer based on Hinze's breakage model (Figure 6.1)

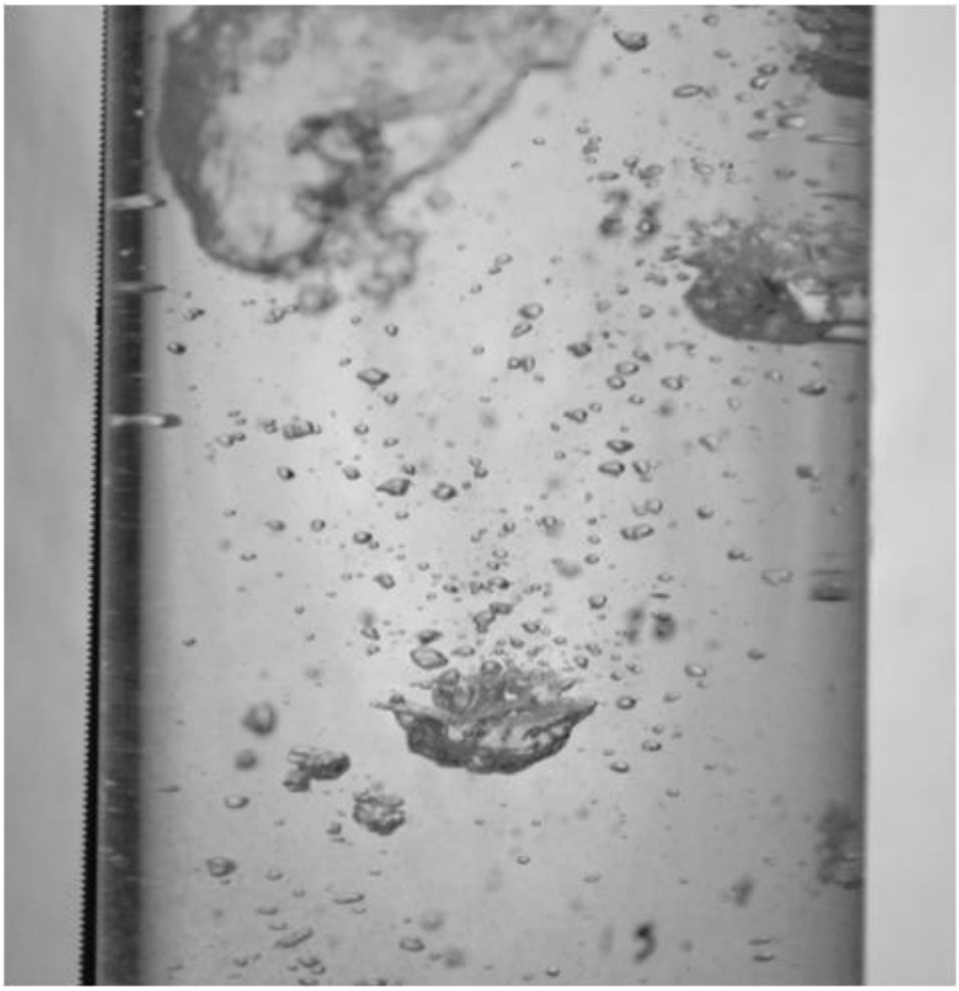

Figure 6.1: Photograph of bubble breakage phenomena in vibrating BCR

It was also observed that as vibration power was increased the column location of nearly homogenized mono-disperse bubbles would move closer to the injector. Eventually the point of mono-dispersion reaches the injector and the system stalls until backpressure or bubbles from the interface can coalesce at the column bottom to force the cyclic froth bands discussed. It would be an interesting study to determine the relationship between vibration frequency and amplitude and this "entry length" point of homogenized bubbles. One could see an analogy to fully developed flow entry length in pipes for single phase flow.

- Bjerknes vs. P_m effects: It was a noted outcome of this work that there are correlations and models needed to predict mass transfer and void fraction from Bj, P_m, and U_{SG} influences. There are deficiencies still in the models presented for k_La by Waghmare. It is recommended that a set of balanced, orthogonal, statistically designed experiments be performed to determine the exact nature of the input parameters on mass transfer and void fraction. Physics based models can more easily be determined or adjusted from the results of this type of research.
- Heat transfer, co-current/counter-current flow, etc.: A host of modifications could be made to the BCR to adapt the current set up in order to perform a variety of tests. Interesting experiments would include the effect of vibration on heat transfer systems that could have a unique impact on compact heat exchanger design. Additionally the BCR could be turned into a co-current flow or counter current flow reactor or pipe to test the effect of vibration on non-batched multiphase systems.

The imagination and reasonable engineering need are the only limits to the studies that could be performed using this experimental set up. It is hoped that a host of beneficial research projects can be performed with the shaker system and experimental set up in the future.

REFERENCES

Bai, W., Deen, N.G., Mudde, R.F., and Kuipers, J.A.M. (2008), Accuracy of Bubble Velocity Measurement With a Four-Point Optical Fibre Probe, 6th International Conference on CFD in Oil & Gas, Metallurgical and Process Industries SINTEF/NTNU, Trondheim, Norway, 10-12 June 2008.

Baird, M.H.I. (1963), Resonant Bubbles in a Vertically Vibrating Liquid Column, The Canadian Journal of Chemical Engineering, pp. 52-55.

Baird, M.H.I. and Davidson, J.F. (1962), Gas Absorption by Large Rising Bubbles, Chemical Engineering Science, Vol. 17, pp. 87-93.

Baird, M.H.I. and Garstang, J.H. (1967), Power Consumption and Gas Hold-Up in a Pulsed Column, Chemical Engineering Science, Vol. 22, pp. 1663-1673

Baird, M.H.I. and Garstang, J.H. (1972), Gas Absorption in a Pulsed Bubble Column, Chemical Engineering Science, Vol. 27, pp. 823-833.

Benedek, A.A. and Heideger, W.J. (1970), Polarographic Oxygen Analyzer Response: The Effect of Instrument Lag in the Non-Steady State Reaeration Test, Water Research, Vol. 4, pp. 627-640.

Bjerknes, V.F.K. (1906), Fields of Force: Supplementary Lectures, Applications to Meteorology, Reproduced by Cornell University Library, Ithaca, New York, Original by The Columbia University Press/The Macmillan Company, London.

Bretsznajder, S., Jaszczak, M., and Pasiuk, W. (1963), Increasing the Rate of Certain Industrial Chemical Processes by the Use of Vibration, International Chemical Engineering, Vol. 3, Issue 4, pp. 496-502.

Buchanan, R.H., Jameson, G., and Oedjoe, D. (1962), Cyclic Migration of Bubbles in Vertically Vibrating Liquid Columns, I&EC Fundamentals, Vol. 1, No. 2, pp. 82-86.

Cartellier, A. (2001), Optical Probes for Multiphase Flow Characterization: Some Recent Improvements, Chemical Engineering Technology, Vol. 24, No. 5, pp. 535-538.

Çengel, Y. and Ghajar, A. (2011), Fundamentals of Heat and Mass Transfer, 4th ed., McGraw-Hill, New York, NY., pp. xx.

Clark, N.N., Atkinson, C.M. and Flemmer, R.L.C. (1987), Turbulent Circulation in Bubble columns, AIChE Journal, Vol. 33, No. 3, pp. 515-518.

Cook, W. (2004), An Experimental Apparatus for Measurement of Pressure Drop, Void Fraction, and Non-Boiling Two-Phase Heat Transfer and Flow Visualization in Pipes for All Inclinations, M.S. Thesis, Oklahoma State University, Stillwater, OK.

Dudukovic, M.P., Fan, L.-S., Chang, M. (1999), Novel Techniques for Slurry Bubble Column Hydrodynamics, Final Technical Report, Department of Energy Award No. DE FG 22-95 PC 95212.

Ellenberger, J. and Krishna, R. (2003), Shaken, Not Stirred, Bubble Column Reactors: Enhancement of Mass Transfer by Vibration Excitement, Chemical Engineering Science, Vol. 58, pp. 705-710.

Ellenberger, J., van Baten, J.M, and Krishna, R. (2005), Exploiting the Bjerknes Force in Bubble Column Reactors, Chemical Engineering Science, Vol. 60, pp. 5962-5970.

Environmental Leader (2010), United Airlines Tests Synthetic Jet Fuel on Commercial Flight, www.environmentalleader.com.

Fan, J.M. and Cui, Z. (2005), Effect of Acoustic Standing Wave in a Bubble Column, Industrial and Engineering Chemistry Research, Vol. 44, pp. 7010-7018.

Fan, L-S. (1989), Gas-Liquid-Solid Fluidization Engineering, 1st Edition, Butterworth Publishers, Stoneham, MA.

Frijlink, J.J. (1987), Physical Aspects of Gassed Suspension Reactors, PhD Dissertation, Delft University, Delft, Netherlands.

George, D.L., Shollenberger, K.A. and Torczynski, J.R. (2000), Sparger Effects on Gas Volume Fraction Distributions in Vertical Bubble-Column Flows as Measured by Gamma-Densitometry Tomography, Proceedings of 2000 ASME Fluids Engineering Division Summer Meeting, Boston, MA, June 11-15.

Ghiaasiaan, S.M. (2008), Two Phase Flow, Boiling, and Condensation in Conventional and Miniature Systems, 1st Edition, Cambridge University Press, Ithaca, NY.

Guet, S., Fortunati, R.V., Mudde, R.F. and Ooms, G. (2003), Bubble Velocity and Size Measurement with a Four-Point Optical Fiber Probe, Particle and Particle Systems Characterization, Vol. 20, pp. 219-230.

Guet, S., Luther, S. and Ooms, G. (2005), Bubble Shape and Orientation Determination With a Four-Point Optical Fibre Probe, Experimental Thermal and Fluid Science, Vol. 29, pp. 803-812.

Harbaum, K.L. and Houghton, G. (1960), Effects of Sonic Vibrations on the Rate of Absorption of Gases From Bubble Beds, Chemical Engineering Science, Vol. 18, pp. 90-92.

Harbaum, K.L. and Houghton, G. (1962), Effects of Sonic Vibrations on the Rate of Absorption of Carbon Dioxide in Gas Bubble-Beds, Journal of Applied Chemistry, Vol. 12, pp.234-240.

Hinze, J.O. (1955), Fundamentals of the Hydrodynamic Mechanism of Splitting in Dispersion Processes, AIChE Journal, Vol. 1, No. 3, pp. 289-295.

Houghton, G. (1963), The Behaviour of Particles in a Sinusoidal Velocity Field, Proceedings of the Royal Society of London, Series A, Mathematical and Physical Sciences, Vol. 272, No. 1348, pp. 33-43.

Huang, Z., Wang, B., and Li, H. (2003), Application of Electrical Capacitance Tomography to the Void Fraction Measurement of Two-Phase Flow, IEEE Transactions on Instrumentation and Measurement, Vol. 52, No. 1, pp. 7-12.

Jameson, G.J. (1966), The Motion of a Bubble in a Vertically Oscillating Viscous Liquid, Chemical Engineering Science, Vol. 21, pp. 35-48.

Jameson, G.J. and Davidson, J.F. (1966), The Motion of a Bubble in a Vertically Oscillating Liquid: Theory For an Inviscid Liquid, and Experimental Results, Chemical Engineering Science, Vol. 21, pp. 29-34.

Julia, J.E., Hartveld, W.K., Mudde, R.F. and Van den Akker, H.E.A. (2005), On the Accuracy of the Void Fraction Measurements Using Optical Probes in Bubbly Flows, Review of Scientific Instruments, Vol. 76, pp. 1-13.

Khonsari, M.M. and Booser, E.R. (2001), Applied Tribology: Bearing Design and Lubrication, 1st ed., John Wiley & Sons, Inc., New York, New York.

Knopf, F.C., Ma, J., Rice, R.G. and Nikitopoulos, D. (2005a), Pulsing to Improve Bubble Column Performance: I. Low Gas Rates, AIChE Journal, Vol. 52, No. 3, pp. 1103-1115.

Knopf, F.C., Waghmare, Y., Ma, J. and Rice, R.G. (2005b), Pulsing to Improve Bubble Column Performance: II. Jetting Gas Rates, Association of International Chemical Engineers Journal, Vol. 52, No. 3, pp. 1116-1126.

Krishna, R., Ellenberger, J., Urseanu, M.I., Keil, F.J. (2000), Utilisation of Bubble Resonance Phenomena to Improve Gas-Liquid Contact, Naturwissenschaften, Vol. 87, pp. 455-459.

Krishna, R. and Ellenberger, J. (2002), Improving Gas-Liquid Contacting in Bubble Columns by Vibration Excitement, International Journal of Multiphase Flow, Vol. 28, pp. 1223-1234.

Kulkarni, A.A. and Joshi, J.B. (2005), Bubble Formation and Bubble Rise Velocity in Gas-Liquid Systems: A Review, Industrial Engineering Chemical Resources, Vol. 44, pp. 5873-5931.

Lewis, D.A. and Davidson, J.F. (1983), Bubble Sizes Produced by Shear and Turbulence in a Bubble Column, Chemical Engineering Science, Vol. 38, No. 1, pp. 161-167.

Luther, S., Rensen, J. and Guet, S. (2004), Bubble Aspect Ratio and Velocity Measurement Using a Four-Point Fiber-Optical Probe, Experiments in Fluids, Vol. 36, pp. 326-333.

Lowery, R.L., Personal Communication, 6 Feb 2012.

Manasseh, R., LaFontaine, R.F., Davy, J., Shepher, I. and Zhu, Y.-G. (2001), Passive Acoustic Bubble Sizing in Sparged Systems, Experiments in Fluids, Vol. 30, pp. 672-682.

Minnaert, M. (1933), On Musical Air-Bubbles and the Sounds of Running Water, The London, Edinburgh and Dublin Philosophical Magazine and Journal of Science, Vol 16, No. 104, pp. 235-248.

Mudde, R.F. and Saito, T. (2001), Hydrodynamical Similarities Between Bubble Column and Bubbly Pipe Flow, Journal of Fluid Mechanics, Vol. 437, pp. 203-228.

Nakanoh, M., Yoshida, F. (1980), Gas Absorption by Newtonian and Non-Newtonian Liquids in a Bubble Column, Industrial Engineering Chemical Process Design and Development, Vol. 19, pp. 190-195.

Ni, X. and Gao, S. (1996), Scale-Up Correlation for Mass Transfer Coefficients in Pulsed Baffled Reactors, Chemical Engineering Journal, Vol. 63, pp. 157-166.

Oliveira, M.S.N. and Ni, X. (2001), Gas Hold-Up and Bubble Diameters in a Gassed Oscillatory Baffled Column, Chemical Engineering Science, Vol. 56, pp. 6143-6148.

Product Bulletin (2008), Weld-On 10 Structural Adhesive, IPS Corporation, Compton, CA.

Raju, K.S.N. (2011), Fluid Mechanics, Heat Transfer, and Mass Transfer: Chemical Engineering Practice, John Wiley and Sons, Inc., Hoboken, New Jersey, pp. 455-473.

Redfield, J.A. and Houghton, G. (1965), Mass Transfer and Drag Coefficients for Single Bubbles at Reynolds Numbers of 0.02-5000, Chemical Engineering Science, Vol. 20, pp. 131-139.

Shah, Y.T., Kelkar, B.G., Godbole, S.P. (1982), Design Parameters Estimations for Bubble Column Reactors, AIChE Journal, Vol. 28, No. 3, pp. 353-379.

Smith, F.D. (1935), On the Destructive Mechanical Effects of the Gas Bubbles Liberated by the Passage of Intense Sound Through a Liquid, Philosophy Magazine, Vol. 8.

Rice, R.G., Barbe, D.T. and Geary, N.W. (1990), Correlation of Nonverticality and Entrance Effects in Bubble Columns, AIChE Journal, Vol. 36, No. 9, pp. 1421-1424.

Rodgers, A. and Hughes, D.E. (1960), The Disintegration of Micro-organisms by Shaking with Glass Beads, Journal of Biochemical and Microbiological Technology and Engineering, Vol. 2, No. 1, pp. 49-70.

Tapley, B.D. (1990), Eschbach's Handbook of Engineering Fundamentals, 4th ed., John Wiley & Sons, Inc., New York, NY., pp.14.33.

Torobin, L.B. and Gauvin, W.H. (1961), The drag coefficients of single spheres moving in a steadily accelerated motion in a turbulent fluid , AIChE Journal, Vol. 7, pp. 615-619.

U.S. Air Force (2007), C-17 uses synthetic fuel blend on transcontinental flight, http://www.af.mil/news/story.asp?id=123079891.

U.S. Department of Defense (2010), A-10 Flies on Synthetic Fuel Blend, http://www.defense.gov/news/newsarticle.aspx?id=58488.

Vogelaar, Rob (2011), F-22 Raptor Flown on Synthetic Biofuel, aviationnews.eu, http://www.aviationnews.eu/2011/03/24/f-22-raptor-flown-on-synthetic-biofuel.

Vogelaar, Rob (2010), Lufthansa and Airbus Launch Worlds First Passenger Bio-Fuel Flights, aviationnews.eu, http://www.aviationnews.eu/2010/11/29/lufthansa-and-airbus-launch-worlds-first-passenger-bio-fuel-flights.

Waghmare, Y.G. (2008), Vibrations for Improving Multiphase Contact, PhD Dissertation, Louisiana State University, Baton Rouge, LA.

Waghmare, Y.G., Knopf, F.C. and Rice, R.G. (2007), The Bjerknes Effect: Explaining Pulsed-Flow Behavior in Bubble Columns, AIChE Journal, Vol. 53, No. 7, pp. 1678-1686.

Waghmare, Y.G., Rice, R.G. and Knopf, F.C. (2008), Mass Transfer in a Viscous Bubble Column with Forced Oscillations, Industrial and Chemical Engineering Research, Vol. 47, pp. 5386-5394.

Water on the Web (2007), Dissolved Oxygen, http://www.waterontheweb.org/under/waterquality/oxygen.html.

Wu, C., Suddard, K. and Al-Dahhan, M.H. (2008), Bubble Dynamics Investigation in a Slurry Bubble Column, AIChE Journal, Vol. 54, No. 5, pp. 1203-1212.

Xue, J., Al-Dahhan, M.H. and Dudukovic, M.P. (2008a), Bubble Velocity, Size, and Interfacial Area Measurements in a Bubble Column by Four-Point Optical Probe, AIChE Journal, Vol. 54, No. 2, pp. 350-363.

Xue, J., Al-Dahhan, M.H., Dudukovic, M.P. and Mudde, R.F. (2008b), Four-Point Optical Probe for Measurement of Bubble Dynamics: Validation of the Technique, Flow Measurement and Instrumentation, Vol. 19, pp. 293-300.

Xue, J. (2004), Bubble Velocity, Size and Interfacial Area Measurements in Bubble Columns, PhD Dissertation, Washington University, St. Louis, MO.

Youssef, A.A. and Al-Dahhan, M.H. (2009), Impact of Internals on the Gas Holdup and Bubble Properties of a Bubble Column, Industrial and Chemical Engineering Research, Vol. 48, pp. 8007-8013.

Zhu, Y., Wu, J. and Manasseh, R. (2001), Rapid Measurement of Bubble Size in Gas-Liquid Flows Using a Bubble Detection Technique, 14th Australasian Fluid Mechanics Conference, Adelaide University, Adelaide, Australiea, 10-14 December 2001.

APPENDIX A

CALCULATIONS AND DERIVATIONS

A.1: Derivation of Oscillatory Motion

Let the position of the body be described by,

$$z = A\sin(\omega t)$$

where A is the amplitude of motion (m) as shown in the Figure A1, ω is the angular frequency (rad/s) and t is the time (s). Note: $\omega = 2\pi f$ with f being the frequency (s^{-1})

The velocity (m/s) of the object can be described by the time derivative of the displacement as,

$$u = \frac{dz}{dt} = Aw\cos(\omega t)$$

Finally, the acceleration (m/s^2) of the body is described by taking the time derivative of the velocity as,

$$a = \frac{du}{dt} = \frac{d^2z}{dt^2} = -Aw^2\sin(\omega t)$$

A.2: Derivation of Specific Power Input (P_m) (Waghmare 2008)

The derivation which follows for the specific power input for bubbly flow is taken in part from Baird and Rice (1975.

Assuming all forces and gas/liquid velocities act only in the z-direction, power can be determined by the product of force and velocity by,

$$P = F \cdot v$$

Consider a unit volume of dispersed bubbly flow in the column acted upon by liquid hydrostatic pressure and traveling at superficial gas velocity (Figure A.1).

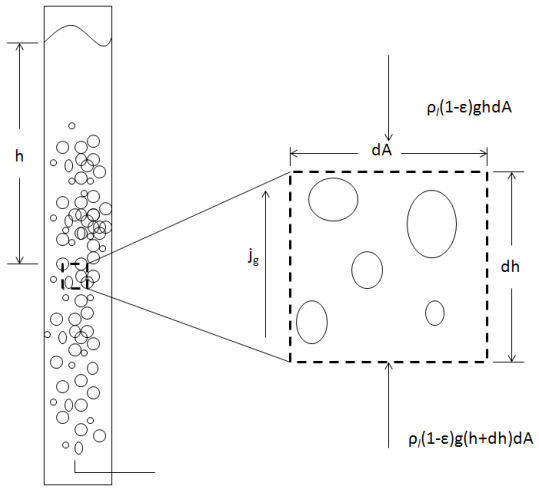

Figure A.1: Force balance diagram of dispersed bubbly flow in a liquid column

A force balance on the control volume would show,

$$dF = \rho(1-\varepsilon)gdhdA$$

Therefore integration over the column height of the unit volume ($dA = 1$) gives,

$$F = \rho(1-\varepsilon)ghA$$

Thus the power is simply,

$$P = \rho(1-\varepsilon)ghAU_{SG}$$

Dividing by the unit volume mass gives the specific power input of the gas flow from the injector (W/kg),

$$P_b = \frac{\rho(1-\varepsilon)ghAU_{SG}}{\rho(1-\varepsilon)hA} = gU_{SG}$$

Additionally for the case of an oscillating column the fluid volume is acted upon by the vibration pressure and speed. Taking the force to be,

$$F_v = -\rho(1-\varepsilon)V_0\omega^2 A\sin\omega t$$

The power can be determined by,

$$P_v = -\rho(1-\varepsilon)V_0\omega^3 A^2 \sin\omega t\cos\omega t$$

Similarly, dividing by the unit volume mass gives the specific power input through vibration as,

$$P_v = \frac{-\rho(1-\varepsilon)V_0\omega^3 A^2 \sin\omega t\cos\omega t}{\rho(1-\varepsilon)V_0} = \omega^3 A^2 \sin\omega t\cos\omega t$$

Notice that the equation above reaches a maximum and minimum at $\omega t = \pi/4$. Since we are interested only in scaling effects we can take the magnitude of the power to be,

$$P_v = \frac{1}{2}\omega^3 A^2$$

Therefore, the combined specific power input to the system, assuming negligible energy dissipation in the gas bubble is simply the sum of the power input from the injector and the power input from vibration given by,

$$P_m = gU_{SG} + \frac{1}{2}\omega^3 A^2$$

A.3: Flywheel and Motor Power Calculations (Mathcad Document)

$$Energy := \int_0^{\frac{1}{\omega}\frac{\pi}{2}} Power(t)\,dt = 191.345 \quad (ft - lbf / sec) \qquad PctLoss := 10 \qquad FlywheelEnergy := Energy \cdot \frac{100}{PctLoss} = 1.913 \times 10^3 \quad (ft - lbf)$$

$$I := \frac{2 \cdot FlywheelEnergy}{\omega^2} = 0.027 \quad (lbf - ft^2) \qquad I_{add} := 0.01795 \quad \text{<------from Pro-E calculation of Iyy of crankshaft}$$

$$flywheelmass := \frac{13.5}{32.2} = 0.419 \quad (slug) \qquad r := \sqrt{\frac{2 \cdot (I - I_{add})}{flywheelmass}} \cdot 12 = 2.483 \quad (in) \qquad 2 \cdot r = 4.966 \quad (in)$$

$$FlywheelEnergy - Energy = \frac{1}{2} \cdot I \cdot \omega_{min}^2 \qquad \omega_{min} := \sqrt{\frac{2 \cdot (FlywheelEnergy - Energy)}{I}} = 357.645 \quad (rad / sec) \qquad \frac{\omega_{min}}{\omega} = 0.949$$

$$newPctLoss := \frac{\omega - \omega_{min}}{\omega_{min}} \cdot 100 = 5.409$$

$$MotorPwr := Energy \cdot \frac{newPctLoss}{100} \cdot f = 621.02 \quad (ft - lbf / sec) \qquad MotorTorque := \frac{MotorPwr}{\omega} = 1.647 \quad (ft - lbf)$$

$$MotorHP := \frac{MotorPwr}{550} = 1.129$$

$$SF := 1.5$$

$$MotorHP_{SF} := SF \cdot MotorHP = 1.694$$

A.4: Sizing of Bearing Pins and Drive Shafts

Early shaft sizing for bearing pins was determined based on distortion due to bending and the limiting case of angular deflection at the bearing. Shigley and Mischke (1996) recommend no more than 0.004 rad of angular deflection at the centerline of deep groove roller bearings. This value is also taken as a measure for the journal bearings used for the RB design.

Final shaft sizing and hollow bearing pins were done in Pro-E Mechanica using FEM to analyze stress and deflection.

Based upon Shigley and Mischke (1996) the minimum shaft diameter for a selected deflection angle, input forces, input moments and material properties is given for the left bearing as,

$$d = \left(\frac{32n}{3\pi E l \Sigma\theta} \left\{ \begin{matrix} \left[\sum F_i b_i \left(b_i^2 - l^2 \right) + \sum M_i \left(3a_i{}^2 - 6a_i l + 2l^2 \right) \right]_H^2 + \\ \left[\sum F_i b_i \left(b_i^2 - l^2 \right) + \sum M_i \left(3a_i{}^2 - 6a_i l + 2l^2 \right) \right]_V^2 \end{matrix} \right\}^{1/2} \right)^{1/4}$$

and for the right bearing as,

$$d = \left(\frac{32n}{3\pi E l \Sigma\theta} \left\{ \begin{matrix} \left[\sum F_i a_i \left(l^2 - a_i^2 \right) + \sum M_i \left(3a_i{}^2 - l^2 \right) \right]_H^2 + \\ \left[\sum F_i b_i \left(l^2 - a_i^2 \right) + \sum M_i \left(3a_i{}^2 - l^2 \right) \right]_V^2 \end{matrix} \right\}^{1/2} \right)^{1/4}$$

where n is the safety factor, E is Young's Modulus (psi), and Σθ is the maximum deflection angle (rad) and the other parameter follow from Figure A.2.

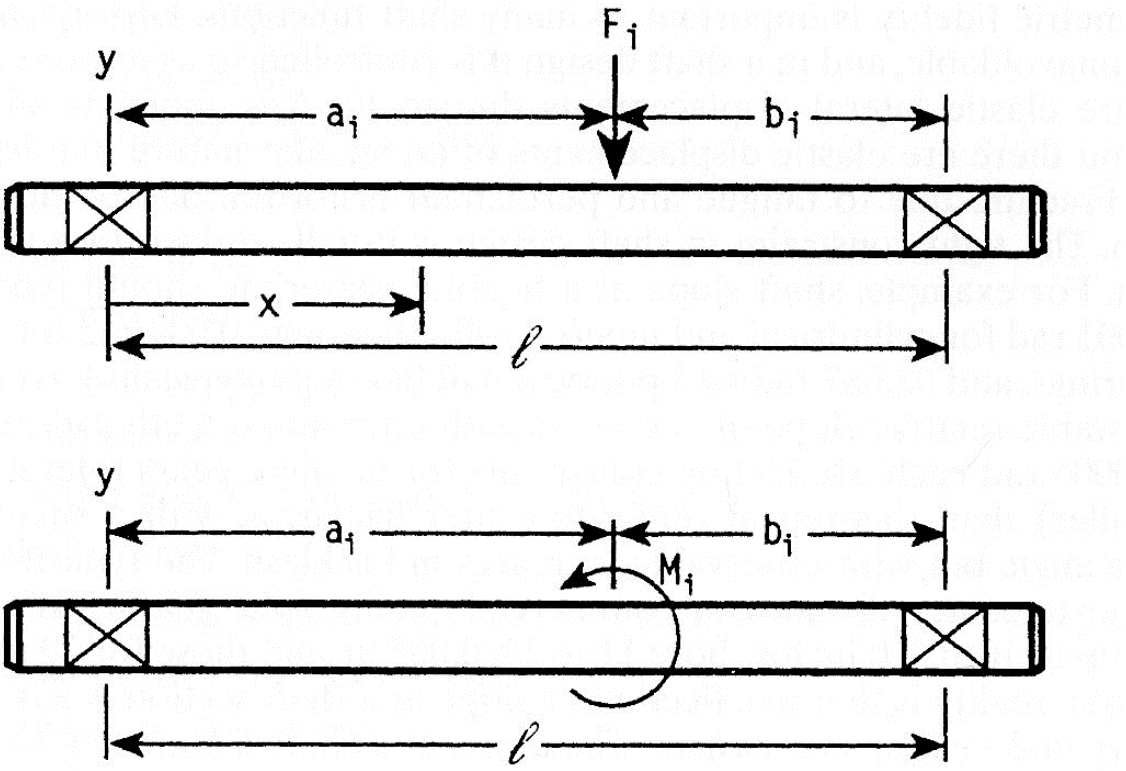

Figure A.2: Force and Moment diagram for a simply supported shaft (Shigley and Mischke, 1996)

The following calculations for the RB journal bearings pins were performed using Mathcad.

Bearing location at the table and pivot,

$theta := .004$

$L := 4$ inches

$F_1 := 9200$

$SF := 2$

$E := 29 \cdot 10^6 = 2.9 \times 10^7$

$b_1 := \frac{L}{2}$

$S_y := 70.3 \times 10^3$

$a_1 := L - b_1$

$$Ldiam := \left[\frac{32 \cdot SF}{3 \cdot \pi \cdot E \cdot L \cdot theta} \cdot \left[\left[F_1 \cdot b_1 \cdot \left({b_1}^2 - L^2 \right) \right]^2 \right]^{\frac{1}{2}} \right]^{\frac{1}{4}} = 1.341$$

$$Rdiam := \left[\frac{32 \cdot SF}{3 \cdot \pi \cdot E \cdot L \cdot theta} \cdot \left[\left[F_1 \cdot a_1 \cdot \left(L^2 - {a_1}^2 \right) \right]^2 \right]^{\frac{1}{2}} \right]^{\frac{1}{4}} = 1.341$$

Check yield stress for symmetrically loaded shafts

$$M_{max} := \frac{F_1 \cdot L}{2} = 1.84 \times 10^4$$

$$diam_2 := \left(\frac{32 \cdot M_{max} \cdot SF}{\pi \cdot S_y} \right)^{\frac{1}{3}} = 1.747$$

Thus it is seen that bearing deflection is not actually the limiting case for such short shafts (pins), but rather the yield stress is critical. The shaft diameter at the table location was chosen to be 1.75 inches.

For the bearing location at the crankshaft,

$$\text{theta} := .004$$

$$L := 4 \quad \text{inches}$$

$$F_1 := 5500$$

$$SF := 2$$

$$E := 29 \cdot 10^6 = 2.9 \times 10^7$$

$$b_1 := \frac{L}{2}$$

$$S_y := 70.3 \times 10^3$$

$$a_1 := L - b_1$$

$$Ldiam := \left[\frac{32 \cdot SF}{3 \cdot \pi \cdot E \cdot L \cdot \text{theta}} \cdot \left[\left[F_1 \cdot b_1 \cdot \left(b_1^{\,2} - L^2 \right) \right]^2 \right]^{\frac{1}{2}} \right]^{\frac{1}{4}} = 1.179$$

$$Rdiam := \left[\frac{32 \cdot SF}{3 \cdot \pi \cdot E \cdot L \cdot \text{theta}} \cdot \left[\left[F_1 \cdot a_1 \cdot \left(L^2 - a_1^{\,2} \right) \right]^2 \right]^{\frac{1}{2}} \right]^{\frac{1}{4}} = 1.179$$

Check yield stress for symmetrically loaded shafts

$$M_{max} := \frac{F_1 \cdot L}{2} = 1.1 \times 10^4$$

$$diam_2 := \left(\frac{32 \cdot M_{max} \cdot SF}{\pi \cdot S_y} \right)^{\frac{1}{3}} = 1.472$$

The pin diameter at the crankshaft was thus designed to be 1.50 inches.

For the drive shaft diameter of the EDM design the limiting load is determined by the roller bearing dynamic load (3400 lb). It is not recommended to exceed this load during experimentation, but considering a load case that is 150% greater gives 5200 lbs. The load acts on the cylinder which is assumed to distributed to the drive shaft equally through the two adjustment bolts separated by 4.6 inches. The total length of the shaft is 9 in. from bearing center to center. The design calculation follows as,

$theta := .004$

$L := 9$ inches

$F_1 := 2600 \qquad F_2 := 2600$

$SF := 2$

$E := 29 \cdot 10^6 = 2.9 \times 10^7$

$b_1 := 2.2 \qquad b_2 := b_1 + 4.6$

$S_y := 70.3 \times 10^3$

$a_1 := L - b_1 \qquad a_2 := L - b_2$

$$Ldiam := \left[\frac{32 \cdot SF}{3 \cdot \pi \cdot E \cdot L \cdot theta} \cdot \left[\left[F_1 \cdot b_1 \cdot \left(b_1^2 - L^2 \right) \right]^2 + \left[F_2 \cdot b_2 \cdot \left(b_2^2 - L^2 \right) \right]^2 \right]^{\frac{1}{2}} \right]^{\frac{1}{4}} = 1.488$$

$$Rdiam := \left[\frac{32 \cdot SF}{3 \cdot \pi \cdot E \cdot L \cdot theta} \cdot \left[\left[F_1 \cdot a_1 \cdot \left(L^2 - a_1^2 \right) \right]^2 + \left[F_2 \cdot a_2 \cdot \left(L^2 - a_2^2 \right) \right]^2 \right]^{\frac{1}{2}} \right]^{\frac{1}{4}} = 1.488$$

Check yield stress for symmetrically loaded shafts

$$M_{max} := \frac{F_1 \cdot L}{2} = 7.875 \times 10^3$$

$$diam_2 := \left(\frac{32 \cdot M_{max} \cdot SF}{\pi \cdot S_y} \right)^{\frac{1}{3}} = 1.317$$

A.5: Sizing of Slider Rod

The Pro-E results showed that the maximum X component (transverse) bearing loads were on the order of 1300 pounds. Assuming these loads to act upon both sliding rods and be distributed evenly allowed each rod to encounter a load of approximately 650 lbs. The minimum diameter of the shaft was thus sized using the same approach as previously described for the bearing pins. The length between the bearings is designed to be 6 in. However, the force does not act between the bearings but past both so the length of b1 is actually a negative value to account for the shift.

$$\text{theta} := .004$$

$$L := 6 \quad \text{inches}$$

$$F_1 := 650 \qquad F_2 := 00$$

$$SF := 2$$

$$E := 29 \cdot 10^6 = 2.9 \times 10^7$$

$$b_1 := -3 \qquad b_2 := b_1 + 6$$

$$S_y := 70.3 \times 10^3$$

$$a_1 := L - b_1 \qquad a_2 := L - b_2$$

$$\text{Ldiam} := \left[\frac{32 \cdot SF}{3 \cdot \pi \cdot E \cdot L \cdot \text{theta}} \cdot \left[\left[F_1 \cdot b_1 \cdot \left(b_1^2 - L^2 \right) \right]^2 + \left[F_2 \cdot b_2 \cdot \left(b_2^2 - L^2 \right) \right]^2 \right]^{\frac{1}{2}} \right]^{\frac{1}{4}} = 0.847$$

$$\text{Rdiam} := \left[\frac{32 \cdot SF}{3 \cdot \pi \cdot E \cdot L \cdot \text{theta}} \cdot \left[\left[F_1 \cdot a_1 \cdot \left(L^2 - a_1^2 \right) \right]^2 + \left[F_2 \cdot a_2 \cdot \left(L^2 - a_2^2 \right) \right]^2 \right]^{\frac{1}{2}} \right]^{\frac{1}{4}} = 1.266$$

Therefore the shaft size was selected as 1.5 in. based on available stock size.

A.6 Calculation of Saturation Oxygen Concentration for Excel (Water on the Web, 2007)

The following equations can be solved to give the equilibrium concentration at specific temperature (and pressure

$$\ln p = 5.25 \ln\left(1 - \frac{h_{alt}}{44.3}\right)$$

$$C_p = C^* p\left[\frac{(1 - p_{WV}/p)(1 - \theta p)}{(1 - p_{WV})(1 - \theta)}\right]$$

$$\theta = 9.75\times10^{-4} - 1.426\times10^{-5} T_{^\circ C} + 6.436\times10^{-8} T_{^\circ C}{}^2$$

$$\ln p_{wv} = 11.86 - \frac{3.841\times10^3}{T_K} - \frac{2.170\times10^5}{T_K{}^2}$$

where, h_{alt}, C_p, C^*, p_{wv}, and θ are the altitude (km), equilibrium oxygen concentration at nonstandard pressure (mg/L), equilibrium oxygen concentration at standard pressure (mg/L), the nonstandard pressure (atm) respectively. This equation can be solved in excel using the following:

```
=(($C$3*EXP(7.7117-1.31403*LN(B7+45.93)))*(1-EXP(11.8571-
(3840.7/(B7+273.15))-(216961/((B7+273.15)^2)))/$C$3)*(1-(0.000975-
(0.00001426*B7)+(0.00000006436*(B7^2)))*$C$3))/(1-EXP(11.8571-
(3840.7/(B7+273.15))-(216961/((B7+273.15)^2)))/$C$3)/(1-(0.000975-
(0.00001426*B7)+(0.00000006436*(B7^2))))
```

where pressure (atm) is C3 and water temperature (°C) is B7

A.7 ImageJ Macro for Analyzing Bubble Size Distributions

```
run("Subtract Background...", "rolling=80 light sliding");
setAutoThreshold("Default");
//run("Threshold...");
```

```
setThreshold(0, 240);

setThreshold(0, 240);

run("Convert to Mask");

run("Fill Holes");

run("Analyze Particles...", "size=0.75-Infinity circularity=0.05-1.00 show=Outlines display include in_situ");

run("Open Next");
```

A.8 VBA Routine to Filter DO Data

```
Sub DOcalc()
    Dim i As Integer, j As Integer, N As Integer, M As Integer, count As Integer
    Dim DOx(1000) As Double, DOx_avg As Double, time As Double, time_interval As Integer
    Dim sample_rate As Double

    'set the time interval desired
    time_interval = 3

    'set sample rate
    sample_rate = 1
    'set number of total ending data points
    N = 90

    'set number of points to average
    M = time_interval * sample_rate

    'initialize counters
    count = 0
    time = 0
    'set zero data point as DO_avg
    DOx_avg = Cells(5, 2)
```

```
'print DOx_avg
Cells(5, 6) = DOx_avg
'print initial time
Cells(5, 5) = time
'loop through data

For i = 1 To N
    'run through set to be averaged
    DOx_avg = 0
    For j = 0 To M - 1
        DOx(j) = Cells(6 + count, 2)
        count = count + 1
        DOx_avg = DOx_avg + DOx(j)
    Next j
    'update time
    time = time + time_interval
    'average DOx
    DOx_avg = DOx_avg / M
    'print time
    Cells(5 + i, 5) = time
    'print DOx avg
    Cells(5 + i, 6) = DOx_avg
Next i

'print time interval for reference
Cells(1, 9) = "time interval ="
Cells(1, 10) = time_interval
'print headings
Cells(2, 5) = "t*"
```

```
    Cells(3, 5) = "s"
    Cells(2, 6) = "DO AVG"
    Cells(3, 6) = "mg/L"
End Sub
```

APPENDIX B

UNCERTAINTY ANALYSIS

To evaluate the validity of the experimental setup and the results of the experiments performed an analysis of measurement uncertainty was performed. Three parameters are primarily discussed which include: vibration frequency and amplitude, acceleration, differential pressure, void fraction, bubble size, and volumetric mass transfer. The methods used to determine uncertainty are unique to each case, but in most cases the uncertainty is determined by a "general" formula for error propagation given by,

$$\sigma_k = \sqrt{\left(\frac{\partial k}{\partial x}\sigma_x\right)^2 + \ldots + \left(\frac{\partial k}{\partial z}\sigma_z\right)^2} \tag{B.1}$$

Different approaches are presented which combine the method above with meaningful statistical methods to offer a conservative estimate of uncertainty. The parameters are discussed in the same order as found in Chapter 5.

B.1. Vibration Frequency and Amplitude

The uncertainty in the amplitude and frequency of the vibration input has been quantified by measuring the individual components. The vibration amplitude is controlled by the speed controller and is assumed to be constant around the nominal value with a variation of ± 0.1 (Hz). The speed controller was randomly monitored and was never seen to exceed this value except for at high amplitudes (A > 6.5 mm) during which it would vary ± 0.2 (Hz). The variation at higher

amplitude was seen to be a result of control overshoot by the speed controller to compensate for the increased torque requirement. Therefore, assuming worst case for all conditions gives a conservative estimate of error thus the uncertainty for frequency is ± 0.2 (Hz)

The amplitude is calculated by dividing the stroke measurement. The stroke was measured before and after each run using a precision ruler with an accuracy of ± 0.25 mm. After several runs of the final shaker version no change was noticed in the amplitude before and after the run. Therefore no measurements were made after the amplitude was set. The final quoted amplitude is given an uncertainty of ± 0.13 mm, taken as half of the stroke.

The uncertainty in the peak acceleration (g's) imposed on the column can be calculated by modifying Eq. B.1 given the amplitude and frequency uncertainties. In this case it is more convenient that the uncertainty be expressed as a ratio given by,

$$\frac{\sigma_a}{|a|} = \pm\sqrt{\left(\frac{\sigma_A}{A}\right)^2 + \left(\frac{\sigma_f}{\pi f}\right)^2} \tag{B.2}$$

where the peak acceleration (g's) is given by,

$$a = \frac{4\pi^2 A f^2}{g} \tag{B.3}$$

Partial differentiation of Eq. B.3 gives,

$$\frac{\partial a}{\partial A} = \frac{4\pi^2 f^2}{g} \tag{B.4}$$

$$\frac{\partial a}{\partial f} = \frac{4\pi A f}{g} \tag{B.5}$$

A summary of the error involved for each test point is given in Table B.1.

Table B.1: Summary of acceleration error

		Amplitude (mm)														
		1.5			2.5			4.5			6.5			9.5		
		$\partial a/\partial A$	$\partial a/\partial f$	σ_a	$\partial a/\partial A$	$\partial a/\partial f$	σ_a	$\partial a/\partial A$	$\partial a/\partial f$	σ_a	$\partial a/\partial A$	$\partial a/\partial f$	σ_a	$\partial a/\partial A$	$\partial a/\partial f$	σ_a
Frequency (Hz)	7.5										2.0%	0.8%	2.8%	1.4%	0.8%	2.2%
	10	8.7%	0.6%	9.3%	5.2%	0.6%	5.8%	2.9%	0.6%	3.5%	2.0%	0.6%	2.6%	1.4%	0.6%	2.0%
	12.5	8.7%	0.5%	9.2%	5.2%	0.5%	5.7%	2.9%	0.5%	3.4%	2.0%	0.5%	2.5%	1.4%	0.5%	1.9%
	15	8.7%	0.4%	9.1%	5.2%	0.4%	5.6%	2.9%	0.4%	3.3%	2.0%	0.4%	2.4%	1.4%	0.4%	1.8%
	17.5	8.7%	0.4%	9.0%	5.2%	0.4%	5.6%	2.9%	0.4%	3.3%						
	19				5.2%	0.3%	5.5%									
	20	8.7%	0.3%	9.0%	5.2%	0.3%	5.5%									
	21				5.2%	0.3%	5.5%									
	22.5				5.2%	0.3%	5.5%									

B.2. Volumetric Mass Transfer Coefficient (k_La)

The volumetric mass transfer coefficient (k_La) is determined by linear regression of time based measurements of dissolved oxygen concentration. The model used to predict k_La is based upon an unsteady state mass balance of the system described by Equation 2.58. The solution to Eq. 2.58 gives Eq. 2.59 as described in §2.2.2. The linearization of Eq. 2.59 and solution of k_La from the regression is described in §4.2.3. Since k_La is determined from a linear regression it is appropriate that the uncertainty associated with the result is statistical.

Linear regression following a least squares approximation can be used to determine the coefficients A and B of the equation (Taylor, 1997):

$$y = A + Bx \tag{B.6}$$

where,

$$A = \frac{\sum x^2 \sum y - \sum x \sum xy}{N\sum x^2 - \left(\sum x\right)^2} \tag{B.7}$$

and,

$$B = \frac{N\sum xy - \sum x \sum y}{N\sum x^2 - \left(\sum x\right)^2} \tag{B.8}$$

The uncertainty in coefficient *B* can be determined using the "general" formula, and simplification gives,

$$\sigma_B = \sigma_y \sqrt{\frac{N}{N\sum x^2 - \left(\sum x\right)^2}} \tag{B.9}$$

For an in depth derivation of Eq. B.5 the reader is referred to Bevington and Robinson (2003). Since determination of k_La is equivalent to finding the coefficient *B* the uncertainty is simply,

$$\sigma_{k_La} = \sigma_{-Ln(C')} \sqrt{\frac{N}{N\sum t^2 - \left(\sum t\right)^2}} \tag{B.10}$$

The calculation of uncertainty can be performed using the Linear Regression tool found in the Excel Data Analysis Add-In. The two inputs (x,y) are input and the tool calculates the linear regression coefficients A and B as well as their individual standard error. Therefore, using time and $-\ln(C')$ as the x and y input ranges respectively, the Linear Regression Add In will output k_La and the standard error (σ_{kLa}) which is equivalent to Eq. B.6.

B.3. Void Fraction (ε)

The uncertainty of the void fraction is determined through a combination of statistics and use of Eq. B.1. At least 15 – 20 measurements are made using the procedure described in §4.2.5. The average of the samples is taken to represent the final added height. The standard error (a.k.a. standard error of the mean) is taken to be the uncertainty of the average measurement given by,

$$\overline{\sigma} = \frac{\sigma}{\sqrt{N}} \tag{B.11}$$

The final void fraction uncertainty is determined by modifying Eq. (B.1),

$$\sigma_{\varepsilon} = \pm\sqrt{\left(\frac{\partial\varepsilon}{\partial H_0}\sigma_{H_0}\right)^2 + \left(\frac{\partial\varepsilon}{\partial H}\sigma_{H}\right)^2} \tag{B.12}$$

where the partial derivatives of Eq. 2.56 are given by,

$$\frac{\partial\varepsilon}{\partial H_0} = -\frac{1}{H} \tag{B.13}$$

$$\frac{\partial\varepsilon}{\partial H} = \frac{H_0}{H^2} \tag{B.14}$$

B.4. Bubble Size as Sauter Mean Diameter (d_{32})

The bubble size distributions are determined using ImageJ to process pictures of 3 sections of the BCR as described in §4.2.2. There is considerable difficulty in establishing a definite uncertainty in measurements from a theoretical basis since the bubble distributions are taken from processed pictures. The best that can be said for the different distributions is a summary of the varying mean diameters including the Sauter Mean Diameter, the Mass Mean Diameter and the Average Diameter. Additionally the histogram of the distributions provides some insight, but these distributions have been found not to match well with a Gaussian or Normal distribution. In lieu of a theoretical analysis of uncertainty an attempt was made to qualify the uncertainty experimentally.

Approximately 20 airsoft pellets were placed in the filled column, and pictures were taken of the column section in the same manner as the bubble photographs from which the bubble size distributions were taken. Airsoft pellets are small (d ~ 6 mm) spherical pellets made from plastic. The pellets are not buoyant but when the column is agitated they will rise with the fluid currents where they can be photographed. A series of 22 photographs were available for

processing in ImageJ using the same routine as in §4.2.2. Only the calculated areas of the known pellets were taken from the processed images. The processing of the data followed the same pattern as the bubble size distribution. The pellets were taken from the column after draining and the diameter of each was measured 3 times using a precision 0 – 1 in. micrometer with an accuracy of ± 0.0001 in. The three measurements were averaged for each pellet and the lot was averaged to give the final average measured pellet diameter. The standard error of the Average Diameter is calculated using the standard deviation and Eq. 11. The standard error of the Mass Mean Diameter is calculated using Eq. B.11 where the standard deviation of the mass mean is given by,

$$\sigma_M = \pm\sqrt{\sum_{i=1}^{N}\left(d_i - \overline{d_M}\right)^2 f_M(d_i)} \tag{B.15}$$

The error associated with the Sauter Mean Diameter is calculated by assuming the worst case as either the largest diameter cubed divided by the smallest diameter squared or vice versa. Written mathematically this becomes,

$$\sigma_{d_{32}} = \pm\left(d_{32}{}^{worst} - d_{32}\right) \tag{B.16}$$

where,

$$d_{32}{}^{worst} = \frac{\sum_{i=1}^{N} n_i\left(d_i + \sigma_d\right)^3}{\sum_{i=1}^{N} n_i\left(d_i - \sigma_d\right)^2} \tag{B.17}$$

Determination of the uncertainty in diameter is derived from the uncertainty in the measured area produced by processing in ImageJ. Ultimately the uncertainty of the measured area is a product of the uncertainty of the calibration. The uncertainty of each calibration is given as the standard

error of a collection of 30 calibration measurements. The process to calculate Sauter Mean Diameter uncertainty is given by,

$$\sigma_{xs} = \frac{\partial A_{xs}}{\partial l_p} \bar{\sigma}_p \tag{B.18}$$

Since individual pixels are squares the cross-section area is simply a summation of square areas with sides l_p. Thus differentiating gives,

$$\frac{\partial A_{xs}}{\partial l_p} = 2 l_p \tag{B.19}$$

where l_p is the pixel to length conversion (pixels/mm) and $\bar{\sigma}_p$ is the standard error of the conversion (pixels/mm). When area is calculated the output is converted to mm^2 and the error is propagated through linearly. Converting the cross section area to an equivalent uniform sphere with diameter, d_{eq}, the uncertainty of which is calculated as,

$$\sigma_d = \frac{\partial d_{eq}}{\partial A_{xs}} \sigma_{xs} \tag{B.20}$$

where,

$$\frac{\partial d_{eq}}{\partial A_{xs}} = \frac{2\sigma_{xs}}{\pi d_{eq}} \tag{B.21}$$

The theoretical uncertainty associated with each average and the error in comparison to the measured pellet diameter is summarized in Table B.2. It should be noted that the uncertainty of the measured pellet diameter is much smaller than the average uncertainties and thus will be considered the absolute value when calculating the error between the average values and the known diameter.

Table B.2: Summary and comparison of bubble size uncertainty

Measured Pellet Diameter, d (mm)	5.90	±	0.01	Error (%)
Average Diameter, d_N (mm)	7.56		0.16	28
Mass Mean Diameter, d_M (mm)	8.35		0.22	41
Sauter Mean Diameter, d_{32} (mm)	8.03		0.11	36
Minimum Diameter	5.94			0.6
Maximum Diameter	11.97			103
Mode Diameter	6.62			12

As with the bubble size distributions it is valuable to give the histogram of the data (Figure B.1).

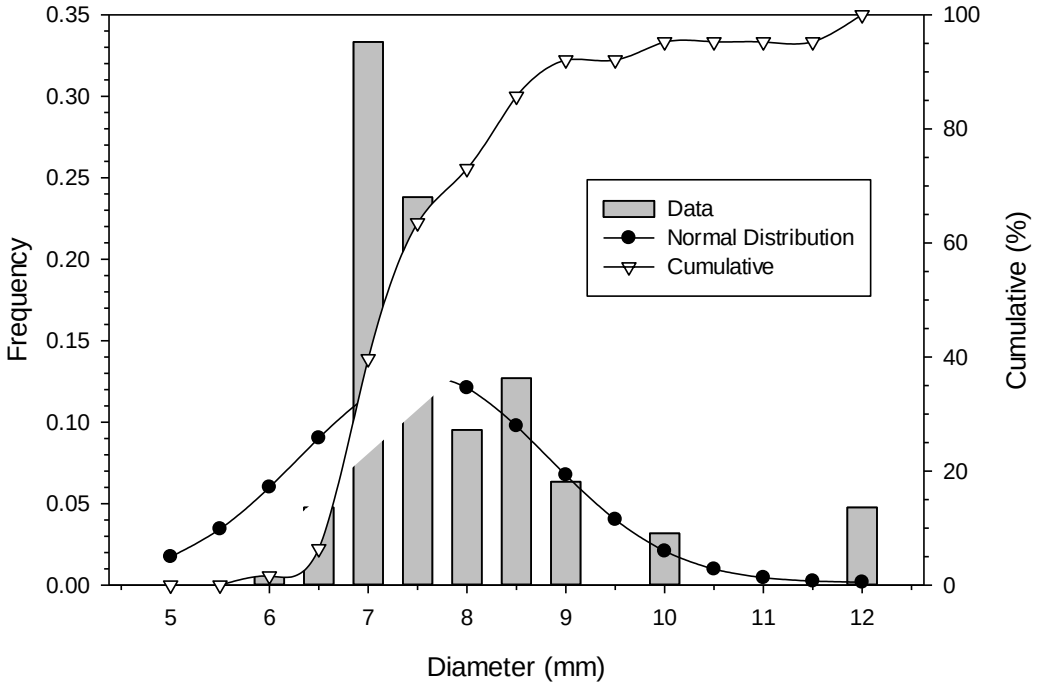

Figure B.1: Statistical summary of pellet size

A comparison of the data in Figure B.1 shows that the data for the pellets found through photographic processes does not follow a normal distribution. In fact this is a positive sign that shows the image calculation results give consistent results. It should be expected that of the different average diameters (number mean, mass mean, Sauter mean) the more accurate result is the number mean. The results also show a systematic error caused by the method of processing which gives a larger apparent diameter than the true diameter. This can be seen physically when

looking at raw vs. processed photographs. There is one condition of processing the photos, and one condition of optical distortion and both conditions contribute to overall systematic error.

The first processing error is the enlargement of the measured area ("area swelling") due to the object sharpness combined with interference objects. During processing the background subtraction causes a "halo" around objects that tends to capture nearby interfering or overlapping objects. The halo itself is caused by the rolling ball radius parameter. When the threshold is set some of the interference captured in the halo is translated as the apparent object image which swells the overall area of the object from that of the true area. An exaggerated example is given in Figure B.2.

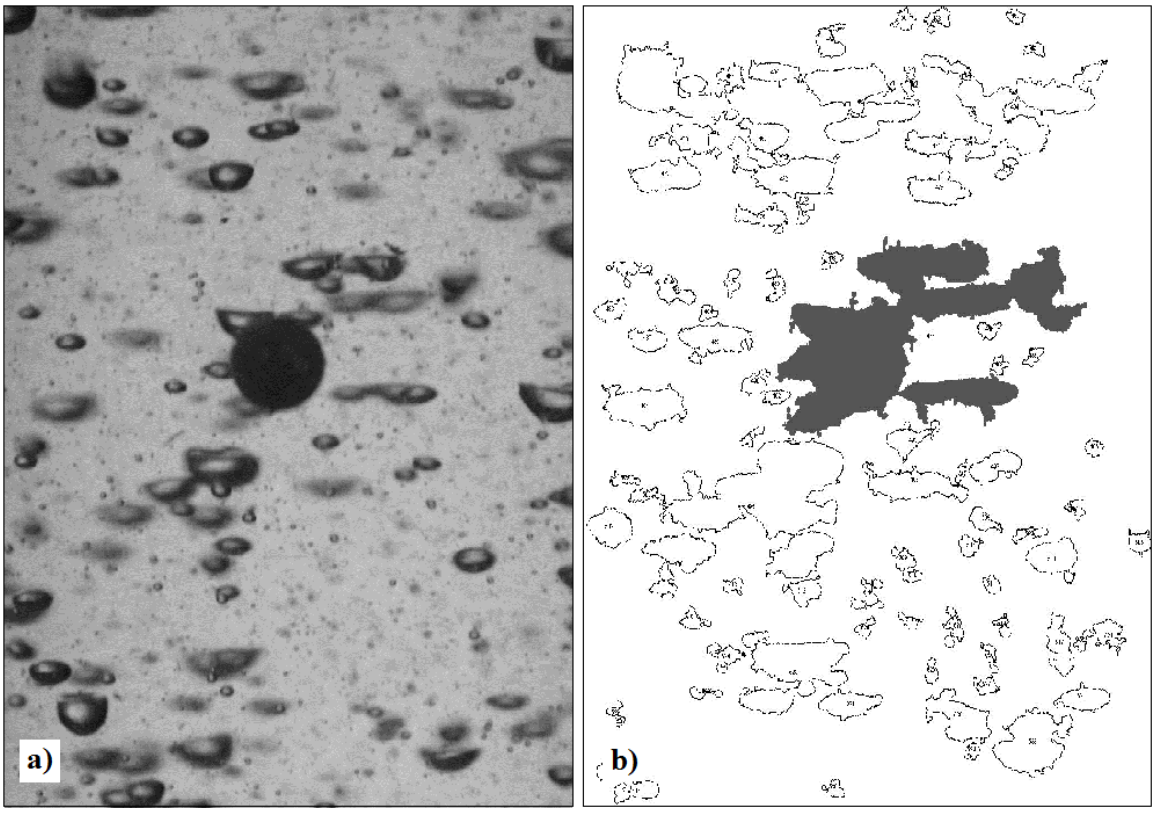

Figure B.2: Raw vs. processed image apparent area error

The second contribution to systematic error is a due to the optical distortion of the image. Optical distortion of the object occurs because of the change in refractive index between the fluid

medium, cylinder wall and air, the curvature of the wall, and the focus point of the camera. A simple Snell's Law analysis of a theoretical object in a curved cylinder has shown that the curvature of the wall actually creates more distortion than the changes in refractive index alone. Assuming the focus point of the camera is adjusted to the centerline of the column, a bubble will appear larger than its true size when it is farther away from the focus point fore and aft as well as left and right. It has been observed that more significant distortion occurs because of focal point error. Distortion error will also increase due to the coupling of focus point error with wall curvature distortion. An example of this can be seen in Figure B.3 when comparing the airsoft pellets near the center of the column (d_1 = 6.51 mm) with that to the right in focus (d_2 = 7.02 mm) and out of focus (d_3 = 8.28 mm) as well as to the right and out of focus (d_4 = 11.75).

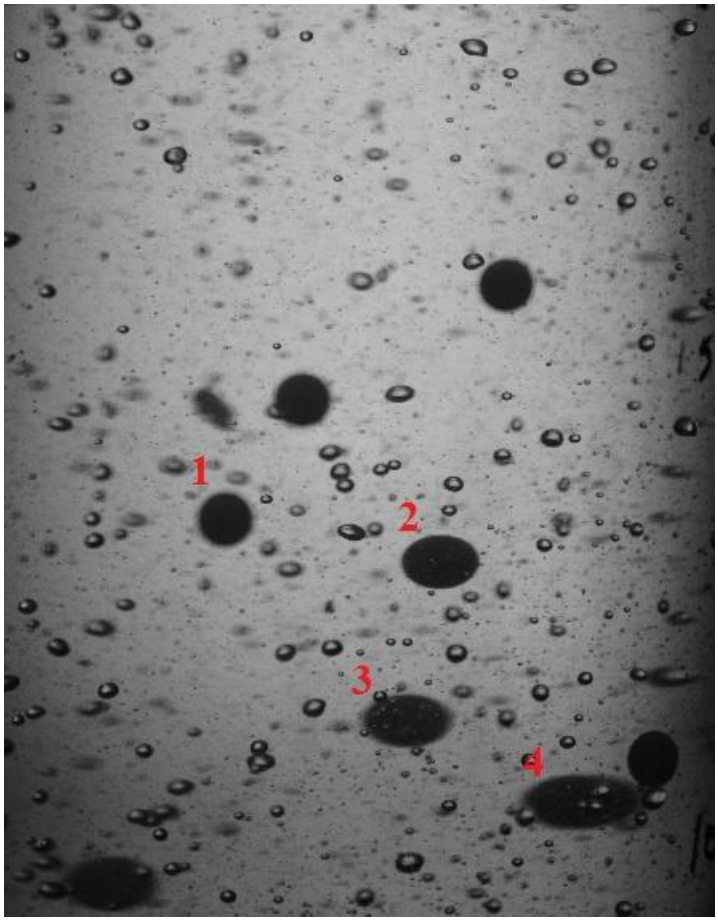

Figure B.3: Example of optical distortion error

The optical distortion portion of the systematic error can be partially mitigated by narrowing the field of view to a section of the column closer to the centerline. This mitigation will affect how many bubbles can be captured per picture, but since the number of pictures taken and analyzed can be increased relatively simply the additional processing is justified by achieving more accurate results. The effect of focus fore and aft of the centerline cannot be avoided, and neither can the error due to area swelling. In fact, for sections of the column where frothing is present such as at higher frequencies and amplitudes, the processed results cannot be relied upon based on the gross error due to area swelling.

APPENDIX C

SELECTED BIBLIOGRAPHY

Bennett, M.A., Luke, S.P., Jia, X., West, R.M., Williams, R.A. (1999), Analysis and Flow Regime Identification of Bubble Column Dynamics, 1st World Congress on Industrial Process Tomography, Buxton, Greater Manchester, April 14-17.

Buchholz, H., Buchholz, R., Lucke, J., and Shugerl, K. (1978), Bubble Swarm Behavior and Gas Absorption in Non-Newtonian Fluids in Sparged Columns, Chemical Engineering Science, Vol. 33, pp. 1061-1070.

Burgess, J.M. and Calderbank, P.H. (1975), The Measurement of Bubble Parameters in Two-Phase Dispersions I: The Development of an Improved Probe Technique, Chemical Engineering Science, Vol. 30, pp. 743-750.

Cartellier, A. (1990), Optical Probes for Local Void Fraction Measurements: Characterization of Performance, Review of Scientific Instruments, Vol. 61, No. 2, pp. 874-896.

Fand, R.M. and Cheng, P. (1963), The Influence of Sound on Heat Transfer From a Cylinder in Crossflow, International Journal of Heat and Mass Transfer, Vol. 6, pp. 571-596.

Gibbons, J.H. and Houghton, G. (1961), Effects of Sonic Vibrations on Boiling, Chemical Engineering Science, Vol. 15, No. 1 & 2, pp. 146-148.

Groen, J.S., Oldeman, R.G.C., Mudde, R.F. and Van den Akker, H.E.A. (1996), Coherent Structures and Axial Dispersion in Bubble Column Reactors, Chemical Engineering Science, Vol. 51, No. 10, pp. 2511-2520.

Kunii, D., Levenspiel, O. (1969), Fluidization Engineering, 1st ed., Wiley, New York.

Mueller, S.G. (2009), Optical Measurements in Gas-Liquid Stirred Tanks, PhD Dissertation, Washington University, St. Louis, MO.

Nakanoh, M. and Yoshida, F. (1980), Gas Absorption by Newtonian and Non-Newtonian Liquids in a Bubble Column, Industrial and Chemical Engineering Process Design and Development, Vol. 19, pp. 190-195.

Nyborg, W.L. and Rodgers, A. (1967), The Motion of Liquid Inside a Closed Vibrating Vessel, Biotechnology and Bioengineering, Vol. 9, pp. 235-256.

Shah, Y.T., Kelkar, B.G. and Godbole, S.P. (1982), Design Parameters Estimations for Bubble Column Reactors, AIChE Journal, Vol. 28, No. 3, pp. 353-379.

Shigley,J.E. and Mischke, C.R. (1996), Standard Handbook of Machine Design, 2nd ed., McGraw-Hill, New York, New York.

VITA

Adam Leland Still

Candidate for the Degree of

Master of Science

Thesis: MULTIPHASE PHENOMENA IN A VIBRATING COLUMN REACTOR

Major Field: Mechanical and Aerospace Engineering

Biographical:

Education:

Bachelor of Science degree in Aerospace Engineering, Oklahoma State University, Stillwater, Oklahoma in May 2010.

Bachelor of Science degree in Mechanical Engineering, Oklahoma State University, Stillwater, Oklahoma in May 2010.

Master of Science in Mechanical and Aerospace Engineering at Oklahoma State University, Stillwater, Oklahoma in May, 2012.

Experience:

2000-2004	F-15E Aircraft Maintenance Technician	United States Air Force
2004-2007	Technical Instructor	United States Air Force
2008-2010	Student Engineering Intern	Tinker Air Force Base
2010 -	Technical Staff	Sandia National Laboratories

Professional Memberships:

American Institute for Astronautics and Aeronautics (AIAA)

American Society of Mechanical Engineers (ASME)

Name: Adam L. Still Date of Degree: July, 2012

Institution: Oklahoma State University Location: Stillwater, Oklahoma

Title of Study: MULTIPHASE PHENOMENA IN A VIBRATING COLUMN REACTOR

Pages in Study: 212 Candidate for the Degree of Master of Science

Major Field: Mechanical and Aerospace Engineering

Scope and Method of Study:

The scope of the project includes the design, construction and validation of an experimental setup as well as an experiment to determine the effect of increasing amplitude on mass transfer, void fraction, and bubbles size. The design of the experimental set up includes a shaker device and an instrumented bubble column reactor. Mass transfer measurements were taken using a dissolved oxygen probe while void fraction and bubble sizes were determined from photographs of the air-water interface and bubbles in the column section respectively.

Findings and Conclusions:

An experimental set up was designed and built and the results of preliminary tests were used to compare the mass transfer, void fraction and bubble size data with previous research. The results show good agreement with the literature in form and magnitude. Observations of bubble stability phenomena were also seen to agree with previous findings. A stability frequency model was expanded to show application to vacuum head pressures, previously untested. The experimental set up was validated based upon the comparison with previous research. The results from the effect of amplitude experiments showed maxima within the trends similar to that found for lower amplitudes for both mass transfer and void fraction. An optimum amplitude was found to be independent of frequency for mass transfer, but not for void fraction or bubble size which did not show maxima in the frequency range tested. Mass transfer results did not agree well with theory predicted by Waghmare (2008), but upon further inspection of author's data it was found not to agree either, contrary to his report. ANOVA was used to show that Bjerknes number is a more influential factor for both this research and Waghmare (2008) than previously predicted. A similar analysis was performed for the void fraction data. The void fraction data of Waghmare showed a dependence on specific input power and superficial gas velocity as predicted, but the results of this research showed a contrary dependence on Bjerknes number. The difference was presumed to be caused by the different methodologies used.

ADVISER'S APPROVAL: Dr. Afshin J. Ghajar